

**MODELING THE CHEMOTAXIS BEHAVIORS
OF *C. ELEGANS* USING NEURAL
NETWORKS: FROM ARTIFICIAL
TO BIOLOGICAL APPROACH**

BY

XIN DENG

B. Eng., Jilin University

M. Eng., Chongqing University

**A THESIS SUBMITTED
FOR THE DEGREE OF DOCTOR OF PHILOSOPHY
DEPARTMENT OF ELECTRICAL AND COMPUTER ENGINEERING
NATIONAL UNIVERSITY OF SINGAPORE**

2013

DECLARATION

I hereby declare that this thesis is my original work and it has been written by me in its entirety. I have duly acknowledged all the sources of information which have been used in the thesis.

This thesis has also not been submitted for any degree in any university previously.

A handwritten signature in black ink, reading 'Deng Xin', is written over a horizontal line. The signature is fluid and cursive.

22 January 2013

Acknowledgments

I would like to express my deepest appreciation to Prof. Xu Jian-Xin for his inspiration, excellent guidance, support and encouragement. His erudite knowledge and deepest insights on the fields of inter-discipline have been the most inspirations and made this research work a rewarding experience. I owe an immense debt of gratitude to him for having given me the curiosity about the learning and research in the domains of control and computational neuroscience. Also, his rigorous scientific approach and endless enthusiasm have influenced me greatly. The progress of this PhD program would not be possible without his guidance. I consider myself most fortunate to work under his supervision, which has made the past four years such an enjoyable and rewarding experience.

Thanks also go to Electrical & Computer Engineering Department in National University of Singapore, for the financial support during my pursuit of a PhD.

I would like to thank my Thesis Advisory Committee members, A/Prof. K. C. Tan and A/Prof. Peter, C. Y. Chen at National University of Singapore, who provided me a lot of suggestive questions for my research. Furthermore, it is a wonderful experience for me to become the teaching assistant of their module EE4305. I am also grateful to all my friends in Control and Simulation Lab, the National University of Singapore. Their kind assistance and consideration have made my life in Singapore easy and colorful.

To my wonderful parents, thank you for supporting me in my decision of pursuit of PhD. And finally to lawyer Guo Jingjing, my darling wife, thanks for your consideration and supporting during these years.

Contents

Acknowledgments	I
Summary	VIII
List of Tables	X
List of Figures	XI
Nomenclature	XXIII
1 Introduction	1
1.1 <i>C. elegans</i>	2
1.2 Neural Networks	4
1.3 Current Models	6
1.4 Contribution	10
1.5 Synopsis of The Thesis	12
2 Modeling the Chemotaxis Behaviors of <i>C. elegans</i> Based on the Artificial Dynamic Neural Networks	14
2.1 Introduction	14
2.2 Mathematical Model and Training Method	16
2.2.1 Kinematic Model	16

2.2.2	Attractant and Repellent Concentration	17
2.2.3	DNN Model	18
2.2.4	Training Method	19
2.3	Dual-sensory Behavioral Model	24
2.3.1	DNN for Dual-sensor Model	24
2.3.2	Learning Tasks	25
2.3.3	Testing Results	29
2.4	Single-sensory Behavioral Model	32
2.4.1	DNN for Single-sensory Model	32
2.4.2	Learning Tasks	33
2.4.3	Testing Results	37
2.5	Conclusion	40

3 Modeling the Chemotaxis Behaviors of *C. elegans* Based on the Biological Wire Diagram with Invariant Speed **42**

3.1	Dual-sensory Behavioral Model	43
3.1.1	Wire Diagrams	43
3.1.2	Learning Tasks	46
3.1.3	Testing Results	46
3.2	Single-sensory Behavioral Model	48
3.2.1	Wire Diagrams	49
3.2.2	Learning Tasks	50
3.2.3	Testing Results	51
3.3	Integrated Behavioral Model	53
3.3.1	Wire Diagrams	54

3.3.2	Learning Tasks	56
3.3.3	Testing Results	56
3.4	Conclusion	58

4 Modeling the Chemotaxis Behaviors of *C. elegans* Based on the Biological Wire Diagram with Speed Regulation 60

4.1	Introduction	61
4.2	Kinematics Models	63
4.3	Dual-sensory Behavioral Model	64
4.3.1	Learning Tasks	64
4.3.2	Testing Results	70
4.4	Single-sensory Behavioral Model	72
4.4.1	Learning Tasks	72
4.4.2	Testing Results	77
4.5	Integrated Dual-sensory Behavioral Model	79
4.5.1	Learning Tasks	79
4.5.2	Testing Results	83
4.6	Integrated Single-sensory Behavioral Model	86
4.6.1	Learning Tasks	87
4.6.2	Testing Results	89
4.7	Comparative Analysis	93
4.7.1	Wire Diagram Analysis	94
4.7.2	Behaviors Analysis	98
4.7.3	Performance with Noises	101
4.8	Conclusion	105

5 Modeling the 3D Undulatory Locomotion Behavior of *C. elegans*

Based on the Artificial DNN	106
5.1 Introduction	106
5.2 Anatomical Structure of <i>C. elegans</i> for Locomotion	111
5.2.1 Muscle and Body Structure	111
5.2.2 Neuronal Structure for Locomotion	113
5.3 Locomotion System Modeling	114
5.3.1 Head DNN	114
5.3.2 CPG	116
5.3.3 Body DNN	118
5.3.4 Model of Muscle	119
5.4 3D Locomotion Behaviors Modeling	121
5.4.1 Motion Modality	121
5.4.2 Muscle Length and Joint Angle	123
5.4.3 Muscle Lengths and Outputs of Motor Neurons	126
5.4.4 Shape Determination in 3D	132
5.5 Optimization	133
5.5.1 Head DNN for Decision Making	133
5.5.2 Body DNN for Signal Transmission	138
5.6 Testing Results	140
5.6.1 Periodically Changing of Muscle Length	140
5.6.2 Forward and Backward Locomotion	141
5.6.3 The Shape During Locomotion	142
5.6.4 Finding Food	145

5.6.5	Avoiding Toxin	146
5.6.6	Finding Food and Avoiding Toxin Simultaneously	146
5.7	Comparative Analysis	148
5.7.1	Validation by Analyzing the Video of the Real Worm	148
5.7.2	Turning Behaviors Analysis	150
5.7.3	Trajectory Analysis	151
5.7.4	Head DNN Analysis	153
5.8	Conclusion	155

6 Modeling the Undulatory Locomotion Behavior of *C. elegans* Based

on the Biological Wire Diagram		156
6.1	Biological Model for Undulatory Locomotion	157
6.1.1	Head Wire Diagram	157
6.1.2	Motor Neurons and Muscles	158
6.2	Undulatory Locomotion Modeling	160
6.2.1	Sensory Neurons	160
6.2.2	CPG	161
6.2.3	Motor Neuron	162
6.2.4	Muscle	163
6.2.5	Body Segment	166
6.3	Testing Results	168
6.3.1	Optimization and Parameter Setting	168
6.3.2	Chemotaxis Behavior	172
6.3.3	Quantitative Analysis	175
6.3.4	Wire Diagram Patterns	177

6.4	Worm-like Robot	178
6.4.1	Hardware Components	178
6.4.2	Components Assembly	181
6.4.3	Experimental Results	182
6.5	Conclusion and Discussion	187
7	Conclusions	190
7.1	Summary and Conclusion	190
7.2	Suggestions for Future Work	194
	Bibliography	196
	Appendix: Publication List	211

Summary

C. elegans is a tiny nematode worm with a largely invariant nervous system, consisting of exactly 302 neurons with known connectivity and functions. Recently, various experimental techniques, such as targeted cell killing and genetic mutations, are implemented to explore the behavioral roles of these neurons. This tiny worm provides us with the first possibility of understanding the complex behaviors of an organism from the genetic level up to the system level. The main objective of this thesis is to reveal the mechanisms underlying the chemotaxis behaviors of *C. elegans* based on its nervous system. In this thesis, several complex chemotaxis behaviors of *C. elegans* are explored, which include food attraction, toxin avoidance, and varying locomotion speed. The research strategy for this thesis is using both artificial and biological neural networks to model the chemotaxis behavior and undulatory locomotion of *C. elegans*. At the first step, *C. elegans* is considered as a point mass, and the chemotaxis behaviors for food attraction and toxin avoidance are explored based on the artificial neural networks. Then the biological wire diagrams are provided to investigate these chemotaxis behaviors. At the second step, the body segment is added, and the undulatory locomotion behaviors of *C. elegans* are investigated by using both artificial and biological neural networks. The novelty and the uniqueness of the proposed behavioral models are characterized by six attributes. First, all the biological behavioral models are constructed by extracting the neural wire diagram from sensory neurons to motor neurons, where sensory neurons are specific for chemotaxis behaviors. Second, the turning and the speed regulation mechanisms are investigated. Thus, these behavioral models can mimic the slight turn and Ω turn, as well as reduce the speed when approaching the food and leaving far from the

toxin. Third, chemotaxis behaviors are characterized by a set of switching logic functions that decide the orientation and speed. All models are implemented by using dynamic neural networks (DNN). The real time recurrent learning (RTRL) algorithm and the differential evolution (ED) are adopted to train these DNNs. Fourth, the 3D undulatory locomotion behaviors of *C. elegans* are explored based on the artificial undulatory model. Fifth, the undulatory locomotion behaviors of *C. elegans* are further investigated based on the biological neural wire diagram and muscle structure. Both the artificial and biological undulatory locomotion models can perform the chemotaxis behaviors of finding food and avoiding toxin simultaneously. At last, the testing results of these behavioral models are analyzed by comparing with the experiment results, which are used to verify the validity and effectiveness of these models. Furthermore, a worm-like robot has been constructed to perform the undulatory locomotion based on the theoretical results. The research in the thesis provides a new way to investigate and model the essence of chemotaxis and locomotion of low level animals. These chemotaxis and locomotion models could serve as the prototypes for other footless animals and facilitate the biomimetic motion in robotics.

List of Tables

1.1	The differences between gap junction and chemical synapse	5
5.1	Parameters settings	139
6.1	Neuromuscular connection	168
6.2	Parameters setting	171

List of Figures

1.1	Image of <i>C. elegans</i> [1]	2
1.2	Life circle of <i>C. elegans</i> [1]	2
1.3	Ω turn of <i>C. elegans</i>	3
2.1	<i>C. elegans</i> ' movement in the x-y plane. The head of <i>C. elegans</i> is modeled as a point source in the x-y plane with velocity vector V at head angle θ measured from the x-axis [2].	17
2.2	The potential field of concentration distributed in a square area with the range $[-0.2, 0.2]$ meters, where $C_{\max} = 2$ mM and $S = 0.01$	18
2.3	Topological structure for a dual-sensory model. V_1 and V_2 are the right and left sensory neurons, and V_6 and V_7 are the right and left motor neurons, respectively.	24
2.4	SLFs for food attractant. The x-axis depicts the food concentration difference between the left-side and right-side sensors, which are located 2×10^{-5} m apart spatially [3]. The y-axis shows the voltage of the output neurons. V_6 stands for the right motor neuron and V_7 stands for the left motor neuron, both with the range from -1 to 1 V.	25
2.5	The movement of dual-sensory model during food attraction. When $\Delta C = C_{f, \text{left}} - C_{f, \text{right}} > 0$, the food locates on the left side. From SLFs, motor neuron outputs satisfy $V_6 > V_7$ ($V_{\text{right}} > V_{\text{left}}$), namely, the right-side speed is faster than the left-side speed, so <i>C. elegans</i> turns left. Similarly when $C_{f, \text{left}} - C_{f, \text{right}} < 0$, so $V_{\text{left}} > V_{\text{right}}$ and <i>C. elegans</i> turns right. If $\Delta C_f = 0$, the direction cannot be determined and information of $\Delta C(t - 1) = 0$ will be required.	26
2.6	SLFs for toxin avoidance. The x-axis depicts the toxin concentration difference between the left-side and right-side sensors, which are located 2×10^{-5} m apart spatially. The y-axis describes the motor neurons' outputs. V_6 is the right motor neuron and V_7 is the left motor neuron. Their values are between -1 and 1	27

- 2.7 The movement of dual-sensory model during toxin avoidance. When $\Delta C = C_{tx,left} - C_{tx,right} > 0$, the toxin locates on the left side. From the switching logic, $V_7 > V_6$ or $V_{left} > V_{right}$, namely, the left-side speed is faster than the right-side speed, so *C. elegans* turns right. Similarly when $C_{tx,left} - C_{tx,right} < 0$, $V_6 > V_7$ or $V_{left} < V_{right}$ and *C. elegans* turns left. 27
- 2.8 SLFs for the multi-tasks. The input signals are $C_{f,left}$, $C_{f,right}$, $C_{tx,left}$, $C_{tx,right}$. When $\Delta C_{f,tx} > 0$ ($\Delta C_f > \Delta C_{tx}$), $\tanh(\Delta C_{f,tx}) > 0$ makes $V_6 > V_7$, resulting the worm turn left. It is vice versa for $\Delta C_{f,tx} < 0$. . . 28
- 2.9 The behavior of dual-sensory model of *C. elegans* near a food source. The point of highest food concentration is point (0,0). *C. elegans* starts at (0.1, -0.1) and finally finds the food source at (0,0). 30
- 2.10 The behavior of dual-sensory model of *C. elegans* near four toxin sources. Four toxin resources are located at points of (-0.2, 0), (-0.1, -0.15), (0, 0.2), and (0.1, -0.1), respectively. The worm starts at three different positions (-0.11, -0.1), (0.07, -0.1), (-0.03, 0.15) with head angle 135°, 180°, 180°, respectively. The worm avoids the toxin repellents and moves towards a safe position away from toxin. 30
- 2.11 The behavior of dual-sensory model of *C. elegans* in between food attractant and toxin repellent. The food and toxin are put at points (-0.1, 0) and (0.1, 0), respectively. *C. elegans* starts at (0.08, 0.05) with head angle 90° and finally arrives at the food source placed at (-0.1, 0.0). 31
- 2.12 Topological structure for a single-sensory model. The network architecture consists of one sensory neuron V_1 , which mimics the biological sensory neuron ASE. The memory neuron is V_2 , which plays a similar role as the biological neuron AIY. Two motor neurons V_6 for right and V_7 for left are outputs of DNN. V_3 , V_4 , V_5 are three hidden neurons. 32
- 2.13 SLFs for the single-sensory model for food attraction. The x-axis depicts the food concentration difference between two consecutive time instances, $\Delta C(t) = C(t) - C(t - 1)$. The y-axis shows the output of the motor neurons according to the $\Delta C(t)$. V_6 is the right side motor neuron and V_7 is the left side motor neuron, and their values change between -1 and 1. 34
- 2.14 SLFs for the single-sensory model for toxin avoidance. The x-axis depicts the toxin concentration difference between two consecutive time instances, $\Delta C(t) = C(t) - C(t - 1)$. The y-axis presents the output of the motor neurons according to $\Delta C(t)$. V_6 is the right side motor neuron and V_7 is the left side motor neuron, and their values change between -1 and 1. . . 34

2.15	Movement demonstration for food attraction. If $C_f(t) > C_f(t-1)$, $C. elegans$ is in the correct direction, so $V_{left}(V_7) = V_{right}(V_6)$ and it goes straightly. When $C_f(t) \leq C_f(t-1)$ (wrong direction), the output of V_{right} is smaller than the output of V_{left} , which makes $C. elegans$ turn right. . .	35
2.16	Movement demonstration for toxin avoidance. If $C_{tx}(t) < C_{tx}(t-1)$, $C. elegans$ is in the correct direction, so $V_{left}(V_7) = V_{right}(V_6)$ and it goes straightly. If $C_{tx}(t) \geq C_{tx}(t-1)$ (wrong direction), the output of V_{right} is smaller than V_{left} , which makes $C. elegans$ turn right.	35
2.17	The logic switch surface for the integrated behavior. When $\Delta C_{f,tp}(t) = C_f(t) - C_f(t-1) = 1$ and $\Delta C_{tx,tp}(t) = C_{tx}(t) - C_{tx}(t-1) = -1$, it is the most favorable direction, $V_6(t) = V_7(t)$ and $C. elegans$ moves straightforward. When $\Delta C_{f,tp}(t) = -1$ and $\Delta C_{tx,tp}(t) = 1$, it is the most unfavorable direction, the difference between $V_6(t)$ and $V_7(t)$ is maximum and $C. elegans$ turns right as sharp as possible. When $\Delta C_{f,tp}(t)$ and $\Delta C_{tx,tp}(t)$ have similar values, the information is unclear to $C. elegans$ due to the mixture of food and toxin, and the worms turns right in a gentle way for further exploration.	36
2.18	Food attraction behavior for single-sensory model. A food source is located at point $(0,0)$. $C. elegans$ starts at $(-0.1, -0.1)$ with head angle 135° . . .	38
2.19	Single-sensory model for toxin avoidance. Four toxin resources are located at points $(-0.2, 0)$, $(-0.1, -0.15)$, $(0, 0.2)$, and $(0.1, -0.1)$. $C. elegans$ starts at three different positions $(-0.12, -0.13)$, $(-0.03, 0.18)$, $(0.08, -0.1)$ with head angle 180° , and it successfully avoids the toxin sources. . . .	39
2.20	Single-sensory model for integrated behavior. A food source and a toxin source are put at points $(-0.1, 0)$ and $(0.1, 0)$, respectively. $C. elegans$ starts at the toxin area $(0.03, 0)$ with head angle 270° . It moves towards food, and ends at food source.	40
3.1	The wire diagram of dual-sensory behavioral model for food attraction. Neuron ASEL and ASER are the left and right sensory neurons for food, respectively. The outputs are neurons DB and VB for left and right sides, and the rest are hidden neurons.	43
3.2	The wire diagram of dual-sensory behavioral model for toxin avoidance. The neuron ASHL and ASHR are the left and right toxin sensory neurons respectively. DB and VB are the left and right motor neurons. Others are hidden neurons.	44
3.3	The chemotaxis behavior of $C. elegans$ produced by the dual-sensory behavioral model for food attractant. One food source locates at the point $(0,0)$. $C. elegans$ starts at $(-0.1, 0.1)$ with the head angle 180° and ends at the food source $(0,0)$	47

3.4	The chemotaxis behavior of <i>C. elegans</i> produced by the dual-sensory behavioral model nearby four toxin repellents. Four toxin resources locate at $(-0.2,0)$, $(-0.1,-0.15)$, $(0,0.2)$, and $(0.1,-0.1)$, respectively. The worm starts at three different positions $(-0.11,0.1)$, $(0.08,-0.1)$, $(-0.02,0.17)$ with head angles 135° , 180° , and 180° , respectively. The worm avoids the toxin repellents and moves towards a safe position away from toxin.	47
3.5	The wire diagram for food attraction. Neuron ASE is the sensory neuron for food. Neuron AIY functions as the memory neuron recording the previous food concentration information $C_f(t-1)$. The outputs are neurons DB and VB for left and right sides, and the rest are hidden neurons. . . .	49
3.6	The wire diagram for toxin avoidance. The neuron ASH is the toxin sensory neuron. The neuron AIY functions as a memory neuron to record the previous toxin concentration $C_{tx}(t-1)$. DB and VB are the left and right motor neurons. Others are hidden neurons.	50
3.7	The chemotaxis behavior of <i>C. elegans</i> produced by the single-sensory behavioral model for food attraction. One food source locates at the point $(0,0)$. <i>C. elegans</i> starts at $(0.1, -0.15)$ with the head angle 180° and ends at the food source $(0,0)$	52
3.8	The chemotaxis behavior of <i>C. elegans</i> produced by the single-sensory behavioral model nearby four toxin repellents. Four toxin resources locate at $(-0.2,0)$, $(-0.1,-0.15)$, $(0,0.2)$, and $(0.1,-0.1)$, respectively. The worm starts at three different positions $(-0.16, -0.01)$, $(0,0.18)$, $(0.08,-0.05)$ with head angle 180° , respectively. The worm avoids the toxin repellents and moves towards a safe position away from toxin.	53
3.9	Neural diagram for a dual-sensory behavioral model for both food attraction and toxin avoidance. ASEL and ASER are left-side and right-side input neurons for food concentration. ASHL and ASHR are left-side and right-side input neurons for toxin concentration. VB and DB are right-side and left-side motor neurons, and the rest are hidden neurons.	54
3.10	Neural diagram for a single-sensory behavioral model for both food attraction and toxin avoidance. ASE is the input neuron for food concentration. ASH is the input neuron for toxin concentration. AIY is a memory neuron. VB and DB are right-side and left-side motor neurons, and the rest are hidden neurons.	55
3.11	The chemotaxis behavior of the dual-sensory behavioral model for food attraction and toxin avoidance. The food and toxin locate at $(-0.1,0)$ and $(0.1,0)$, respectively. <i>C. elegans</i> starts at $(0.08,0.04)$ with the head angle 90° , and at the end reaches the food source.	56

3.12	The chemotaxis behavior of the single-sensory behavioral model for food attraction and toxin avoidance. The food and toxin locate at $(-0.1,0)$ and $(0.1,0)$ respectively. <i>C. elegans</i> starts at $(0.08,0.04)$ with the head angle 270° , and at the end reaches the food source.	57
3.13	The chemotaxis behavior of the single-sensory behavioral model nearby a toxin repellent located at $(0.1,0)$. The <i>C. elegans</i> starts from $(0.07,0.04)$ with head angle 90° , and finally it avoids the toxin.	57
4.1	Plot of switching logic function for food attraction with speed changing based on dual-sensory neuron models. When $\Delta C_{f,sp}(t) = 0$, <i>C. elegans</i> goes straightly. When $\Delta C_{f,sp}(t) > 0$, $V_{right}(t) > V_{left}(t)$, the worm turns left and vice versa. When $\overline{C}_f(t)$ is smaller, outputs are larger and vice versa. Here $C_{max,f}$ is set to be 2. The inputs of $C_{f,left}(t)$ and $C_{f,right}(t)$ range from 0 to 2, hence the range of $\overline{C}_f(t)$ is $[0, 2]$, and $\Delta C_{f,sp}(t)$ is $[-2, 2]$	66
4.2	Movement of <i>C. elegans</i> during food attraction. When $\Delta C_{f,sp}(t) = 0$, <i>C. elegans</i> goes straightly. When $\Delta C_{f,sp}(t) > 0$, the worm turns left (left figure) and vice versa (right figure).	67
4.3	Plot of switching logic function for toxin avoidance with speed changing based on dual-sensory neuron models. When $\Delta C_{tx,sp}(t) = 0$, <i>C. elegans</i> goes straightly. when $\Delta C_{tx,sp}(t) > 0$ the outputs are $V_{left}(t) > V_{right}(t)$ that make the worm turns right and vice versa. When $\overline{C}_{tx}(t)$ is large, the outputs are large. When the $\overline{C}_{tx}(t)$ is near to 0, the outputs are down to zero.	68
4.4	Movement of <i>C. elegans</i> during toxin avoidance. When $\Delta C_{tx,sp}(t) = 0$, <i>C. elegans</i> goes straightly. When $\Delta C_{tx,sp}(t) > 0$ the worm turns right (left figure) and vice versa (right figure).	69
4.5	The test results of food attraction with speed changing for dual-sensory model. One food source is located at point $(0,0)$ with Gaussian distribution. The worm starts at three different locations $(-0.1, -0.1)$, $(0.12, -0.06)$, $(1, 0.14)$ with initial angle $\theta(0) = 0^\circ$. Finally the worm finds the correct direction towards the food and stops after approaches food.	70
4.6	The test results of toxin avoidance with speed changing. Four toxin resources locate at $(-0.2, 0)$, $(-0.1, -0.15)$, $(0, 0.2)$, and $(0.1, -0.1)$. The worm starts at three different positions $(-0.18, -0.03)$, $(0, 0.15)$, $(0.08, -0.1)$ with initial head angle randomly. Finally the worm successfully finds the lower toxin concentration place to settle down.	71

- 4.7 The SLFs for the single sensory model during food attraction. If $C_f(t) > C_f(t-1)$, *C. elegans* moves in the correct direction and will move the same direction. When $C_f(t) \leq C_f(t-1)$ (wrong direction), the output of V_{right} is smaller than the V_{left} , then *C. elegans* turns right. When the input $C_f(t)$ is approaching to $C_{max,f}$, the outputs of both motor neurons will approach to zero. In general, a smaller $C(t)$ will yield relative larger outputs. 74
- 4.8 Movement of the single sensory model for (a) food attraction, and (b) toxin avoidance. In (a), if $C_f(t) \geq C_f(t-1)$, *C. elegans* is in the correct direction, thus goes straightly. When $C_f(t) < C_f(t-1)$ (wrong direction), the output of V_{right} is smaller than V_{left} , which makes *C. elegans* turn right. In figure (b), the behavior of toxin avoidance is opposite to the food attraction. If $C_{tx}(t) \geq C_{tx}(t-1)$, *C. elegans* turns right. When $C_{tx}(t) < C_{tx}(t-1)$, it go straightly. 74
- 4.9 The SLFs for single sensory model during toxin avoidance. If $C_{tx}(t) < C_{tx}(t-1)$, *C. elegans* moves in the correct direction and will move the same direction. When $C_{tx}(t) \geq C_{tx}(t-1)$ (wrong direction), the output of V_{right} is smaller than the V_{left} , then *C. elegans* turns right. When the input $C_{tx}(t)$ is near to zero, the outputs of both motor neurons will approach to zero. In general, a smaller $C_{tx}(t)$ will yield relative smaller outputs. 76
- 4.10 Simulation results for the food attraction of single-sensory model. Food source is located at the point (0,0) with Gaussian distribution. *C. elegans* starts at two different locations $(-0.08, -0.07)$, $(0, 0.12)$ with initial angle 180° . The worm moves towards the food source and settles down when it approaches the food after some right turns. 78
- 4.11 Simulation results for the toxin avoidance on single-sensory model. Four toxin resources locate at $(-0.2, 0)$, $(-0.1, -0.15)$, $(0, 0.2)$, and $(0.1, -0.1)$. *C. elegans* starts at three different positions $(-0.13, -0.11)$, $(0.07, -0.1)$, $(0, 0.18)$ with head angle randomly. It successfully finds the lower toxin concentration place to settle down. 78
- 4.12 Plots of SLFs for the integrated model. In (a) $\overline{C}_f(t)$ and $\overline{C}_{tx}(t)$ determine the motor neurons outputs. In (b), $\Delta C_{sp}(t)$ controls the orientation changing by spatial information, function as dual-sensory model. In (c), $\Delta C_{tp}(t)$ controls the orientation changing by temporal information, function as single-sensory model. 81
- 4.13 (a) is the test results of integrated model. (b) is the enlarged area of (a) with x-axis $[-120 -40]$ and y-axis $[-180 -120]$ 84

4.14	(a) is the 3-D plot of food and toxin distributions with a large overlapping. (b) illustrates the corresponding gradient information of (a). From (b) we can see that there are some areas where the gradients of food and toxin are identical (intersection places).	85
4.15	The test results when the food and toxin sources are overlapped largely.	86
4.16	Plot of switching logic function for the integrated chemotaxis behavioral model. In (a), $C_f(t)$ and $C_{tx}(t)$ determine the outputs of motor neurons for speed regulation. In (b), $\Delta C_{ft}(t)$ controls the orientation.	88
4.17	Testing results for the integrated chemotaxis behavioral model in the first scenario. One food is located at point $(-0.11, 0)$ and one toxin is located at point $(0.11, 0)$ with slightly overlapped concentration.	90
4.18	Testing results for the integrated chemotaxis behavioral model in the second scenario. One food source is located at $(-0.03, 0)$ and one toxin source is located at $(0.03, 0)$ with largely overlapped concentration.	91
4.19	(a) 2D concentration distributions of food and toxin along x -axis. (b) The gradients of food and toxin concentrations along the positive direction (direction of x -axis).	91
4.20	Testing results for the integrated behavioral model in the third scenario. Twenty-five toxin resources are distributed as a 5×5 grid. One food source is located at $(0, 0.45)$	93
4.21	The similarity analysis of the resultant wire diagrams. (a) Thirty wire diagrams for the food attraction behavioral model are clustered into three groups by k-means algorithm. (b) Thirty wire diagrams for the toxin avoidance behavioral model are clustered into three groups by k-means algorithm. (c) Thirty wire diagrams for the integrated behavioral model are clustered into the same group.	94
4.22	(a) Resultant wire diagram for food attraction behavioral model. After the “all-off” neurons are removed and the “all-on” neurons are moved to downstream neurons, the simplified network contains six interneurons instead of twelve. (b) Resultant wire diagram for toxin avoidance behavioral model. After the “all-off” neurons are removed and the “all-on” neurons are moved to downstream neurons, the simplified network contains seven interneurons instead of thirteen.	96
4.23	Statistical analysis of trajectories for food attraction behavior model. (a) The relationship between speed and concentration. (b) The relationship between turning rate and concentration. (c) The relationship between turning rate and $dC(t)/dt$. (d) The relationship between probability of turning and $dC(t)/dt$	99

4.24	Testing results by adding the external noise.	102
4.25	Testing results by adding the internal noise.	102
4.26	Statistical analysis for food attraction behavior with noises. (a) The relationship between turning rate and concentration with the external and internal noises. (b) The relationship between probability of turning and $dC(t)/dt$ with the external and internal noises.	104
5.1	The image of <i>C. elegans</i> during locomotion. The arrows indicate the lifted parts of <i>C. elegans</i>	108
5.2	(a) Muscle structure of <i>C. elegans</i> . The muscles are divided into 4 quadrants on the transverse plane. (b) Body structure of <i>C. elegans</i> . Each quadrant contains 23 or 24 muscle cells. (c) The whole body is divided into 11 muscle segments according to the muscle structure and depicted as a multi-joint rigid link system with 13 joints and 12 links.	112
5.3	Neuronal circuit of <i>C. elegans</i> for locomotion. Motor neurons DB and VB are for forward locomotion; DA and VA are for backward locomotion; VD and DD are inhibitory neuron for muscles coordination.	113
5.4	DNN and the muscle structure of <i>C. elegans</i> . DNN is classified into three parts: head DNN, CPG, and body DNN. The head DNN contains six neurons that achieves the decision making function for chemotaxis behavior. CPG involves four neurons, C_1 and C_2 generating the sinusoid waves and C_3 and C_4 adjusting the phase lag. In the body DNN, two command neurons “PVC, AVB” and “AVA, AVD” switch the circuits for forward and backward locomotion. The signals are passed from the first segment to the last segment in sequence for forward locomotion (vice versa for backward locomotion), and are also transmitted to muscles. The muscles function as actuators and act according to motor neurons’ outputs.	115
5.5	<i>C. elegans</i> lies aside on the ground. We assume that the right side of <i>C. elegans</i> touches the ground. The ventral side is our left-hand side, and the dorsal side is our right-hand side, For simplicity and directviewing, muscles in four quadrants are renamed as: ld (left-down) for ventral-right, lu (left-up) for ventral-left, rd (right-down) for dorsal-right, and ru (right-up) for dorsal-left.	119
5.6	The connection between muscles and motor neurons.	121
5.7	(a) The shape of <i>C. elegans</i> on the x-y plane. The whole body is represented as 12 links and shapes as a sinusoid wave with 1.5 periods. (b)The shape of <i>C. elegans</i> on the x-z plane. It is obviously that some of the body parts lift up the ground, and the frequency is twice of that on the horizontal plane.	122

- 5.8 (a) One muscle segment i is shown in 3D. The lengths of muscles in four quadrants are denoted as l_{ru} , l_{lr} , l_{rd} , and l_{ld} . (b) The projection of the middle plane of the muscle segment of (a) (dotted line) on the x-y plane without shape change, which means all the four quadrant muscles are relaxed. (c) The projection of (a) on the x-y plane during sinusoid locomotion. (d) The projection of (a) on the x-z plane during sinusoid locomotion. Joint angles between link i and link $i + 1$ are measured as θ on the x-y plane and θ_v on the x-z plane, as shown in (c) and (d), respectively. 124
- 5.9 SLFs for food attraction and toxin avoidance. When $\Delta C_{ft}(t) \geq 0$, *C. elegans* goes towards the correct direction. $D_{OUT}(t) = 0$ means *C. elegans* does not need to turn its direction. When $\Delta C_{ft}(t) < 0$, *C. elegans* goes towards the wrong direction. In this case, $D_{OUT}(t)$ is greater than zero, which sends the turning signal to the body DNN. 134
- 5.10 Periodically changing of the lengths of muscles. (a) The four muscles vary in the first muscle segment. (b) The four muscles vary in the second muscle segment. 140
- 5.11 The 3D forward locomotion behavior of *C. elegans*. (a) The shape of *C. elegans* when it begins to move at the point (-0.5, 0, 0.02) at $t = 0$ s. (b) The shape of *C. elegans* at $t = 1$ s. (c) The shape of *C. elegans* at $t = 2$ s. During one period (2 s), it is obviously that some body parts lift up during forward locomotion. 142
- 5.12 The 3D backward locomotion behavior of *C. elegans*. (a) The shape of *C. elegans* at the beginning time $t = 0$ s. (b) The shape of *C. elegans* at $t = 1$ s. (c) The shape of *C. elegans* at $t = 2$ s. From these figures, it is obviously that *C. elegans* lifts up parts of its body during backward locomotion. 143
- 5.13 The shape of *C. elegans* during locomotion. (a) The outline of *C. elegans* at a random time. Joints 2, 6, and 10 are bent mostly and lifted up highest. Joints 0, 4, 8, and 12 touch the ground. (b) The projection of (a) on the x-y plane. It appears as a formal sinusoid wave. c) The projection of (a) on the x-z plane. Some body parts of *C. elegans* lift up to the ground. 144
- 5.14 Testing results for food attraction. One food source is located at (0,0) with Gaussian distribution. *C. elegans* starts at three different locations (-30,30), (0,-30), and (40,40), respectively. It moves towards the food source and finally moves around it. 145
- 5.15 Testing results for toxin avoidance. Nine toxin resources are distributed nonuniformly as a 3×3 grid. The locomotion model starts at three different positions (0,20), (20,30), and (10,-20), respectively. It successfully finds the zero toxin concentration places to settle down. 146

5.16	Testing results for finding food and avoiding toxin simultaneously. (a) Nine sources are distributed as a 3×3 grid. One food source (asterisk) is located at $(-30, 0)$ and other dots denote the toxin sources. <i>C. elegans</i> starts at two different locations $(0, 15)$ and $(30, -10)$, respectively. It successfully escapes from the toxin sources. Furthermore, once <i>C. elegans</i> smells the food concentration (starting from $(0, 15)$), it navigates itself towards the food source and finally moves around it. (b) The zoomed image of the rectangular area in (a). It shows the Ω turn in 2D. (c) The zoomed image of the rectangular area in (a). It shows the Ω turn in 3D. It can be observed that some parts of the body lift above the ground.	147
5.17	Image of actual <i>C. elegans</i> body are divided into 12 links in computer software to analyze.	148
5.18	Images of <i>C. elegans</i> during fast forward locomotion at time $t=0, 1, 2$ s. The body shape is 1.5 periods of sinusoid wave length, and one periods time is 2 s	149
5.19	Analysis of the turning behaviors. (a) The decision making of the model happens at Point A and B. Track a is the trajectory of straightly forward locomotion. Track b is the trajectory of turning starting at Point A. The turning degree is decided by V_{OUT} . If V_{OUT} is large enough, Ω turn happens, otherwise the slightly turning happens. (b) Track c is the trajectory of straightly forward locomotion. Track d is the trajectory of turning starting at Point B. In this case, Ω turn cannot happen.	150
5.20	Trajectory analysis. (a) Trajectory of turning with small magnitude. (b) Trajectory of the straight forward locomotion. (c) Trajectory of the slight turn. (d) Trajectory of the Ω turn.	152
5.21	Two patterns in the optimized networks. For both patterns, direct connections from the input neurons to the output neuron exist, and the self-connection exists for the interneuron. The difference between them is the signs of the weights for interneuron.	153
5.22	Two features are extracted among the simplified networks. The feature in (a) functions as a differentiator, and the feature in (b) functions as the time delay.	154
6.1	Head wire diagram. Three ellipses represent the sensory neurons. Circles represent the interneurons. Diamonds represent the command neurons. Rectangles represent the motor neurons.	157
6.2	Wire diagram of motor neurons and neuromuscular connections of <i>C. elegans</i>	159
6.3	(a) One body segment without body changing. (b) One body segment with body changing.	166

6.4	Activations of <i>on-cell</i> and <i>off-cell</i> according to temporal concentration difference.	169
6.5	SLF for the chemotaxis behavior of <i>C. elegans</i>	170
6.6	Testing result in the scenario that only one food is existed.	173
6.7	Testing result in the scenario that food and toxin concentrations are slightly overlapped.	173
6.8	Testing result in the scenario that food and toxin concentrations are heavily overlapped.	174
6.9	Quantitative analysis of the trajectories for food attraction. (a) The relation between turning rate and concentration. (b) The relation between average curving rate and $dC(t)/dt$. (c) The relation between probability of turning and $dC(t)/dt$	176
6.10	(a) The first pattern contains three sensory neurons. (b) The second pattern contains two sensory neurons.	177
6.11	Servomotor Dynamixel AX-12A	178
6.12	ArbotiX micro-controller	179
6.13	XBee wireless module	180
6.14	Distance sensor	180
6.15	Battery	181
6.16	Frames	181
6.17	Worm-like robot	181
6.18	Head of the worm-like robot	182
6.19	Ax-12 Goal Position	183
6.20	Forward locomotion	184
6.21	Backward locomotion	184
6.22	Right-side turning	185
6.23	Left-side turning	186
6.24	C-shape towards the right-side	186

6.25	C-shape towards the left-side	187
7.1	Structure of one segment of 3D robot	194
7.2	3D worm-like robot	194

Nomenclature

Chapters 2 & 3

$x(t)$	Location of <i>C. elegans</i> in x -axis at time t
$y(t)$	Location of <i>C. elegans</i> in y -axis at time t
V	Speed of <i>C. elegans</i>
T	Sampling time
$\theta(t)$	The angle between locomotion direction and x -axis at time t
$V_{right}(t)$	Voltage of right side motor neuron at time t
$V_{left}(t)$	Voltage of left side motor neuron at time t
γ	Turning rate
C_{max}	Peak value of food or toxin concentration
S	Variance of food or toxin concentration distribution
DNN	Dynamic Neural Network
α_i	Parameter of activation function for neuron i
β_i	Parameter of activation function for neuron i
b_i	Parameter of activation function for neuron i
w_{ij}	Weight of neuronal connection from j to i
\overline{V}_j	Center of the conductance for neuron j
δ_i	Decide whether there exists the outside input to neuron i
$E(t)$	Total errors for training at time t
$d_i(t)$	Desired value of neuron i at time t
$e_i(t)$	Error at time t
W	Weight during training
ΔW	Changing of weight during training
η	Learning rate during training

RTRL	Real-time recurrent learning
BPTT	Back-propagation through time
SLF	Switching Logic Function
$C_{f,left}$	Food concentration on the left side
$C_{f,right}$	Food concentration on the right side
ΔC_f	Food concentration difference between left and right sides
$C_{tx,left}$	Toxin concentration on the left side
$C_{tx,right}$	Toxin concentration on the right side
ΔC_{tx}	Toxin concentration difference between left and right sides
ΔC	Food or toxin concentration difference between left and right sides
$\Delta C_{f,tx}$	Result of $\Delta C_f - \Delta C_{tx}$
$\Delta C(t)$	Temporal concentration difference for food or toxin
$\Delta C_f(t)$	Food concentration at time t
$\Delta C_{tx}(t)$	Toxin concentration at time t
$\Delta C_{f,tp}(t)$	Temporal concentration difference for food between t and $t - 1$
$\Delta C_{tx,tp}(t)$	Temporal concentration difference for toxin between t and $t - 1$
$\Delta C_{f,tx,tp}(t)$	Result of $\Delta C_{f,tp}(t) - \Delta C_{tx,tp}(t)$
C_{left}	Food or toxin concentration on the left side
C_{right}	Food or toxin concentration on the right side
C	Food or toxin concentration
$\Delta C_{tp}(t)$	Temporal concentration difference for food or toxin between t and $t - 1$
$C_f(t)$	Food concentration at time t
$C_{tx}(t)$	Toxin concentration at time t

Chapter 4

$x(t)$	Location of <i>C. elegans</i> in x -axis at time t
$y(t)$	Location of <i>C. elegans</i> in y -axis at time t
$v(t)$	Speed of <i>C. elegans</i> at time t
T	Sampling time
$\theta(t)$	The angle between locomotion direction and x -axis at time t

$\Delta\theta(t)$	The change of θ at time t
$V_{right}(t)$	Voltage of right side motor neuron at time t
$V_{left}(t)$	Voltage of left side motor neuron at time t
V_{max}	Maximum speed value
γ	Turning rate
C	Food or toxin concentration
C_{max}	Maximum concentration of food or toxin
$C_{max,f}$	Maximum concentration of food
C_f	Concentration of food
C_{tx}	Concentration of toxin
C_{left}	Concentration of food or toxin on the left side
C_{right}	Concentration of food or toxin on the right side
\overline{C}	Average food or toxin concentration of left and right sides
\overline{C}_f	Average food concentration of left and right sides
\overline{C}_{tx}	Average toxin concentration of left and right sides
$C_{f,left}$	Food concentration on the left side
$C_{f,right}$	Food concentration on the right side
$C_{tx,left}$	Toxin concentration on the left side
$C_{tx,right}$	Toxin concentration on the right side
ΔC_{sp}	Spatial concentration difference between left side and right side
$\Delta C_{f,sp}$	Spatial food concentration difference between left side and right side
$\Delta C_{tx,sp}$	Spatial toxin concentration difference between left side and right side
ΔC_{tp}	Temporal concentration difference between two consecutive steps
$\Delta C_{f,tp}$	Temporal food concentration difference between two consecutive steps
$\Delta C_{tx,tp}$	Temporal toxin concentration difference between two consecutive steps
ΔC_{ft}	The value of $\Delta C_{tx,tp} - \Delta C_{tx,tp}$

V_i	Voltage of i th neuron
w_{ij}	Weight from neuron j to i

Chapter 5

τ_i	Time constant for neuron i
$V_i(t)$	Voltage of neuron i
β_i	Parameter of activation function for neuron i
w_{ij}	Weight of neuronal connection from j to i
\bar{V}_j	Center of the conductance for neuron j
b_i	Parameter of activation function for neuron i
δ_i	Decide whether there exists the outside input to neuron i
V_{C_1}	Voltage of CPG neuron C_1
V_{C_2}	Voltage of CPG neuron C_2
V_{C_3}	Voltage of CPG neuron C_3
V_{C_4}	Voltage of CPG neuron C_4
$L_{lu,i}$	Length of relaxed muscle i on left-up side
$L_{ld,i}$	Length of relaxed muscle i on left-down side
$L_{ru,i}$	Length of relaxed muscle i on right-up side
$L_{rd,i}$	Length of relaxed muscle i on right-down side
$\Delta l_{lu,i}(t)$	Length change of muscle i on left-up side at time t
$\Delta l_{ld,i}(t)$	Length change of muscle i on left-down side at time t
$\Delta l_{ru,i}(t)$	Length change of muscle i on right-up side at time t
$\Delta l_{rd,i}(t)$	Length change of muscle i on right-down side at time t
ϕ_i	Angle between link $i + 1$ and x -axis
$\phi_{v,i}$	Angle between link $i + 1$ and x - y plane
θ_i	Angle between links i and $i + 1$ on x - y plane
$\theta_{v,i}$	Angle between links i and $i + 1$ on x - z plane
ω	Angular speed
$D_{OUT}(t)$	Output of SLF at time t
$V_{OUT}(t)$	Output of Head DNN at time t
V_{max}	Maximum output of V_{OUT}
x_i	Position of joint i in x -axis

y_i	Position of joint i in y -axis
z_i	Position of joint i in z -axis
N_s	Scalar for fitness function
DE	Differential evolution
τ_{VA}	Time constant
τ_{DA}	Time constant
w_{Mi,VB_i}	Weight from neuron VB_i to muscle M_i
w_{Mi,DB_i}	Weight from neuron DB_i to muscle M_i
w_{Mi,VA_i}	Weight from neuron VA_i to muscle M_i
w_{Mi,DA_i}	Weight from neuron DA_i to muscle M_i
w_{Mi,VD_i}	Weight from neuron VD_i to muscle M_i
w_{Mi,DD_i}	Weight from neuron DD_i to muscle M_i
A	Magnitude of ϕ
ω	Speed of sinusoid wave
ϕ_{start}	Starting phase
ϕ_{Lag}	Phase lag
A_v	Magnitude of ϕ_v
l	Length of each link
ϕ_0	ϕ_0 at the beginning time
d	Height of the muscle segment
τ	Time constant of CPG
$A_{\theta,i}$	Magnitude of θ
$A_{\theta_v,i}$	Magnitude of θ_v
Δw_{MV_i}	Weight from $V_{VB,i}$ to the left side muscle
Δw_{MD_i}	Weight from $V_{DB,i}$ to the right side muscle
a_S	Parameter of SLFs
b_S	Parameter of SLFs
c_S	Parameter of SLFs
d_S	Parameter of SLFs
$x_{j,max}$	Maximum value
$x_{j,min}$	Minimum value
N	Population size

C_r	Crossover rate
V_{Max}	Largest value
N_t	Number of training data
$\Delta\tau$	Time delay for each segment
$w_{DD,VB}$	Weight from VB to DD
$w_{VD,DB}$	Weight from VD to DB
$w_{VD,DA}$	Weight from VD to DA
$w_{DD,VA}$	Weight from DD to VA

Chapter 6

$D(t)$	Temporal concentration difference for food or toxin
C_N	Average concentration over time $[t - N, t]$
C_M	Average concentration over time $[t - (N + M), t - N]$
V_{on}	Voltage of <i>on-cell</i> neuron
V_{off}	Voltage of <i>off-cell</i> neuron
V_{ASH}	Voltage of neuron ASH
M	Time duration
N	Time duration
A	Magnitude of activation function
k_s	Steepness of activation function
x_0	Constant in activation function
$C_{tx}(t)$	Toxin concentration at time t
τ_{RIG}	Time constant for CPG
τ_{RIB}	Time constant for CPG
τ_{URY}	Time constant for CPG
V_{RIG}	Voltage of neuron RIG
V_{RIB}	Voltage of neuron RIB
V_{URY}	Voltage of neuron URY
I_{shape}	Proprioceptive feedback from muscles
I_{AVB}	Input from the command neuron AVB
C_B	Time constant for motor neuron
G_B	Membrane conductance

E_{rev}	Constant for cell's potential
A_p	Magnitude of activation function for proprioceptive feedback
k_p	Steepness of activation function for proprioceptive feedback
l_0	Original muscle length
b_p	Constant for proprioceptive feedback activation function
C_D	Time constant for D-type neuron
G_D	Membrane conductance
$w_{mVB,ij}$	Connection weight from VB_j to muscle i
$w_{mVD,ij}$	Connection weight from VD_j to muscle i
$w_{mDD,ij}$	Connection weight from DD_j to muscle i
$w_{mDB,ij}$	Connection weight from DB_j to muscle i
τ_M	Time constant for muscle activation function
$A_{M,i}^{D,V}$	Activation state of dorsal or ventral side muscle i
$l_{D,i}$	Length of dorsal side muscle i
$l_{V,i}$	Length of ventral side muscle i
A_l	Magnitude of muscle activation function
k_l	Steepness of muscle activation function
A_M^0	Constant for muscle activation function
b_l	Constant for muscle activation function
θ_i	Angle between link i and $i + 1$
d	Diameter of body
$D_{fo}(t)$	Output of SLF at time t
α_{fo}	Parameters for the magnitude of SLF
b_{fo}	Parameters for the steepness of SLF
c_{fo}	Parameters for the location of SLF
d_{fo}	Parameters for the location of SLF

Chapter 1

Introduction

Recent developments in the fields of biology and engineering have led to a renewed interest in neuroscience, which is a way to understand the apparent miracles of life in nature world. Nowadays the development of neural network (NN) technology provides a powerful tool for us to study and approximate the nervous system of animal. In the engineering field, the neural basis of behavior is one of the most interesting topics. However, there is a problem to choose the proper animal as research object. The ideal organism should own the sensory and motor components, as well as a simple nervous system, which are relatively easy to study since they interface directly with the outside world: sensory stimulus as input and motor behavior as output via the nervous system. In higher animals like mammals, the input and output are coupled with a extraordinarily complex system, the brain. For this reason, it is convenient to find the simple organism, whose nervous system is much simpler. One such animal, that could almost be considered as a biological robot, is the subject of this thesis. Its name is *Caenorhabditis elegans*, short for *C. elegans*.



Figure 1.1: Image of *C. elegans* [1]

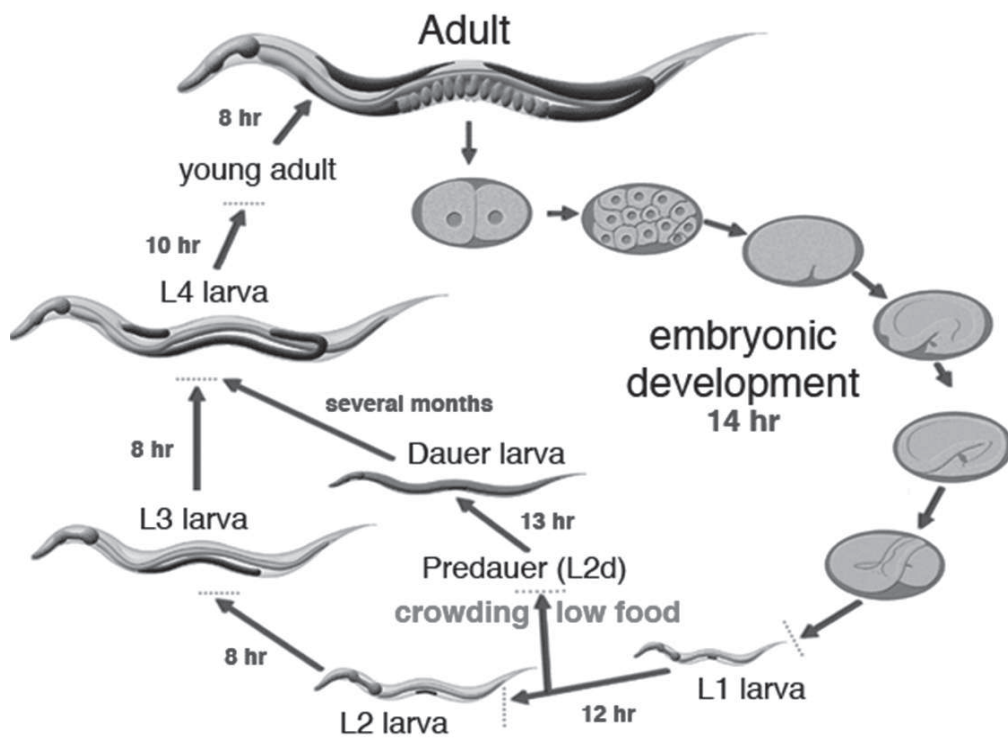


Figure 1.2: Life circle of *C. elegans* [1]

1.1 *C. elegans*

Known as a soil-dwelling nematode, *C. elegans*, as shown in Fig. 1.1, has been used as a model organism for several decades. This tiny transparent nematode is the object of a great many scientific researchers and the works based on *C. elegans* have received Nobel Prize three times [4, 5, 6, 7, 8, 9, 10, 11]. It is selected as a model organism because it has fully understood genetics [12, 13], and completely known anatomical connectivity within

its nervous system [14]. Furthermore, with its short life circle and rapid production, it is convenient for us to do the biological experiment in the lab. As shown in Fig. 1.2, *C. elegans* only takes 70 hours from egg to grow up as adult, and it is relatively easy for us to record the evolving of every cell. The nervous system of *C. elegans* consists of only 302 neurons connected with approximately 6000 synaptic connections and gap junctions. With this tiny nervous system, *C. elegans* can exhibit several characterized behaviors, including chemotaxis, thermotaxis, mechanosensation, osmotic avoidance, dauer formation (a kind of hibernation), male mating, and egg laying. Among these behaviors, the chemotaxis behavior is widely investigated from scientific aspects.

Chemotaxis behavior is one of the fundamental surviving skills for *C. elegans*. For chemotaxis, *C. elegans* orients towards a maximal concentration of chemical attractant, such a number of water-soluble chemicals, including amons, cations, and small organic molecules [15, 16, 17]. Additionally, *C. elegans* also exhibits avoidance behavior in response to noxious stimuli. In the thesis, we use the single word “*food*” to denote all the attractants, and the word “*toxin*” to denote all the repellent stimuli.



Figure 1.3: Ω turn of *C. elegans*

By receiving the outside stimuli, *C. elegans* moves as a long series of undulatory movements, called a run, and it is interrupted approximately twice a minute by sharps turn and reversals [18, 19, 20]. Sharp turn is called Omega turn because it shapes as the

Greek alphabet Ω , as shown in Fig. 1.3. For Ω turn, *C. elegans*' head curls back, touching or crossing the tail, and it continues to move forward with a sharp direction changing. For reversal, *C. elegans* moves backward for several seconds and then moves forward again following by a slight turn, Ω turn, or going straight. With these behaviors, *C. elegans* can navigate itself towards the food source and preferred temperature area, as well as leave far away from the unpleasant place. These behaviors can be attributed to two strategies: klinokinesis and klinotaxis [21]. For klinokinesis, *C. elegans* changes its turning frequency according to the magnitude of outer stimulus; for klinotaxis, *C. elegans* moves forward with identical stimulus from both left and right sides. Furthermore, *C. elegans* has two distinct circuits for locomotion, one for forward and the other for backward [22]. The circuit for forward locomotion achieves the dominant role, and it results in the frequency of backward locomotion far less than that of forward locomotion. Moreover, the activation of the sensory neurons for repellent can active the backward circuit [23] that yields more reversals or Ω turns. For orientation, the mechanism called biased random walk achieves the fundamental role for navigation [19]. In large time-scale, the biased random walk can be considered as the forward moving accompanied with the turning towards the preferred direction [24].

1.2 Neural Networks

Biologically, a neuron contains three main components: dendrites, a cell body (soma), and the axon. The dendrites receive signals from other neurons, and the cell body integrates the signal and redistributes it outward to the axon. The axon distributes the signal from the cell body to different neurons, muscles and glands.

According to the neural activities, there are two types of neurons: spiking (or action

potentials) neuron and graded (or localized potentials) neuron. For the spiking neuron, the cell body integrates synaptic inputs and activates until a threshold is reached. The spiking neuron is ideal for transmitting a maximum amount of information over long distances and most neurons in the mammalian nervous system are spiking neurons [25]. By contrast, for the graded neuron, the synaptic input within the center of the neuron's range yields a quasi-linear response. If stimulated by a large excitatory synaptic input, the graded neuron saturates. This type neuron is ideal for integrating highly sensitive input to be transmitted over a short distance. The graded neurons exist in some smaller organisms, such as *Ascaris* [26] and *C. elegans* [27].

After the neuron is activated, the signal is transmitted to other neurons through the synapses. The synapses are the junctions between neurons, and there are two general types of synapses: *gap junctions* (or electrical synapse) and *chemical synapse*. A gap junction behaves like a passive wire, readily passing current in two directions. By contrast, the chemical synapse releases the chemical transmitter from the presynaptic axon terminals to the receptors of the postsynaptic dendrites. The differences between gap junction and chemical synapse are listed in Table. 1.1.

Table 1.1: The differences between gap junction and chemical synapse

	Gap Junction	Chemical Synapse
1	Two directions, where signal can be transmitted either way.	Transmitters are released from the pre-synaptic axon to the post synaptic dendrite neuron, namely, one direction.
2	Usually excites downstream neuron.	Can both excite and inhibit downstream neural activity.
3	Transmission of current is roughly linear.	Transmission is usually amplified due to the non-linear effects of the neuron transmitters.

In engineering field, neural network technology is adopted to simulate the nervous system of animal. Most of the neural network structures used presently are static (feed-

forward) neural networks [28]. These neural networks that have a number of neurons respond instantaneously to the inputs. However, the neuron in this kind neural network is not dynamic and performs a simple summation operation. It also does not take into account the time delays that affect the dynamics of the system. Unlike a static neural network, a dynamic neural network (DNN) uses extensive feedback between the neurons. This feedback implies that the network has local memory characteristics. The node equations in dynamic neural networks are described by differential or difference equations. Thus, DNN is suitable for system modeling, identification, control and filtering owing to its dynamical nature. In this thesis, DNN is adopted to model the nervous system of *C. elegans*.

1.3 Current Models

To date, there are limited publications concerning the modeling of chemotaxis behaviors of *C. elegans*. There are four main research groups involving the research on chemotaxis behavior and locomotion of *C. elegans*, who have published several papers within recent twenty years. Among them, two different methods are adopted: one from the engineering aspect, and the other from the biology aspect. In this section, we provide the literature review about these models.

Niebur and Erdös

The first group that played a leading role in exploring the locomotion of *C. elegans* is Ernst Niebur and Paul Erdös. In [29], a locomotion model is provided based on the nervous system of *C. elegans*. The excitation wave is spread passively by the neurons that simulate the membrane properties of biological neurons to propagate the wave for locomotion. The simulation in their work is to address the assumption that the sinusoid

wave of *C. elegans* is produced by the propagated exciting neurons along its body. In [30], a two dimensional mechanical model of *C. elegans* is carried out. In that model, the head contains an oscillatory generator to guide the body to perform the undulatory locomotion. At last, in [31], the authors extend their previous work and provide the first integrated undulatory locomotion model of *C. elegans*. In the model, there is a CPG in the head to generate the sinusoid wave and control the turning during locomotion. However, the drawback of this work is that these models do not provide any details of biological grounding.

Cohen et al.

The group of Cohen et al. began the research on locomotion of *C. elegans* around the year of 2003. In [32], the first true neural locomotion model of *C. elegans* is presented, in which the motor neuron stretch receptors are used to mediate the sensory feedback to generate and coordinate oscillations. However, the oscillation frequency of this model is unrealistically high and far from the biologically plausible range. In [33], the authors present the first integrated neuro-mechanical model for forward locomotion of *C. elegans*. This integrated model produces oscillation with a more realistic frequency and waveform than the model in [32]. In [34, 35, 36], they verify that the behaviors of swimming and crawling of *C. elegans* belong to a single gait. In [37], they construct a forward locomotion model of *C. elegans* that includes a neuromuscular control system. Integrated with the outside environment, the model relies on the sensory feedback mechanism to generate undulations. This model can reproduce the entire transition from swimming to crawling, as well as the locomotion in complex environments. The transition from swimming to scrawling is achieved with no modulatory mechanism, except via the proprioceptive response to the physical environment. Furthermore, based on their theoretical results, in

[38] the first prototype of worm-like robot using electroactive polymer is presented and a digital image processing technique is developed. Recently, in [39], a novel robot of *C. elegans* based on the neural control mechanism is constructed by Boyle et al. This robot is capable of effective serpentine locomotion and exhibits sensorless path finding based purely on the proprioceptive feedback of body shape. Their testing results show that the robot can find its path successfully in the complicated testing environment.

Suzuki et al.

The locomotion models constructed by this group involve a high level neural control and the generating of the actual locomotion wave. The range of the behaviors of these locomotion models is much broader than that of other groups' models. These behaviors include forward locomotion, backward locomotion, resting, and Ω turn. They explored the head turning [40], direction control [41, 42], and touch response for forward or backward movement [43]. The strength of their work includes both physical body and local neural control. The model in their work contains 13 rigid links with 12 joints and the angle of each joint is determined independently from the local neuromuscular activity. However, the neural control is similarly simplified that makes these models unlikely to provide new insight into the worm's locomotion system biologically.

Lockery et al.

Lockery et al. initiated their research on *C. elegans* from 1990s from both engineering and biology aspects and obtained many achievements. From engineering aspect, they first used the artificial neural networks to simulate the chemotaxis behavior of *C. elegans* [3], and then constructed a robot to implement the chemotaxis behavior [2]. Later, a lineal model and several computation rules for chemotaxis behavior of *C. elegans* are provided

in [44, 45]. In [46, 47] the excitatory, inhibitory and self-connections are found, and in [48, 49] different functional classes and motifs are identified by the clustered neural dynamics methods. From the biology aspect, the electrical properties of the sensory neuron ASER are investigated in [50]. Later, the step-response analysis of neuron ASE is provided in [51], and the different functions of ASEL and ASER are investigated in [52, 53]. In [54], the authors find that ADF serves as the on-cells and ASH serves as the off-cells. Furthermore, they also explore the turning behaviors of *C. elegans*. In [19, 55], the authors have verified the fundamental role of pirouettes and the effects of turning bias for *C. elegans* to approach the attractant. Their recent research work [56, 57, 21] unveils three strategies for the locomotion of *C. elegans*: klinotaxis, klinokinesis, and the functional asymmetry of sensory neurons.

Others

Except for the models of the four groups, there are some individual work related to the modeling of *C. elegans*. In [58], a detailed and biologically accurate model is provided. This model focusses exclusively on the neural circuit for head oscillation without including a physical component. In [59], the decision tree method is adopted to simulate the gradient navigation strategy of *C. elegans*. In [60], the author uses a formal particle system to model the worm and its environment, including attractants and repellents. Unfortunately, without including any form of motor nervous system, this model suffers from the lack of biological grounding. The work in [61] uses the biological experiment results to construct an artificial network model to show how a sinusoid wave can be propagated through the body. In [62], a 3D locomotion model of *C. elegans* is constructed and displayed mainly in the game engine. However, this model lacks the precise mathematical description. Furthermore, two robots in [63] and [64] are constructed to mimic

the undulatory behavior of *C. elegans*. Both robots are constructed based on the Shape Memory Alloy.

To the best of our knowledge, all the models concerning the chemotaxis behavior and locomotion of *C. elegans* are discussed. In our research, we focus on the investigation of chemotaxis behavior and locomotion of *C. elegans* from engineering aspect, and also incorporate the biological results to verify the effectiveness and realness of our models.

1.4 Contribution

In the previous subsections, we have reviewed all the existing models of the nematode *C. elegans*. Comparing with these models, the contributions and novelties of this work contain seven aspects that are listed below.

- **From artificial to biological approach:** For the artificial approach, artificial neural networks are adopted to model the nervous system of *C. elegans* without following its anatomical structure, which is the first step. For the next step, the biological approach, biological wire diagrams that are strictly based on the nervous system of *C. elegans* are adopted to explore the chemotaxis behaviors.
- **Modeling the chemotaxis behaviors of *C. elegans*:** There are two kinds of chemotaxis behaviors are investigated in the thesis, food attraction and toxin avoidance. First, these two behaviors are explored individually, and then the integrated behavioral models are provided to perform the two behaviors simultaneously. The chemotaxis behaviors of *C. elegans* can be represented as a set of nonlinear functions, which are constructed based on the logic of chemotaxis behaviors. The well trained models can be put into different environments to perform their desired tasks without retraining. These nonlinear functions called switching

logic functions provide a new way to model the animal's behaviors.

- **Speed regulation mechanism:** The speed regulation mechanism is incorporated into the chemotaxis behavioral models so that the navigation is completed with both orientation control and speed control. For food attraction (toxin avoidance), the models will reduce its speed to zero spontaneously when it arrives at (leaves far from) the food (toxin) source.
- **Undulatory locomotion behavior modeling:** At the beginning, *C. elegans* is considered as a point to perform the chemotaxis behaviors. Next, the undulatory locomotion is investigated in 3D by artificial approach. After that, through the biological approach the undulatory locomotion behavior is explored based on the biological neural wire diagram and muscle structure. Both artificial and biological undulatory locomotion behavioral models can well perform the chemotaxis behaviors of finding food and avoiding toxin.
- **Test and comparative analysis:** These locomotion models are tested in different scenarios and the quantitative analyses are provided by comparing with other work. All the simulation scenarios are constructed based on the biological experiments without being stochastically generated, which aim to keep the biological reality.
- **Justification and prediction for biological issues:** The work in the thesis justifies three biological issues. First, the biased turning mechanism is sufficient to accomplish the chemotaxis behaviors of *C. elegans*. Second, the chemotaxis behaviors is achieved by computing the input concentration gradient. Third, the proprioceptive mechanism plays the critical role for propagating the undulatory wave throughout the body. Furthermore, three predictions are made in the thesis. First, there should be a group of neurons that function as the differentiator for the

decision making during chemotaxis. Second, there should be a pattern generator in the head to produce the undulatory wave and the muscles use the proprioceptive mechanism to propagate the wave. Third, some sensory neurons such as ASEL may achieve the redundancy function.

- **A worm-like robot:** A worm-like robot has been constructed to perform the undulatory locomotion based on the theoretical results. The worm-like robot can well perform the undulatory behaviors such as forward and backward movements, left-side turning and right-side turning, as well as the C-shape movement.

It should be noted that this work is based on many existing biological results, especially for those chapters involving the biological approach. This is because as the multiple-disciplinary study, we need follow the methods and rules from both engineering and biology disciplines. All the existing work cited in the thesis is to justify the claims and hypotheses, which could preserve the biological reality of the work.

1.5 Synopsis of The Thesis

The thesis is organized as follows. In Chapter 2, two artificial chemotaxis behavioral models, one for dual-sensory model and the other for single-sensory model, are constructed to perform the chemotaxis behaviors of finding food and avoiding toxin. In Chapter 3, we extracted the biological neural wire diagram to construct the biological models and make them perform the chemotaxis behaviors. In Chapter 4, based on the work of Chapter 3, the speed regulation mechanism is incorporated. Six biological behavioral models in this chapter not only could approach the food source (avoid the toxin source), but also reduce its speed when getting close to the food source (far away from the toxin source) in different circumstances. Quantitative analysis of these behavioral models is carried

out and we also compare our data with the experimental data to verify the effectiveness and authenticity of our models. Chapter 5 provides a 3D undulatory locomotion model based on artificial DNN. This model can perform the chemotaxis behaviors of finding food and avoiding toxin based on the 3D undulatory movement. In Chapter 6, instead of the artificial DNN, we investigate the undulatory locomotion behavior of *C. elegans* directly on its biological neural wire diagram and muscle structure. Finally, a worm-like robot has been constructed to perform the undulatory behavior based on the theoretical results. Chapter 7 concludes the thesis and provides the future work.

It is understood that our work is restricted into the engineering aspects such as mechanic engineering, electrical engineering, and computer engineering. Some models, which focus on the lower level research such as gene mutations, are outside the scope of the current work.

Chapter 2

Modeling the Chemotaxis Behaviors of *C. elegans* Based on the Artificial Dynamic Neural Networks

2.1 Introduction

The synaptic connections and morphology of *C. elegans* have been explored clearly [14]. Among the 302 neurons, *C. elegans* has at least 12 classes of chemosensory neurons, and each class has a pair of neurons that is physically symmetrical but functionally different from one another [53]. For the locomotion, *C. elegans* can move forward or backward for the chemotaxis, thermotaxis and touch response.

Among the previous work, the sinusoidal movement of *C. elegans* was studied, which involved the head turning [40], direction control [41, 42], and touch response [43]. These papers developed both kinematical and dynamical models of *C. elegans* that could perform two dimensional movements. Furthermore, several models were constructed to perform the chemotaxis behaviors of *C. elegans*. In [45], a linear network was used to simulate

the behaviors of food attraction. In [47], the excitatory, inhibitory, and self connections were found. By using the clustered neural dynamics method, different function classes of neurons were identified in [48].

This chapter initiates the research on the chemotaxis behavior of *C. elegans* based on the artificial approach. In our work, we adopt DNN to model the nervous system of *C. elegans* that performs chemotaxis tasks. There are a large number of literatures to prove that DNN performs well in areas such as prediction, information processing and feature extraction, and it also lies in its close relation to biological neural networks in terms of its structure similarity and dynamical characteristics such as memory [28, 65, 66, 67]. By choosing nonlinear activation functions, time constants, and various weights for input neurons, hidden neurons and output neurons, DNN can approximate any mapping relationship, such as the biological mapping from sensory inputs to motor outputs. It is pointed out that the convergence of DNN does not totally depend its initial input conditions, which is advantageous in application such as decision making [68, 69, 70, 71]. Supervised learning can be used to direct the system to a desired response [72].

Following the methods in [3, 45, 47], the wire diagram of *C. elegans* is modeled as a DNN in our work. The sensory neurons are the input neurons and the motor neurons are the output neurons. With the sensory neurons, *C. elegans* directs itself towards the region of higher food concentrations and away from the region of higher toxin concentrations. However, it is a biologically issue whether *C. elegans* can detect the gradient of concentrations. We first investigate the chemotaxis behaviors of *C. elegans* based on the assumption that the pair of sensory neurons can distinguish the concentration difference between left and right sides . Next, as said in [45], the size of *C. elegans* is very small (1 mm in length) and the left and right sensory neurons are too near to detect the

difference of concentration, so we combine the left and right sensory neurons to be one sensory neuron. In this case, the gradient of concentration is the decisive information for *C. elegans* to navigate. The temporal gradient of concentration is achieved because DNN has inherent memory components [72]. This chapter is organized as follows. Sections 2.2 describes the kinematics, distributions of food and toxin concentrations, DNN, and the training method. Section 2.3 focuses on the dual-sensory model of *C. elegans* that produces finding food and avoiding toxin behaviors, while Section 2.4 explores the single-sensory model of *C. elegans*. Section 2.5 concludes this chapter.

2.2 Mathematical Model and Training Method

2.2.1 Kinematic Model

A complete kinematic model of *C. elegans* requires a description of its position at instantaneous time t . As shown in Fig. 2.1, a typical *C. elegans* will have a sinusoidal movement and it is assumed that only the head receives the input of external concentrations. With this assumption, *C. elegans* is modeled as a point source in the x-y plane and its position is updated as follows [2]:

$$x(t+1) = x(t) + VT \cos \theta(t) \quad (2.1)$$

$$y(t+1) = y(t) + VT \sin \theta(t) \quad (2.2)$$

where $x(t)$ and $y(t)$ are the position values at time t , V is a constant speed per second. $\theta(t)$ is the head angle at time t , and T is the sampling interval. In this chapter, T is 1 second.

For simplicity, in the work of this chapter we focus on the head movement. The head

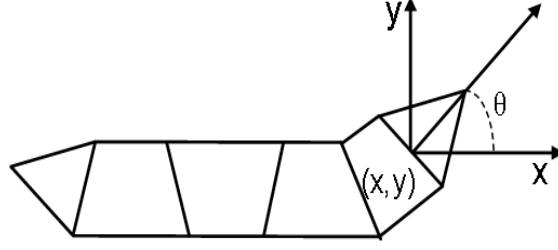


Figure 2.1: *C. elegans*' movement in the x-y plane. The head of *C. elegans* is modeled as a point source in the x-y plane with velocity vector V at head angle θ measured from the x-axis [2].

angle is related to the motor neuron voltages as follows

$$\theta(t+1) = \theta(t) + \gamma(V_{right}(t) - V_{left}(t))T \quad (2.3)$$

where $\theta(t)$ is the angle at time t , and γ is a positive constant that decides the turning rate [3]. V_{right} and V_{left} stand for the outputs of right and left motor neurons VB and DB, respectively.

2.2.2 Attractant and Repellent Concentration

The concentration distribution for food or toxin is assumed in Gaussian distribution [45]:

$$C(x, y) = C_{\max} \exp\left(-\frac{x^2 + y^2}{S}\right), \quad (2.4)$$

where C_{\max} is the peak value of attractant or repellent and S is the variance of the distribution. The unit of the concentration C is millimolar concentration (mmol/L, short for mM). One example of concentration distribution is shown graphically in Fig. 2.2.

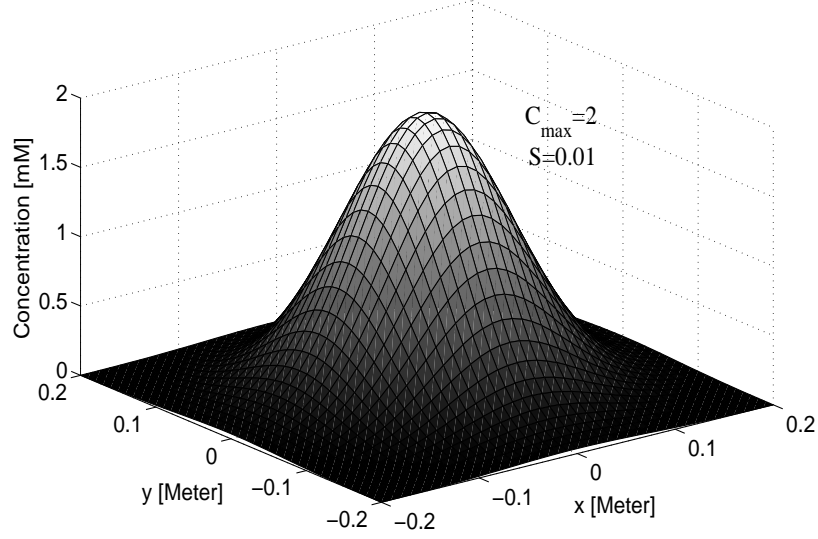


Figure 2.2: The potential field of concentration distributed in a square area with the range $[-0.2, 0.2]$ meters, where $C_{\max} = 2$ mM and $S = 0.01$.

2.2.3 DNN Model

Each neuron in this work is denoted as a dynamic neuron with self-feedback [56]. The state of the i th neuron can be represented as the voltage V_i . In this work, we adopt a discrete DNN:

$$V_i(t+1) = \alpha_i V_i(t) + \beta_i \cdot \tanh\left(\sum_{j=1, i \neq j}^N w_{ij}(V_j(t) - \bar{V}_j)\right) + b_i + \delta_i u_i(t), \quad (2.5)$$

where the exogenous input $u_i(t)$ is the instantaneous chemical concentration sensed by sensory neurons. The constant \bar{V}_j is the center of the conductance of the j th neuron [45], which means at this voltage there is no transmitter released from the j th neuron. w_{ij} represents the strength of synaptic connection from neuron j to i . b_i is a constant bias introduced here to adjust the resting potential value [73]. When neuron i is the sensor neuron, $\delta_i = 1$, otherwise $\delta_i = 0$. The parameters to be determined through training are

$\alpha_i, \beta_i, w_{ij}, \bar{V}_i, b_i$, for $i, j = 1, \dots, N$.

2.2.4 Training Method

When the structure of a neural network is fixed, parametric learning or training is the decisive factor on the success of a given task. In this work, we adopt the continuous training, in which the parameters are updated at each time step. For DNN, two training algorithms are widely used, back-propagation through time (BPTT) [74], and real-time recurrent learning (RTRL) [75]. The BPTT updates weights layer by layer using the gradient method. However, the biological neural circuitry of *C. elegans* does not show a layered structure. Thus, RTRL is more suitable as the learning mechanism, which does not require any layered structure. During the training, the learnable parameters are updated after every time step according to the defined output targets.

The RTRL first defines an error function

$$E(t) = \frac{1}{2} \sum_{i=1}^N [d_i(t) - V_i(t)]^2, \quad (2.6)$$

where $d_i(t)$ is a desired output. Define

$$e_i = d_i(t) - V_i(t). \quad (2.7)$$

The updating law is

$$W(t+1) = W(t) + \Delta W(t), \quad (2.8)$$

$$\begin{aligned} \Delta W(t) &= -\eta \frac{\partial E(t)}{\partial W(t)} = \eta \sum_{i=1}^N [d_i(t) - V_i(t)] \frac{\partial V_i(t)}{\partial W(t)} \\ &= \eta \sum_{i=1}^N e_i(t) \frac{\partial V_i(t)}{\partial W(t)}, \end{aligned} \quad (2.9)$$

where η is a learning rate, and $W(t)$ denotes one of the parameters w_{ij} , \bar{V}_i , α_i , β_i , and b_i . The computations of the gradient information, $\frac{\partial V_i(t)}{\partial W(t)}$, are listed below.

- Updating w_{kl} :

$$w_{kl}(t+1) = w_{kl}(t) + \Delta w_{kl}(t). \quad (2.10)$$

In the equation,

$$\begin{aligned} \Delta w_{kl}(t) &= -\eta \frac{\partial E(t)}{\partial w_{kl}} = \eta \sum_{i=1}^N ((d_i(t) - V_i(t)) \frac{\partial V_i(t)}{\partial w_{kl}}) \\ &= \eta \sum_{i=1}^N (e_i(t) \frac{\partial V_i(t)}{\partial w_{kl}}). \end{aligned} \quad (2.11)$$

According to the equation (2.5), $\frac{\partial V_i(t)}{\partial w_{kl}}$ is:

when $k = i$,

$$\begin{aligned} \frac{\partial V_i(t+1)}{\partial w_{kl}} &= \alpha_i \frac{\partial V_i(t)}{\partial w_{kl}} + \beta_i \sec h^2 \left(\sum_{j=1, j \neq i}^N w_{ij}(V_j(t) - \bar{V}_j) \right) \\ &\quad * \left(\sum_{j=1, j \neq i}^N w_{ij} \frac{\partial V_j(t)}{\partial w_{kl}} + (V_i(t) - \bar{V}_i) \right). \end{aligned} \quad (2.12)$$

When $k \neq i$,

$$\begin{aligned} \frac{\partial V_i(t+1)}{\partial w_{kl}} &= \alpha_i \frac{\partial V_i(t)}{\partial w_{kl}} + \beta_i \sec h^2 \left(\sum_{j=1, j \neq i}^N w_{ij}(V_j(t) - \bar{V}_j) \right) \\ &\quad * \left(\sum_{j=1, j \neq i}^N w_{ij} \frac{\partial V_j(t)}{\partial w_{kl}} \right). \end{aligned} \quad (2.13)$$

- Updating \bar{V}_k :

$$\bar{V}_k(t+1) = \bar{V}_k(t) + \Delta \bar{V}_k(t) = \bar{V}_k(t) + \eta \sum_{i=1}^N e_i(t) \frac{\partial V_i(t)}{\partial \bar{V}_k} \quad (2.14)$$

$$\begin{aligned} \frac{\partial V_i(t+1)}{\partial \bar{V}_k} &= \alpha_i \frac{\partial V_i(t)}{\partial \bar{V}_k} + \beta_i \sec h^2 \left(\sum_{j=1, i \neq j}^N w_{ij} (V_j(t) - \bar{V}_j) \right) \\ &\quad * \left(\sum_{j=1, i \neq j}^N w_{ij} \frac{\partial V_j(t)}{\partial \bar{V}_k} - w_{ik} \right). \end{aligned} \quad (2.15)$$

- Updating α_k :

$$\alpha_k(t+1) = \alpha_k(t) + \Delta \alpha_k(t) = \alpha_k(t) + \eta \sum_{i=1}^N e_i(t) \frac{\partial V_i(t)}{\partial \alpha_k}. \quad (2.16)$$

When $k = i$,

$$\begin{aligned} \frac{\partial V_i(t+1)}{\partial \alpha_k} &= V_i(t) + \alpha_i \frac{\partial V_i(t)}{\partial \alpha_k} + \beta_i \sec h^2 * \left(\sum_{j=1, i \neq j}^N w_{ij} (V_j(t) - \bar{V}_j) \right) \\ &\quad * \left(\sum_{j=1, i \neq j}^N w_{ij} \frac{\partial V_j(t)}{\partial \alpha_k} \right). \end{aligned} \quad (2.17)$$

When $k \neq i$,

$$\begin{aligned} \frac{\partial V_i(t+1)}{\partial \alpha_k} &= \alpha_i \frac{\partial V_i(t)}{\partial \alpha_k} + \beta_i \sec h^2 \left(\sum_{j=1, i \neq j}^N w_{ij} (V_j(t) - \bar{V}_j) \right) \\ &\quad * \left(\sum_{j=1, i \neq j}^N w_{ij} \frac{\partial V_j(t)}{\partial \alpha_k} \right). \end{aligned} \quad (2.18)$$

- Updating β_k :

$$\beta_k(t+1) = \beta_k(t) + \Delta \beta(t) = \beta_k(t) + \eta \sum_{i=1, j \neq i}^N e_i(t) \frac{\partial V_i(t)}{\partial \beta_k} \quad (2.19)$$

When $k = i$,

$$\begin{aligned} \frac{\partial V_i(t+1)}{\partial \beta_k} &= \alpha_i \frac{\partial V_i(t)}{\partial \beta_k} + \tanh \left(\sum_{j=1, i \neq j}^N w_{ij} (V_j(t) - \bar{V}_j) \right) + \\ &\quad \beta_i \sec h^2 \left(\sum_{j=1, i \neq j}^N w_{ij} (V_j(t) - \bar{V}_j) \right) * \left(\sum_{j=1, i \neq j}^N w_{ij} \frac{\partial V_j(t)}{\partial \beta_k} \right). \end{aligned} \quad (2.20)$$

When $k \neq i$,

$$\begin{aligned} \frac{\partial V_i(t+1)}{\partial \beta_k} &= \alpha_i \frac{\partial V_i(t)}{\partial \beta_k} + \beta_i \sec h^2 \left(\sum_{j=1, i \neq j}^N w_{ij} (V_j(t) - \overline{V_j}) \right) \\ &\quad * \left(\sum_{j=1, i \neq j}^{N7} w_{ij} \frac{\partial V_j(t)}{\partial \beta_k} \right). \end{aligned} \quad (2.21)$$

• Updating b_k :

$$b_k(t+1) = b_k(t) + \Delta b_k(t) = b_k(t) + \eta \sum_{i=1}^N e_i(t) \frac{\partial V_i(t)}{\partial b_k}. \quad (2.22)$$

When $k = i$,

$$\begin{aligned} \frac{\partial V_i(t+1)}{\partial b_k} &= \alpha_i \frac{\partial V_i(t)}{\partial b_k} + \beta_i \sec h^2 \left(\sum_{j=1, i \neq j}^N w_{ij} (V_j(t) - \overline{V_j}) \right) \\ &\quad * \left(\sum_{j=1, i \neq j}^N w_{ij} \frac{\partial V_j(t)}{\partial b_k} \right) + 1. \end{aligned} \quad (2.23)$$

When $k \neq i$,

$$\begin{aligned} \frac{\partial V_i(t+1)}{\partial b_k} &= \alpha_i \frac{\partial V_i(t)}{\partial b_k} + \beta_i \sec h^2 \left(\sum_{j=1, i \neq j}^N w_{ij} (V_j(t) - \overline{V_j}) \right) \\ &\quad * \left(\sum_{j=1, i \neq j}^N w_{ij} \frac{\partial V_j(t)}{\partial b_k} \right). \end{aligned} \quad (2.24)$$

All DNN models in Chapters 2, 3, and 4 are trained by RTRL to learn their specific switching logic functions. Training iteration for individual models varies from 8,000 to 50,000 epochs. All neural connection weights are set with initial values randomly between -0.5 and 0.5 . Learning rates are set to 0.002 for w_{ij} and 0.01 for other parameters. The lower learning rates ensure the convergence of training. Furthermore, there are three points should be noted for training.

First, the range of initial weights plays the important role for convergence. It is mentioned that the initial weights should not be too large [76, 77, 78]. Large initial weights are in the extreme regions of the sigmoid functions, hence difficult to adjust or update. This is because the gradient value of the sigmoid function is rather low at extreme regions due to the flatness of the sigmoid function [79]. In our work, the initial weights are range from $[-2, 2]$. When the initial range is between $[-5, 5]$, neuronal active functions of the sigmoid function type, such as $\tanh(x) = (e^x - e^{-x})/(e^x + e^{-x})$, becomes either $+1$ or -1 when x is nearby $+5$ or -5 , namely, deeply saturated. The deep saturation makes the training difficult because the output of neuron would not vary while the inputs vary.

Second, to avoid the local minimum a randomly restart mechanism is adopted. As mentioned in [80], random restarts with a local gradient algorithm may be more effective than a global algorithm at obtaining a low value of the objective function. During the training, if the sum of squared error (SSE) is a constant for a long period, or the SSE is larger than a value, the training procedure will be restarted by randomly re-initializing the weights. We set that if the value of SSE is bigger than 0.01 and not changing for 400 epochs, or if the SSE is greater than 4 (except for the initialization), the training procedure will restart.

Third, the wire diagrams are trained with inputs ranging from 0 to 2. If a wider range of concentration inputs is given, we can introduce a scaling factor into the sensory neurons and normalize the inputs within the range $[0, 2]$, and the same test results can be obtained without re-training.

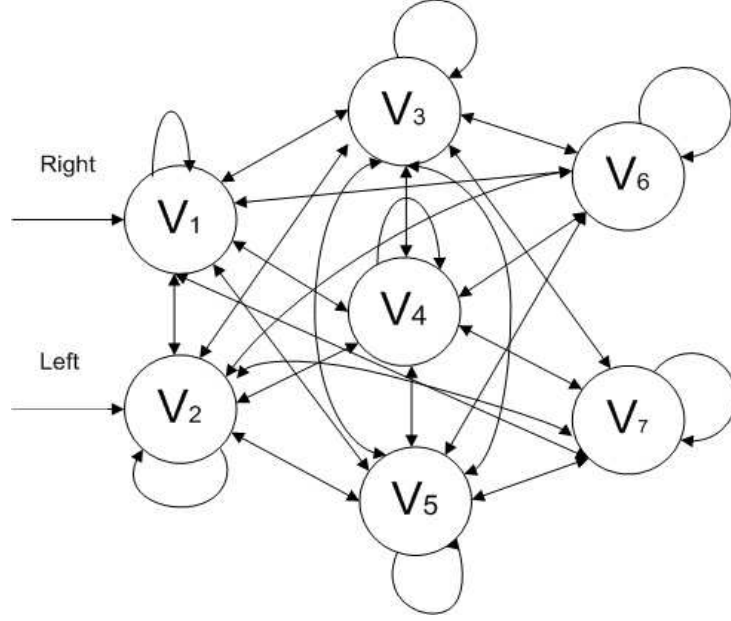


Figure 2.3: Topological structure for a dual-sensory model. V_1 and V_2 are the right and left sensory neurons, and V_6 and V_7 are the right and left motor neurons, respectively.

2.3 Dual-sensory Behavioral Model

2.3.1 DNN for Dual-sensor Model

To explore the capability of DNN, a DNN of 7 neurons is formed as shown in Fig.2.3. This DNN has an interconnected and self-connected structure. The network architecture consists of two sensory neurons V_1 (right) and V_2 (left), which mimic the biological sensory neurons ASEL and ASER as inputs, respectively. The sensory neurons receive chemotaxis signals from left and right sides, which are concentrations $C_{\text{right}}(t)$ and $C_{\text{left}}(t)$, respectively.

Two motor neurons, V_6 for right side and V_7 for left side, are outputs of DNN. V_3 , V_4 , V_5 are three hidden neurons. Here the assumption is that *C. elegans* can distinguish the concentration difference between left and right sides.

The objective of this section is to investigate whether such a simple dual-sensor DNN can perform food-attractant or toxin-repellent behaviors.

2.3.2 Learning Tasks

In our work, the chemotaxis behaviors of *C. elegans* are modeled as a set of nonlinear functions, called switching logic functions (SLFs). The target of the training is to let the DNN learn the SLFs for food attraction and for toxin avoidance. SLFs are constructed based on the logic of chemotaxis behaviors and the way to construct them is not unique. Different SLFs can be designed as long as the logic is correct.

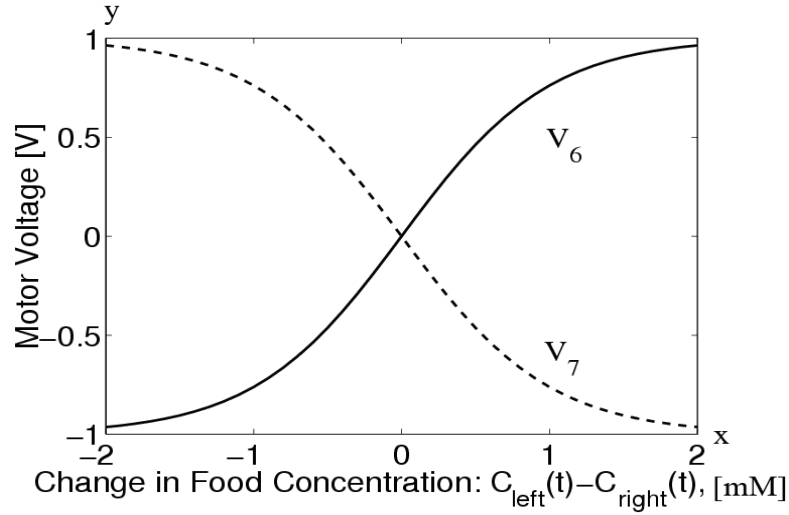


Figure 2.4: SLFs for food attractant. The x-axis depicts the food concentration difference between the left-side and right-side sensors, which are located 2×10^{-5} m apart spatially [3]. The y-axis shows the voltage of the output neurons. V_6 stands for the right motor neuron and V_7 stands for the left motor neuron, both with the range from -1 to 1 V.

For food attractant, the SLFs consist of two hyperbolic tangent functions, as shown in Fig. 2.4,

$$V_6 = \tanh(\Delta C_f), \quad (2.25)$$

$$V_7 = -\tanh(\Delta C_f), \quad (2.26)$$

where $\Delta C_f = C_{f,left} - C_{f,right}$ is food concentration difference between the left-side and right-side sensors.

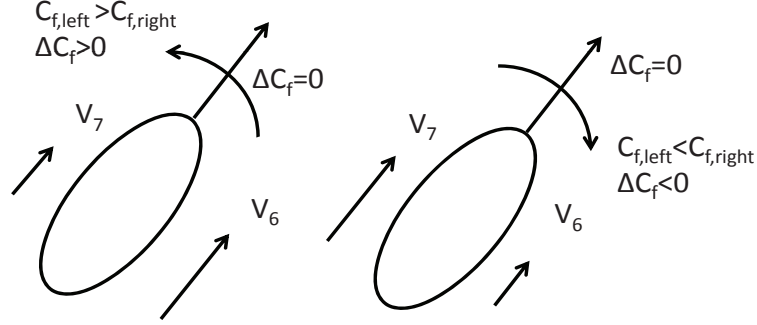


Figure 2.5: The movement of dual-sensory model during food attraction. When $\Delta C = C_{f,left} - C_{f,right} > 0$, the food locates on the left side. From SLFs, motor neuron outputs satisfy $V_6 > V_7$ ($V_{right} > V_{left}$), namely, the right-side speed is faster than the left-side speed, so *C. elegans* turns left. Similarly when $C_{f,left} - C_{f,right} < 0$, so $V_{left} > V_{right}$ and *C. elegans* turns right. If $\Delta C_f = 0$, the direction cannot be determined and information of $\Delta C(t-1) = 0$ will be required.

The rationale of SLFs for food attraction with dual sensors can be explained from Fig. 2.5. When $\Delta C_f = C_{f,left} - C_{f,right} > 0$, implying that the food locates on the left side, then according to SLFs, $V_6 > V_7$ ($V_{right} > V_{left}$). As a result, *C. elegans* turns left. Similarly when $C_{f,left}(t) - C_{f,right}(t) < 0$, implying that the food locates on the right side, $V_7 > V_6$, thus the *C. elegans* turns right. If $\Delta C_f = 0$ at time t , the direction cannot be determined. Instead, the $C_f(t)$ should be compared with $C_f(t-1)$ to decide whether the direction is correct or not. This special case is considered in the single-sensory neuron model.

For toxin avoidance, as shown in Fig. 2.6, SLFs are opposite to that for food attraction,

$$V_6 = -\tanh(\Delta C_{tx}), \quad (2.27)$$

$$V_7 = \tanh(\Delta C_{tx}), \quad (2.28)$$

where $\Delta C_{tx} = C_{tx,left} - C_{tx,right}$ is toxin concentration difference between the left-side and right-side sensors of *C. elegans*.

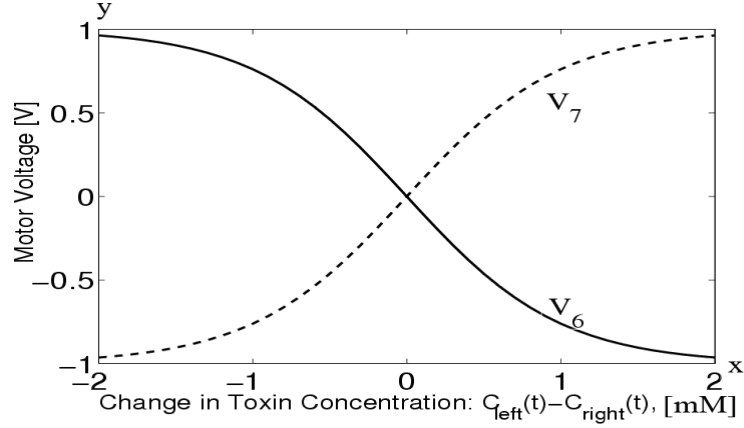


Figure 2.6: SLFs for toxin avoidance. The x-axis depicts the toxin concentration difference between the left-side and right-side sensors, which are located 2×10^{-5} m apart spatially. The y-axis describes the motor neurons' outputs. V_6 is the right motor neuron and V_7 is the left motor neuron. Their values are between -1 and 1 .

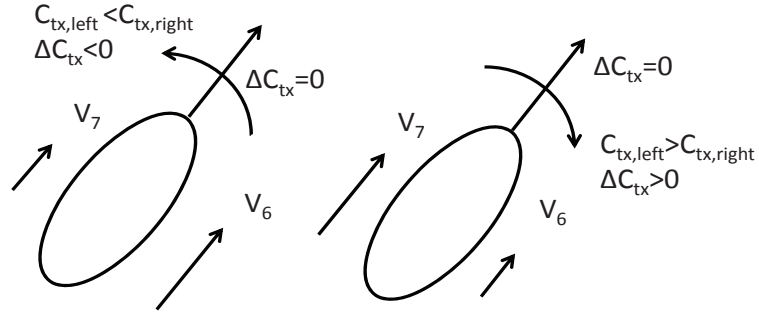


Figure 2.7: The movement of dual-sensory model during toxin avoidance. When $\Delta C = C_{tx,left} - C_{tx,right} > 0$, the toxin locates on the left side. From the switching logic, $V_7 > V_6$ or $V_{left} > V_{right}$, namely, the left-side speed is faster than the right-side speed, so *C. elegans* turns right. Similarly when $C_{tx,left} - C_{tx,right} < 0$, $V_6 > V_7$ or $V_{left} < V_{right}$ and *C. elegans* turns left.

Fig. 2.7 shows the movement of *C. elegans* during toxin avoidance. SLFs describe the mapping from sensory input, ΔC , to motor-neuron outputs, V_6 and V_7 , which are opposite to SLFs for food attraction. Thus the orientation of the toxin avoidance is opposite to that for food attraction, namely, *C. elegans* moves towards food but away from toxin.

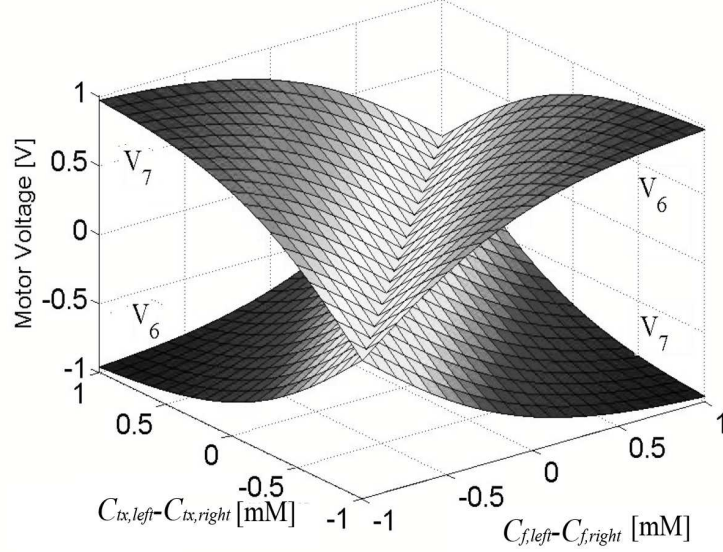


Figure 2.8: SLFs for the multi-tasks. The input signals are $C_{f,left}$, $C_{f,right}$, $C_{tx,left}$, $C_{tx,right}$. When $\Delta C_{f,tx} > 0$ ($\Delta C_f > \Delta C_{tx}$), $\tanh(\Delta C_{f,tx}) > 0$ makes $V_6 > V_7$, resulting the worm turn left. It is vice versa for $\Delta C_{f,tx} < 0$.

For the integrated behavior, SLFs are constructed below

$$V_6 = \tanh(\Delta C_{f,tx}), \quad (2.29)$$

$$V_7 = -\tanh(\Delta C_{f,tx}), \quad (2.30)$$

$$\Delta C_{f,tx} = \Delta C_f - \Delta C_{tx} = (C_{f,left} - C_{f,right}) - (C_{tx,left} - C_{tx,right}),$$

where $C_{f,left}$, $C_{f,right}$, $C_{tx,left}$ and $C_{tx,right}$ denote the left-side food concentration, right-side food concentration, left-side toxin concentration, and right-side toxin concentration, respectively.

From Fig. 2.8, the switch surface is decided by two input signals, $\Delta C_f = C_{f,left} - C_{f,right}$ and $\Delta C_{tx} = C_{tx,left} - C_{tx,right}$. When $\Delta C_{f,tx} = \Delta C_f - \Delta C_{tx} = 0$, it means that $C_{f,left} = C_{f,right}$ and $C_{tx,left} = C_{tx,right}$, which is considered as the worm in correct direction. Thus $\tanh(\Delta C_{f,tx}) = 0$ and $V_6 = V_7$, and the worm goes straightly. When $\Delta C_{f,tx} > 0$ ($\Delta C_f > \Delta C_{tx}$), it indicates three cases. (1) The food source is located at

the left side and the toxin source is located at the right side. Thus *C. elegans* should turn left to approach food. (2) both food source and toxin source are located at the left side. $\Delta C_f > 0$, $\Delta C_{tx} > 0$, and $\Delta C_f > \Delta C_{tx}$, which means *C. elegans* should turn left to approach food. (3) both food source and toxin source are located at the right side. $\Delta C_f < 0$, $\Delta C_{tx} < 0$, and $\Delta C_f > \Delta C_{tx}$, which means *C. elegans* should turn left to avoid the toxin. In these three cases, $\tanh(\Delta C_{f,tx}) > 0$ makes $V_6 > V_7$, resulting the worm turn left. The situation is vice versa for $\Delta C_{f,tx} < 0$.

2.3.3 Testing Results

In this section, simulation experiments are conducted to investigate the performance of the dual-sensory DNN model under three different cases: 1) a single food source, 2) four toxin sources, 3) a food source and a toxin source. The speed of *C. elegans* is 0.22 mm/s [45], and the distance between the left-side and right-side sensors is 0.2 mm, and body length is 1 mm. The RTRL training method described in Section 2.2.4 is used to train the DNN. Without being mentioned, the head angle of the *C. elegans* in all simulations are initialized randomly with different values.

Food attraction

First we test the behavior of *C. elegans* near a single food source. The food locates at point (0,0). *C. elegans* starts at (0.1, -0.1). The movement path in Fig.2.9 indicates the success in the mission of finding food. At the end, the worm finds the food located at point (0,0) and moves around.

Toxin avoidance

Next we test the behavior of the *C. elegans* near four toxin sources that are located at points (-0.2, 0), (-0.1, -0.15), (0, 0.2), and (0.1, -0.1), respectively. *C. elegans* starts at

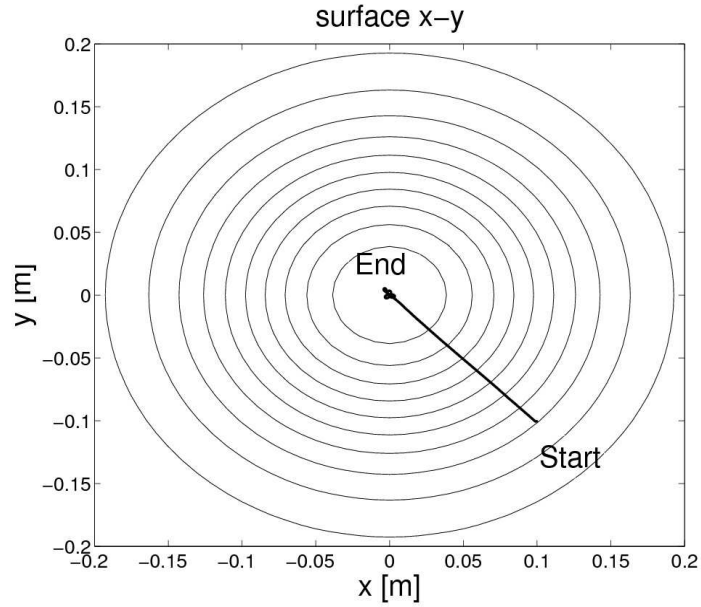


Figure 2.9: The behavior of dual-sensory model of *C. elegans* near a food source. The point of highest food concentration is point $(0,0)$. *C. elegans* starts at $(0.1, -0.1)$ and finally finds the food source at $(0,0)$.

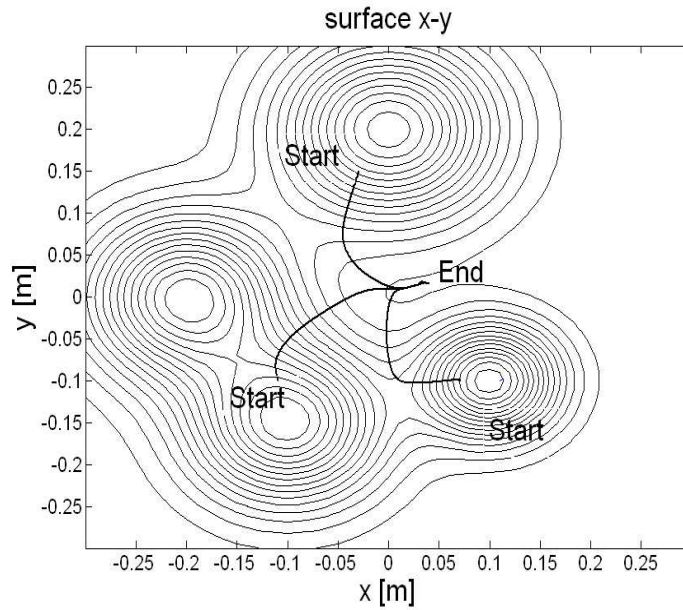


Figure 2.10: The behavior of dual-sensory model of *C. elegans* near four toxin sources. Four toxin resources are located at points of $(-0.2, 0)$, $(-0.1, -0.15)$, $(0, 0.2)$, and $(0.1, -0.1)$, respectively. The worm starts at three different positions $(-0.11, -0.1)$, $(0.07, -0.1)$, $(-0.03, 0.15)$ with head angle 135° , 180° , 180° , respectively. The worm avoids the toxin repellents and moves towards a safe position away from toxin.

three different positions $(-0.11, -0.1)$, $(0.07, -0.1)$, $(-0.03, 0.15)$ with head angle 135° , 18° , and 180° , respectively. The results in Fig.2.10 illustrate that *C. elegans* can avoid toxin by maintaining a maximum distance away from it.

Integrated Behavior

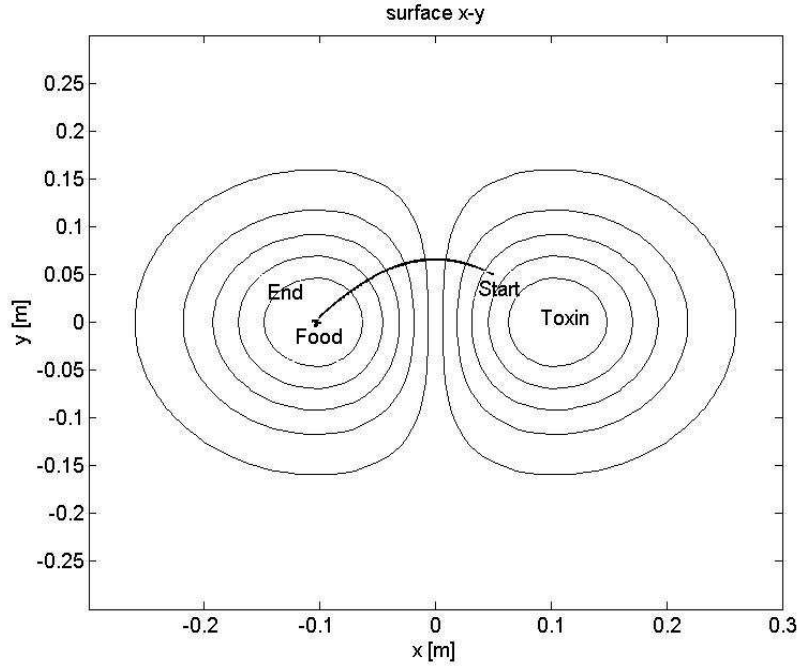


Figure 2.11: The behavior of dual-sensory model of *C. elegans* in between food attractant and toxin repellent. The food and toxin are put at points $(-0.1, 0)$ and $(0.1, 0)$, respectively. *C. elegans* starts at $(0.08, 0.05)$ with head angle 90° and finally arrives at the food source placed at $(-0.1, 0.0)$.

Finally, we test the behavior of *C. elegans* in the presence of both food and toxin sources. In order to let *C. elegans* distinguish the food and toxin, we set the concentration values of food to be positive and toxin to be negative. As such, it is adequate to use only the SLFs described in Fig.2.8. The food and toxin sources are put at $(-0.1, 0)$ and $(0.1, 0)$, respectively. *C. elegans* starts at $(0.08, 0.05)$ with head angle 90° . The results shown in Fig.2.11 indicates that a dual-sensory *C. elegans* can navigate itself to avoid toxin and move towards the food source directly.

2.4 Single-sensory Behavioral Model

2.4.1 DNN for Single-sensory Model

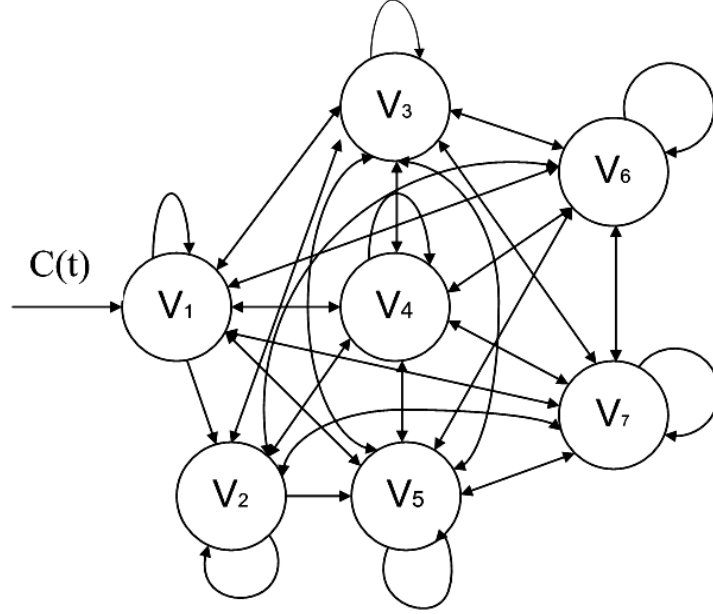


Figure 2.12: Topological structure for a single-sensory model. The network architecture consists of one sensory neuron V_1 , which mimics the biological sensory neuron ASE. The memory neuron is V_2 , which plays a similar role as the biological neuron AIY. Two motor neurons V_6 for right and V_7 for left are outputs of DNN. V_3 , V_4 , V_5 are three hidden neurons.

Biologically, it is assumed that the distance between left-side and right-side sensory neurons is too small for *C. elegans* to detect the spatial difference in concentration [3]. As a consequence, the left-side and right-side sensory neurons work as a single sensor. In this section we will investigate whether the DNN model with a single-sensory neuron can still perform the chemotaxis behaviors. DNN with a single sensory neuron is shown in Fig. 2.12. For the chemotaxis, *C. elegans* memorizes the previous concentration, $C(t-1)$, and then computes the change of concentration with present concentration, $\Delta C(t) = C(t) - C(t-1)$. In order to let *C. elegans* memorize the concentration of $C(t-1)$, a neuron should function as a memory. According to [81], biological neuron AIY possesses a memory function. In the DNN, neuron V_2 is added to mimic the memory

neuron AYI, which records the concentration of $C(t - 1)$. For the single-sensory model, we assume that

1. *C. elegans* compares present and past concentrations to perform chemotaxis [19, 55].
2. The output of the sensory neuron is the value of the attractant or repellant concentration at a single point in space [25].
3. The voltage potential for the motor neuron is in the close interval of $[-1.0V + 1.0V]$.
4. The simulation and computation is performed at the network level instead of cellular level [25].

2.4.2 Learning Tasks

The DNN model is trained to learn SLFs for food attraction as shown in Fig. 2.13, and toxin avoidance as shown in Fig. 2.14. The concentration difference $\Delta C(t) = C(t) - C(t - 1)$ only tells whether the forward direction is correct or not. It remains unclear whether food or toxin is on the left or right side. For instance, when finding food, $\Delta C_f(t) > 0$ means that *C. elegans* is heading the correct direction. When $\Delta C_f(t) < 0$, *C. elegans* is heading a wrong direction and it can turn either left or right. The new direction, either left or right, can be randomly selected. Biologically, *C. elegans* prefers turning towards its ventral side [18, 82], which is the right side for our models. In this work we assume the worm chooses turning right as the preference, hence the value of left-side motor neuron output is always greater than that of the right-side motor neuron.

We design the SLFs for food attraction as

$$V_6(t) = 0.5 \tanh(\Delta C_{f,tp}(t)) - 0.5, \quad (2.31)$$

$$V_7(t) = -0.5 \tanh(\Delta C_{f,tp}(t)) + 0.5. \quad (2.32)$$

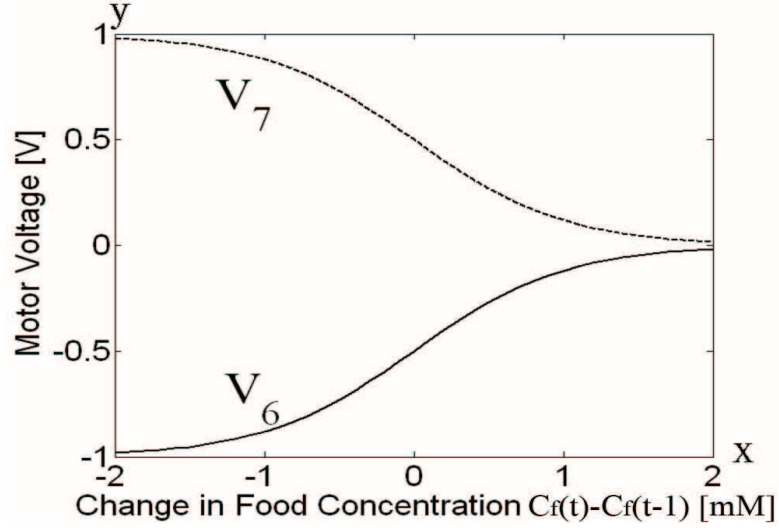


Figure 2.13: SLFs for the single-sensory model for food attraction. The x-axis depicts the food concentration difference between two consecutive time instances, $\Delta C(t) = C(t) - C(t-1)$. The y-axis shows the output of the motor neurons according to the $\Delta C(t)$. V_6 is the right side motor neuron and V_7 is the left side motor neuron, and their values change between -1 and 1 .

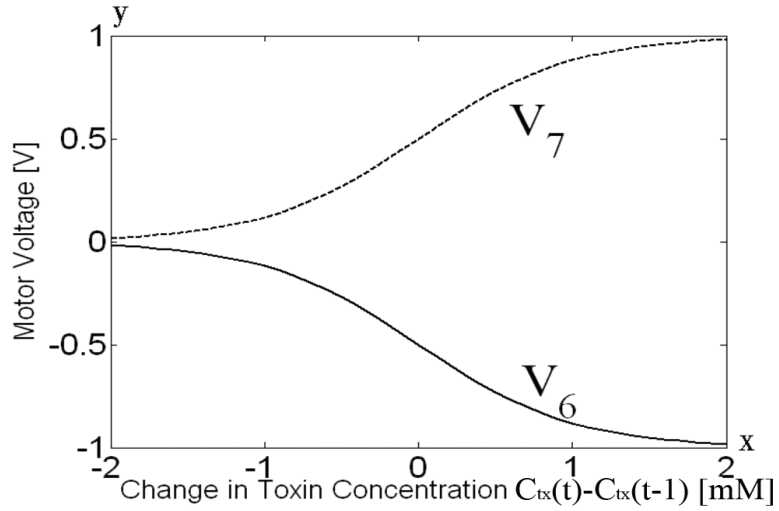


Figure 2.14: SLFs for the single-sensory model for toxin avoidance. The x-axis depicts the toxin concentration difference between two consecutive time instances, $\Delta C(t) = C(t) - C(t-1)$. The y-axis presents the output of the motor neurons according to $\Delta C(t)$. V_6 is the right side motor neuron and V_7 is the left side motor neuron, and their values change between -1 and 1 .

SLFs for toxin avoidance are opposite to those for food attraction,

$$V_6(t) = 0.5 \tanh(-\Delta C_{tx,tp}(t)) - 0.5, \quad (2.33)$$

$$V_7(t) = -0.5 \tanh(-\Delta C_{tx,tp}(t)) + 0.5. \quad (2.34)$$

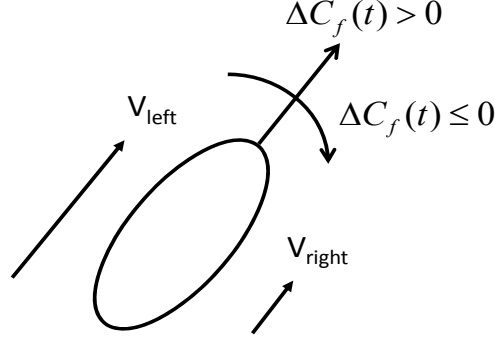


Figure 2.15: Movement demonstration for food attraction. If $C_f(t) > C_f(t-1)$, *C. elegans* is in the correct direction, so $V_{left}(V_7) = V_{right}(V_6)$ and it goes straightly. When $C_f(t) \leq C_f(t-1)$ (wrong direction), the output of V_{right} is smaller than the output of V_{left} , which makes *C. elegans* turn right.

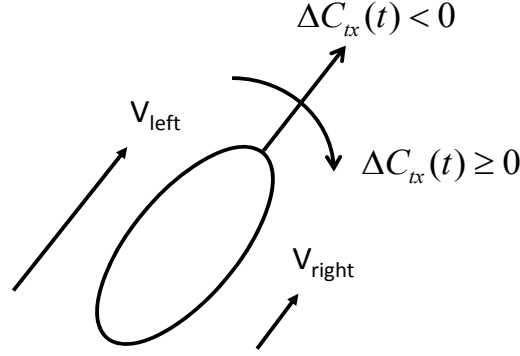


Figure 2.16: Movement demonstration for toxin avoidance. If $C_{tx}(t) < C_{tx}(t-1)$, *C. elegans* is in the correct direction, so $V_{left}(V_7) = V_{right}(V_6)$ and it goes straightly. If $C_{tx}(t) \geq C_{tx}(t-1)$ (wrong direction), the output of V_{right} is smaller than V_{left} , which makes *C. elegans* turn right.

For food attraction, as shown in Fig. 2.15, *C. elegans* computes the change in food concentration between present and past concentrations, $\Delta C_{f,tp}(t) = C_f(t) - C_f(t-1)$. When $C_f(t) - C_f(t-1)$ is positive, *C. elegans* knows that it is heading towards a region of higher food concentration and it generates motor neuron voltages at the same potential level. When $C_f(t) - C_f(t-1)$ is negative, this means that *C. elegans* is heading towards a region of lower food concentration and some action should be taken to turn back. As is assumed, when *C. elegans* detects the wrong direction, the only action to be adopted is turning right, and $V_6(t) < V_7(t)$.

For toxin avoidance, as shown in Fig. 2.16, when $\Delta C_{tx,tp}(t) = C_{tx}(t) - C_{tx}(t-1)$ is positively large, *C. elegans* is heading the wrong way as the toxin concentration increases. Then the left-side speed is larger than the right-side speed, namely $V_7(t) > V_6(t)$, *C. elegans* turns right to escape. When $C_{tx}(t) - C_{tx}(t-1)$ is negative, *C. elegans* is heading the right direction. In this circumstance, the values of $V_6(t)$ and $V_7(t)$ are similar, and *C. elegans* moves either straightly or turn right slightly.

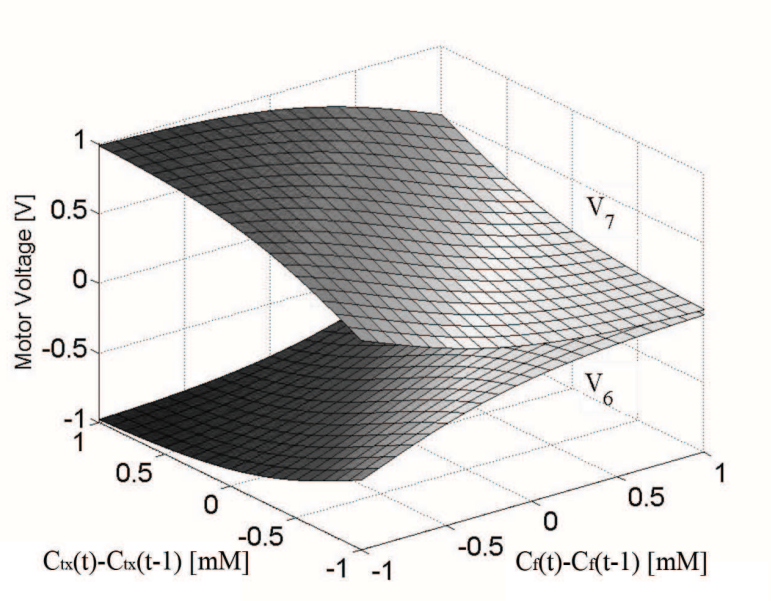


Figure 2.17: The logic switch surface for the integrated behavior. When $\Delta C_{f,tp}(t) = C_f(t) - C_f(t-1) = 1$ and $\Delta C_{tx,tp}(t) = C_{tx}(t) - C_{tx}(t-1) = -1$, it is the most favorable direction, $V_6(t) = V_7(t)$ and *C. elegans* moves straightforward. When $\Delta C_{f,tp}(t) = -1$ and $\Delta C_{tx,tp}(t) = 1$, it is the most unfavorable direction, the difference between $V_6(t)$ and $V_7(t)$ is maximum and *C. elegans* turns right as sharp as possible. When $\Delta C_{f,tp}(t)$ and $\Delta C_{tx,tp}(t)$ have similar values, the information is unclear to *C. elegans* due to the mixture of food and toxin, and the worms turns right in a gentle way for further exploration.

For the integrated behavior, SLFs for single-sensory model are constructed below and plotted in Fig. 2.17.

$$V_6(t) = 0.5 \tanh(\Delta C_{f,tx,tp}(t)) - 0.5, \quad (2.35)$$

$$V_7(t) = -0.5 \tanh(\Delta C_{f,tx,tp}(t)) + 0.5, \quad (2.36)$$

$$\Delta C_{f,tx,tp}(t) = \Delta C_{f,tp}(t) - \Delta C_{tx,tp}(t), \quad (2.37)$$

where

$$\Delta C_{f,tp}(t) = C_f(t) - C_f(t-1)(t),$$

$$\Delta C_{tx,tp}(t) = C_{tx}(t) - C_{tx}(t-1)(t).$$

As shown in Fig. 2.17, the movement is determined jointly by the food and toxin concentrations. When $\Delta C_{f,tp}(t) = C_f(t) - C_f(t-1) = 1$ and $\Delta C_{tx,tp}(t) = C_{tx}(t) - C_{tx}(t-1) = -1$, it is the most favorable direction, $V_6(t) = V_7(t)$ and *C. elegans* moves straightforward. When $\Delta C_{f,tp}(t) = -1$ and $\Delta C_{tx,tp}(t) = 1$, it is the most unfavorable direction, the difference between $V_6(t)$ and $V_7(t)$ is maximum and *C. elegans* turns right as sharp as possible. When $\Delta C_{f,tp}(t)$ and $\Delta C_{tx,tp}(t)$ have similar values, the information is unclear to *C. elegans* due to the mixture of food and toxin, and the worms turns right in a gentle way for further exploration.

2.4.3 Testing Results

Simulation experiments are conducted to observe the performance of the single-sensory model under three different chemotaxis environments: 1) single food source, 2) four toxin sources, 3) one food source and one toxin source.

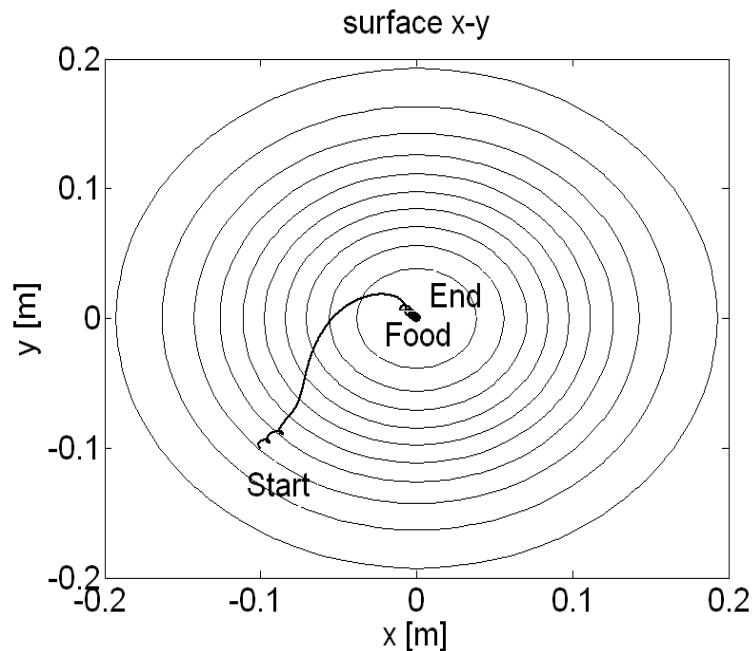


Figure 2.18: Food attraction behavior for single-sensory model. A food source is located at point $(0,0)$. *C. elegans* starts at $(-0.1, -0.1)$ with head angle 135° .

Food Attraction

To test the single-sensory model for food attraction, a food source is located at the origin $(0,0)$. The result can be seen in Fig. 2.18. *C. elegans* starts at $(-0.1, -0.1)$ with head angle 135° and finally it finds the food source at $(0,0)$ through a series of right turns.

Toxin Repellent

To test the single-sensory for toxin avoidance, four toxin resources are located at points $(-0.2,0)$, $(-0.1,-0.15)$, $(0,0.2)$, and $(0.1,-0.1)$, respectively. Fig. 2.19 shows three tests in which *C. elegans* starts from three different positions $(-0.12, -0.13)$, $(-0.03, 0.18)$, and $(0.08, -0.1)$, with head angle 180° . *C. elegans* successfully avoids toxin through a series of right turns.

Comparing with the movement of dual-sensory model shown in Fig.2.10, it is more

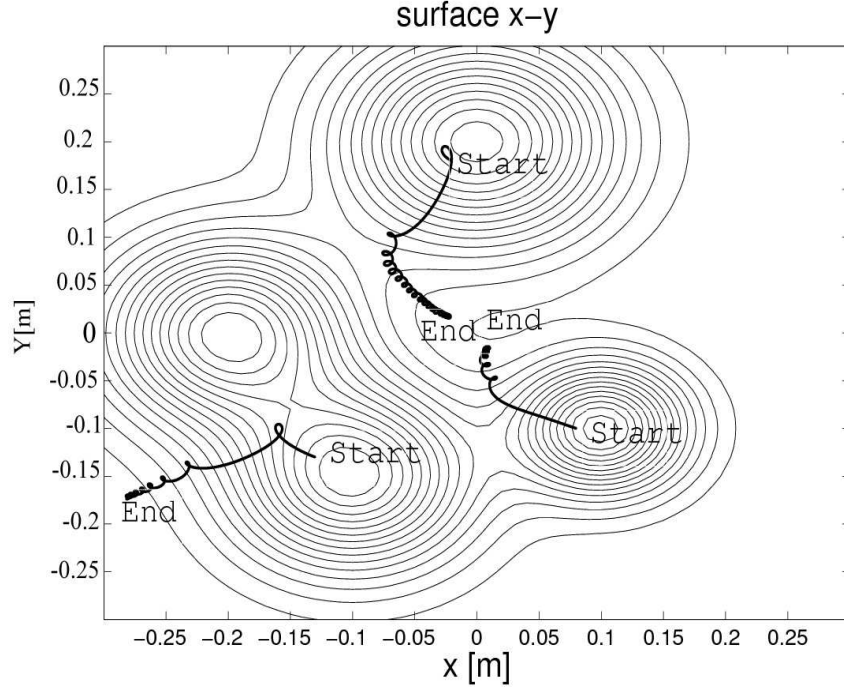


Figure 2.19: Single-sensory model for toxin avoidance. Four toxin resources are located at points $(-0.2, 0)$, $(-0.1, -0.15)$, $(0, 0.2)$, and $(0.1, -0.1)$. *C. elegans* starts at three different positions $(-0.12, -0.13)$, $(-0.03, 0.18)$, $(0.08, -0.1)$ with head angle 180° , and it successfully avoids the toxin sources.

difficult for the single-sensory model to make the correct movement, because the gradient information of the toxin concentration can only be captured after two steps of motion.

Integrated Behavior

In this test, we set the concentration of food to be positive and toxin to be negative. SLFs are shown as Fig. 2.17 and the test result is shown in Fig. 2.20. A food source is put at point $(-0.1, 0)$ and a toxin source is put at $(0.1, 0)$. *C. elegans* starts at the toxin area $(0.03, 0)$, with head angle 270° . During the movement, *C. elegans* avoids the toxin and moves towards the food source. Finally it finds the food source and circles around the food source.

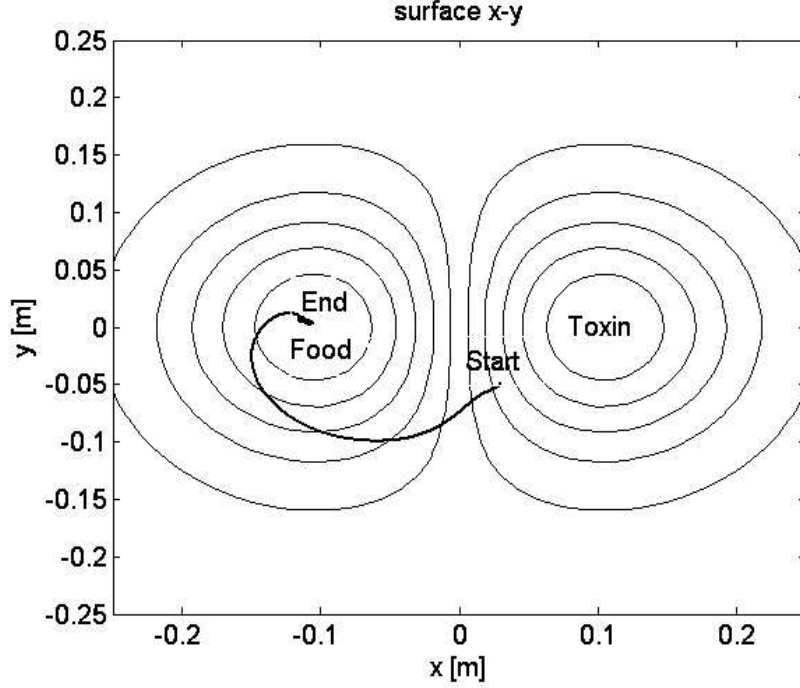


Figure 2.20: Single-sensory model for integrated behavior. A food source and a toxin source are put at points $(-0.1, 0)$ and $(0.1, 0)$, respectively. *C. elegans* starts at the toxin area $(0.03, 0)$ with head angle 270° . It moves towards food, and ends at food source.

2.5 Conclusion

In this chapter, we have modeled the chemotaxis behaviors of *C. elegans* based on the artificial neural network. The chemotaxis behaviors of *C. elegans* involve finding food and avoiding toxin. DNN is chosen to model the nervous system and the chemotaxis behaviors are modeled as SLFs that decide the locomotion direction. Both dual-sensory model and single-sensory model are investigated in this chapter. The dual-sensory model is based on the assumption that *C. elegans* can distinguish the concentration difference between the left-side and right-side sensors, whereas the single-sensory model is based on the assumption that *C. elegans* cannot distinguish the concentration difference between the left-side and right-side sensors. From the testing results, both the dual-sensory model and the single-sensory model can successfully find the food source and avoid the toxin source. The dual-sensory model produces much smoother motion patterns than

the single-sensor DNN model does. With only 7 neurons, the DNN models can learn to generate complex chemotaxis behaviors.

In next chapter, the chemotaxis behaviors such as finding food and avoiding toxin will be investigated based on the biological wire diagrams.

Chapter 3

Modeling the Chemotaxis Behaviors of *C. elegans* Based on the Biological Wire Diagram with Invariant Speed

In Chapter 2, we have investigated the chemotaxis behavior of *C. elegans* based on the artificial DNN. However, since the full neuronal connections of the nervous system are known, in the chapter we explore the chemotaxis behavior of *C. elegans* directly on its biological wire diagram. The stimuli to sensory neurons are modeled as inputs, and the motor neuron voltages acting on muscles are modeled as outputs. The biological models for the chemotaxis behavior of *C. elegans* are extracted from the original biological wire diagram [83]. In this chapter, six biological models are provided, namely, the dual-sensory models and the single-sensory models for food, toxin, and integrated behavior, respectively. With the sensory neurons, *C. elegans* can direct itself towards the region of high food concentrations and away from the region of high toxin concentrations.

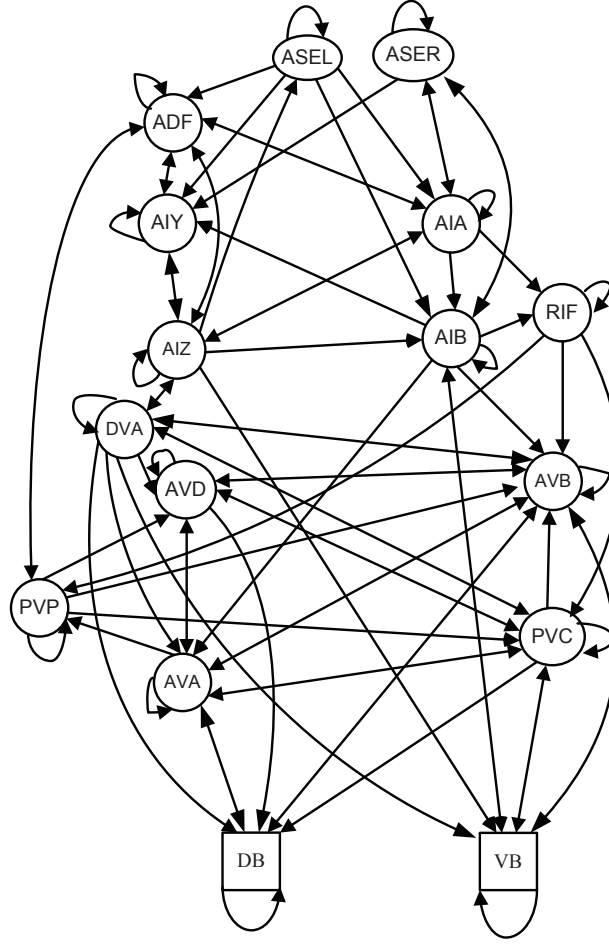


Figure 3.1: The wire diagram of dual-sensory behavioral model for food attraction. Neuron ASEL and ASER are the left and right sensory neurons for food, respectively. The outputs are neurons DB and VB for left and right sides, and the rest are hidden neurons.

3.1 Dual-sensory Behavioral Model

3.1.1 Wire Diagrams

Wire Diagram for Food Attraction

According to anatomy, the wire diagram of dual-sensory behavioral model for food attraction is shown in Fig. 3.1. This wire diagram is extracted based on the data provided by [83]. We fix the sensory neurons ASEL and ASER as input neurons for food attraction [15], two motor neurons DB and VB as the left and right output neurons, respectively. Other interneurons are added by two rules: (1) with the shortest paths from ASE(L/R)

For toxin avoidance behavior, the input neurons are ASHL and ASHR, which are responsible for nose touch, hyperosmolarity, and volatile repellent chemicals. The output neurons are DB for left-side and VB for right-side. Other interneurons are extracted following the same way as wire diagram for food attraction. The wire diagram for toxin avoidance is shown in Fig. 3.2. We obtain the wire diagram with the same interneurons compared to those for food attraction as shown in Fig. 3.1. However, the neuronal connections for food attraction and toxin avoidance wire diagrams are different. For example, ASH(L/R) for toxin avoidance have the direct connections to command neurons AVD and AVA, but ASE(L/R) for food attraction do not have.

As shown in Fig. 3.1 and Fig. 3.2, there are twelve interneurons in each model. By comparing to other research works [40, 18], it is interesting that we share the same eight interneurons: AIA, AIB, AIY, AIZ, DVA, AVA, AVB, and PVC. Biologically, these eight interneurons play the critical role for the locomotion behaviors. Half of all synaptic outputs from the amphid neurons are directed to the interneurons AIA, AIB, AIY, and AIZ [18]. Furthermore, AIY functions as a memory neuron that records the previous concentration information [81]. AVD, AVB, AVA, and PVC are four critical command neurons for movement [85]. It should be noted that the neuron AVD in our work represents both AVD and AVE. The reason that we combine AVD and AVE together is because AVE has the same postsynaptic partners as AVD [86], and it is in accordance with the locomotion circuit of *C. elegans* in [85], which deals with AVD and AVE as one neuron. Four additional neurons are involved in our model that function as interneurons: ADF, PVP, RIF, DVA. Biologically, ADF contributes to a residual chemotactic response after ASE is killed [1], and DVA is an interneuron that serves as the stretch sensitive neuron which is significant for undulatory movement [61].

The model as shown in Fig. 3.1 and Fig. 3.2 are simplified biological wire diagrams with sixteen neurons. Each neuron in this model possesses an active function as Eq. (2.5), so the whole wire diagram is a DNN. DNN has the ability to approximate arbitrary non-linear functions. If DNN can map the input-output relations of the chemotaxis behaviors, then DNN can perform the chemotaxis behaviors after training.

3.1.2 Learning Tasks

The RTRL training method described in Section 2.2.4 is used. The DNN learns the same SLFs for food attraction as shown in Fig. 2.4, and for toxin avoidance as shown in Fig. 2.6, in which V_6 is V_{right} and V_7 is V_{left} .

Analogous to Fig. 2.5, $C_{left} - C_{right} > 0$ implies that the food locates on the left side, so $V_{right} > V_{left}$ and the right-side speed is more than the left-side speed. Thus, *elegans* turns left. Similarly when $C_{left} - C_{right} < 0$, $V_{right} > V_{left}$, and *C. elegans* turns right.

Analogous to Fig. 2.7, when the left-side sensor detects more toxin concentration than the right-side sensor, $C_{left} - C_{right} > 0$, implying that the toxin locates at the left side. In order to avoid the toxin, $V_{left} > V_{right}$ or the left-side speed is more than right-side speed, and *C. elegans* turns right. Similarly when $C_{left} - C_{right} < 0$, $V_{right} < V_{left}$, *C. elegans* turns left.

3.1.3 Testing Results

Simulation experiments are conducted to observe the performance of the dual-sensory behavioral model under two different chemotaxis environments in the presence of 1) single food attractant, 2) four toxin repellents.

First we test *C. elegans* behaviors near a single food attractant. The food locates at

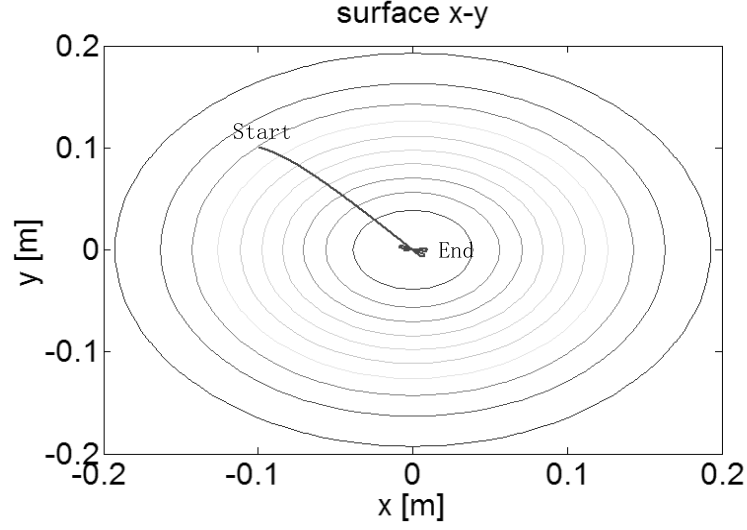


Figure 3.3: The chemotaxis behavior of *C. elegans* produced by the dual-sensory behavioral model for food attractant. One food source locates at the point $(0,0)$. *C. elegans* starts at $(-0.1, 0.1)$ with the head angle 180° and ends at the food source $(0, 0)$.

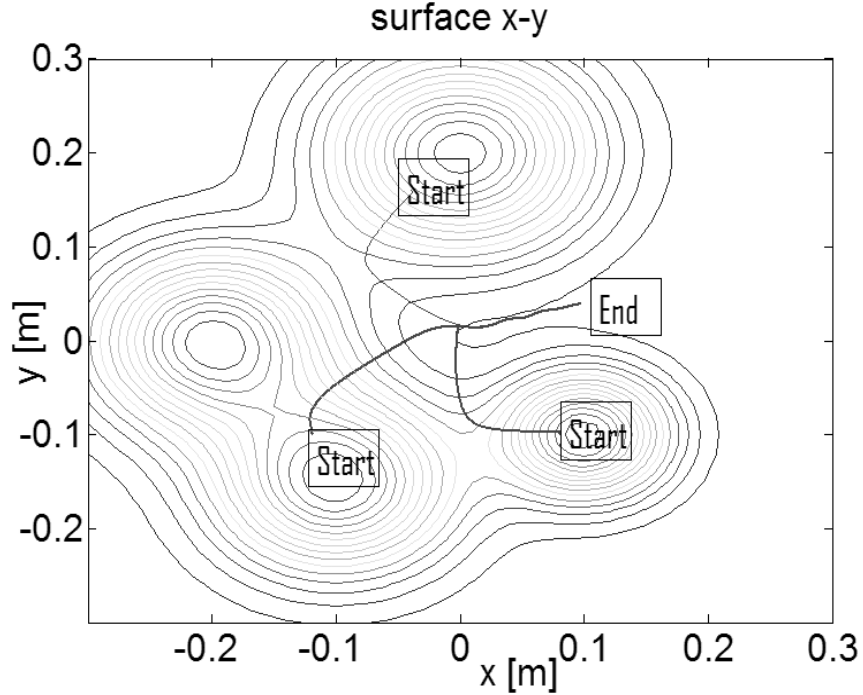


Figure 3.4: The chemotaxis behavior of *C. elegans* produced by the dual-sensory behavioral model nearby four toxin repellents. Four toxin resources locate at $(-0.2, 0)$, $(-0.1, -0.15)$, $(0, 0.2)$, and $(0.1, -0.1)$, respectively. The worm starts at three different positions $(-0.11, -0.1)$, $(0.08, -0.1)$, $(-0.02, 0.17)$ with head angles 135° , 180° , and 180° , respectively. The worm avoids the toxin repellents and moves towards a safe position away from toxin.

point $(0,0)$. The worm starts at $(-0.1,0.1)$. The movement path in Fig. 3.3 indicates the success in the mission of food seeking. At the end, the worm finds the food located at point $(0,0)$ and moves around it.

Next we test the chemotaxis behavior of *C. elegans* near four toxin repellents that are located at points $(-0.2,0)$, $(-0.1,-0.15)$, $(0,0.2)$, and $(0.1,-0.1)$, respectively. *C. elegans* starts at three different positions with different head angles 135° , 180° , and 180° , respectively. The results in Fig. 3.4 illustrate that *C. elegans* can avoid toxin by maintaining a maximum distance away from it, and always reach the same place with the minimum concentration.

3.2 Single-sensory Behavioral Model

As discussed in Section 2.4, single-sensory mode is another navigation strategy for *C. elegans* during locomotion. When the concentration difference between left-side and right-side sensors is too small for *C. elegans* to detect, the left and right sides sensors work as a single sensor [55]. It is necessary to investigate whether the DNN model with single sensory neuron can still perform chemotaxis behaviors. In the chemotaxis, *C. elegans* changes its strategy from space to time, in which a memory neuron is needed to memorize the previous concentration $C(t-1)$. With this memory neuron, *C. elegans* can compute the temporal change of concentration, $\Delta C_{tp}(t) = C(t) - C(t-1)$, for navigation.

In this section, the behaviors of single-sensory models for food attraction and toxin avoidance are explored. Our objective is to investigate whether *C. elegans* with one sensory neuron can direct itself towards the region of high food concentration or away from the region of high toxin concentration, respectively.

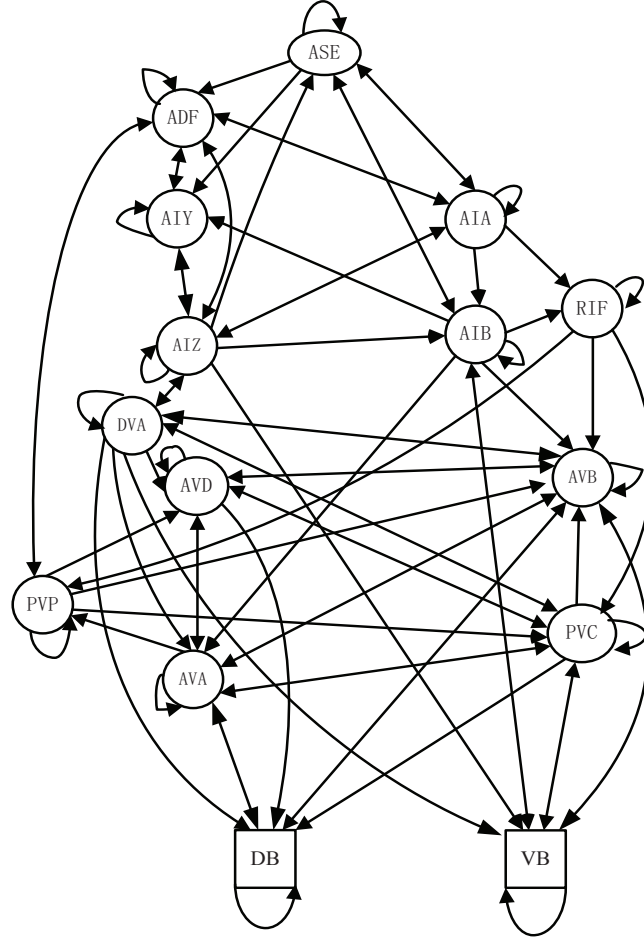


Figure 3.5: The wire diagram for food attraction. Neuron ASE is the sensory neuron for food. Neuron AIY functions as the memory neuron recording the previous food concentration information $C_f(t-1)$. The outputs are neurons DB and VB for left and right sides, and the rest are hidden neurons.

3.2.1 Wire Diagrams

The biological neural model is shown in Fig. 3.5, which is almost the same as the dual-sensory model Fig. 3.1 except that two sensory neurons ASEL and ASER are merged into a single ASE. Similarly in toxin avoidance, ASHL and ASHR as shown in Fig. 3.2 are merged into a single-sensory neuron ASH, as shown in Fig. 3.6. According to reference[81], neuron AIY functions as a memory neuron to record the previous concentration information $C(t-1)$ (C_f for food and C_{tx} for toxin). In the chemotaxis, *C. elegans* computes the change in food concentration between the present and past con-

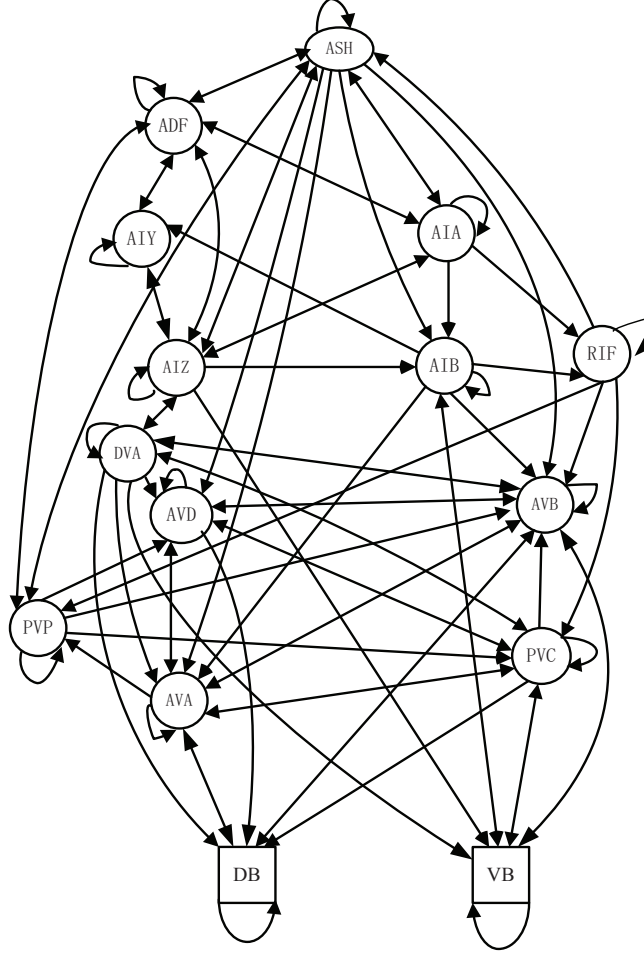


Figure 3.6: The wire diagram for toxin avoidance. The neuron ASH is the toxin sensory neuron. The neuron AIY functions as a memory neuron to record the previous toxin concentration $C_{tx}(t-1)$. DB and VB are the left and right motor neurons. Others are hidden neurons.

centrations, $C(t) - C(t-1)$. The outputs of the biological models are neurons DB and VB, and the rest are hidden neurons.

3.2.2 Learning Tasks

As discussed in Section 2.4, for single-sensory models, *C. elegans* uses the temporal concentration difference $\Delta C_{tp}(t) = C(t) - C(t-1)$ for navigation. However, with $\Delta C_{tp}(t)$, *C. elegans* only knows the forward direction is correct or not. For instance, for food attraction, when $\Delta C_{f,tp}(t) > 0$, *C. elegans* is heading the correct direction. When

$\Delta C_{f,tp}(t) \leq 0$, *C. elegans* is heading a wrong direction and it should turn. The new direction, either left or right, can be randomly selected. In this work we assume the worm chooses right turning as its preference. Hence the left-side motor neuron output is always higher than or equal to the right motor neuron.

The RTRL training method described in Section 2.2.4 is applied to train the single-sensory biological models. The biological models are trained to learn the SLFs illustrated in Fig. 2.13 for food attraction, and Fig. 2.14 for toxin avoidance.

3.2.3 Testing Results

Food Attraction

The training data for the single-sensory behavioral model for food attraction involve two terms, $C_f(t)$ and $C_f(t-1)$, which range from 0 to 2 with interval 0.1. To train this model, it needs two neurons to receive the input training data, $C_f(t)$ and $C_f(t-1)$. ASE functions as the attractant sensory neuron [85] to receive the input $C_f(t)$. As claimed by [81], AIY has the memory ability. Based on this result, AIY is assigned by us to serve as the memory neuron to receive the input $C_f(t-1)$. However, as shown in Fig. 3.5, AIA, AIZ, and AIB share the similar connections and these neurons may serve as the memory neurons. To the best of our knowledge, there are not any references to mention their memory ability. Thus AIA, AIZ, and AIB only function as interneurons in our models. Target data for the two output neurons, V_{left} for DB and V_{right} for VB, are calculated according to Eqs. (2.31) and (2.32), respectively.

The simulation scenario is the same as Section 2.4.3 for the single-sensory behavioral model for food attraction. The result for food attraction is shown in Fig. 3.7. One food attractant is located at point (0,0). The model starts at (0.1, -0.15) with the head angle 180° and it ends at the food source (0,0).

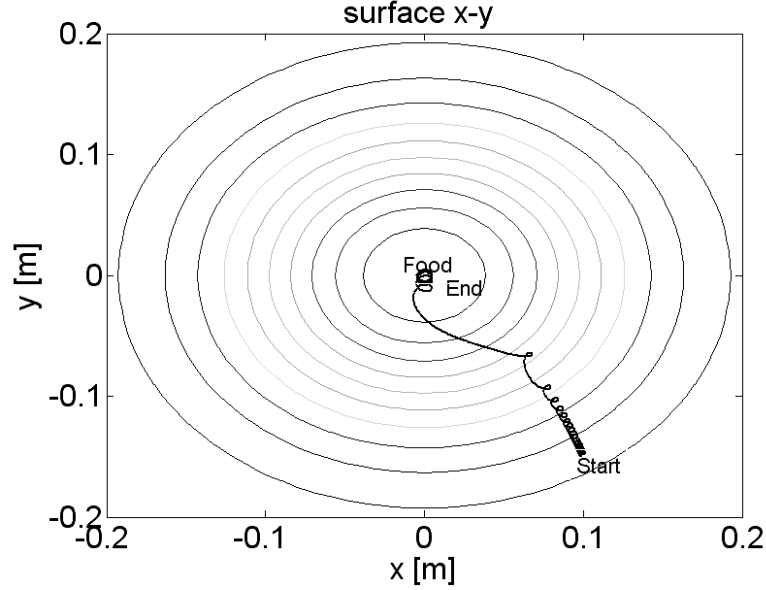


Figure 3.7: The chemotaxis behavior of *C. elegans* produced by the single-sensory behavioral model for food attraction. One food source locates at the point (0,0). *C. elegans* starts at (0.1, -0.15) with the head angle 180° and ends at the food source (0,0).

Toxin Avoidance

The training data for the single-sensory behavioral model for toxin avoidance include two terms, $C_{tx}(t)$ and $C_{tx}(t-1)$, which range from 0 to 2 with interval 0.1. To train this model, ASH functions as the input neuron to receive the training data $C_{tx}(t)$, and AIY is assigned to be the memory neuron to receive the training data $C_{tx}(t-1)$. Target data for the two output neurons, V_{left} for DB and V_{right} for VB, are calculated by Eqs. (2.33) and (2.33), respectively.

The results of toxin avoidance are shown in Fig. 3.8. Four toxin resources locate at (-0.2,0), (-0.1,-0.15), (0,0.2), and (0.1,-0.1), respectively. The worm starts at three different positions (-0.16, -0.01), (0,0.18), (0.08,-0.05) with head angle 180° , respectively. It avoids the toxin repellents and moves towards a safe position away from toxin.

Comparing Fig. 3.3 with Fig. 3.7 for food attraction, Fig. 3.4 with Fig. 3.8 for toxin avoidance, the single-sensory behavioral models, though still achieve the desired chemo-

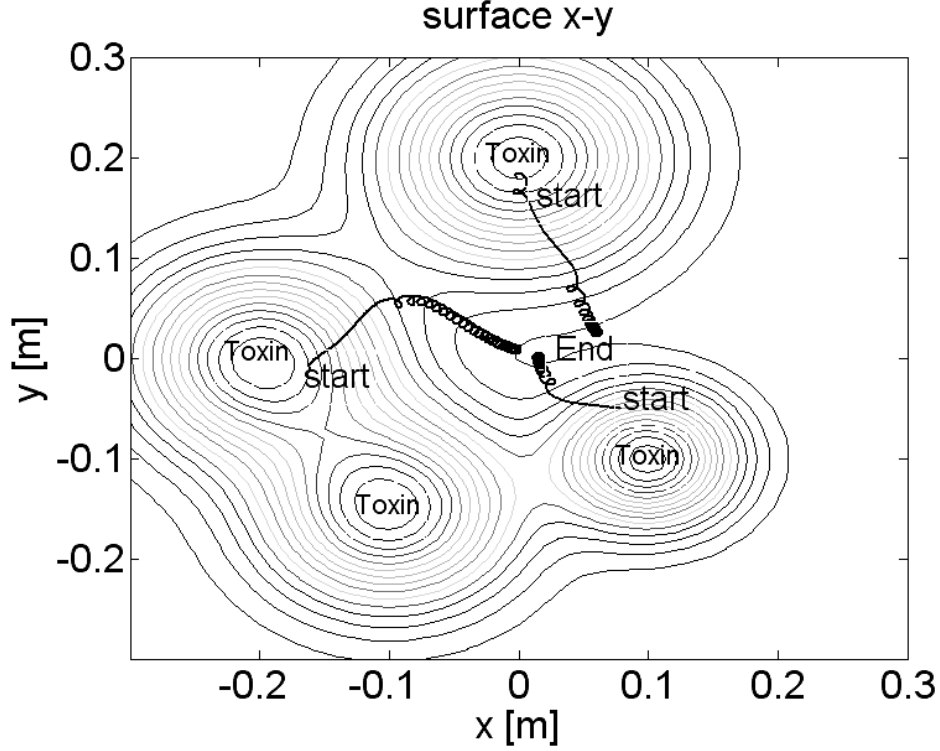


Figure 3.8: The chemotaxis behavior of *C. elegans* produced by the single-sensory behavioral model nearby four toxin repellents. Four toxin resources locate at $(-0.2, 0)$, $(-0.1, -0.15)$, $(0, 0.2)$, and $(0.1, -0.1)$, respectively. The worm starts at three different positions $(-0.16, -0.01)$, $(0, 0.18)$, $(0.08, -0.05)$ with head angle 180° , respectively. The worm avoids the toxin repellents and moves towards a safe position away from toxin.

taxis behaviors, do not move as smooth as the that generated by the dual-sensory behavioral models, due to the lack of the gradient information of the concentration.

3.3 Integrated Behavioral Model

In previous sections we explore four chemotaxis behavioral models individually, which include dual-sensory model for food attraction, dual-sensory model for toxin avoidance, single-sensory model for food attraction, and single-sensory model for toxin avoidance. In this section, we combine the dual-sensory models for food attraction and toxin avoidance together, as well as the single-sensory models. Our objective of the combination is to investigate whether these combined models can perform the task of finding

food and avoiding simultaneously.

3.3.1 Wire Diagrams

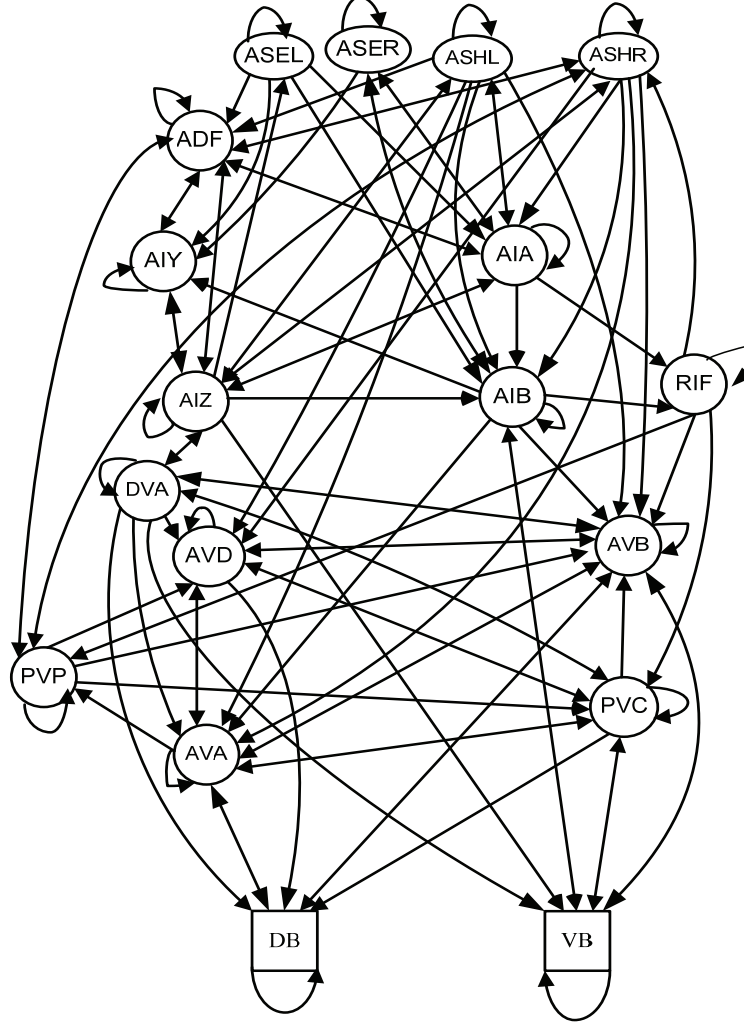


Figure 3.9: Neural diagram for a dual-sensory behavioral model for both food attraction and toxin avoidance. ASEL and ASER are left-side and right-side input neurons for food concentration. ASHL and ASHR are left-side and right-side input neurons for toxin concentration. VB and DB are right-side and left-side motor neurons, and the rest are hidden neurons.

The wire diagram for the integrated dual-sensory behavioral model is shown in Fig. 3.9, which is the combination of Fig. 3.1 and Fig. 3.2. Note that all four sensory neurons, ASEL, ASER, ASHL, and ASHR, are included. ASEL and ASER are left-side and right-side input neurons for food concentration. ASHL and ASHR are left-side and

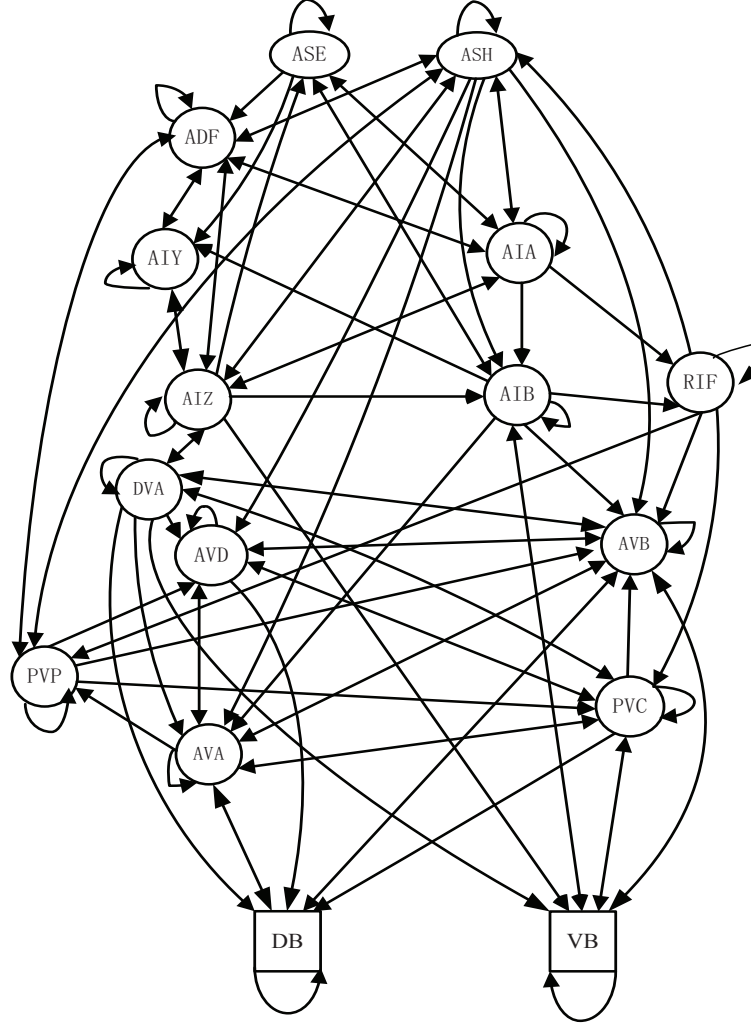


Figure 3.10: Neural diagram for a single-sensory behavioral model for both food attraction and toxin avoidance. ASE is the input neuron for food concentration. ASH is the input neuron for toxin concentration. AIY is a memory neuron. VB and DB are right-side and left-side motor neurons, and the rest are hidden neurons.

right-side input neurons for toxin concentration. VB and DB are right-side and left-side motor neurons, and the rest neurons are hidden neurons.

The wire diagram for the integrated single-sensory behavioral model is shown in Fig. 3.10, which is the combination of Fig. 3.5 and Fig. 3.6, including both ASE and ASH. ASE is the input neuron for food concentration. ASH is the input neuron for toxin concentration. AIY is a memory neuron. VB and DB are right-side and left-side motor neurons, and the rest are hidden neurons.

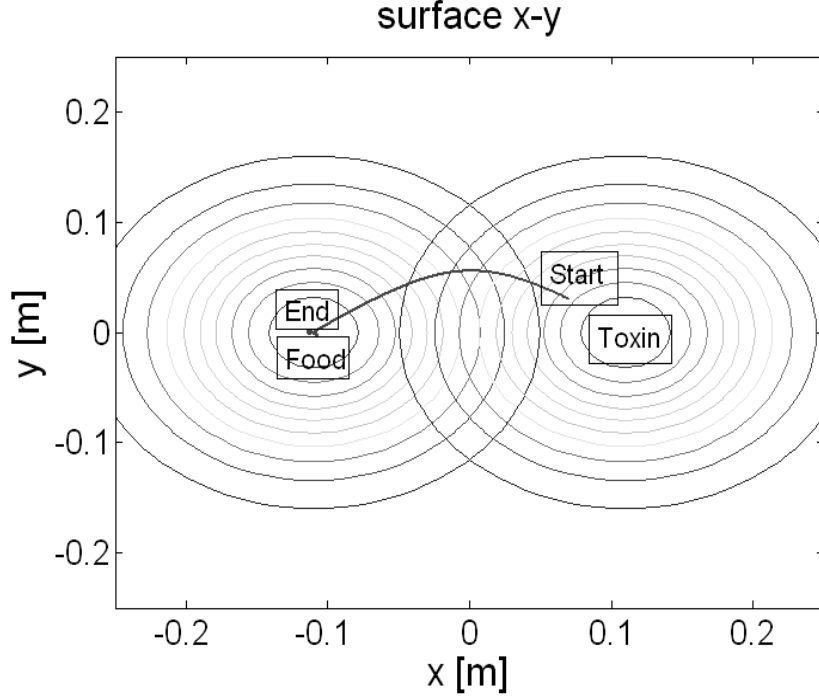


Figure 3.11: The chemotaxis behavior of the dual-sensory behavioral model for food attraction and toxin avoidance. The food and toxin locate at $(-0.1, 0)$ and $(0.1, 0)$, respectively. *C. elegans* starts at $(0.08, 0.04)$ with the head angle 90° , and at the end reaches the food source.

3.3.2 Learning Tasks

Analogous to Section 2.3 and Section 2.4, the biological models are trained to learn the SLFs as shown in Fig. 2.8 for the dual-sensory biological model and Fig. 2.17 for the single-sensory biological model. The two wire diagrams, as shown in Fig. 3.9 and Fig. 3.10, are trained by RTRL, which is described in Section 2.2.4.

3.3.3 Testing Results

When both food and toxin exist, the well trained biological models can perform the expected chemotaxis behaviors. Fig. 3.11 shows the chemotaxis behavior of the dual-sensory biological model. One food and one toxin locate at $(-0.1, 0)$ and $(0.1, 0)$, respectively. *C. elegans* starts at $(0.08, 0.04)$ with the head angle 90° , and at the end reaches the food source.

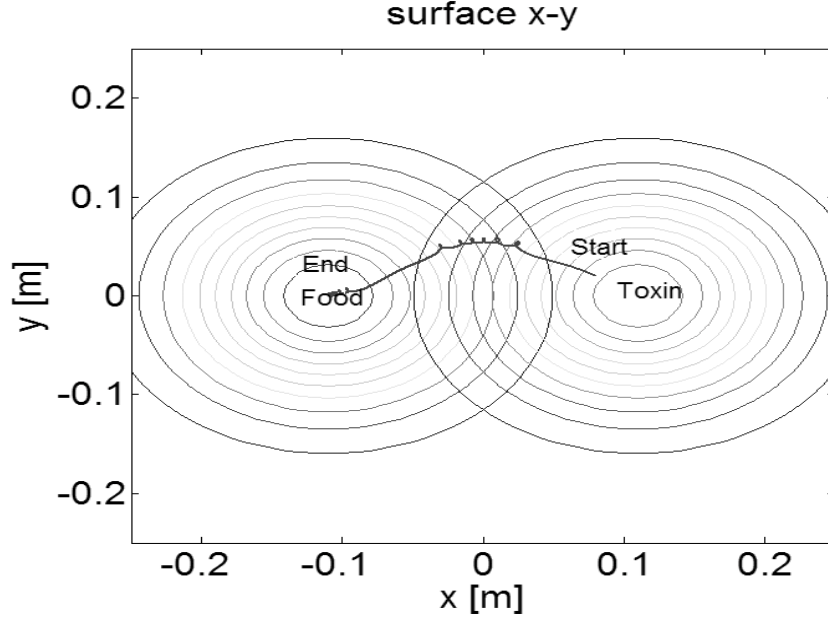


Figure 3.12: The chemotaxis behavior of the single-sensory behavioral model for food attraction and toxin avoidance. The food and toxin locate at $(-0.1, 0)$ and $(0.1, 0)$ respectively. *C. elegans* starts at $(0.08, 0.04)$ with the head angle 270° , and at the end reaches the food source.

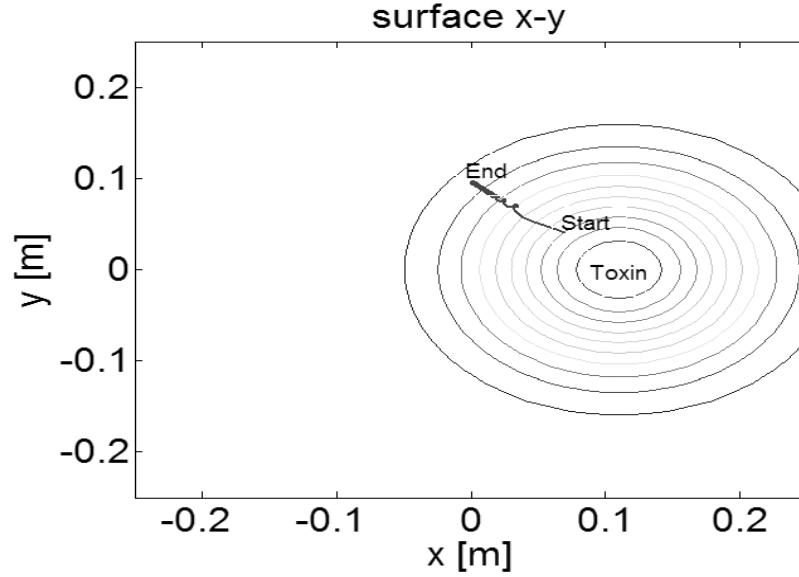


Figure 3.13: The chemotaxis behavior of the single-sensory behavioral model nearby a toxin repellent located at $(0.1, 0)$. The *C. elegans* starts from $(0.07, 0.04)$ with head angle 90° , and finally it avoids the toxin.

Fig. 3.12 shows the chemotaxis behavior of the single-sensory biological model. One food and one toxin locate at $(-0.1, 0)$ and $(0.1, 0)$ respectively. *C. elegans* starts at

(0.08,0.04) with the head angle 270° , and at the end it reaches the food source.

It would be interesting to investigate whether the integrated behavioral models can perform equally well for a single task such as food attraction or toxin avoidance. For simplicity we only illustrate the toxin avoidance by the single-sensory biological model. As shown in Fig. 3.13, a toxin source is located at (0.1,0). The *C. elegans* model starts from (0.07,0.04) with head angle 90° , and finally it leaves far from the toxin source.

Above all, comparing the performances between artificial and biological models, we cannot observe there are any obvious differences between them except that the first class are the simplified neural connection models and the other is the biological models. However, for the integrated behavior, biological models can mimic the actual mechanism of *C. elegans* when both food and toxin existed concurrently during chemotaxis, because the ASE is only responsible for the food attraction and the ASH is only for the toxin avoidance, which contrasts to the artificial models in which the food and toxin concentrations are sensed by the same neuron.

3.4 Conclusion

In this chapter, the chemotaxis behaviors of *C. elegans* are investigated based on its biological neural wire diagrams with the focus on food attraction, toxin avoidance, and the integrated behaviors. DNN is chosen as the mathematical model for the biological wire diagram. Our work based on the biological wire diagrams extends the existing results based on the artificial DNN. These biological neural wire diagrams are extracted from chemosensory neurons to motor neurons directly. It is the first time for us to explore the biological neuron connections and train the biological models directly using RTRL algorithm. Through intensive simulation tests on various scenarios, it is verified that

the biological wire diagrams can successfully mimic the *C. elegans* to perform complex chemotaxis behaviors. However, these biological behavioral models in this chapter keep a constant speed. Even arriving at the food source or leaving far from the toxin source, the *C. elegans* cannot stop spontaneously. In the next chapter, we will incorporate the speed regulation mechanism into the biological behavioral models.

Chapter 4

Modeling the Chemotaxis Behaviors of *C. elegans* Based on the Biological Wire Diagram with Speed Regulation

Currently there are two opposite points of view about the relationship between the concentration input and speed of *C. elegans*. One opinion is that the speed of *C. elegans* is constant [87, 45], and the other one is that *C. elegans* will reduce its speed when encountering the food [86]. In Chapter 3, we have investigated the chemotaxis behavior of *C. elegans* by assuming its speed to be a constant and obtained the similar results as [45]. To the best of our knowledge, the actual causation of the speed reducing is still unknown. Thus in this chapter we assume its speed can be regulated according to the concentration input.

4.1 Introduction

The content in this chapter is to extend the work in Chapter 3. First, we use the biological behavioral models in Chapter 3, which are constructed by extracting the biological wire diagrams directly from sensory neurons to motor neurons. There are six chemotaxis behavioral models, which are classified into two kinds, one for dual-sensory model and the other for single-sensory model. For each kind there are three models, one for food attraction, one for toxin avoidance, and one integrated model for both food attraction and toxin avoidance. As the same as Chapter 3, the wire diagram for each model is represented by a dynamic neural network (DNN), and each neuron is described as a non-linear active function. DNN is suitable for chemotaxis behavioral modeling owing to its dynamical nature, since its connections can be made analogous to the nature ones such as synapses.

Second, we incorporate speed regulation into these biological behavioral models, so that navigation is complete with orientation control and speed control. During the locomotion, *C. elegans* can not only approach the food source (leave the toxin source), but also reduce its speed when near to the food source (far from the toxin source).

Third, the synergy of dual-sensory and single-sensory models is explored. Gradient information varies with respect to the distance between sources (food and toxin). *C. elegans* behaves in dual-sensory behavioral mode when gradient difference (namely, the concentration difference) between left and right sides is sufficiently large, whereas it behaves in single-sensory mode if this gradient difference is too low to detect. In this chapter, we provide an integrated behavioral model (based on the dual-sensory behavior model) to perform the chemotaxis behaviors of food attraction and toxin avoidance simultaneously, and this model works under either dual-sensory model or single-sensory

mode based on the available gradient information. With concentration information, *C. elegans* also can regulate the speed spontaneously.

Fourth, we test our models in different scenarios. In each scenario, *C. elegans* successfully approaches the food source or escapes from the toxin source. It verifies that SFLs can well capture the chemotaxis behaviors. Furthermore, once *C. elegans* is trained to learn the SFLs, it can perform its corresponding behaviors in different scenarios without re-training.

Fifth, without losing the biological reality, we quantitatively analyze the results of the single-sensory integrated model by comparing with other biological results. First, we analyze the neuronal connectivities of the resultant wire diagrams by following the method of [25]. In this way, we have investigated the similarity of these wire diagrams and simplified them to smaller networks. Next, we use quantitative analysis method to compare the trajectories of the resultant wire diagrams with the experiment results provided by [19] and [87]. At last, we add the external noise and internal noise to the resultant wire diagrams and test their robustness. We also quantitatively analyze the trajectories of these wire diagrams affected by noises and compare them with the experiment data provided in [87, 19].

This chapter is organized as following. Section 4.2 provides several preliminary results for subsequent sections, including the kinematics of locomotion, distribution of food and toxin concentrations, DNN model, and the training method. Section 4.3 investigates dual-sensory biological models with speed regulation for food attraction and toxin avoidance. Section 4.4 investigates the single-sensory models with speed regulation for food attraction and toxin avoidance. In Section 4.5, dual-sensory models are integrated to one behavioral model to perform all the chemotaxis behaviors synchronously. In Section 4.6,

the single-sensory integrated behavioral model is also produced to perform these chemotaxis behaviors synchronously. In Section 4.7, quantitative analysis are carried out by comparing with the biological experiment results. In each section, the corresponding neural wire diagrams, switching logic functions and testing results are demonstrated in details. Section 4.8 concludes the chapter.

4.2 Kinematics Models

C. elegans performs the sinusoid form during locomotion. Only the head receives the external concentration. In this chapter, *C. elegans* is modeled as a point source in the $x - y$ plane with velocity $v(t)$ at head, and angle $\theta(t)$ measured from the x -axis at time t , shown in Fig. 2.1.

The kinematic updating equations are:

$$x(t+1) = x(t) + v(t)T \cos \theta(t), \quad (4.1)$$

$$y(t+1) = y(t) + v(t)T \sin \theta(t), \quad (4.2)$$

$$\theta(t) = \theta(t-1) + \Delta\theta(t), \quad (4.3)$$

$$v(t) = \frac{1}{2}V_{\max} \cdot [V_{left}(t) + V_{right}(t)], \quad (4.4)$$

$$\Delta\theta(t) = \gamma(V_{right}(t) - V_{left}(t))T, \quad (4.5)$$

where $x(t)$ and $y(t)$ are the position values at time t . $v(t)$ is the velocity of worm, which is the average value of the left and right output neurons multiplying by the worm's maximum speed V_{max} , 0.0022m/s. $\theta(t)$ is determined by the difference of left and right output neurons multiplying by one constant γ , which is called turning rate [3]. T is the sampling period. .

From the kinematic model above, it can be seen that the speed $v(t)$ is changing

according to the summation of two outputs: $V_{left}(t) + V_{right}(t)$, and the direction of the worm θ is determined by the subtraction of two outputs: $V_{right}(t) - V_{left}(t)$. When $V_{left}(t) > V_{right}(t)$, the worm turns right, and vice versa. When $V_{left}(t) = V_{right}(t)$, the worm goes straightly. When $V_{left}(t)$ and $V_{right}(t)$ become small and approach to 0, the worm slows down to stop. Thus, both the speed and the direction are changeable concurrently.

4.3 Dual-sensory Behavioral Model

In this section, we explore behaviors of dual-sensory models for food attraction and toxin avoidance. For dual-sensory models, we assume that *C. elegans* is able to sense the spatial difference of concentrations between the left-side and right-side sensory neurons. Our target is to investigate whether the worm can direct itself towards the region of high food concentration or away from the region of high toxin concentration, respectively. Meanwhile, *C. elegans* can change its speed to zero when approaches the food or leaves far away from the toxin source. The concentration distribution and the training method are the same as those in Section 2.2.2 and Section 2.2.4, respectively.

4.3.1 Learning Tasks

The wire diagram of dual-sensory behavioral model for food attraction is shown as Fig. 3.1, and for toxin avoidance is shown as Fig. 3.2. To construct the SLFs, we solve $V_{left}(t)$ and $V_{right}(t)$ from Eqs. (4.4) and (4.5):

$$V_{left}(t) = \underbrace{\frac{v(t)}{V_{max}}}_{speed} - \underbrace{\frac{\Delta\theta(t)}{2\gamma T}}_{orientation}, \quad (4.6)$$

$$V_{right}(t) = \underbrace{\frac{v(t)}{V_{max}}}_{speed} + \underbrace{\frac{\Delta\theta(t)}{2\gamma T}}_{orientation}. \quad (4.7)$$

From Eqs. (4.6) and (4.7), both $V_{left}(t)$ and $V_{right}(t)$ are determined by two components: speed and orientation. In this work, we assume that the speed $v(t)$ is determined by the average value of concentration $C_{left}(t)$ and $C_{right}(t)$, and the orientation is determined by the difference between $C_{left}(t)$ and $C_{right}(t)$. Thus, SLFs can be constructed as:

$$V_{left}(t) = \underbrace{\phi(\bar{C}(t))}_{speed} - \underbrace{\sigma(\bar{C}(t), \Delta C_{sp}(t))}_{orientation}, \quad (4.8)$$

$$V_{right}(t) = \underbrace{\phi(\bar{C}(t))}_{speed} + \underbrace{\sigma(\bar{C}(t), \Delta C_{sp}(t))}_{orientation}. \quad (4.9)$$

Here $\phi(\bar{C}(t))$ is a SLF of speed with the average concentration, $\bar{C}(t) = (C_{left}(t) + C_{right}(t))/2$. $\sigma(\bar{C}(t), \Delta C_{sp}(t))$ is a SLF of orientation with the arguments $\bar{C}(t)$ and spatial concentration difference, $\Delta C_{sp}(t) = C_{left}(t) - C_{right}(t)$.

SLFs for Food Attraction

SLFs for food are chosen to be:

$$\phi(\bar{C}_f(t)) = \frac{1}{2} \sqrt{C_{\max,f}^2 - \bar{C}_f^2(t)}, \quad (4.10)$$

$$\sigma(\bar{C}_f(t), \Delta C_{f,sp}(t)) = \frac{1}{2} \sqrt{C_{\max,f}^2 - \bar{C}_f^2(t)} \cdot \tanh(\Delta C_{f,sp}(t)), \quad (4.11)$$

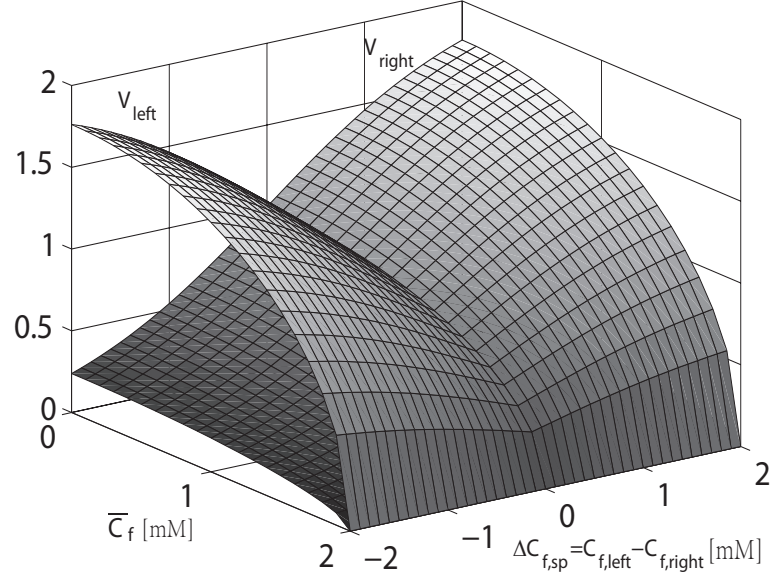


Figure 4.1: Plot of switching logic function for food attraction with speed changing based on dual-sensory neuron models. When $\Delta C_{f,sp}(t) = 0$, *C. elegans* goes straightly. When $\Delta C_{f,sp}(t) > 0$, $V_{right}(t) > V_{left}(t)$, the worm turns left and vice versa. When $\bar{C}_f(t)$ is smaller, outputs are larger and vice versa. Here $C_{max,f}$ is set to be 2. The inputs of $C_{f,left}(t)$ and $C_{f,right}(t)$ range from 0 to 2, hence the range of $\bar{C}_f(t)$ is $[0, 2]$, and $\Delta C_{f,sp}(t)$ is $[-2, 2]$.

where $\bar{C}_f(t) = \frac{C_{f,left}(t) + C_{f,right}(t)}{2}$ is the average concentration of food, and $\Delta C_{f,sp}(t) = C_{f,left}(t) - C_{f,right}(t)$ is the concentration difference of food. $C_{max,f}$ is the highest concentration value of food source. The final motor neural outputs, $V_{right}(t)$ and $V_{left}(t)$, as functions of arguments $C_f(t)$ and $\Delta C_{f,sp}(t)$, are illustrated in Fig. 4.1.

From Fig. 4.1, we can see that when $\bar{C}_f(t)$ is small, the outputs of $V_{left}(t)$ and $V_{right}(t)$ are large. When the $\bar{C}_f(t)$ becomes larger, the outputs of $V_{left}(t)$ and $V_{right}(t)$ decrease and finally down to zero. By this mechanism, *C. elegans* achieves the speed regulation ability. For the orientation control, as shown in Fig. 4.1 and Fig. 4.2, we can observe that when $\Delta C_{f,sp}(t) = 0$, the outputs $V_{left}(t) = V_{right}(t)$, *C. elegans* goes straightly. When $\Delta C_{f,sp}(t) > 0$, which means that food located on the left side, the outputs are $V_{left}(t) < V_{right}(t)$, which make the worm turns left and vice versa.

The choice of SLFs is not limited to Eqs. (4.10) and (4.11). Generally speaking,

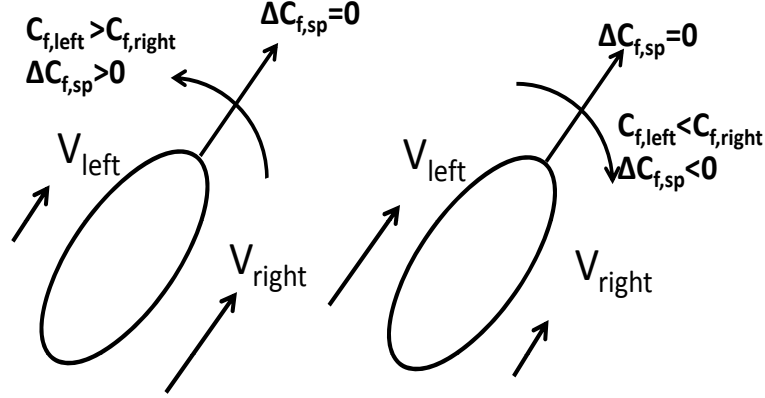


Figure 4.2: Movement of *C. elegans* during food attraction. When $\Delta C_{f,sp}(t) = 0$, *C. elegans* goes straightly. When $\Delta C_{f,sp}(t) > 0$, the worm turns left (left figure) and vice versa (right figure).

$\phi(\overline{C}_f(t))$ should be reciprocal to $\overline{C}_f(t)$ for food attraction. *C. elegans* must stop when it reaches a food source, namely, $\overline{C}_f(t)$ reaches maximum. For the orientation control, $\sigma(\overline{C}_f(t), \Delta C_{f,sp}(t))$ is reciprocal to $\overline{C}_f(t)$ but proportional to $\Delta C_{f,sp}(t)$. When approaching a food source, sharp turning is not necessary even if $\Delta C_{f,sp}(t)$ is very large. However, when *C. elegans* leaves far from the food source, a large $\Delta C_{f,sp}(t)$ leads to a sharp turning.

SLFs for Toxin Avoidance

During toxin avoidance, the speed of *C. elegans* should decrease gradually when leaving away from the toxin source, i.e., the concentration decreases. Thus, the SLF of speed should be proportional to the average concentration. Also, the orientation of toxin avoidance should be right opposite to food attraction. For instance, *C. elegans* should turn left when the toxin source is on the right-hand side, and vice versa. For simplicity,

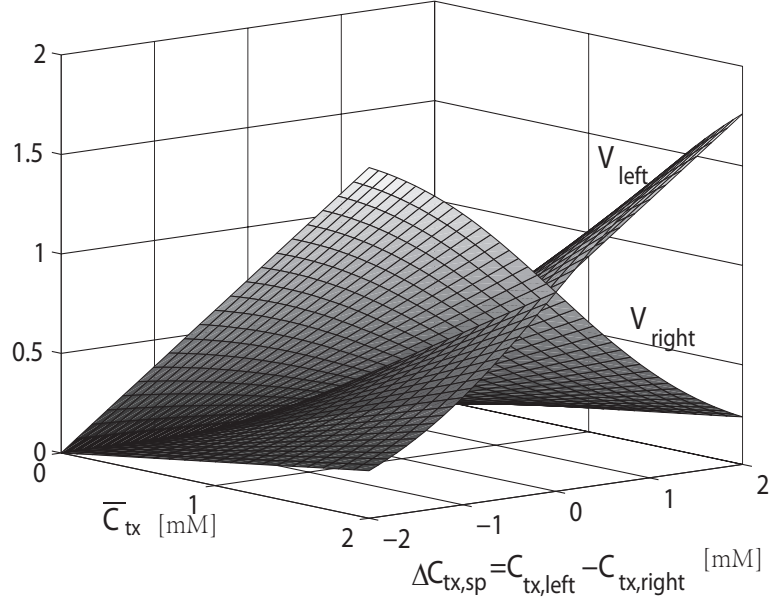


Figure 4.3: Plot of switching logic function for toxin avoidance with speed changing based on dual-sensory neuron models. When $\Delta C_{tx,sp}(t) = 0$, *C. elegans* goes straightly. when $\Delta C_{tx,sp}(t) > 0$ the outputs are $V_{left}(t) > V_{right}(t)$ that make the worm turns right and vice versa. When $\overline{C}_{tx}(t)$ is large, the outputs are large. When the $\overline{C}_{tx}(t)$ is near to 0, the outputs are down to zero.

$\phi(\overline{C}(t))$ are chosen linearly proportional to average concentration. The SLFs are:

$$\phi(\overline{C}_{tx}(t)) = \frac{\overline{C}_{tx}(t)}{2}, \quad (4.12)$$

$$\sigma(\overline{C}_{tx}(t), \Delta C_{tx,sp}(t)) = -\frac{\overline{C}_{tx}(t)}{2} \tanh(\Delta C_{tx,sp}(t)), \quad (4.13)$$

where $\overline{C}_{tx}(t) = \frac{C_{tx,left}(t) + C_{tx,right}(t)}{2}$ is the average concentration of toxin, and $\Delta C_{tx,sp}(t) = C_{tx,left}(t) - C_{tx,right}(t)$ is the concentration difference of toxin. It can be seen that $\overline{C}_{tx}(t)$ regulates the speed and $\Delta C_{tx,sp}(t)$ determines the turning. The final motor neural outputs, $V_{right}(t)$ and $V_{left}(t)$, as functions of arguments $C_{tx}(t)$ and $\Delta C_{tx,sp}(t)$, are illustrated in Fig. 4.3.

The movement of *C. elegans* during toxin avoidance is demonstrated in Fig. 4.4. When $\Delta C_{tx,sp}(t) > 0$, implying that the toxin source is on the left side, then $V_{left}(t) > V_{right}(t)$, the left-side speed is faster than the right-side speed. Thus *C. elegans* turns right.

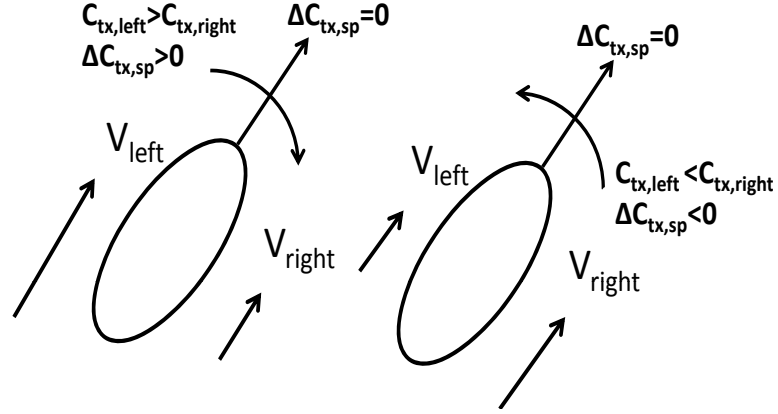


Figure 4.4: Movement of *C. elegans* during toxin avoidance. When $\Delta C_{tx,sp}(t) = 0$, *C. elegans* goes straightly. When $\Delta C_{tx,sp}(t) > 0$ the worm turns right (left figure) and vice versa (right figure).

Similarly, when $\Delta C_{tx,sp}(t) < 0$, then $V_{left}(t) < V_{right}(t)$, and *C. elegans* turns left. When $\Delta C_{tx,sp}(t) = 0$, $V_{left}(t) = V_{right}(t)$, *C. elegans* goes straightly. For the speed regulation, when $\bar{C}_{tx}(t)$ is large, the outputs of $V_{left}(t)$ and $V_{right}(t)$ are large. When the $\bar{C}_{tx}(t)$ decreases, $V_{left}(t)$ and $V_{right}(t)$ also decrease linearly and finally down to zero.

From the Eqs. (4.10) and (4.12), we can observe that SLFs of speed are opposite for food attraction and toxin avoidance, due to the nature of tasks. For food attraction, the gradient is

$$\frac{\partial \phi(\bar{C}_f(t))}{\partial \bar{C}_f(t)} = -\frac{\bar{C}_f(t)}{2\sqrt{C_{\max,f}^2 - \bar{C}_f^2(t)}},$$

which is negative. For toxin avoidance, the gradient is

$$\frac{\partial \phi(\bar{C}_{tx}(t))}{\partial \bar{C}_{tx}} = \frac{1}{2},$$

which is positive. In such circumstances, when concentration is higher, or *C. elegans* is nearby the source, *C. elegans* is going to stop before food or move quickly from toxin.

Comparing Eqs. (4.11) and (4.13), and noting the “-” sign in (4.13), SLFs of orientation

are made to function in an opposite manner due to the nature of tasks. When concentration is higher on one side, *C. elegans* should turn to this side for food attraction, whereas turn to the opposite side for toxin avoidance.

4.3.2 Testing Results

The wire diagram models of food attraction and toxin avoidance, shown in Fig. 3.1 and Fig. 3.2, respectively, are trained to remember the input-output mappings for food attraction (Fig. 4.1) and toxin avoidance (Fig. 4.3), where inputs are the average concentration and concentration difference, and outputs are motor neuron voltages V_{left} and V_{right} given by Eqs. (4.8) and (4.9).

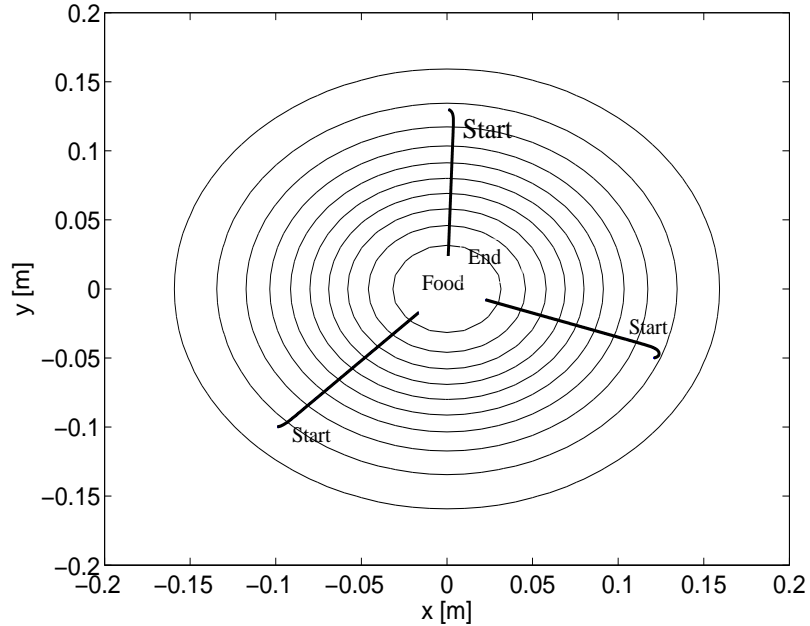


Figure 4.5: The test results of food attraction with speed changing for dual-sensory model. One food source is located at point (0, 0) with Gaussian distribution. The worm starts at three different locations $(-0.1, -0.1)$, $(0.12, -0.06)$, $(0.14, 0.14)$ with initial angle $\theta(0) = 0^\circ$. Finally the worm finds the correct direction towards the food and stops after approaches food.

The training data are randomly generated in the interval $[0, 2]$ for average concentra-

tion, and $[-2, 2]$ for concentration difference. The corresponding output data of DNN for training are calculated using the input-output mapping shown in Fig. 4.1 and Fig. 4.3 for food attraction and toxin avoidance, respectively.

For food attraction, Fig. 4.5 shows the test results. One food source is located at point $(0,0)$ with Gaussian distribution. The worm starts at three different locations $(-0.1, -0.1)$, $(0.12, -0.06)$, $(1, 0.14)$ with initial angle $\theta(0) = 0^\circ$. The worm is able to find the correct direction towards the food and reduces its speed when approaches the source, and stops at the place nearby the food.

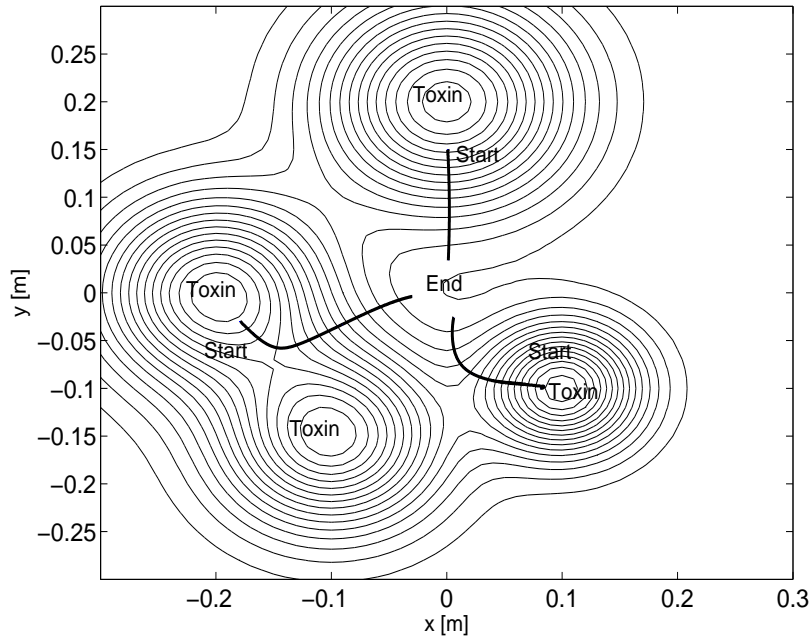


Figure 4.6: The test results of toxin avoidance with speed changing. Four toxin resources locate at $(-0.2, 0)$, $(-0.1, -0.15)$, $(0, 0.2)$, and $(0.1, -0.1)$. The worm starts at three different positions $(-0.18, -0.03)$, $(0, 0.15)$, $(0.08, -0.1)$ with initial head angle randomly. Finally the worm successfully finds the lower toxin concentration place to settle down.

For toxin avoidance, Fig. 4.6 shows the test results. Four toxin sources are located at $(-0.2, 0)$, $(-0.1, -0.15)$, $(0, 0.2)$, and $(0.1, -0.1)$. *C. elegans* starts at three different positions $(-0.18, -0.03)$, $(0, 0.15)$, $(0.08, -0.1)$ with initial head angle θ randomly generated.

C. elegans escapes from the toxin sources and towards the lower toxin concentration places. With the toxin concentration decreasing, *C. elegans* gradually reduces its speed and finally stops.

4.4 Single-sensory Behavioral Model

In this section, the behaviors of single-sensory modes for food attraction and toxin avoidance are explored. Our objective is to investigate whether *C. elegans* with one sensory neuron can direct itself towards the region of higher food concentration or away from the region of higher toxin concentration, respectively. At the same time, *C. elegans* can change its speed to zero when it approaches the food or leaves far away from the toxin source. The concentration distribution and the training method are the same as those in Section 2.2.2 and Section 2.2.4, respectively.

4.4.1 Learning Tasks

The wire diagram of dual-sensory behavioral model for food attraction is shown as Fig. 3.5, and for toxin avoidance is shown as Fig. 3.6. Following the same method in Section 2.4.2, we assume that *C. elegans* uses the temporal concentration difference $\Delta C_{tp}(t) = C(t) - C(t-1)$ for navigation. However, with $\Delta C_{tp}(t)$, *C. elegans* only knows whether the forward direction is correct or not. For instance, for food attraction, when $\Delta C_{f,tp}(t) > 0$, *C. elegans* is heading the correct direction. When $\Delta C_{f,tp}(t) \leq 0$, *C. elegans* is heading a wrong direction and it should turn. In this work we assume the worm choose right turning as its preference. Hence the left-side motor neuron output is always higher than or equal to the right motor neuron. SLFs for the single-sensory

models are constructed as:

$$V_{left}(t) = \underbrace{\phi(C(t))}_{speed}, \quad (4.14)$$

$$V_{right}(t) = \underbrace{\phi(C(t))}_{speed} + \underbrace{\sigma(C(t), \Delta C_{tp}(t))}_{orientation}, \quad (4.15)$$

where $\phi(C(t))$ is a SLF of speed with the concentration input $C(t)$, $\sigma(C(t), \Delta C_{tp}(t))$ is a SLF of orientation with the arguments $C(t)$ and temporal concentration difference, $\Delta C_{tp}(t) = C(t) - C(t-1)$. This SLF of orientation only appears in (4.15). In this way, if the direction of *C. elegans* is correct, $\Delta C_{tp}(t) > 0$, and then $\sigma(C(t), \Delta C_{tp}(t)) = 0$, which has no influence in V_{right} . When $\Delta C_{tp} \leq 0$, $\sigma(C(t), \Delta C_{tp}(t))$ outputs a negative value. Thus, *C. elegans* turns right.

Compared with SLFs for dual-sensory mode Eqs. (4.8) and (4.9), the SLFs for single-sensory mode Eqs. (4.14) and (4.15) are not symmetric. This is because in single-sensory mode we assume that the worm can only turn right or go straightly. Thus it is adequate to add the term $\sigma(C(t), \Delta C_{tp}(t))$ to the $V_{right}(t)$ only.

SLFs for Food Attraction

SLFs for the single-sensory mode during food attraction are designed as:

$$\phi(C_f(t)) = C_{\max,f} - C_f(t), \quad (4.16)$$

$$\sigma(C_f(t), \Delta C_{f,tp}(t)) = (C_{\max,f} - C_f(t)) \cdot (\tanh(\Delta C_{f,tp}(t) + 1) - 1), \quad (4.17)$$

where $C_f(t)$ is the concentration input of food, and $\Delta C_{f,tp}(t) = C_f(t) - C_f(t-1)$ is the temporal food concentration difference between two time steps at t and $t-1$. $C_{\max,f}$ is the maximum value of the food concentration. The final motor neural outputs, $V_{left}(t)$ and $V_{right}(t)$, as functions of arguments $C_f(t)$ and $\Delta C_{f,tp}(t)$, are shown in Fig. 4.7.

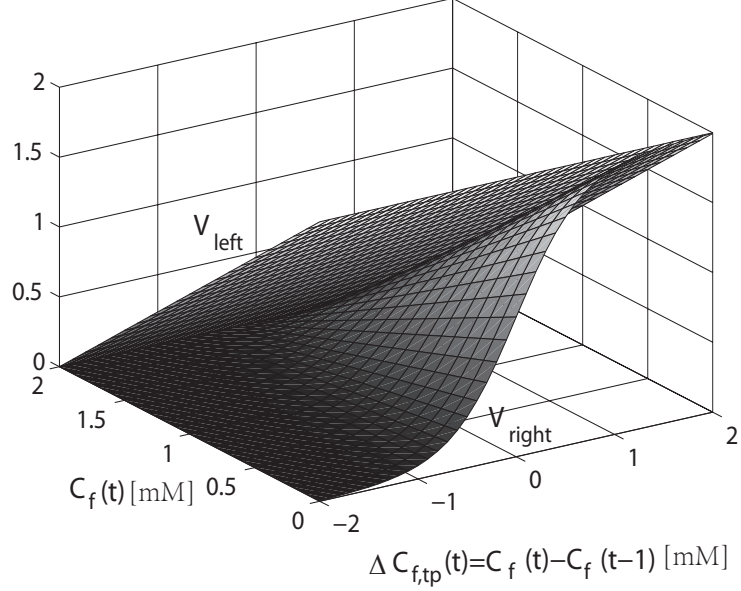


Figure 4.7: The SLFs for the single sensory model during food attraction. If $C_f(t) > C_f(t-1)$, *C. elegans* moves in the correct direction and will move the same direction. When $C_f(t) \leq C_f(t-1)$ (wrong direction), the output of V_{right} is smaller than the V_{left} , then *C. elegans* turns right. When the input $C_f(t)$ is approaching to $C_{max,f}$, the outputs of both motor neurons will approach to zero. In general, a smaller $C(t)$ will yield relative larger outputs.

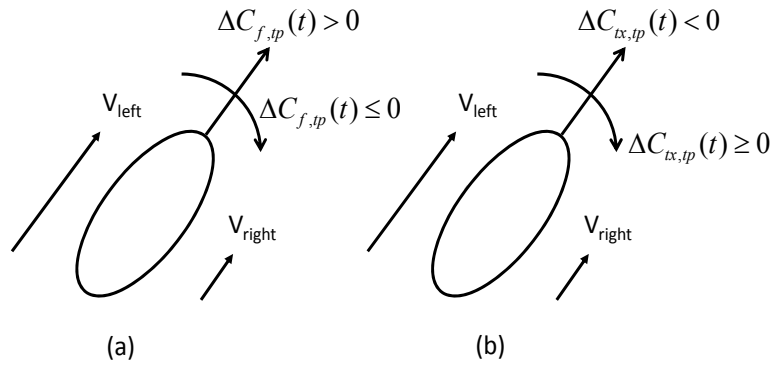


Figure 4.8: Movement of the single sensory model for (a) food attraction, and (b) toxin avoidance. In (a), if $C_f(t) \geq C_f(t-1)$, *C. elegans* is in the correct direction, thus goes straightly. When $C_f(t) < C_f(t-1)$ (wrong direction), the output of V_{right} is smaller than V_{left} , which makes *C. elegans* turn right. In figure (b), the behavior of toxin avoidance is opposite to the food attraction. If $C_{tx}(t) \geq C_{tx}(t-1)$, *C. elegans* turns right. When $C_{tx}(t) < C_{tx}(t-1)$, it go straightly.

The movements of *C. elegans* during food attraction are shown in Fig. 4.7 and Fig. 4.8 (a). If $C_f(t)$ is small, the outputs of $V_{left}(t)$ and $V_{right}(t)$ are large. When $C_f(t)$ becomes larger, the amplitudes of $V_{left}(t)$ and $V_{right}(t)$ decrease and finally become zero. Through this mechanism, *C. elegans* achieves the speed regulation ability. For the orientation control, when $\Delta C_{f,tp} > 0$, *C. elegans* moves towards the correct direction. Thus $\sigma(C_f(t), \Delta C_{f,tp}(t)) = 0$, that is $V_{left} = V_{right}$, and *C. elegans* goes straightly. When $\Delta C_{f,tp} \leq 0$, which means *C. elegans* moves towards the wrong direction, $\sigma(C_f(t), \Delta C_{f,tp}(t)) < 0$, resulting in $V_{left} < V_{right}$. Thus, *C. elegans* turns right.

The choice of SLFs is not limited to Eqs. (4.16) and (4.17). $\phi(C_f(t))$ should be reciprocal to $C_f(t)$ for food attraction. *C. elegans* needs to stop when it reaches the food source, namely, $C_f(t)$ reaches maximum. For the orientation control, $\sigma(C_f(t), \Delta C_{f,tp}(t))$ is reciprocal to $C_f(t)$ but proportional to $\Delta C_{f,tp}(t)$. Furthermore, when nearby the food source, sharp turning is not necessary even if $\Delta C_{f,tp}(t)$ is very negative. However, when *C. elegans* leaves far from the food source, a large $\Delta C_{f,tp}(t)$ leads to a sharp turning.

SLFs for Toxin Avoidance

The SLFs of toxin avoidance for the single-sensory model should be opposite to the SLFs of food attraction. The SLFs are designed as:

$$\phi(C_{tx}(t)) = C_{tx}(t), \quad (4.18)$$

$$\sigma(C_{tx}(t), \Delta C_{tx,tp}(t)) = C_{tx}(t) \cdot (-\tanh(\Delta C_{tx,tp}(t) + 1) - 1), \quad (4.19)$$

where $C_{tx}(t)$ is the toxin concentration input at time t , and $\Delta C_{tx,tp}(t) = C_{tx}(t) - C_{tx}(t-1)$ is the temporal toxin concentration difference between two consecutive time steps. In

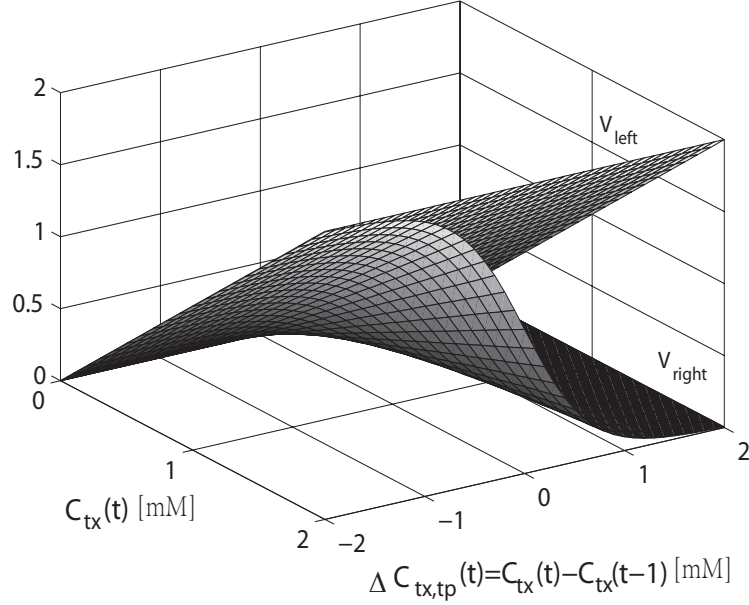


Figure 4.9: The SLFs for single sensory model during toxin avoidance. If $C_{tx}(t) < C_{tx}(t-1)$, *C. elegans* moves in the correct direction and will move the same direction. When $C_{tx}(t) \geq C_{tx}(t-1)$ (wrong direction), the output of V_{right} is smaller than the V_{left} , then *C. elegans* turns right. When the input $C_{tx}(t)$ is near to zero, the outputs of both motor neurons will approach to zero. In general, a smaller $C_{tx}(t)$ will yield relative smaller outputs.

Eq. (4.18) $\phi(C_{tx}(t))$ controls the speed, and in Eq. (4.19) $\sigma(C_{tx}(t), \Delta C_{tx,tp}(t))$ controls the orientation. The plot of the SLFs is shown in Fig. 4.9.

The movements of *C. elegans* during toxin avoidance can be referred in Fig. 4.9 and Fig. 4.8(b). When $C_{tx}(t) \geq C_{tx}(t-1)$, *C. elegans* moves towards the wrong direction. In this case, $\sigma(C_{tx}(t), \Delta C_{tx,tp}(t)) < 0$, which yields $V_{right} < V_{left}$, and *C. elegans* turns right. When $\sigma(C_{tx}(t), \Delta C_{tx,tp}(t)) = 0$, thus $V_{right} = V_{left}$ and *C. elegans* goes straightly. For the speed regulation, when the input $C_{tx}(t)$ approaches to 0, the outputs V_{left} and V_{right} also approach to zero, so *C. elegans* reduces its speed down to zero. When $C_{tx}(t)$ is large, V_{left} and V_{right} are also large, maintaining a high speed.

From the Eqs. (4.16) and (4.18), we can observe that SLFs of speed for food attraction and toxin avoidance are in opposite manners due to the nature of tasks. For food

attraction, the gradient is

$$\frac{\partial \phi(C_f(t))}{\partial C_f(t)} = -1, \quad (4.20)$$

which is negative. For toxin avoidance, the gradient is

$$\frac{\partial \phi(C_{tx}(t))}{\partial C_{tx}(t)} = 1, \quad (4.21)$$

which is positive. In such circumstances, when concentration is higher, *C. elegans* is going to stop before food or move quickly from toxin. By comparing (4.17) and (4.19), SLFs of orientation have the opposite logics for food attraction and for toxin avoidance. When concentration at time t is higher than that at the previous time $t - 1$, *C. elegans* should go straightly for food attraction, or turn for toxin avoidance.

4.4.2 Testing Results

The single-sensory wire diagram models of food attraction and toxin avoidance, shown in Fig. 3.5 and Fig. 3.6, respectively, are trained to remember the input-output mappings for food attraction (Fig. 4.7) and toxin avoidance (Fig. 4.9).

For the training data, the input data includes two terms, $C(t)$ and $C(t - 1)$, which range from 0 to 2, with interval 0.1. Outputs are motor neuron voltages V_{left} and V_{right} given by Eqs. (4.14) and (4.15).

The test results for food attraction are shown in Fig. 4.10. The food source is located at the point $(0, 0)$ with Gaussian distribution. *C. elegans* starts at two different locations $(-0.08, -0.07)$, $(0, 0.12)$ with initial angle 180° . *C. elegans* moves towards the food source and finally stops when it approaches the food after some right turns.

The test results for toxin avoidance are shown in Fig. 4.11. Four toxin resources

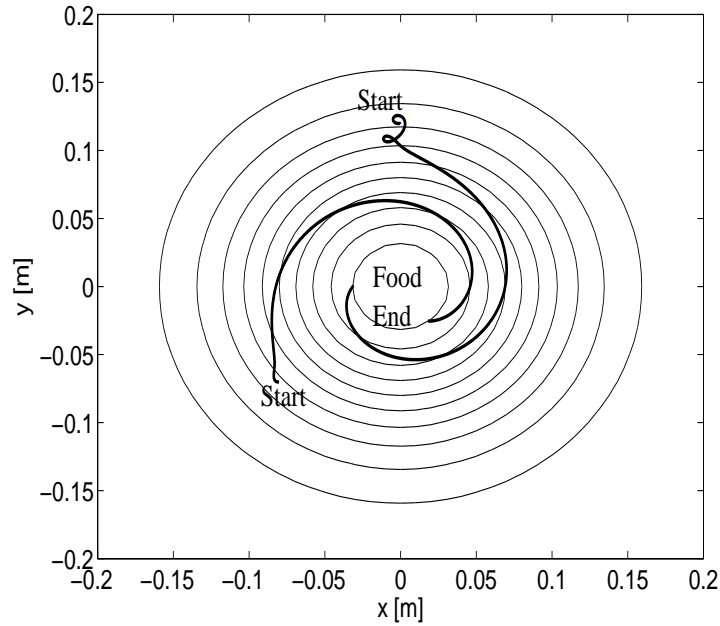


Figure 4.10: Simulation results for the food attraction of single-sensory model. Food source is located at the point (0,0) with Gaussian distribution. *C. elegans* starts at two different locations $(-0.08, -0.07)$, $(0, 0.12)$ with initial angle 180° . The worm moves towards the food source and settles down when it approaches the food after some right turns.

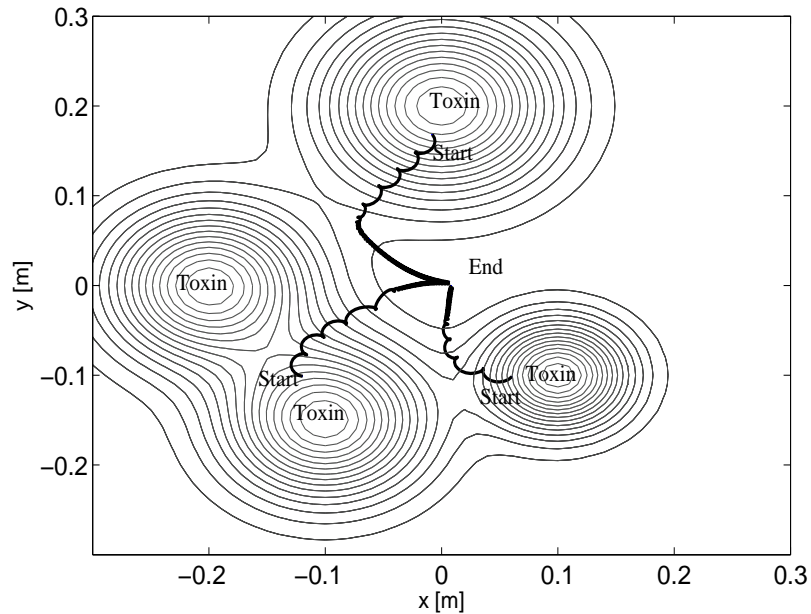


Figure 4.11: Simulation results for the toxin avoidance on single-sensory model. Four toxin resources locate at $(-0.2, 0)$, $(-0.1, -0.15)$, $(0, 0.2)$, and $(0.1, -0.1)$. *C. elegans* starts at three different positions $(-0.13, -0.11)$, $(0.07, -0.1)$, $(0, 0.18)$ with head angle randomly. It successfully finds the lower toxin concentration place to settle down.

are located at $(-0.2, 0)$, $(-0.1, -0.15)$, $(0, 0.2)$, and $(0.1, -0.1)$, respectively. *C. elegans* starts at three different positions $(-0.13, -0.11)$, $(0.07, -0.1)$, $(0, 0.18)$ with head angle randomly generated. *C. elegans* successfully finds the lower toxin concentration places after several right turns and finally stops.

4.5 Integrated Dual-sensory Behavioral Model

In previous sections we explore the chemotaxis behaviors of food attraction and toxin avoidance separately. In this section we construct an integrated behavioral model that can learn and replicate all chemotaxis behaviors, including food attraction and toxin avoidance under either single-sensory or dual-sensory models with speed regulation. The wire diagram for this integrated dual-sensory behavioral model is shown as Fig. 3.9.

4.5.1 Learning Tasks

To perform the chemotaxis tasks under dual-sensory mode, single-sensory mode, and speed regulation, four inputs are sensed by input neurons: 1) food concentration on the left side ($C_{f,left}$) by ASEL, 2) food concentration on the right side ($C_{f,right}$) by ASER, 3) toxin concentration on the left side ($C_{tx,left}$) by ASHL, 4) toxin concentration on the right side ($C_{tx,right}$) by ASHR. Outputs of motor neurons consist of several SLFs as

below.

$$V_{left}(t) = \underbrace{[\phi_1(\bar{C}_f(t)) + \phi_2(\bar{C}_{tx}(t))]}_{speed} - \underbrace{[\phi_1(\bar{C}_f(t)) + \phi_2(\bar{C}_{tx}(t))] \cdot \sigma_1(\Delta C_{sp}(t))}_{orientation \text{ by spatial information}} \quad (4.22)$$

$$V_{right}(t) = \underbrace{[\phi_1(\bar{C}_f(t)) + \phi_2(\bar{C}_{tx}(t))]}_{speed} + \underbrace{[\phi_1(\bar{C}_f(t)) + \phi_2(\bar{C}_{tx}(t))] \cdot \sigma_1(\Delta C_{sp}(t))}_{orientation \text{ by spatial information}} + \underbrace{[\phi_1(\bar{C}_f(t)) + \phi_2(\bar{C}_{tx}(t))] \cdot \sigma_2(\Delta C_{tp}(t))}_{orientation \text{ by temporal information}}, \quad (4.23)$$

where the SLFs are defined as:

$$\phi_1(\bar{C}_f(t)) = -0.5\bar{C}_f(t) + 1, \quad (4.24)$$

$$\phi_2(\bar{C}_{tx}(t)) = 0.5\bar{C}_{tx}(t), \quad (4.25)$$

$$\sigma_1(\Delta C_{sp}(t)) = \tanh(\Delta C_{sp}(t)), \quad (4.26)$$

$$\sigma_2(\Delta C_{tp}(t)) = \tanh(\Delta C_{tp}(t) + 1) - 1, \quad (4.27)$$

and inputs are defined below:

$$\bar{C}_f(t) = \frac{C_{f,left}(t) + C_{f,right}(t)}{2}, \quad (4.28)$$

$$\bar{C}_{tx}(t) = \frac{C_{tx,left}(t) + C_{tx,right}(t)}{2}, \quad (4.29)$$

$$\Delta C_{sp}(t) = C_{f,left}(t) - C_{f,right}(t) - C_{tx,left}(t) + C_{tx,right}(t), \quad (4.30)$$

$$\Delta C_{tp}(t) = \bar{C}_f(t) - \bar{C}_f(t-1) - \bar{C}_{tx}(t) + \bar{C}_{tx}(t-1). \quad (4.31)$$

For the speed regulation mechanism, the speed of *C. elegans* is determined by both food and toxin concentrations. The effect of the food concentration makes *C. elegans* stop only when it arrives at the food source, otherwise it will cruise continually. It is

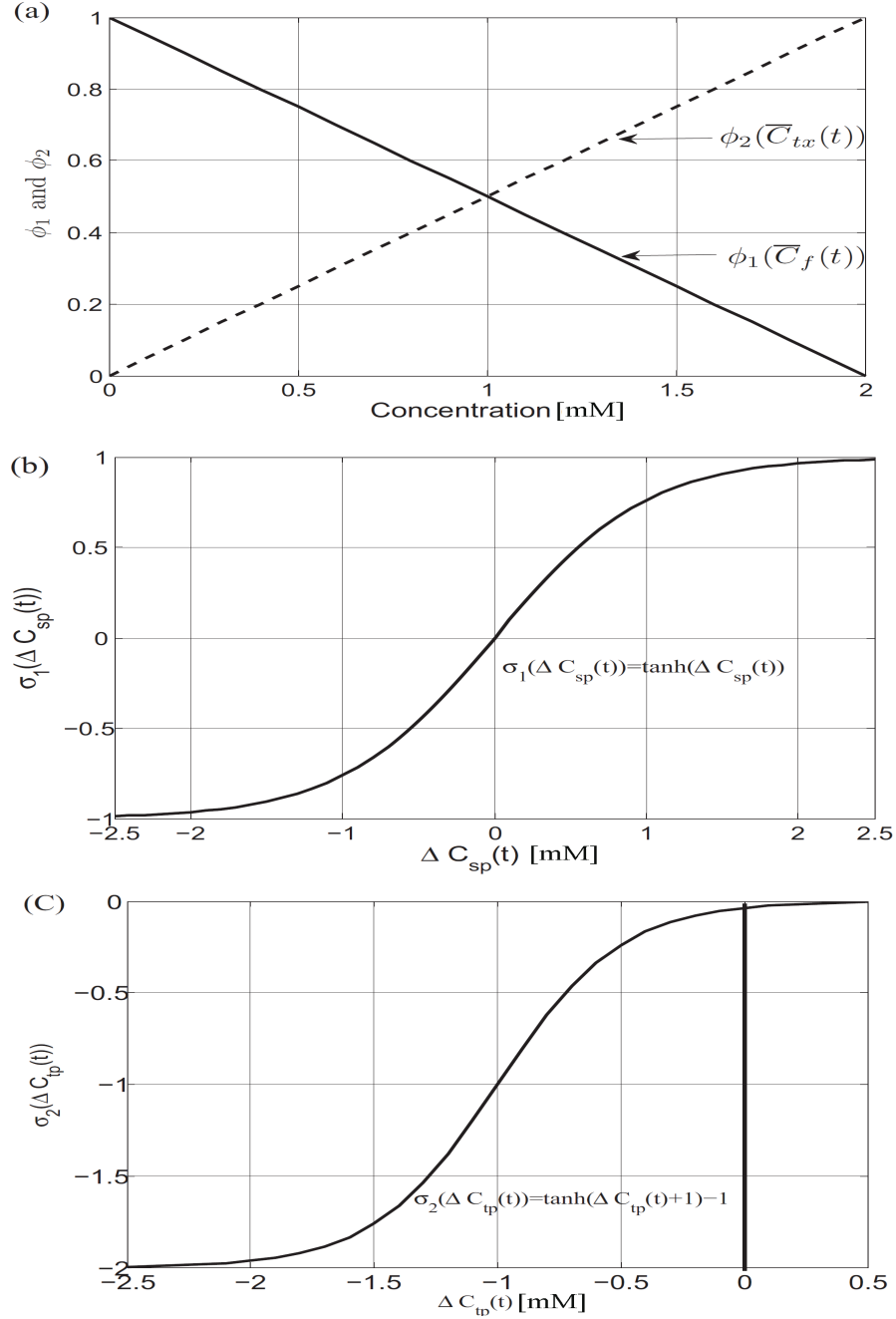


Figure 4.12: Plots of SLFs for the integrated model. In (a) $\overline{C}_f(t)$ and $\overline{C}_{tx}(t)$ determine the motor neurons outputs. In (b), $\Delta C_{sp}(t)$ controls the orientation changing by spatial information, function as dual-sensory model. In (c), $\Delta C_{tp}(t)$ controls the orientation changing by temporal information, function as single-sensory model.

in accord with the statement of reference [88] that *C. elegans* spends nearly all of its time grazing on bacterial lawns, and if there is no bacteria, it moves around the plate to search for food. The effect of the toxin concentration makes *C. elegans* continue moving and changing its direction as long as toxin concentration is smelled. In Eqs. (4.22) and (4.23), $\phi_1(\bar{C}_f(t))$ and $\phi_2(\bar{C}_{tx}(t))$ determine the speed. The SLFs for the speed is shown in Fig. 4.12 (a). When *C. elegans* approaches the food source, the high value of $\bar{C}_f(t)$ yields a low output value of $\phi_1(\bar{C}_f(t))$; or when *C. elegans* is faraway from the toxin, the low value of $\bar{C}_{tx}(t)$ yields a low output value of $\phi_2(\bar{C}_{tx}(t))$. Thus both the $V_{right}(t)$ and $V_{left}(t)$ are near to zero, and the worm comes to stop.

For the the orientation changing, the $V_{left}(t)$ in Eq. (4.22) is only determined by $\Delta C_{sp}(t)$. In contrast, $V_{right}(t)$ in Eq. (4.23) is determined by both $\Delta C_{sp}(t)$ and $\Delta C_{tp}(t)$. If *C. elegans* cannot distinguish the concentration difference between left-hand and right-hand sides, which means $\Delta C_{sp}(t) = 0$ and $\sigma_1(\Delta C_{sp}(t)) = 0$, the worm can still guide itself by the temporal information $\sigma_2(\Delta C_{tp}(t))$. In such circumstances, the integrated biological model behaviors like a single-sensory mode. In the contrary, if temporal concentration difference $\Delta C_{tp}(t) = 0$, then $\sigma_2(\Delta C_{tp}(t)) = 0$ and *C. elegans* must navigate according to $\Delta C_{sp}(t)$ as the dual-sensory mode. The mechanism of orientation changing can refer to Fig. 4.12 (b) for $\sigma_1(\Delta C_{sp}(t))$ (dual-sensory mode) and Fig. 4.12(c) for $\sigma_2(\Delta C_{tp}(t))$ (single-sensory mode). In Fig. 4.12(b), when $\Delta C_{sp}(t) > 0$, it means the summation of left-hand side food and right-hand side toxin concentration is bigger than the summation of right-side food and left-side toxin concentration. Thus $\sigma_1(\Delta C_{sp}(t)) > 0$, namely, $V_{right} > V_{left}$, the worm turns left. It is vice versa for $\Delta C_{sp}(t) < 0$. In Fig. 4.12(c), if $\Delta C_{tp}(t) \geq 0$, the food concentration is higher than that at the previous time, or the toxin concentration is lower than that at the previous time. Thus, the output $\sigma_2(\Delta C_{tp}(t)) = 0$

and *C. elegans* does not turn. If the $\Delta C_{tp}(t) < 0$, *C. elegans* goes wrongly, and the output $\sigma_2(\Delta C_{tp}(t)) < 0$ yielding $V_{left} > V_{right}$. Thus, the worm turns right.

4.5.2 Testing Results

In this section, we test the locomotion behaviors of *C. elegans* in two conditions: 1) food source and toxin source are overlapped slightly; 2) food source and toxin source are overlapped largely. For the training data, the inputs of the wire diagram contain four variables $[C_{f,left}, C_{f,right}, C_{t,left}, C_{t,right}]^T$. Each variable ranges from 0 to 2, with interval 0.1. The output data are computed according to Eqs. (4.22) and (4.23). The learning rate for the training is set between 0.0005 and 0.002. Satisfactory training results are obtained after 20 thousand epochs of training.

A. Test in Scenario with Food Source and Toxin Source Slightly Overlapped

We first test *C. elegans* in a scenario with food and toxin concentration slightly overlapped. Three toxin sources are located at $(-200, 0)$, $(-100, -150)$, $(0, 200)$ and a food source is located at $(100, -100)$, as shown in Fig. 4.13(a). Fig. 4.13(b) is the enlarged area of Fig. 4.13(a) with x-axis $[-120, -40]$ and y-axis $[-180, -120]$. Starting from point $(-80, -150)$ with initial head angle 200° , shown in Fig. 4.13(b), *C. elegans* behaves in the single-sensory mode because the concentration difference between left and right sides is very small. As a result, *C. elegans* turns right. It should be noted that *C. elegans* should turn left in this case according to the dual-sensory mode. *C. elegans* switches to the dual-sensory mode when it arrives the point $(-75, -138)$, and leaves the toxin. When it “smells” the food concentration at point $(-47, -125)$, it goes straightly to the food source and finally switches to the single-sensory mode again, rights turning, and at last stops.

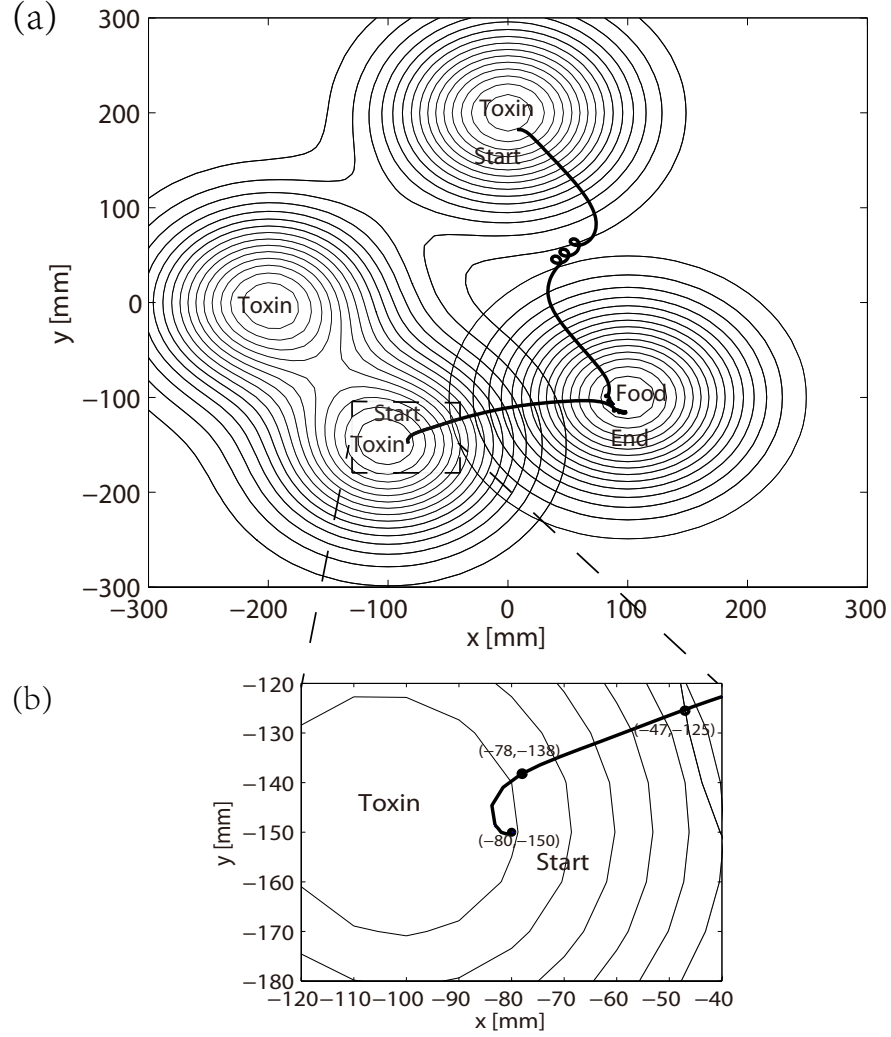


Figure 4.13: (a) is the test results of integrated model. (b) is the enlarged area of (a) with x-axis [-120 -40] and y-axis [-180 -120].

When starting from point (50,180) with head angle 90° , as shown in Fig. 4.13(a), *C. elegans* escapes from the toxin quickly. When *C. elegans* arrives at the low toxin concentration places, it cannot distinguish the concentration difference between the left and right sides. Consequently *C. elegans* behaviors in the single-sensory mode, navigates itself by a serial of right turns. After detecting the food concentration, it goes towards the food source first in the single-sensory mode and then switches to the dual-sensory mode. Finally it switches to the single-sensory mode again, after several right turns it stops.

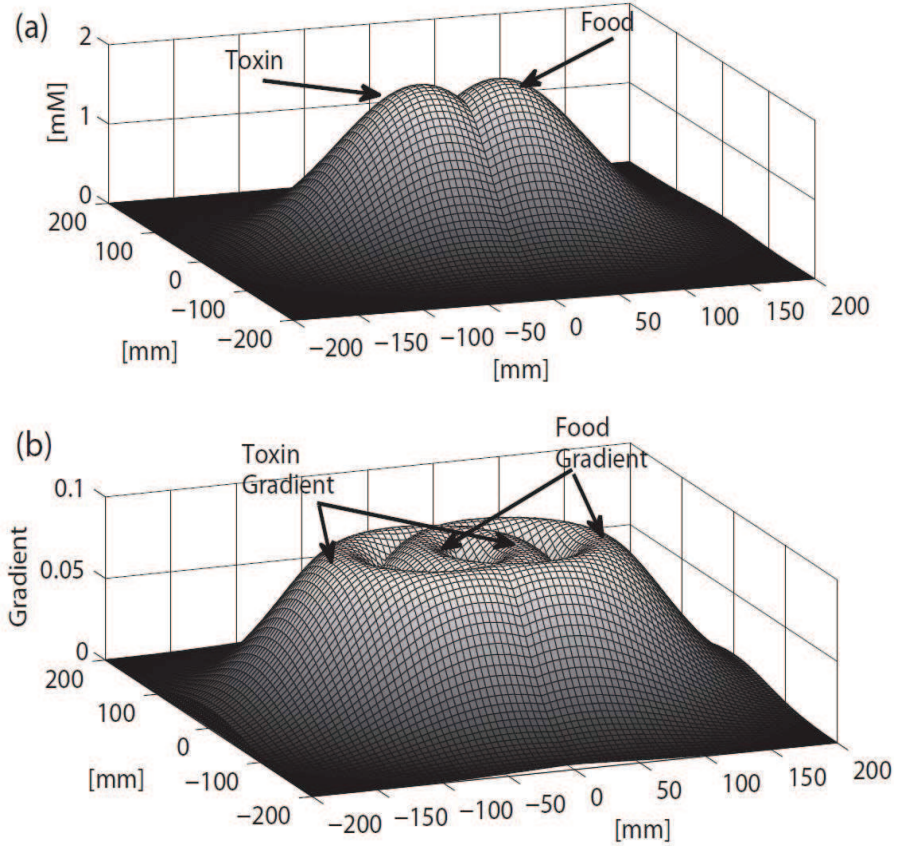


Figure 4.14: (a) is the 3-D plot of food and toxin distributions with a large overlapping. (b) illustrates the corresponding gradient information of (a). From (b) we can see that there are some areas where the gradients of food and toxin are identical (intersection places).

B. Test in Scenario with Food Source and Toxin Source Largely Overlapped

In this test, we investigate the scenario where the food and toxin concentrations located at $(30, 0)$ and $(-30, 0)$ are largely overlapped with Gaussian distribution, as shown in Fig. 4.14(a). The gradient distribution of the food and toxin concentration is shown in Fig. 4.14(b). When the food and toxin concentration overlapping severely, the best place for the worm is the one furthest to the toxin source and nearest to the food source, namely, gradients of food and toxin concentrations at this place are identical. Theoretically, this location can be calculated according to $\nabla C_f = \nabla C_{tx}$, where $\nabla C_f = \frac{\partial C_f}{\partial x} \hat{i} + \frac{\partial C_f}{\partial y} \hat{j}$ and $\nabla C_{tx} = \frac{\partial C_{tx}}{\partial x} \hat{i} + \frac{\partial C_{tx}}{\partial y} \hat{j}$. In this test example, the location is $(65.72, 0)$.

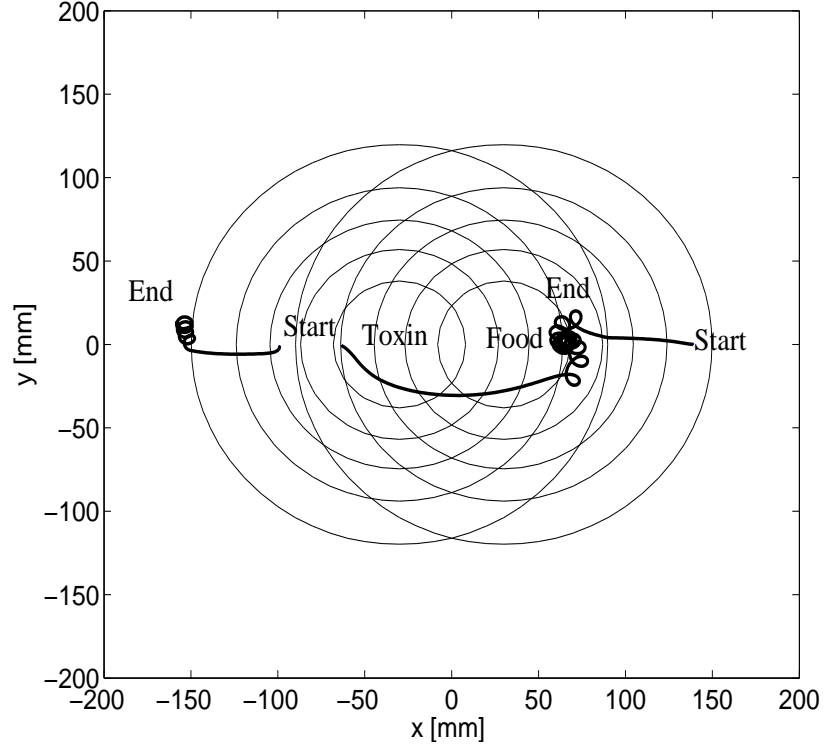


Figure 4.15: The test results when the food and toxin sources are overlapped largely.

The test results are shown in Fig. 4.15. When *C. elegans* starts from $(-90, 0)$ with initial angle 0° (face to the toxin), where there is no food concentration, it avoids the toxin by a right turn and settles down at the place with the lowest toxin concentration. When starting from the point $(-65, 0)$ with initial angle 0° (face to the toxin) where the toxin and food concentration are overlapping, *C. elegans* bypasses the toxin source and circles around the point $(65.72, 0)$. When starting from the point $(140, 0)$ with initial angle 180° (face to the food), *C. elegans* moves towards the food initially and circles around the point $(65.72, 0)$.

4.6 Integrated Single-sensory Behavioral Model

In Section 4.5, although the integrated dual-sensory behavioral model can perform in both dual-sensory model and single-sensory model, it lacks the biological grounding.

From the biological aspect, most of the experiment results show that *C. elegans* navigates its direction by using the concentration gradient through time [87, 45, 20], namely, temporal concentration information. Thus, in this section, we explore the integrated single-sensory behavioral model to achieve the chemotaxis behaviors of finding food and avoiding toxin concurrently, as well as speed regulation.

The wire diagram for the integrated single-sensory behavioral model is shown in Fig. 3.10. Biologically, in other works [18, 61] the head swing neurons such as RMD, SMB, SMD, RIA, and RIB are involved. In this work, we focus on the relationship between the chemotaxis concentration and the outputs of motor neurons, VB and DB. Thus, these head swing neurons are out of the scope of this chapter.

4.6.1 Learning Tasks

SLFs for the integrated single-sensory behavioral model are designed as:

$$V_{left}(t) = \underbrace{\phi_1(C_f(t)) + \phi_2(C_{tx}(t))}_{speed}, \quad (4.32)$$

$$V_{right}(t) = \underbrace{\phi_1(C_f(t)) + \phi_2(C_{tx}(t))}_{speed} + \underbrace{[\phi_1(C_f(t)) + \phi_2(C_{tx}(t))] \cdot \sigma(\Delta C_{ft}(t))}_{orientation}, \quad (4.33)$$

where

$$\phi_1(C_f(t)) = -0.5C_f(t) + 1, \quad (4.34)$$

$$\phi_2(C_{tx}(t)) = 0.5C_{tx}(t), \quad (4.35)$$

$$\sigma(\Delta C_{ft}(t)) = \tanh(\Delta C_{ft}(t) + 1) - 1, \quad (4.36)$$

$$\Delta C_{ft}(t) = C_f(t) - C_f(t-1) - C_{tx}(t) + C_{tx}(t-1). \quad (4.37)$$

The SLFs of the speed are shown in Fig. 4.16(a). In Eqs. (4.32) and (4.33), $\phi_1(C_f(t))$ and $\phi_2(C_{tx}(t))$ determine the speed. When *C. elegans* approaches the food source, the

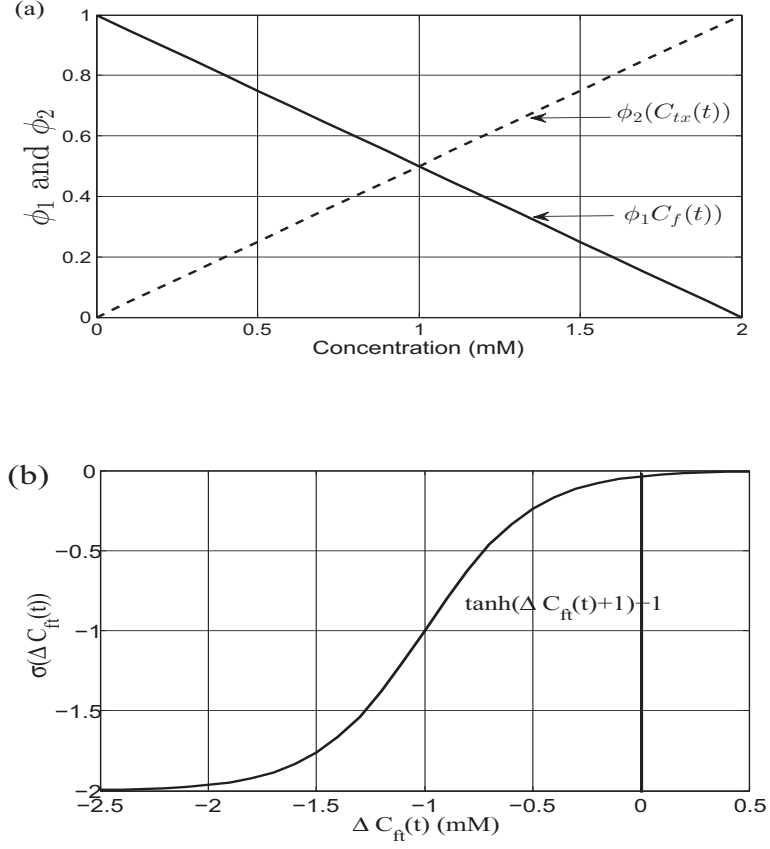


Figure 4.16: Plot of switching logic function for the integrated chemotaxis behavioral model. In (a), $C_f(t)$ and $C_{tx}(t)$ determine the outputs of motor neurons for speed regulation. In (b), $\Delta C_{ft}(t)$ controls the orientation.

high input value of $C_f(t)$ yields a low output value of $\phi_1(C_f(t))$; when *C. elegans* is far-away from the toxin, the low input value of $C_{tx}(t)$ yields a low output value of $\phi_2(C_{tx}(t))$. In this case, both the $V_{right}(t)$ and $V_{left}(t)$ are near zero, and the worm comes to stop. Otherwise, *C. elegans* will keep moving.

For the orientation control, based on the assumption that *C. elegans* can only turn right or go straightly, it is adequate to add the term $\sigma(\Delta C_{ft}(t))$ to $V_{right}(t)$ only. In Fig. 4.16(b), $\Delta C_{ft}(t) \geq 0$ means the food concentration is higher than that at the previous time, or the toxin concentration is lower than that at the previous time. In

this case, for equation (4.36), $\sigma(\Delta C_{ft}(t))$ is near zero and *C. elegans* does not turn. If $\Delta C_{ft}(t) < 0$, *C. elegans* goes wrongly, and $\sigma(\Delta C_{ft}(t)) < 0$, yielding $V_{left} > V_{right}$. Thus the worm turns right.

4.6.2 Testing Results

The integrated chemotaxis behavioral model, as shown in Fig. 3.10, is trained to remember the input-output mapping (Fig. 4.16). The inputs of training data include $C_f(t)$ for ASE, $C_{tx}(t)$ for ASH, and $C_f(t-1) - C_{tx}(t-1)$ for AIY. The range of input data is from 0 to 2 with interval 0.1. Target data for the two motor neurons, V_{left} for DB and V_{right} for VB, are calculated by Eqs. (4.32) and (4.33), respectively.

The tests are carried out in three different scenarios. In the first scenario, as shown in Fig. 4.17, one food is located at point $(-0.11, 0)$ and one toxin is located at point $(0.11, 0)$ with slightly overlapped concentration. *C. elegans* starts at $(0.09, 0.03)$ where it is near the toxin without food concentration. It escapes from toxin first, and when *C. elegans* detects the food concentration it moves towards to the food and finally stops.

In the second scenario, as shown in Fig. 4.18, one food source is located at $(-0.03, 0)$ and one toxin source is located at $(0.03, 0)$ with concentrations largely overlapped. The 2D concentration distribution along x -axis is shown in Fig. 4.19(a). Here we assume that the direction of x -axis is the positive direction. Accordingly, the gradients of food and toxin concentrations along the positive direction are shown in Fig. 4.19(b). There are two points where the gradients of food and toxin concentrations are identical: $x = -0.07$ and $x = 0.07$. The direction is determined by Eq. (4.37), which can be written as $\Delta C_{ft}(t) = \Delta C_f(t) - \Delta C_{tx}(t)$, where $\Delta C_f(t) = C_f(t) - C_f(t-1)$ and $\Delta C_{tx}(t) = C_{tx}(t) - C_{tx}(t-1)$. As shown in Fig. 4.16(b), if $\Delta C_{ft}(t) > 0$ ($\Delta C_f(t) > \Delta C_{tx}(t)$), *C. elegans* goes straightly. Otherwise, it will turn. As shown in Fig. 4.19(b), along the positive direction, when

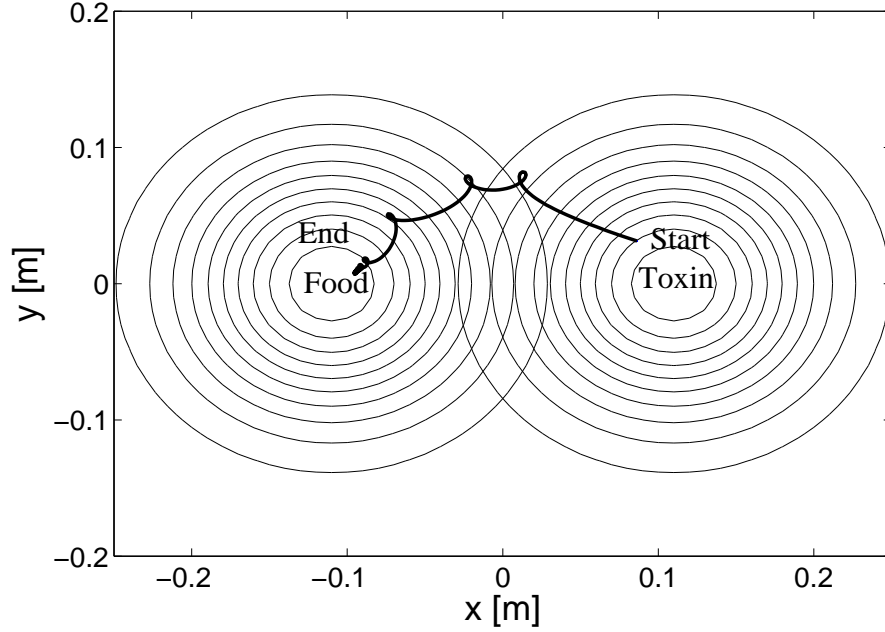


Figure 4.17: Testing results for the integrated chemotaxis behavioral model in the first scenario. One food is located at point $(-0.11, 0)$ and one toxin is located at point $(0.11, 0)$ with slightly overlapped concentration.

$x < -0.07$, i.e., on the left of the point P, $\Delta C_f(t) > \Delta C_{tx}(t)$, resulting $\Delta C_{ft}(t) > 0$, so *C. elegans* will move towards the positive direction until it reaches the point P, namely, the stable equilibrium. When $-0.07 < x < 0.07$, i.e., in between the points P and Q, $\Delta C_f(t) < \Delta C_{tx}(t)$, resulting $\Delta C_{ft}(t) < 0$, so *C. elegans* will turn its direction and move towards the negative direction until it arrives at $x = -0.07$, namely, the stable equilibrium P. When $x > 0.07$, i.e., on the right of the point Q, $\Delta C_f(t) > \Delta C_{tx}(t)$, resulting $\Delta C_{ft}(t) > 0$. *C. elegans* will move towards the positive direction until the toxin concentration disappears, namely, away from the unstable equilibrium Q. In conclusion, the target places of this case are the point $(-0.07, 0)$ and where no toxin concentration exists on the toxin side.

The testing results are shown in Fig. 4.18. When *C. elegans* starts from $(0.08, 0)$, i.e., on the right side of the unstable equilibrium Q, and with initial angle 180° (facing the

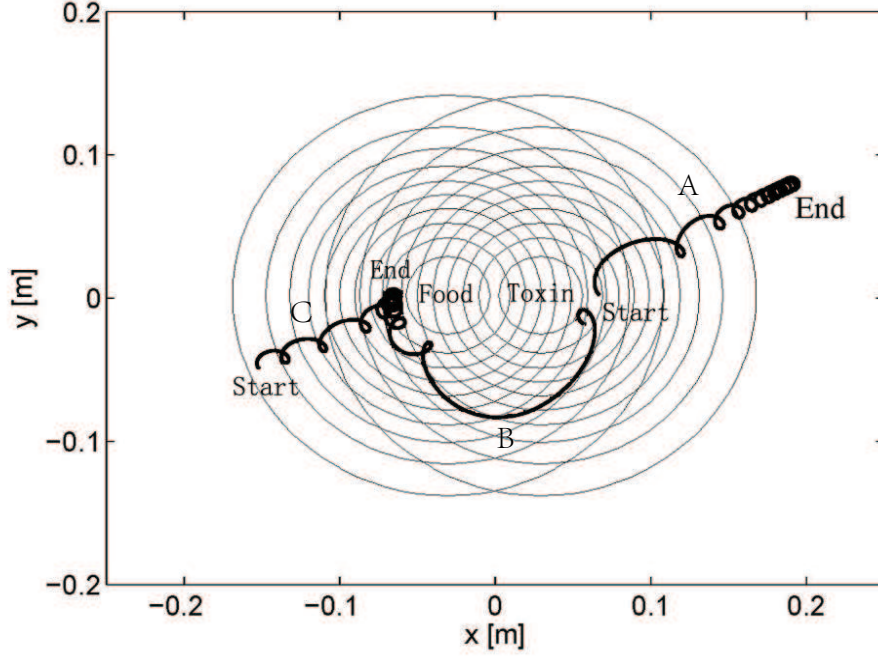


Figure 4.18: Testing results for the integrated chemotaxis behavioral model in the second scenario. One food source is located at $(-0.03, 0)$ and one toxin source is located at $(0.03, 0)$ with largely overlapped concentration.

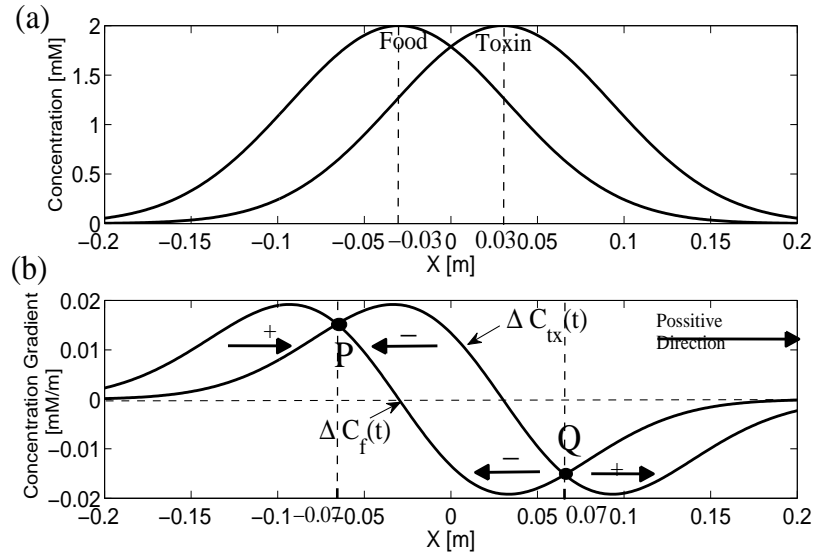


Figure 4.19: (a) 2D concentration distributions of food and toxin along x -axis. (b) The gradients of food and toxin concentrations along the positive direction (direction of x -axis).

toxin, shown as track A), where both food and toxin concentrations are present at the same time, the worm avoids the toxin by a right turn and leaves faraway from the toxin

source. Finally it settles down at the place without toxin concentration. When starting from the point $(0.06, -0.02)$, i.e., in between points P and Q, and with initial angle 135° (facing the toxin, shown as track B) where both toxin and food concentrations exist simultaneously, *C. elegans* bypasses the toxin source and navigates itself towards the food source, and finally it settles down around the stable equilibrium P at $(-0.07, 0)$. When starting from the point $(-0.15, -0.05)$, i.e., on the left side of the stable equilibrium P, and with initial angle 180° (facing against the food, shown as track C), *C. elegans* moves towards to the food and finally settles down around the the stable equilibrium P at $(-0.07, 0)$. It can be seen that when food concentration and toxin concentration are largely overlapping, the testing results are consistent with the gradient-based analysis, namely, *C. elegans* is attracted towards the stable equilibrium, point P, and repelled from the unstable equilibrium, point Q.

In the last scenario, twenty-five toxin sources are distributed as a 5×5 grid. As shown in Fig. 4.20, black dots depict the toxin sources and circle lines are the boundaries of toxin concentration. One food source is located at $(0, 0.45)$. *C. elegans* starts at three different locations, $(-0.02, -0.01)$, $(0, 0.02)$, and $(0.02, -0.02)$ respectively, with random initial angles. All the three starting points are very near the central toxin source. From the tracks, it is obvious that *C. elegans* escapes from the toxin by passing the boundary areas where the toxin gradient and magnitude are relatively low. *C. elegans* successfully escapes from the toxin and settles down at the places where no toxin concentration exists (see the left and bottom tracks). Furthermore, if *C. elegans* smells the food concentration (see the top track), it navigates itself towards the food source and finally stops.

From the test results, we can conclude that the integrated chemotaxis behavioral model can well performs the chemotaxis behaviors on finding food and avoiding toxin

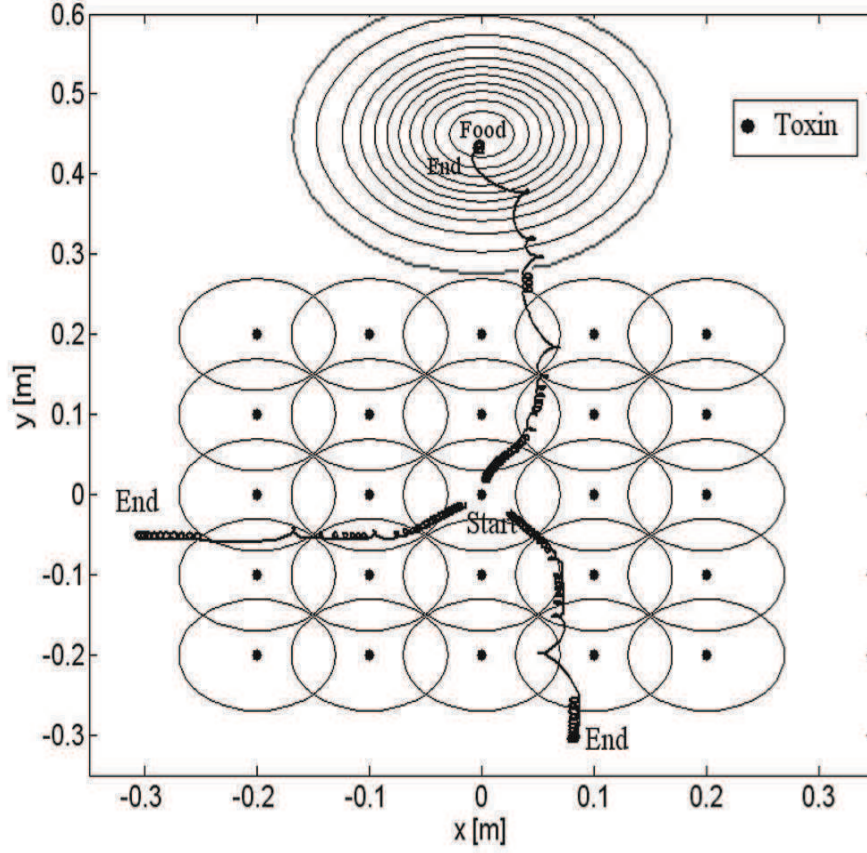


Figure 4.20: Testing results for the integrated behavioral model in the third scenario. Twenty-five toxin resources are distributed as a 5×5 grid. One food source is located at $(0, 0.45)$.

simultaneously with speed regulation. Furthermore, it also verifies that when SLFs are learned, *C. elegans* can perform the chemotaxis behaviors in different environments.

4.7 Comparative Analysis

In this section, we provide the comparison of our results to other works. To our best knowledge, the existing results of other works are based on the opinion that *C. elegans* uses the temporal concentration information for navigation, namely, single-sensory behavioral model. Thus in this section, we only analyze the results of our single-sensory behavioral models and compare them with other works.

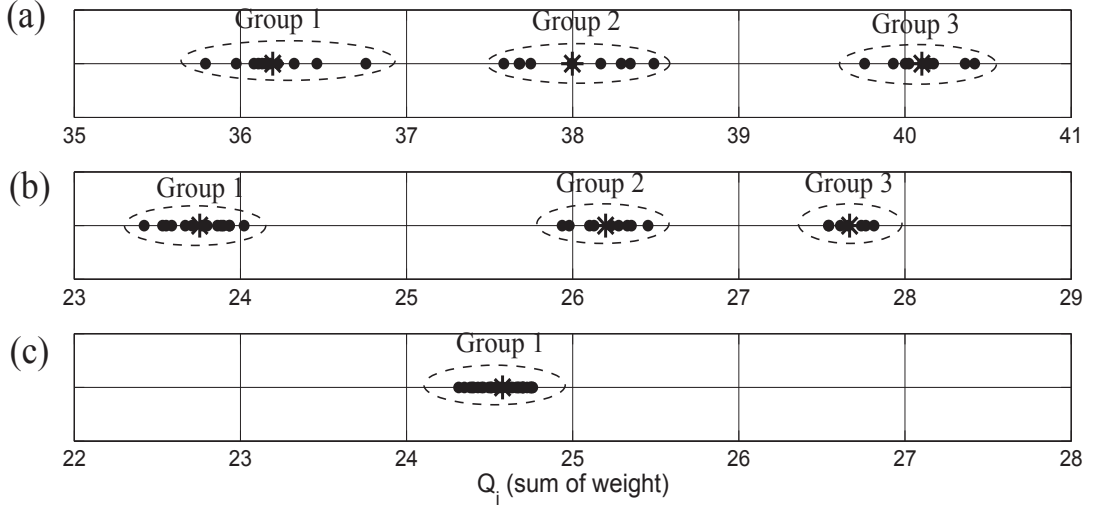


Figure 4.21: The similarity analysis of the resultant wire diagrams. (a) Thirty wire diagrams for the food attraction behavioral model are clustered into three groups by k-means algorithm. (b) Thirty wire diagrams for the toxin avoidance behavioral model are clustered into three groups by k-means algorithm. (c) Thirty wire diagrams for the integrated behavioral model are clustered into the same group.

4.7.1 Wire Diagram Analysis

In our work, we obtain thirty wire diagrams for each single-sensory behavioral model after providing random initial weights and training. The successful training rates are about 60% for both food attraction and for toxin avoidance behavioral models, and about 47% for the integrated chemotaxis behavioral model. When the learned behaviors become more sophisticated, the training would be more difficult. Furthermore, we also optimized the wire diagrams by Genetic Algorithm and obtained the same results.

For the network similarity, we first cluster the thirty wire diagrams in each behavioral model by using k-means algorithm, and then verify the clustering results by Analysis of Variance (ANOVA). For each kind of behavioral model, we calculate the summation of absolute weight values of every wire diagram, denoted as Q_i , $i = 1, \dots, N_m$ ($N_m = 30$), and then apply k-means algorithm to cluster these wire diagrams according to the value of Q_i . The results are shown in Fig. 4.21. As shown in Fig. 4.21(a), each dot represents its

corresponding wire diagram for food attraction behavioral model, and the value in x-axis denotes the summation of the absolute weight values of its corresponding wire diagram. The asterisks represent the clustering centers. These dots are clustered into three groups by k-means algorithm. The inter-group mean squared error (MSE) is 1.60 for Groups 1, 2, and 3. The intra-group MSEs are 0.23 for Group 1, 0.32 for Group 2, and 0.19 for Group 3. The clustering result is analyzed by ANOVA. By setting the significance level $\alpha = 0.05$ in ANOVA analysis, we obtain the observed value $F = 559.71$ and the critical value $F_{Critical} = 3.35$. $F > F_{Critical}$ denotes the three groups are significantly different, which means the clustering is effective. As shown in Fig. 4.21(b), the dots denote the wire diagrams for toxin avoidance behavioral model. These dots can be clustered into three groups and the asterisks represent the clustering centers. The inter-group MSE is 1.61 for Groups 1, 2, and 3. The intra-group MSEs are 0.17 for Group 1, 0.16 for Group 2, and 0.10 for Group 3. By setting $\alpha = 0.05$, we obtain $F = 1450.76$ and $F_{Critical} = 3.35$. $F > F_{Critical}$ denotes the effectiveness of this clustering. As shown in Fig. 4.21(c), the dots denote the wire diagrams for integrated behavioral model. These dots are difficult to be clustered by k-means algorithm, so we cluster them to be one group. Within the group, the intra-group MSE is 0.13. From these results we can conclude that the solution is not unique for each behavioral model. The wire diagrams in the same group have small MSE, which are less than 0.32, and the wire diagrams in different groups have relatively larger MSE, which are greater than 1.60.

Furthermore, following the method of [25], we first find out the “all-off” neurons that are inactive and the “all-on” neurons that are saturated active. Next, we remove these “all-off” neurons from the wire diagrams and move these “all-on” neurons to their downstream neurons as bias. In this way, the wire diagrams are simplified and the

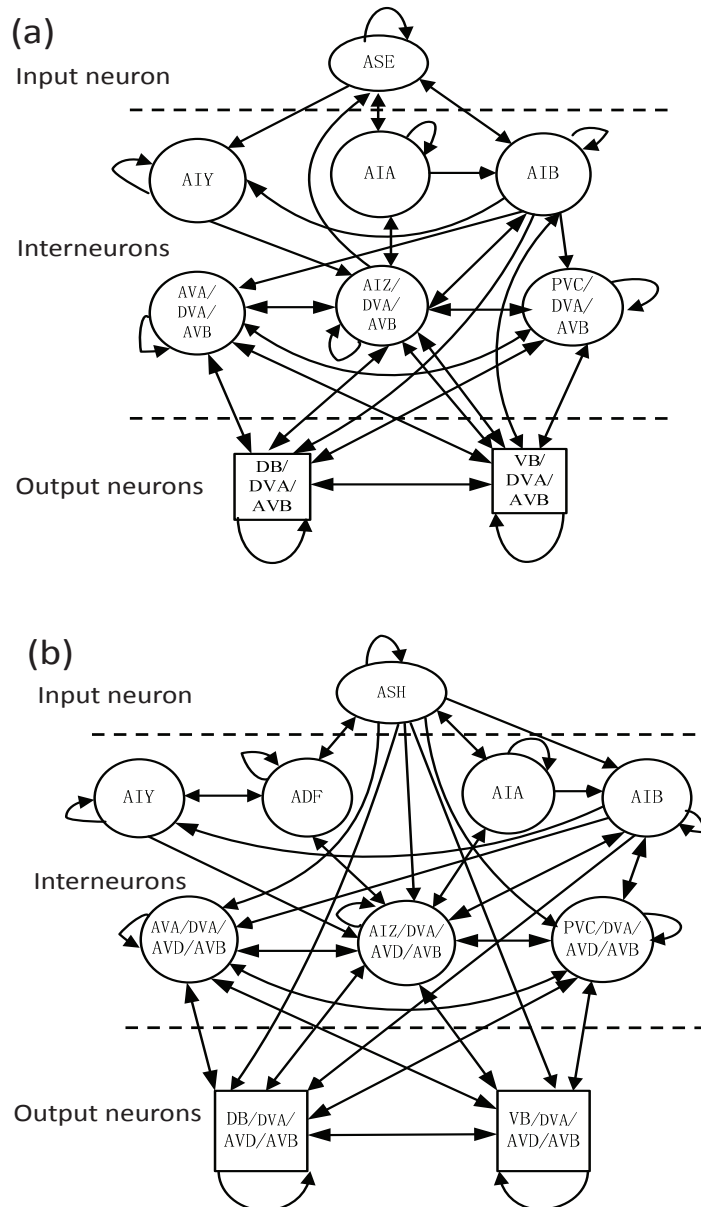


Figure 4.22: (a) Resultant wire diagram for food attraction behavioral model. After the “all-off” neurons are removed and the “all-on” neurons are moved to downstream neurons, the simplified network contains six interneurons instead of twelve. (b) Resultant wire diagram for toxin avoidance behavioral model. After the “all-off” neurons are removed and the “all-on” neurons are moved to downstream neurons, the simplified network contains seven interneurons instead of thirteen.

relevant networks are obtained. For the food attraction behavioral model, the “all-off” neurons are PVP, ADF, RIF, and AVD, because all weights of these neurons are small and near to zero. The wire diagrams without these neurons can still perform the behavior for food attraction well. The “all-on” neurons for the food attraction behavioral model are DVA and AVB. After we move these neurons to their downstream neurons, the resultant wire diagram is shown in Fig. 4.22(a). As shown in Fig. 4.22(a), there are six interneurons instead of twelve interneurons after simplifying. By following the same way, the resultant wire diagram for toxin avoidance behavioral model is shown in Fig. 4.22(b). The “all-off” neurons are PVP and RIF that are removed from wire diagram. The “all-on” neurons are DVA, AVD, and AVB. After simplification, we can see that there are seven interneurons instead of thirteen interneurons. By comparing Figs. 4.22(a) and (b), one additional neuron ADF exists in the wire diagram of toxin avoidance behavior model. This is because there is no direct connection from sensory neuron ASH to memory neuron AIY biologically, and the function of ADF here is to transmit the signal from ASH to AIY. For the integrated behavioral model, the “all-off” neuron is PVP that can be removed from the wire diagram. However, we haven’t found any neurons that can serve as the “all-on” neurons since all neurons are not saturated activated.

By comparing with another similar work [44] that provides a model for food attraction, our model contains three more interneurons. This is because we not only consider the turning mechanism, as [44] did, but also incorporate the speed regulation mechanism. Moreover, the integrated behavioral model needs eleven interneurons (after PVP is removed). If we remove one or more interneurons, till now we have not obtained any satisfactory wire diagrams after training. The reason that more interneurons are needed

in our models is aroused by the complexity of our learning task: finding food, avoiding toxin, and regulating speed synchronously.

4.7.2 Behaviors Analysis

In this subsection we provide the quantitative analysis of the trajectories of our models by comparing with experiment results. To the best of our knowledge, the references about the quantitative analysis of the trajectories for toxin avoidance behaviors and integrated behaviors (for both food and toxin) are limited. Thus in this subsection we only provide the analysis of the food attraction behavioral model by comparing with the experiment results of wild type *C. elegans* provided by [87] and [19].

We analyze the relationships between (1) speed and concentration, (2) turning rate and concentration, (3) turning rate and change of concentration ($dC(t)/dt$), and (4) probability of turning and $dC(t)/dt$ by following the methods in [87] and [19]. The simulation time is 1500 seconds, and we record the location, concentration, and direction per second. Hence, for each relationship analysis, there are 1500 tracking data, and these data are classified into 15 groups. Every group contains 100 data and is represented as a dot in Fig. 4.23. The values of each dot in x -axis and y -axis are calculated by taking the average of the 100 data in the same group. The error bar for each dot indicates the standard deviation of the data within the same group. The solid lines in each sub-figure are the best-fitting quadratic functions of their corresponding dots. The dotted lines represent the experiment results of [87] and [19].

In this work, Least Square Method is adopted to fit these dots, as shown in Fig. 4.23. The quality of fitting is analyzed by using R^2 method [89]. R^2 is defined as $R^2 = 1 - SS_{err}/SS_{tot}$, where $SS_{tot} = \sum_{i=1}^N (y_i - \bar{y})^2$ and $SS_{err} = \sum_{i=1}^N (y_i - f_i)^2$. y_i ($i = 1, \dots, N$) are the testing results that should be fitted, and each testing result has an

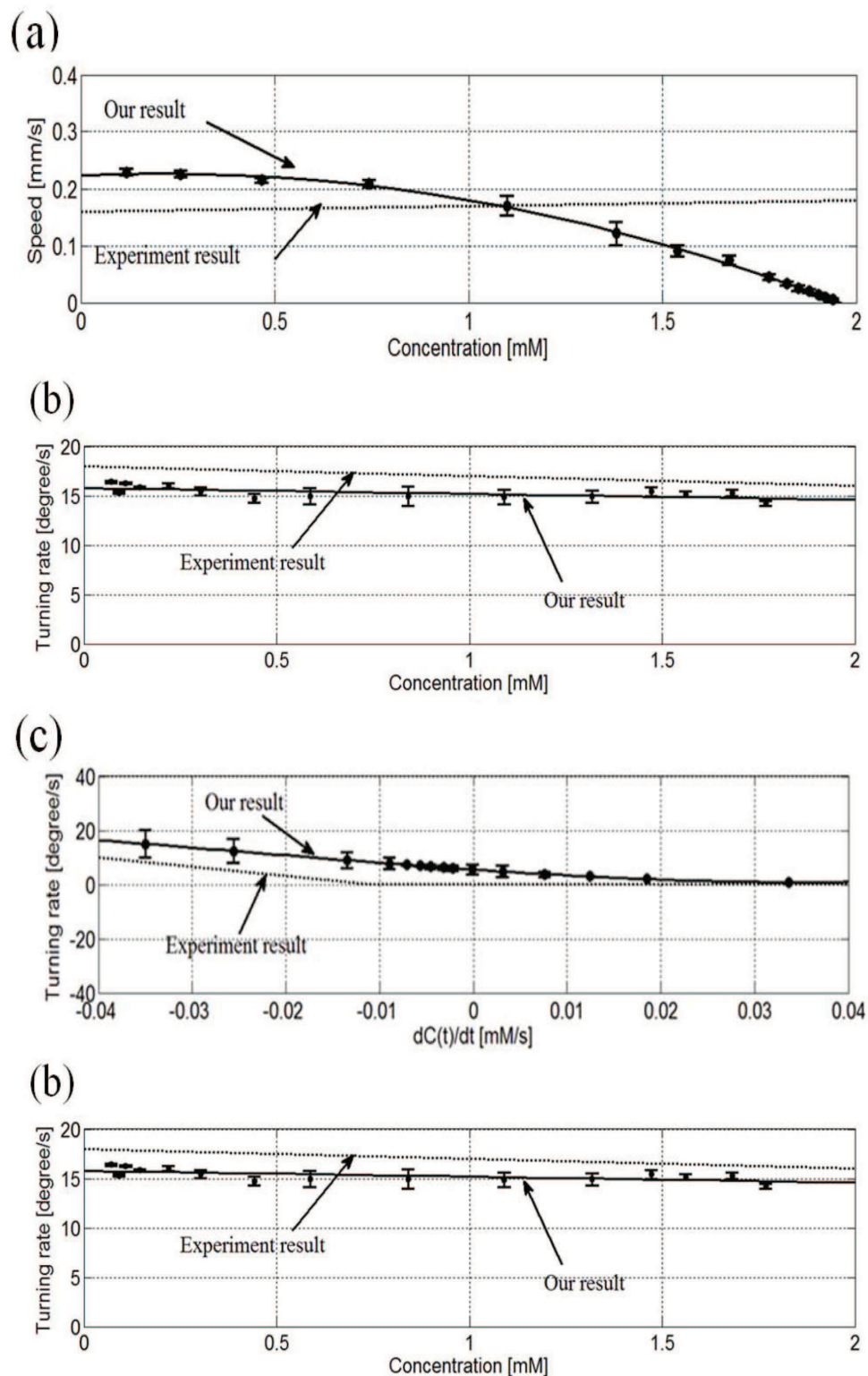


Figure 4.23: Statistical analysis of trajectories for food attraction behavior model. (a) The relationship between speed and concentration. (b) The relationship between turning rate and concentration. (c) The relationship between turning rate and $dC(t)/dt$. (d) The relationship between probability of turning and $dC(t)/dt$.

associated experiment result f_i ($i = 1, \dots, N$). N is the number of the testing results, and \bar{y} is the average value of y_i ($i = 1, \dots, N$). The value of R^2 is equal to or less than 1, which is used to describe how well a regression curve fits the testing results. An R^2 near 1 indicates that the regression curve fits the testing results well, while the more negative value of R^2 indicates the worse of fitting. In this work, we analyze (1) the degree of the curves to fit the dots (testing results), measured by R_{dot}^2 , and (2) the degree of the curves to fit the experiment results, measured by R_{ep}^2 .

In Fig. 4.23(a), the fitted polynomial equation (solid line) is $y = -0.073x^2 + 0.0287x + 0.224$ ($R_{dot}^2 = 1.00$, $R_{ep}^2 = -0.92$). We can observe that the speed is inversely proportional to the concentration. However, our result is different from the experiment data of [19] (dotted line), which concludes that the speed of *C. elegans* is weakly dependent on the food concentration. The reason for this difference is that in this work we assume *C. elegans* will reduce its speed by following the increasing of food concentration.

As shown in Fig. 4.23(b), the fitted polynomial equation (solid line) is $y = -0.5959x + 15.7926$ ($R_{dot}^2 = 0.40$, $R_{ep}^2 = -25.58$). We can observe that the turning rate weakly depends on the food concentration, and it is similar to the experiment result of [19] (dotted line). The relationship between turning rate and $dC(t)/dt$ is shown in Fig.4.23(c). The fitted polynomial equation (solid line) is $y = 27291x^3 + 1953x^2 - 236x + 6$ ($R_{dot}^2 = 1.00$, $R_{ep}^2 = -2.18$). In this figure, the larger negative value of $dC(t)/dt$ yields the larger magnitude of turning rate, and once $dC(t)/dt$ is positive, the turning rate reduces to zero. This result is similar to the experiment data of [87] (dotted line). At last, we follow the same way of [87] to analyze the relationship between probability of turning and $dC(t)/dt$. As shown in Fig. 4.23(d), these dots can be approximated by formula $y = 0.023/(a + e^{bx+d}) + c$, where y is the probability of turning, and x is the change of

concentration $dC(t)/dt$, and a, b, c, d are constants. For our case, the values of these parameters are $a = 0.3448$, $b = 300$, $c = 0$, and $d = -0.8$. The fitted formula is plotted as the solid line in Fig. 4.23(d), with $R_{dot}^2 = 0.99$ and $R_{ep}^2 = 0.67$. The experiment data of [87] is plotted as the dotted line in Fig. 4.23(d). The parameters obtained by [87] are $a = 0.40$, $b = 140$, $c = 0.0033$, and $d = 0$. From both our result and the experiment result, we can observe that they share the same shape and the probability of turning is higher when $dC(t)/dt$ is more negative.

Above all, except for the first relationship (speed and concentration), other three relationships are in accord with the experiment results. Furthermore, we can explain the abrupt turn and continue turn of our models through Fig. 4.23(c) and (d). More negative values in $dC(t)/dt$ yield larger magnitudes of the turning rate and higher probability of turning, which lead to the abrupt turn. In contrast, small negative values of $dC(t)/dt$ only yield small magnitudes of the turning rate and low probability of turning, which lead to the slight and continual turn. Additionally, if $dC(t)/dt$ is positive, the turning rate and the probability of turning will approach zero, which make *C. elegans* move straightly.

4.7.3 Performance with Noises

This subsection discusses the robustness of the DNN-based behavioral models in the presence of noises. We test the performance of our behavioral models by adding the external noise and internal noise. For the external noise, we add the randomly generated noise with the range $[0, 0.02]$ and $[0, 0.2]$ (1% and 10% of the largest magnitude of input concentration) to concentration signals. Due to the page limitation, we only present the results for food attraction. The result is shown in Fig. 4.24. It can be seen that, with the external noise, there are more turns appearing and the tracks are less smooth than

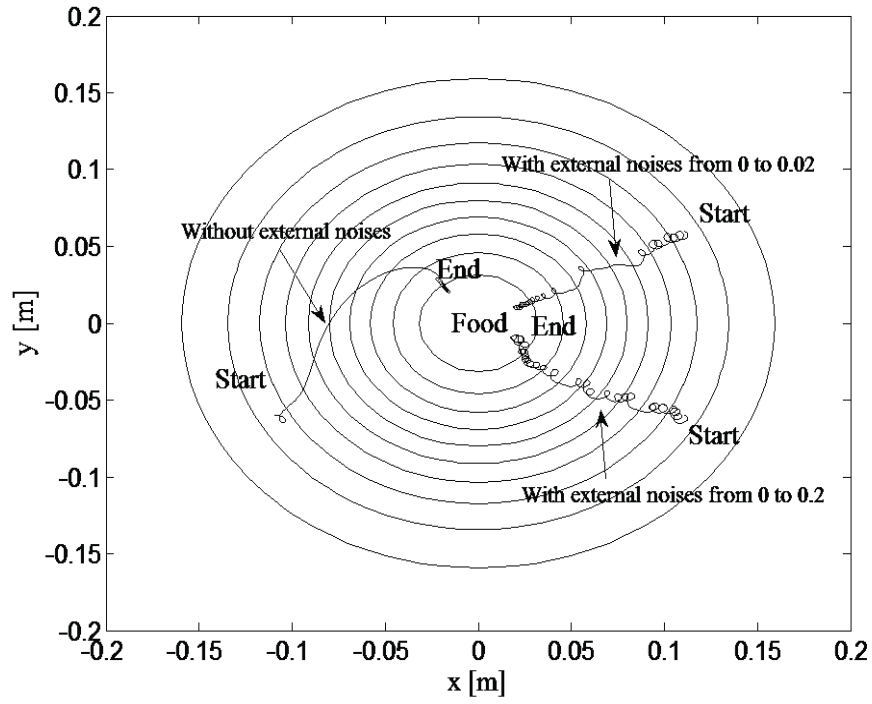


Figure 4.24: Testing results by adding the external noise.

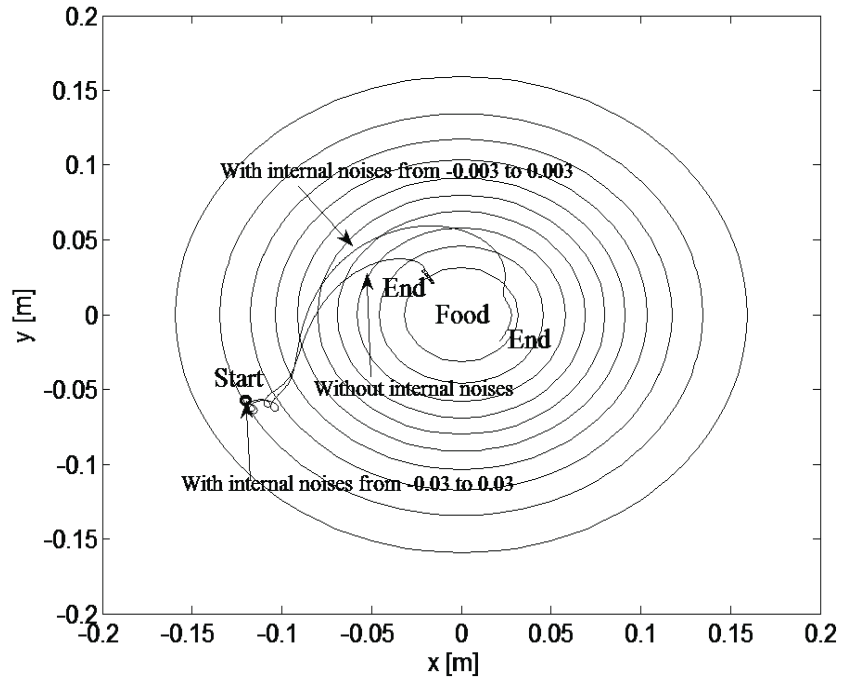


Figure 4.25: Testing results by adding the internal noise.

that without the external noise. However, the worm can still reach the final destination correctly.

Next we add the internal noise to the wire diagram for food attraction. By following the method in [90], we add the synaptic noise (one kind of the internal noise) to the wire diagram. The testing result is shown in Fig. 4.25. The internal noise range is between -0.003 and 0.003 (about 1% of the average weight value), and between -0.03 and 0.03 (about 10% of the average weight value). As shown in Fig. 4.25, *C. elegans* without the internal noise can guide itself towards the food source. When the noise range is between -0.003 and 0.003 , *C. elegans* can still move towards the food source. When the noise range is between -0.03 and 0.03 , *C. elegans* circles around the starting place. In comparison, DNN-based models are more robust for the external noise.

Furthermore, we quantitatively analyze the trajectories that are affected by the external and internal noises. By following the methods in [87] and [19], we analyze the relationship between (1) turning rate and concentration, and (2) probability of turning and $dC(t)/dt$ as what we have done in subsection 4.7.2.

The relationship between turning rate and concentration are shown in Fig. 4.26(a). The results with the external noise (solid line: $y = -0.5959x + 15.7926$, $R_{dot}^2 = 0.40$, $R_{ep}^2 = -25.58$) and with the internal noise (dashed line: $y = -0.3657x + 1.0066$, $R_{dot}^2 = 0.24$, $R_{ep}^2 = -4278.3$) indicate that the turning rate weakly depends on the concentration, which are the same as the conclusion of [19]. As shown in Fig. 4.26 (a), we can observe that the fitting result for experimental data with the internal noise (dashed line, $R_{ep}^2 = -4278.3$) is much worse than that with the external noise (solid line, $R_{ep}^2 = -25.58$). This poor fitting is due to the internal noise that greatly affects the locomotion behaviors of our models.

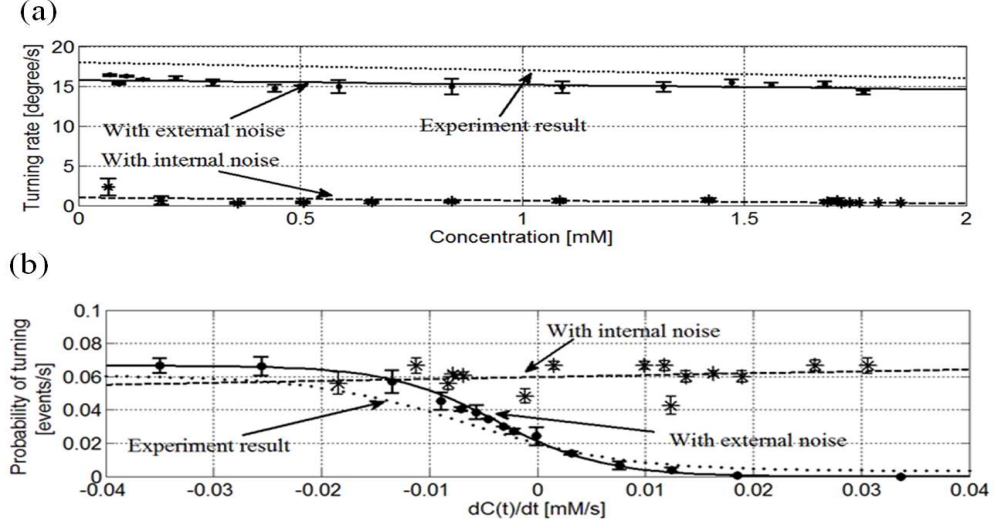


Figure 4.26: Statistical analysis for food attraction behavior with noises. (a) The relationship between turning rate and concentration with the external and internal noises. (b) The relationship between probability of turning and $dC(t)/dt$ with the external and internal noises.

The relationship between probability of turning and $dC(t)/dt$ is shown in Fig. 4.26(b).

The result with the external noise can be approximated by formula $y = 0.023/(a + e^{bx+d}) + c$, where $a = 0.3448$, $b = 200$, $c = 0$, and $d = -0.3$, shown as the solid line. $R_{dot}^2 = 0.99$ and $R_{ep}^2 = 0.89$ for this fitting. However, for the result with the internal noise (asterisks), the relationship between probability of turning and $dC(t)/dt$ is not apparent, and it cannot be approximated by the formula $y = 0.023/(a + e^{bx+d}) + c$. Instead, we approximate these data by $y = 0.1149x + 0.0598$, but the fitting is poor, since $R_{dot}^2 = 0.05$ and $R_{ep}^2 = -782.83$. The poor fitting is also due to the internal noise that greatly affects the locomotion behaviors of our models. Additionally, it is interesting to note that the result with the internal noise is similar to the results shown as Fig. 7 (E) and Fig. 7 (I) in [87], which are the experiment results with neurons ablation.

From the analysis results, the behavior of our model with the external noise is similar to the behavior of wild-type *C. elegans*, whereas the behavior of the model with the internal noise is similar to the behavior of *C. elegans* with neuron ablation.

4.8 Conclusion

In this chapter, the chemotaxis behaviors of *C. elegans* for food attraction and toxin avoidance, as well as speed regulation are investigated. First, biological wire diagrams are used to investigate the chemotaxis behaviors. Second, we design the kinematic model to describe the locomotion behaviors, that is, turning and speed regulation. Third, a set of switching logic functions are constructed to represent the chemotaxis behaviors of food attraction, toxin avoidance, integrated behaviors, as well as speed regulation. All these switching logic functions can be learned by DNN models with RTRL. The testing results verify that these chemotaxis behavioral models can well perform the complex chemotaxis behaviors in different circumstances, and their behaviors are similar to the real *C. elegans* by comparing with the experimental data .

Till now, all the chemotaxis behaviors are investigated on the condition that *C. elegans* moves as a point mass. Actually, *C. elegans* uses undulatory movement for locomotion. In the next chapter, we will explore the undulatory movement through DNN approach.

Chapter 5

Modeling the 3D Undulatory Locomotion Behavior of *C. elegans* Based on the Artificial DNN

In previous chapters, we have investigated the locomotion behaviors of *C. elegans* by treating it to be a single point in the simulated environment. However, *C. elegans* performs the undulatory movement during locomotion. From this chapter, we will explore the undulatory locomotion by using both artificial and biological neural networks. In this chapter, a 3D undulatory locomotion model is investigated based on the artificial DNN.

5.1 Introduction

Undulatory locomotion is one of the fundamental behaviors of the footless animals, such as larva, worm, snake, and even some mammals. Among these animals, the snake has been widely studied to disclose the mechanism of undulatory motion. However, due

to the huge amount of neurons and muscle-bone structures of the snake, it is difficult to study the motion mechanism from cellular level. Fortunately, *C. elegans* offers us an ideal model to study the mechanism of undulatory locomotion behavior. The undulatory locomotion of *C. elegans* is similar to some limbless animals, e.g. ascaris and snake, whereas the neural circuit of *C. elegans* is much simpler than those and it can be modeled easily. This enables us to study their undulatory motion at the cellular level. Furthermore, if we realize these mechanisms on the computer, it may be possible to incorporate these biological or biomimetic methods into the undulatory robots, which can achieve at least four tasks: 1) rescuing survivors in complex areas where human cannot enter [91]; 2) checking the inner side of the industrial equipment pipes [92]; 3) crawling on the ground, under the ground, or through the chink for military utilities [93]; 4) checking the stomach, blood vessels, or intestine for clinical use [94].

The study of undulatory locomotion behavior of *C. elegans* began in recent years. Suzuki et al. explored the locomotion behaviors of *C. elegans* in forward movement, backward movement, and turning [42, 43, 40, 42]. Boyle et al. investigated how the muscles and neurons of *C. elegans* created the S wave and how it was propagated from the head to tail [33, 95]. At last, they designed and constructed a robot inspired by *C. elegans* [39]. In another work [61], a locomotion model was constructed based on the experimental results. This computational model can predict the mechanisms underlying various behaviors of mutant *C. elegans*. The above models crawl in 2D, namely, performing the undulatory behavior on the horizontal plane. The model in [42] can lift up its head during moving, but the rest of its body crawls in 2D on the ground. Till now the only 3D locomotion model was constructed in [62]. The body of this 3D model was assembled by 25 boxes and the muscles were represented by the springs. Without

preserving the biological anatomical structure, the locomotion behavior of this 3D model was displayed mainly in the game engine, and no precise mathematical description was given.



Figure 5.1: The image of *C. elegans* during locomotion. The arrows indicate the lifted parts of *C. elegans*.

In this work, we analyze the 3D locomotion behavior of *C. elegans* by observing the video record, as shown in Fig. 5.1. The arrows in Fig. 5.1 indicate the lifted parts when *C. elegans* is in high-speed crawling. This phenomenon is analogous to the locomotion of snake that lifts up the most bent parts during full speed movement [96]. Inspired by this fact, in this chapter we study the 3D locomotion behavior by investigating the cooperation mechanism of nervous system and muscular system. The novelty of this work involves six aspects.

First, without losing the reality, our model is based on the anatomical muscle structure of *C. elegans* provided in [85]. The whole body is divided into 11 muscle segments, and in each muscle segment there are four pieces of muscles located in four quadrants. These 11 muscle segments are represented as a multi-joint rigid link model with 12 links and 13 joints. The first joint and the last joint denote the head and the tail tips, and other eleven joints stand for the center of each muscle segment.

Second, the nervous system of *C. elegans* is represented as a DNN in our model. DNN has the function of mimicking the nervous system and realizing some important functions of real animals, such as dynamic locomotion [97], associate memory [98], etc. Furthermore, the strong learning capability of DNN can make the locomotion system adapt different environment quickly, and it also can generate different locomotion patterns according to different environments. In our model, DNN involves three parts: head DNN, CPG, and body DNN. The head DNN contains two sensory neurons, three interneurons and one output neuron. The function of the head DNN is to smell the outside concentration and make the decision of turning or going straightly. CPG produces the sinusoid waves for undulatory locomotion. The body DNN receives the sinusoid waves generated by the head DNN and CPG, and passes the waves through each segment. In each segment, the structure of the body DNN is identical with biological connections, and the function of the body DNN is to produce the signals to the muscles in four quadrants. The phase lag of the sinusoid wave, which is the critical factor to create the undulatory behavior, is produced by incorporating the time delay when the wave is transferred through DNN in consecutive segments.

Third, the 3D shape of *C. elegans* during locomotion is investigated. The 3D shape is determined by the joint angles projected onto the sagittal plane (dividing the worm into left and right parts, namely, x-y plane) and the coronal plane (dividing the worm into dorsal and ventral parts, namely, x-z plane). Comparing with other existing models, our model uses the lengths of muscles to control the joint angles directly. In our work, the relations between these angles and the lengths of four quadrant muscles are determined. In other words, once we know the lengths of muscles, the 3D shape is fixed.

Forth, the muscle model is designed to associate with the outputs of DNN. When

receiving the sinusoid wave from the DNN, the length of muscle will change according to the magnitude of signal, and the joint angle will also change accordingly. In this way, we can use the outputs of DNN to control the shape of *C. elegans*.

Fifth, with the learning capability of DNN, our model can implement the chemotaxis behaviors of finding food and avoiding toxin concurrently after the head DNN learns a set of nonlinear functions. These nonlinear functions are called switching logic functions (SLFs) to approximate the logic of *C. elegans* during chemotaxis locomotion. Once SLFs are learned well, our model can perform the chemotaxis behaviors in different simulated environments.

At last, image records of actual *C. elegans* are analyzed to verify the effectiveness of our model. Furthermore, quantitative analyses of the trajectories of our model are carried out by comparing the experiment results in [19] and [87]. Finally, we simplify the well optimized head DNN to be smaller ones according to the method of [25] and find out two patterns that are similar to the result in [25].

This chapter is organized as following. Section 5.2 provides the biological background of *C. elegans* consisting of muscle structure and neuronal structure. Section 5.3 discusses the locomotion system, which includes the head DNN, CPG, body DNN, and muscle system. The structure of DNN and muscles, as well as the mathematical models are provided in details. In Section 5.4, we first investigate the 3D body shape, and then explore the relation between the muscle length and the joint angles on the sagittal plane (x-y plane) and the coronal plane (x-z plane). At last the relation between muscle length and motor neuron outputs is determined. Thus, once the outputs of DNN are known, the 3D shape is determined. In Section 5.5, the methods to optimize the head DNN and the body DNN are provided. Section 5.6 gives the testing results. In Section 5.7, the

comparative analyses of our results with the experiment results of real *C. elegans* are provided. Section 5.8 concludes this chapter and discusses the future works.

5.2 Anatomical Structure of *C. elegans* for Locomotion

5.2.1 Muscle and Body Structure

C. elegans with a simply cylindrical body is about 1 millimeter in length. The body wall muscles can be classified into 4 quadrants on the transverse plane, as shown in Fig. 5.2 (a). These four quadrants are dorsal-left (DL), ventral-left (VL), ventral-right (VR), and dorsal-right (DR). Its 95 body wall muscle cells are arranged as pairs located in four quadrants along the body, as shown in Fig. 5.2 (b). Each of DL, VR, and DR quadrants contains 24 muscle cells, except for the VL quadrant, which contains 23 muscle cells. During locomotion, *C. elegans* lies aside (uses the left or right side touching the ground) and moves over a surface by propagating dorsal/ventral flexures along its body [85]. Based on the muscles structure, the body can be divided into 11 muscle segments. The center of each muscle segment in Fig. 5.2 (b) is depicted as a joint in Fig. 5.2 (c). For instance, muscles in Fig. 5.2 (b) denoted as 3 and 4 in each quadrant form the second segment, as shown in Fig. 5.2 (c). Muscles from 21 to 24 (21 to 23 for VL quadrant) form the last segment, because anatomically these three or four muscles in each quadrant are controlled by the same motor neuron [83]. As shown in Fig. 5.2 (c), by adding another 2 joints (denoted as 0 and 12), which denote the head and the tail tips respectively, the whole body is represented by 13 joints. These 13 nodes are connected by 12 links. Thus body of *C. elegans* is depicted as a multi-joint rigid link system.

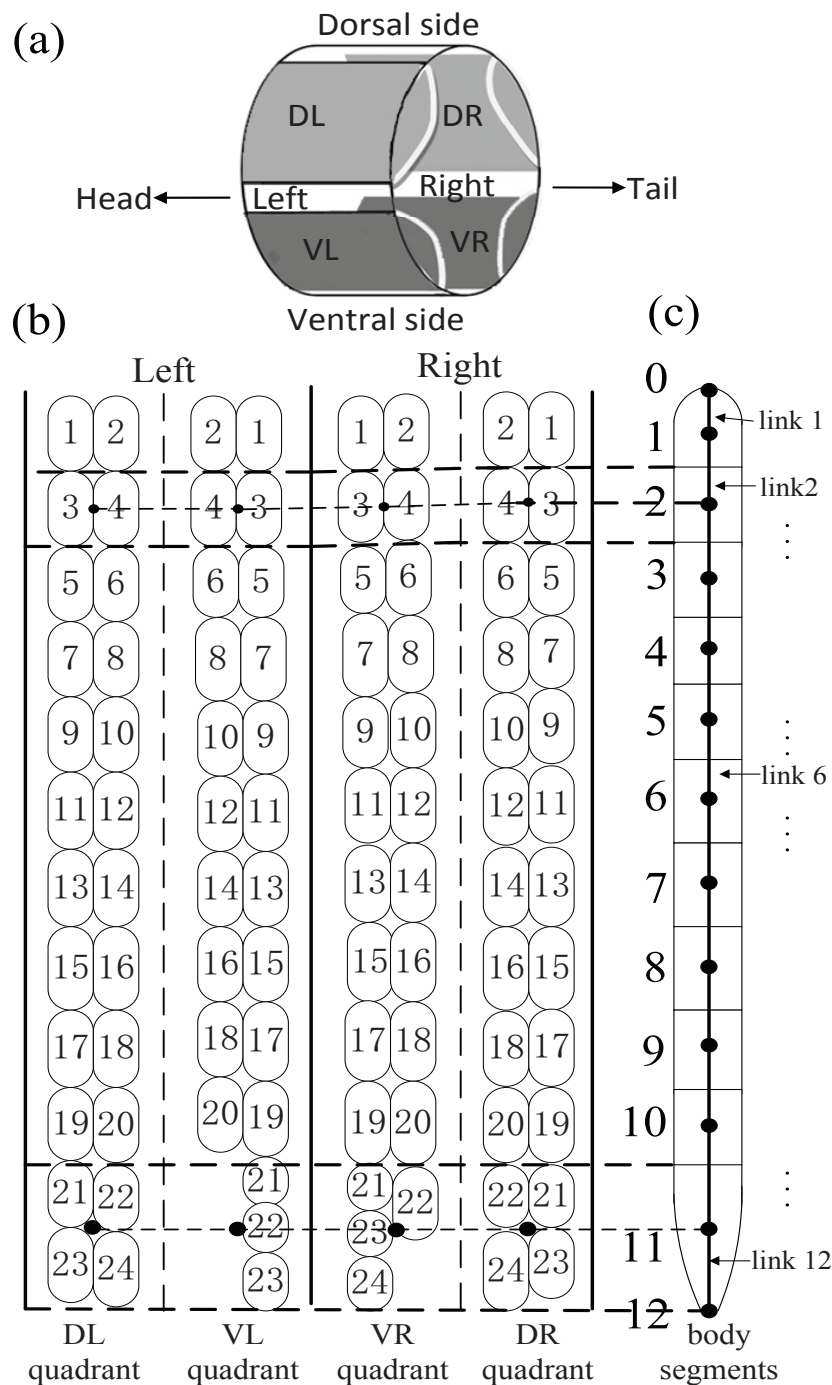


Figure 5.2: (a) Muscle structure of *C. elegans*. The muscles are divided into 4 quadrants on the transverse plane. (b) Body structure of *C. elegans*. Each quadrant contains 23 or 24 muscle cells. (c) The whole body is divided into 11 muscle segments according to the muscle structure and depicted as a multi-joint rigid link system with 13 joints and 12 links.

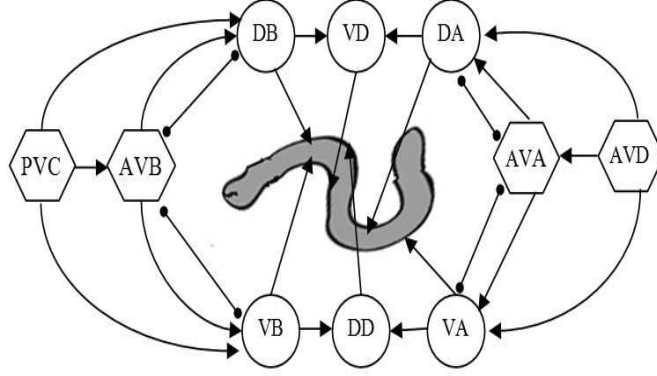


Figure 5.3: Neuronal circuit of *C. elegans* for locomotion. Motor neurons DB and VB are for forward locomotion; DA and VA are for backward locomotion; VD and DD are inhibitory neuron for muscles coordination.

5.2.2 Neuronal Structure for Locomotion

The locomotion behavior of *C. elegans* is determined by the actions of muscles, whereas the muscles are controlled by the motor neurons. The motor neurons are distributed along the ventral side of the body from head to tail. There are three types of motor neurons: B type (DB and VB) for forward locomotion, A type (DA and VA) for backward locomotion, and D type (VD and DD) for muscles coordination. There are 58 motor neurons for the three types. As shown in Fig. 5.3, DB_i ($i=1,\dots,7$) and VB_i ($i=1,\dots,11$) receive the command signals from command neurons PVC and AVB, and active the muscles to perform the forwards locomotion behavior. DA_i ($i=1,\dots,9$) and VA_i ($i=1,\dots,12$) receive the command signals from command neurons AVA and AVD to produce the backward locomotion signals to muscles. DD_i ($i=1,\dots,6$) and VD_i ($i=1,\dots,13$) are inhibitory motor neurons. DB, DA, and DD control the muscles on the dorsal side; VB, VA, and VD control the muscles on the ventral side. During forward locomotion, if DB activates the dorsal side muscle, the VD will inhibit the opposite side muscle (ventral side); if VB activates the ventral side muscle, the DD will inhibit the opposite side muscle (dorsal side). In this way, the forward undulatory movement is generated. The mechanism

for backward locomotion is similar to that for the forward locomotion, except that DA replaces DB and VA replaces VB. The circuits for forward locomotion and backward locomotion work mutual exclusively [85, 23].

5.3 Locomotion System Modeling

In our model, undulatory forward and backward movements require wave signals sent from the nervous system to the motor neurons. Muscles receive the signals from the motor neurons to perform the corresponding behaviors. In our work, we adopt DNN to represent the nervous system of *C. elegans*, which is classified into three parts: head DNN, CPG, and body DNN. Muscle is modeled by investigating the relation between the muscle length and the neuronal inputs.

5.3.1 Head DNN

In our model, the head DNN achieves the decision making function by generating the turning signal to the motor neurons. The head DNN, which is an artificial brain [99], is inspired by the neural networks in [45] and [47]. As shown in Fig. 5.4, the head DNN contains six neurons. ASE and ASH are sensory neurons for food and toxin concentrations, respectively. I1, I2, and I3 are interneurons, while neuron OUT is output neuron. All neurons in the head DNN are fully connected and each neuron has the self-connection. The active function of each neuron is the same as that in our preceding work [100]:

$$\begin{aligned} \tau_i \frac{dV_i(t)}{dt} = & -V_i(t) + \beta_i \tanh\left(\sum_{j=1, j \neq i}^N w_{ij}(V_j(t) - \bar{V}_j)\right) \\ & + b_i + \delta_i C(t) \end{aligned} \quad (5.1)$$

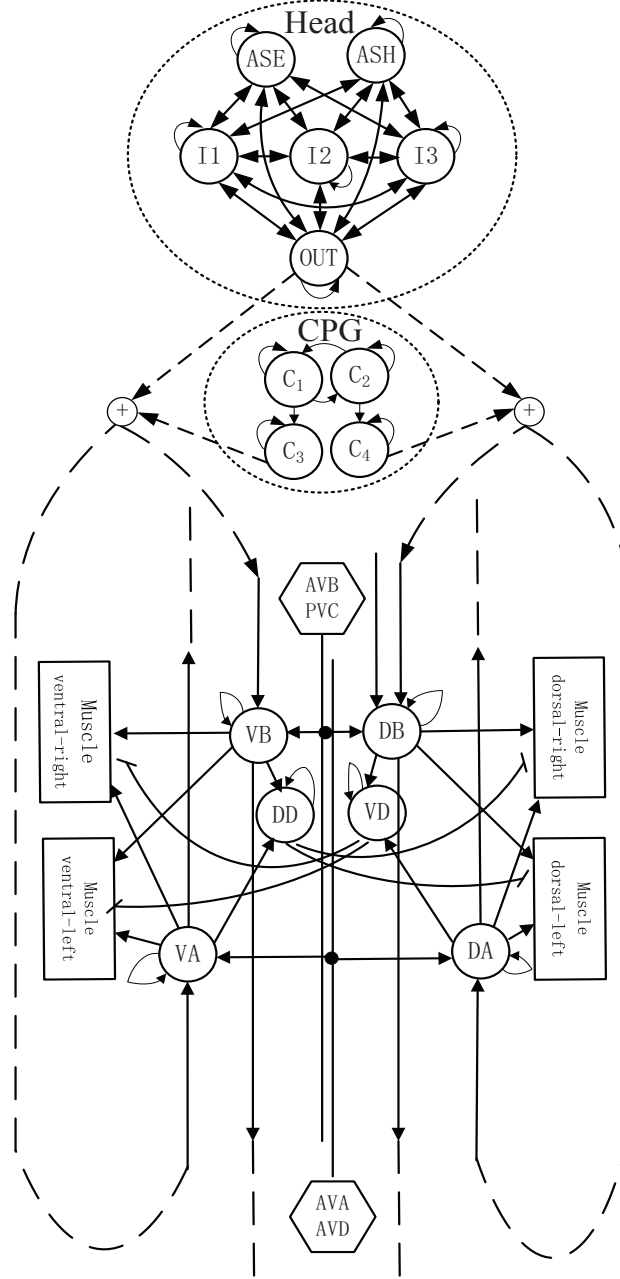


Figure 5.4: DNN and the muscle structure of *C. elegans*. DNN is classified into three parts: head DNN, CPG, and body DNN. The head DNN contains six neurons that achieves the decision making function for chemotaxis behavior. CPG involves four neurons, C_1 and C_2 generating the sinusoid waves and C_3 and C_4 adjusting the phase lag. In the body DNN, two command neurons “PVC, AVB” and “AVA, AVD” switch the circuits for forward and backward locomotion. The signals are passed from the first segment to the last segment in sequence for forward locomotion (vice versa for backward locomotion), and are also transmitted to muscles. The muscles function as actuators and act according to motor neurons’ outputs.

where τ_i is the time constant that controls the time delay. $V_i(t)$ is the voltage of neuron i at time t . $V_j(t)$ is the voltage of input neuron j . w_{ij} is the connection weight from neuron j to i . The constant \bar{V}_j is the center of the conductance of the j th neuron, which means at this voltage there is no transmitter released from the j th neuron [44]. b_i is a constant bias introduced here to adjust the resting potential value [73]. $\delta_i = 1$ if the neuron i is the sensor neuron, otherwise $\delta_i = 0$. β_i is a constant should be determined.

The head DNN has the ability to approximate any arbitrary nonlinear functions [101]. If we can construct some nonlinear functions to map the input-output relations of the decision making of *C. elegans*, the head DNN can generate the desired signals to the motor neurons to perform the chemotaxis behaviors after training. The way to construct the nonlinear functions and the procedure to train the head DNN are discussed in Section 5.5.

5.3.2 CPG

Up to now, there are two ways to model the mechanism of *C. elegans* to generate the undulatory wave: one based on CPG [61] and the other based on the sensory feedback mechanism [35, 37]. Recent research work indicates that *C. elegans* does not use CPG to propagate the undulatory wave [35, 37, 102, 103], and in work [30, 103] they claim that there is a CPG in the head while the sensory feedback mechanism is responsible for propagating the undulatory wave along the body. Our ultimate goal for this chapter is to build a 3D locomotion model for the worm-like robot. Thus, for modeling convenience, it is a relatively easy way to choose a CPG as the undulatory wave generator. The undulatory wave generated by CPG is passed through the motor neurons of each segment to produce the undulatory locomotion behavior. The sensory feedback mechanism is not incorporated into this model.

CPG for this model contains four dynamic neurons, as shown in Fig. 5.4. C_1 and C_2 are used to generate the sinusoid waves. The voltages of C_1 and C_2 are calculated by the following equations.

$$\begin{aligned}\tau \dot{V} &= A_G V, \\ A_G &= \begin{bmatrix} 0 & -2\pi \\ 2\pi & 0 \end{bmatrix}, \\ V &= [V_{C_1}, V_{C_2}]^T,\end{aligned}\tag{5.2}$$

where τ is a constant. According to [104], by choosing the initial values $V_{C_1}(0) = 1$ and $V_{C_2}(0) = 0$, the inner periodic signal generator V_{C_1} and V_{C_2} can produce co-sinusoidal signals, $V_{C_1}(t) = \cos(\omega t)$ and $V_{C_2}(t) = \sin(\omega t)$, where $\omega = 2\pi/\tau$.

After two sinusoid waves are generated by the neurons C_1 and C_2 , two neurons (C_3 and C_4) are involved to adjust the phases of the sinusoid waves to yield the outputs of CPG. The voltages updating of C_3 and C_4 are

$$\tau_{C_3} \dot{V}_{C_3}(t) = -V_{C_3}(t) + V_{C_1}(t),\tag{5.3}$$

$$\tau_{C_4} \dot{V}_{C_4}(t) = -V_{C_4}(t) + V_{C_2}(t),\tag{5.4}$$

where τ_{C_3} and τ_{C_4} are time constants to control the phase lag.

The sinusoid waves pass through DB and VB from head to tail for forward locomotion, and pass through DA and VA from tail to head for backward locomotion. Furthermore, according to [56], the sinusoid waves passed through DB and VB should have the opposite phase to ensure the alternating dorsoventral sweeps. This kind of opposite phase can be obtained by trials to adjust the parameters τ_{C_3} and τ_{C_4} in Eqs. (5.3) and (5.4), respectively.

5.3.3 Body DNN

The body DNN is divided into 11 segments according to the muscle structure. When crawling, *C. elegans* lies aside on the ground. In our work, we assume that the right side of *C. elegans* touches the ground. By overlooking, the ventral side is our left-hand side, and the dorsal side is our right-hand side, as shown in Fig. 5.5. Under the assumption, we divide the 3D space to four directions: left, right, up, and down. For the simplification, we rename the four quadrants muscles as: ld (left-down) for VR, lu (left-up) for VL, rd (right-down) for DR, and ru (right-up) for DL. The connections between neurons and muscles for one body segment are shown in Fig. 5.4. In our model, each segment owns the same structure.

Neurons DB, VB, DA, and VA are active neurons that excite the muscles. VD and DD are inhibitory neurons that inhibit their counterpart muscles. DB, VB, VD, and DD are involved in the circuit for forward locomotion, and DA, VA, VD, and DD are involved in the circuit for backward locomotion. According to [85], the circuits for forward and backward locomotion work mutual exclusively. The command neurons PVC and AVB control the forward locomotion, and AVA and AVD control the backward locomotion by switching on or off their corresponding motor neurons [105] [37]. In this work, we combine PVC and AVB to be one neuron “PVC, AVB”, and AVA and AVD to be “AVA, AVD”. When neuron “PVC, AVB” is active, the neuron “AVA, AVD” is inhibited. Thus when DB and VB neurons are working to propagate the sinusoid wave, DA and VA are not working. It is vice versa if “AVA, AVD” is active.

There are six motor neurons in each segment, which are connected according to the biological wire diagram. These motor neurons are depicted as dynamic neurons [67] with the activity function as Eq. (5.1). During forward locomotion, as shown in

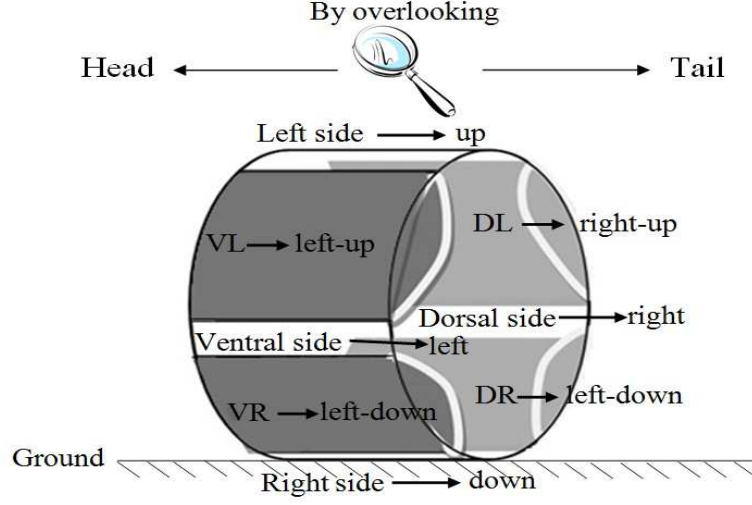


Figure 5.5: *C. elegans* lies aside on the ground. We assume that the right side of *C. elegans* touches the ground. The ventral side is our left-hand side, and the dorsal side is our right-hand side. For simplicity and directviewing, muscles in four quadrants are renamed as: ld (left-down) for ventral-right, lu (left-up) for ventral-left, rd (right-down) for dorsal-right, and ru (right-up) for dorsal-left.

Fig. 5.4, DB, VB are activated by command neuron “AVB, PVC”, and DA, VA are inhibited by command neuron “AVA, AVD”. The sinusoid signals from head or preceding segment are fed into DB and VB. Output signals of DB and VB are transmitted into their corresponding muscles. VB connects two muscles on the left side, and DB connects two muscles on the right side. DD receives signal from VB, and sends its output to the muscles on the right side. VD receives signal from DB, and sends its output to the muscles on the left side. At the same time, DB and VB send their outputs to the next segment. There is a time delay $\Delta\tau$ when the signal passes through each segment. Muscles are actuators that receive the motor neurons’ signals and produce certain activities. The sinusoid shape is produced by the reactions of muscles to the time delayed signals.

5.3.4 Model of Muscle

In our work, the muscles serve as the actuators driven by the outputs of DNN [95]. The connections between muscles and motor neurons in one segment are shown

in Fig. 5.6, which are extracted from Fig. 5.4. The left side muscles receive three inputs from motor neurons VB, VD, and VA. The right side muscles receive three inputs from motor neurons DB, DD, and DA. The arrows indicate the excitatory connections, while the blunted lines indicate the inhibitory connections. For segment i at time t , we let $I_{i,l}(t)$ be the input of anyone of the two muscles for the left side, and $I_{i,r}(t)$ for the right side. The relations between inputs of muscles and voltages of motor neurons are

$$\begin{aligned} I_{l,i}(t) = & w_{Mi,VB_i}V_{VB,i}(t) + w_{Mi,VA_i}V_{VA,i}(t) \\ & + w_{Mi,VD_i}V_{VD,i}(t), \end{aligned} \quad (5.5)$$

$$\begin{aligned} I_{r,i}(t) = & w_{Mi,DB_i}V_{DB,i}(t) + w_{Mi,DA_i}V_{DA,i}(t) \\ & + w_{Mi,DD_i}V_{DD,i}(t), \end{aligned} \quad (5.6)$$

where $V_{VB,i}(t)$, $V_{VA,i}(t)$, and $V_{VD,i}(t)$ are the output voltages of left side motor neurons VB_i , VA_i , and VD_i at time t , respectively. $V_{DB,i}(t)$, $V_{DA,i}(t)$, and $V_{DD,i}(t)$ are the output voltages of right side motor neurons DB_i , DA_i , and DD_i at time t , respectively. w_{Mi,VB_i} , w_{Mi,VA_i} , and w_{Mi,VD_i} are the connection weights from VB_i , VA_i , and VD_i to left side muscle, respectively. w_{Mi,DB_i} , w_{Mi,DA_i} , and w_{Mi,DD_i} are the connection weights from DB_i , DA_i , and DD_i to right side muscle, respectively.

In segment i , the lengths of muscles for left-up, left-down, right-up, and right-down are denoted as $l_{lu,i}$, $l_{ld,i}$, $l_{ru,i}$, and $l_{rd,i}$, respectively. The relation between the lengths of

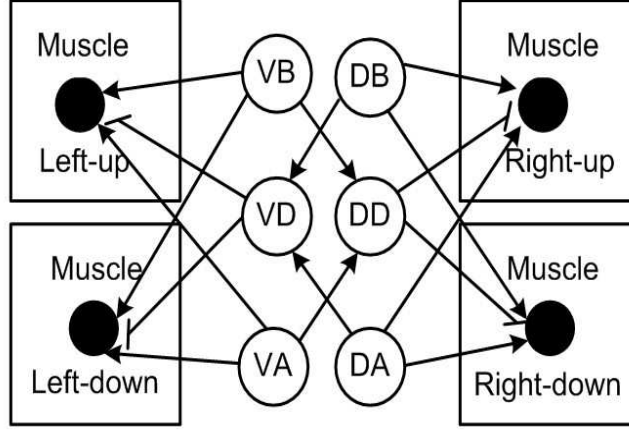


Figure 5.6: The connection between muscles and motor neurons.

muscles and inputs are:

$$l_{lu,i}(t) = L_{lu,i} + \sigma_{lu}(I_{l,i}(t)), \quad (5.7)$$

$$l_{ld,i}(t) = L_{ld,i} + \sigma_{ld}(I_{l,i}(t)), \quad (5.8)$$

$$l_{ru,i}(t) = L_{ru,i} + \sigma_{ru}(I_{r,i}(t)), \quad (5.9)$$

$$l_{rd,i}(t) = L_{rd,i} + \sigma_{rd}(I_{r,i}(t)), \quad (5.10)$$

where $L_{lu,i}$, $L_{ld,i}$, $L_{ru,i}$, and $L_{rd,i}$ are the lengths of relaxed muscles without being affected by neuronal inputs. σ_{lu} , σ_{ld} , σ_{ru} , and σ_{rd} are the nonlinear activity functions, which will be explored in Section 5.4.3.

5.4 3D Locomotion Behaviors Modeling

5.4.1 Motion Modality

Undulatory movement is the primary way for *C. elegans* to move. According to [61], the whole body shapes as a sinusoid wave about 1.5 to 2 periods during locomotion. In our work we consider that the wave length is 1.5 sinusoid wave periods. The form of *C. elegans* during locomotion is shown in Fig. 5.7.

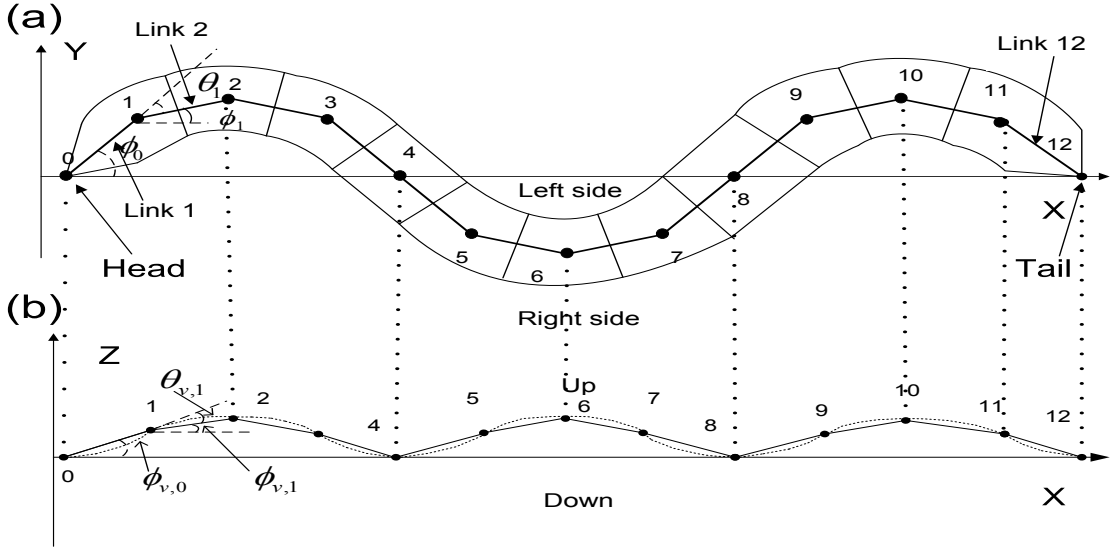


Figure 5.7: (a) The shape of *C. elegans* on the x-y plane. The whole body is represented as 12 links and shapes as a sinusoid wave with 1.5 periods. (b) The shape of *C. elegans* on the x-z plane. It is obviously that some of the body parts lift up the ground, and the frequency is twice of that on the horizontal plane.

In our work, we explore the movements of *C. elegans* in 3D. Fig. 5.7 (a) shows its shape on the horizontal (x-y) plane by overlooking, and (b) shows the shape on the vertical (x-z) plane. It can be seen that *C. elegans* displays a standard sinusoid wave from head to tail on the x-y plane, and it lifts up some parts of its body on the x-z plane. The most bent parts on the x-y plane lift up highest above the ground, and the unbent parts on the x-y plane touch the ground. For example, as shown in Fig. 5.7 (b), links 2, 6, and 10 lift up highest above the ground, and links 0, 4, 8, and 12 touch the ground. The dot line in Fig. 5.7 (b) is the trace of the joints on the x-z plane during locomotion.

To construct the locomotion model in 3D, we should calculate how the angles between two consequent links vary at different time, both on the x-y plane (θ_i) and the x-z plane ($\theta_{v,i}$). According to [106], when *C. elegans* moves as a sinusoid wave on the x-y plane,

as shown in Fig. 5.7 (a),

$$\phi_i = A_i \sin(\omega t + \phi_{start} - i\phi_{Lag,i}), \quad (5.11)$$

$$\theta_i = \phi_{i-1} - \phi_i, \quad (5.12)$$

where ϕ_i ($i = 0, \dots, 11$) is the angle between link $i + 1$ and the x-axis. A_i is the magnitude of the ϕ_i , and ω is the angular velocity. ϕ_{start} is initial angle, and $\phi_{Lag,i}$ is the phase lag. θ_i ($i = 1, \dots, 11$) is the angle between two consecutive links, i and $i + 1$.

On the x-z plane, as shown in Fig. 5.7 (b), the angle $\phi_{v,i}$ ($i = 0, \dots, 11$) between the link $i + 1$ and the ground (x-y plane) is a sinusoid function, but the frequency is double.

$$\phi_{v,i} = A_{v,i} \sin(2\omega t + 2\phi_{start} - 2i\phi_{Lag,i}), \quad (5.13)$$

$$\theta_{v,i} = \phi_{v,i-1} - \phi_{v,i}, \quad (5.14)$$

where $A_{v,i}$ is the magnitude of the $\phi_{v,i}$, and ω , ϕ_{start} , and $\phi_{Lag,i}$ have the same values as those in Eq. (5.11). $\theta_{v,i}$ ($i = 1, \dots, 11$) is the angle between two consecutive links i and $i + 1$ on the x-z plane.

Thus given A_i , $A_{v,i}$, ω , ϕ_{start} , and $\phi_{Lag,i}$, from Eqs. (5.11) to (5.14), we can briefly determine the shape of *C. elegans* at time t .

5.4.2 Muscle Length and Joint Angle

Two angles (θ_i and $\theta_{v,i}$) determine the shape of *C. elegans* during locomotion. These angles are yielded by the contracting or extending of the muscles. In this subsection, we explore the relation between the lengths of muscles and the angles.

We assume that each muscle acts separately. Fig. 5.8 (a) shows one muscle segment of *C. elegans*. The angle between link i and link $i + 1$ can be measured as θ on the x-y

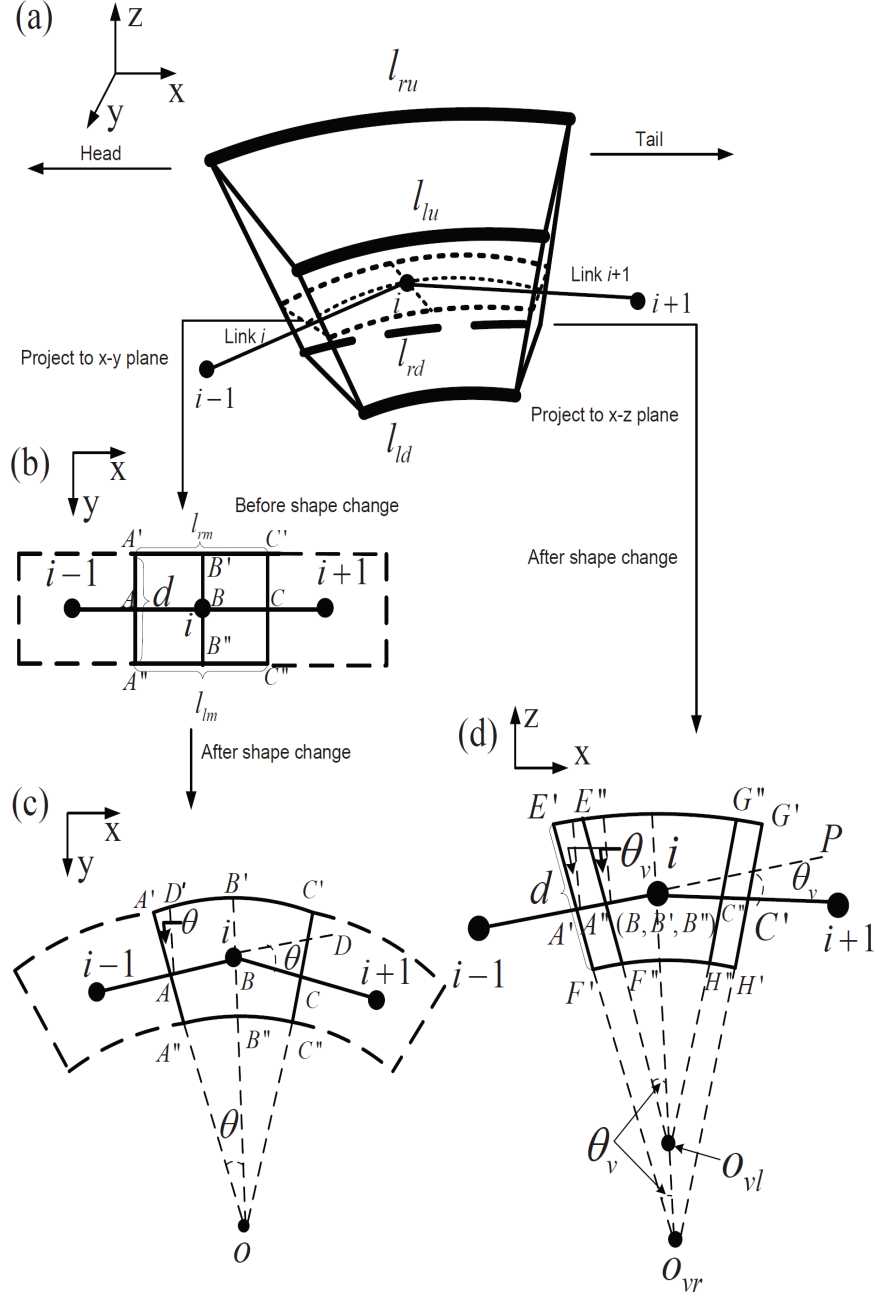


Figure 5.8: (a) One muscle segment i is shown in 3D. The lengths of muscles in four quadrants are denoted as l_{ru} , l_{lr} , l_{rd} , and l_{ld} . (b) The projection of the middle plane of the muscle segment of (a) (dotted line) on the x - y plane without shape change, which means all the four quadrant muscles are relaxed. (c) The projection of (a) on the x - y plane during sinusoid locomotion. (d) The projection of (a) on the x - z plane during sinusoid locomotion. Joint angles between link i and link $i+1$ are measured as θ on the x - y plane and θ_v on the x - z plane, as shown in (c) and (d), respectively.

plane, and θ_v on the x-z plane, as shown in Fig. 5.8 (c) and (d), respectively. The values of θ and θ_v are determined by the lengths of muscles in four quadrants.

As shown in Fig. 5.8 (b), the rectangle ($A'A''C''C'$) is the projection of the middle plane (dotted line) of Fig. 5.8 (a) onto the x-y plane without the shape change. Dashed lines stand for the other two consecutive segments. In Fig. 5.8 (b), $|A'C'| = l_{rm} = (l_{ru} + l_{rd})/2$, which represents the average length of two muscles on the right side, and $|A''C''| = l_{lm} = (l_{lu} + l_{ld})/2$, which represents the average length of two muscles on the left side. During undulatory locomotion, muscles change their lengths, so the shape of one segment as shown in Fig. 5.8 (b) will become to shape as shown in Fig. 5.8 (c). We set the length of each link is l , and in Fig. 5.8 (c) $|AB| = \frac{l}{2}$, $|A'A| = \frac{d}{2}$. It can be proved that $\angle DBC = \angle AOB = \theta$, and drawing $D'A//B'B$ yields $\angle A'AD' = \theta$ and $|AB| = |D'B'| = \frac{l}{2}$. Thus,

$$\begin{aligned}
 l_{rm} &= |\widehat{A'C'}| = 2|\widehat{A'B'}| \\
 &= 2(|\widehat{A'D'}| + |\widehat{D'B'}|) \\
 &= 2(\frac{d}{2}\theta + \frac{l}{2}) \\
 &= l + d\theta.
 \end{aligned} \tag{5.15}$$

Following the same way, the relation between l_{lm} and θ is:

$$l_{lm} = l - d\theta. \tag{5.16}$$

The projection of the muscle segment of Fig. 5.8 (a) on the x-z plane is shown as Fig. 5.8 (d). $\widehat{E'G'}$, $\widehat{E''G''}$, $\widehat{F'H'}$, and $\widehat{F''H''}$ represent four quadrants muscles, l_{ru} , l_{lu} , l_{rd} , and l_{ld} , respectively. $|\widehat{A'C'}| = l_{rm}$ and $|\widehat{A''C''}| = l_{lm}$, which are the projections of $|\widehat{A'C'}|$

and $|\widehat{A''C''}|$ in Fig. 5.8 (c), respectively. It can be proved that $\angle A'O_{vr}B' = \angle A''O_{vl}B'' = \angle PBC' = \theta_v$. Following the same method to deal with Fig. 5.8 (c), we obtain:

$$l_{ru} = l_{rm} + d\theta_v, \quad (5.17)$$

$$l_{lu} = l_{lm} + d\theta_v, \quad (5.18)$$

$$l_{rd} = l_{rm} - d\theta_v, \quad (5.19)$$

$$l_{ld} = l_{lm} - d\theta_v. \quad (5.20)$$

By substituting Eqs. (5.15) and (5.16) to Eqs. (5.17), (5.18), (5.19), and (5.20), for any muscle segment i , we obtain the relation between the lengths of four quadrant muscles and the two angles:

$$l_{ru,i} = l + d\theta_i + d\theta_{v,i}, \quad (5.21)$$

$$l_{lu,i} = l - d\theta_i + d\theta_{v,i}, \quad (5.22)$$

$$l_{rd,i} = l + d\theta_i - d\theta_{v,i}, \quad (5.23)$$

$$l_{ld,i} = l - d\theta_i - d\theta_{v,i}. \quad (5.24)$$

From Eqs. (5.21), (5.23), (5.22), and (5.24), we know that lengths of muscles in four quadrants, l_{ru} , l_{rd} , l_{lu} , and l_{ld} , are related to the joint angles θ_i and $\theta_{v,i}$. Since link length l and body diameter d are two constants, once the lengths of the four quadrant muscles are known, the two joint angles $\theta_{v,i}$ and θ_i can be determined.

5.4.3 Muscle Lengths and Outputs of Motor Neurons

The lengths of muscles are controlled by the outputs of motor neurons. For example, during forward locomotion, muscles on the left side are controlled by motor neurons DB

and DD, and muscles on the right side are controlled by motor neurons VB and VD.

In this subsection, we explore the relation between the outputs of motor neurons and lengths of muscles.

Locomotion Without Turning

We first investigate the undulatory locomotion behavior of *C. elegans* without turning.

Substituting Eq. (5.11) to Eq. (5.12) yields

$$\begin{aligned}\theta_i &= A_{i-1} \sin(wt + \phi_{start} - (i-1)\phi_{Lag,(i-1)}) \\ &\quad - A_i \sin(wt + \phi_{start} - i\phi_{Lag,i}).\end{aligned}\tag{5.25}$$

During straight undulatory locomotion, we assume $A_i = A$ and $\phi_{Lag,i} = \phi_{Lag}$, where $i = 1, \dots, 11$. Eq. (5.25) is simplified as

$$\theta_i = A_{\theta,i} \cos(wt + \phi_{start} - i\phi_{Lag} + \frac{\phi_{Lag}}{2}), (i = 1, \dots, 11),\tag{5.26}$$

where $A_{\theta,i} = 2A \sin(\frac{\phi_{Lag}}{2})$ is a constant.

Furthermore, by substituting Eq. (5.13) to Eq. (5.14), we have

$$\theta_{v,i} = A_{\theta_{v,i}} \cos(2wt + 2\phi_{start} - 2i\phi_{Lag} + \phi_{Lag}), (i = 1, \dots, 11),\tag{5.27}$$

where $A_{\theta_{v,i}} = 2A_{v,i} \sin(\phi_{Lag})$ is a constant.

Now the changes of θ_i and $\theta_{v,i}$ during straight movement of *C. elegans* are determined.

By substituting Eqs. (5.26) and (5.27), Eqs. (5.21)–(5.24) become

$$l_{ru,i}(t) = 2dA_{\theta v,i}M_i^2(t) + dA_{\theta,i}M_i(t) - dA_{\theta v,i} + l, \quad (5.28)$$

$$l_{lu,i}(t) = 2dA_{\theta v,i}M_i^2(t) - dA_{\theta,i}M_i(t) - dA_{\theta v,i} + l, \quad (5.29)$$

$$l_{rd,i}(t) = -2dA_{\theta v,i}M_i^2(t) + dA_{\theta,i}M_i(t) + dA_{\theta v,i} + l, \quad (5.30)$$

$$l_{ld,i}(t) = -2dA_{\theta v,i}M_i^2(t) - dA_{\theta,i}M_i(t) + dA_{\theta v,i} + l, \quad (5.31)$$

where

$$M_i(t) = \cos(wt + \phi_{start} - i\phi_{Lag} + \phi_{Lag}/2). \quad (5.32)$$

In this work we assume the lengths of the relaxed muscles L_{lu} , L_{ld} , L_{ru} , and L_{rd} in Eqs. (5.7)–(5.10) to be l . Thus Eqs. (5.7)–(5.10) and Eqs. (5.28)–(5.31) can be rewritten as

$$\sigma_{lu}(I_{l,i}(t)) = 2dA_{\theta v,i}M_i^2(t) - dA_{\theta,i}M_i(t) - dA_{\theta v,i}, \quad (5.33)$$

$$\sigma_{ld}(I_{l,i}(t)) = -2dA_{\theta v,i}M_i^2(t) - dA_{\theta,i}M_i(t) + dA_{\theta v,i}, \quad (5.34)$$

$$\sigma_{ru}(I_{r,i}(t)) = 2dA_{\theta v,i}M_i^2(t) + dA_{\theta,i}M_i(t) - dA_{\theta v,i}, \quad (5.35)$$

$$\sigma_{rd}(I_{r,i}(t)) = -2dA_{\theta v,i}M_i^2(t) + dA_{\theta,i}M_i(t) + dA_{\theta v,i}. \quad (5.36)$$

$I_{l,i}$ in Eq. (5.33), for example, is determined by $V_{VB,i}$, $V_{VA,i}$, and $V_{VD,i}$ in Eq. (5.5). Furthermore, $V_{VB,i}$ and $V_{VA,i}$ work mutual exclusively [85], and $V_{VB,i}$ and $V_{VD,i}$ are two sinusoid waves with opposite phases [56]. Thus for forward locomotion, Eq. (5.5) can be simplified as

$$I_{l,i}(t) = \Delta w_{MV i} V_{VB,i}(t), \quad (5.37)$$

where $\Delta w_{MV_i} = w_{M_i,VB_i} - w_{M_i,VD_i}$. $V_{VB,i}(t)$ is the sinusoid wave that can be adjusted as $V_{VB,i}(t) = M_i(t)$ in Eq. (5.32). Thus Eq. (5.33) can be rewritten as

$$\sigma_{lu}(V_{VB,i}(t)) = \frac{2dA_{\theta v,i}}{\Delta w_{MV_i}^2} V_{VB,i}^2(t) - \frac{dA_{\theta,i}}{\Delta w_{MV_i}} V_{VB,i}(t) - dA_{\theta v,i}, \quad (5.38)$$

and it also can be written in a general form as below

$$\sigma_{lu}(x) = \frac{2dA_{\theta v,i}}{\Delta w_{MV_i}^2} x^2 - \frac{dA_{\theta,i}}{\Delta w_{MV_i}} x - dA_{\theta v,i}. \quad (5.39)$$

Following the same way, Eqs. (5.34)–(5.36) are rewritten as

$$\sigma_{ld}(x) = -\frac{2dA_{\theta v,i}}{\Delta w_{MV_i}^2} x^2 - \frac{dA_{\theta,i}}{\Delta w_{MV_i}} x + dA_{\theta v,i}, \quad (5.40)$$

$$\sigma_{ru}(x) = \frac{2dA_{\theta v,i}}{\Delta w_{MD_i}^2} x^2 - \frac{dA_{\theta,i}}{\Delta w_{MD_i}} x - dA_{\theta v,i}, \quad (5.41)$$

$$\sigma_{rd}(x) = -\frac{2dA_{\theta v,i}}{\Delta w_{MD_i}^2} x^2 - \frac{dA_{\theta,i}}{\Delta w_{MD_i}} x + dA_{\theta v,i}. \quad (5.42)$$

Till now the Eqs. (5.7)–(5.10) are determined. We can observe that the lengths of four quadrants muscle are determined by the voltages of the motor neurons, $V_{DB,i}$ and $V_{VB,i}$. In other words, once the voltages of $V_{DB,i}$ and $V_{VB,i}$ are known, the lengths of four quadrants are determined.

Locomotion with Turning

During undulatory locomotion, *C. elegans* will change its direction to approach the food or leave faraway from the toxin. The head DNN in our model achieves the decision making mechanism by generating the turning signal to the motor neurons. When *C. elegans* needs turning, the output of V_{OUT} in the head DNN is non-zero, otherwise it keeps its output to be zero. In this subsection we first investigate the effect of V_{OUT} on the lengths of muscles, and next the effect of V_{OUT} on the joint angles, $\Delta\theta$ and $\Delta\theta_v$.

Effected by $V_{OUT}(t)$, Eq. (5.37) becomes

$$I'_{l,i}(t) = \Delta w_{MV,i}(V_{VB,i}(t) + V_{OUT}(t)). \quad (5.43)$$

Thus the change for left-up muscle is

$$\begin{aligned} \Delta l_{lu,i}(t) &= l'_{lu,i}(t) - l_{lu,i}(t) \\ &= \sigma_{lu}(I'_{l,i}(t)) - \sigma_{lu}(I_{l,i}(t)) \\ &= \sigma_{lu}(\Delta w_{MV,i}(V_{VB,i}(t) + V_{OUT}(t))) - \sigma_{lu}(\Delta w_{MV,i}V_{VB,i}(t)) \\ &= 2dA_{\theta v,i}V_{OUT}^2(t) + (4dA_{\theta v,i}V_{VB}(t) - dA_{\theta,i})V_{OUT}(t). \end{aligned} \quad (5.44)$$

Following the same method, the changes of other muscles are

$$\Delta l_{ld,i}(t) = -2dA_{\theta v,i}V_{OUT}^2(t) - (4dA_{\theta v,i}V_{VB}(t) + dA_{\theta,i})V_{OUT}(t), \quad (5.45)$$

$$\Delta l_{ru,i}(t) = 2dA_{\theta v,i}V_{OUT}^2(t) + (4dA_{\theta v,i}V_{DB}(t) + dA_{\theta,i})V_{OUT}(t), \quad (5.46)$$

$$\Delta l_{rd,i}(t) = -2dA_{\theta v,i}V_{OUT}^2(t) - (4dA_{\theta v,i}V_{DB}(t) - dA_{\theta,i})V_{OUT}(t). \quad (5.47)$$

We can observe that the Eqs. (5.44)–(5.47) are quadratic functions. In our work, we set $V_{OUT}(t) \in [0, V_{Max}]$. If $V_{OUT}(t) = 0$, $\Delta l_{lu,i}(t)$, $\Delta l_{ld,i}(t)$, $\Delta l_{ru,i}(t)$, and $\Delta l_{rd,i}(t)$ are equal to zero. Thus the head DNN does not have the effect on the lengths of muscles. Otherwise, the the lengths of muscles will be affected when $V_{OUT}(t) > 0$. It should be noted that $\Delta l_{lu,i}(t)$, $\Delta l_{ld,i}(t)$, $\Delta l_{ru,i}(t)$, and $\Delta l_{rd,i}(t)$ are bounded since $V_{OUT} \in [0, V_{Max}]$ and $V_{VB}(t) \in [-1, 1]$.

Next, we explore the effect of V_{OUT} on θ_i and $\theta_{v,i}$. Since $V_{VB,i}(t) = M_i(t)$ in E-

q. (5.32), Eq. (5.26) can be written as

$$\theta_i(t) = A_{\theta,i} V_{VB,i}(t). \quad (5.48)$$

If influenced by $V_{OUT}(t)$,

$$\theta'_i(t) = A_{\theta,i}(V_{VB,i}(t) + V_{OUT}(t)). \quad (5.49)$$

Thus the change of $\theta_i(t)$ is

$$\begin{aligned} \Delta\theta_i(t) &= \theta'_i(t) - \theta_i(t) \\ &= A_{\theta,i} V_{OUT}(t). \end{aligned} \quad (5.50)$$

Since $V_{OUT} \in [0, V_{Max}]$, the range of $\Delta\theta_i$ is $[0, A_{\theta,i} V_{Max}]$, which is bounded.

For Eq. (5.27),

$$\begin{aligned} \theta_{v,i}(t) &= A_{\theta v,i} \cos(2\omega t + 2\phi_{start} - 2i\phi_{Lag} + \phi_{Lag}) \\ &= A_{\theta v,i} [2\cos^2(\omega t + \phi_{start} - i\phi_{Lag} + \phi_{Lag}/2) - 1] \\ &= A_{\theta v,i} [2V_{VB,i}^2(t) - 1]. \end{aligned} \quad (5.51)$$

If influenced by $V_{OUT}(t)$,

$$\theta'_{v,i}(t) = A_{\theta v,i} [2(V_{VB,i}(t) + V_{OUT}(t))^2 - 1]. \quad (5.52)$$

Thus the change of $\theta_{v,i}(t)$ is

$$\begin{aligned} \Delta\theta_{v,i}(t) &= \theta'_{v,i}(t) - \theta_{v,i}(t) \\ &= 2A_{\theta v,i} V_{OUT}^2(t) + 4A_{\theta v,i} V_{VB,i}(t) V_{OUT}(t). \end{aligned} \quad (5.53)$$

In Eq. (5.53), if $V_{OUT}(t) = 0$, $\Delta\theta_{v,i}(t) = 0$, which means the head DNN does not affect on $\Delta\theta_{v,i}(t)$. However, $V_{OUT}(t) > 0$ means $V_{OUT}(t)$ influences $\Delta\theta_{v,i}(t)$. Since Eq. (5.53) is a formal quadratic function, $\Delta\theta_{v,i}(t)$ is bounded once $V_{VB,i}(t)$ and $V_{OUT}(t)$ are bounded.

Above all, the effects of the head DNN on the lengths of muscles and joint angles have been investigated. The changes of the lengths of muscles and joint angles are bounded as long as the outputs of CPG and the head DNN are bounded.

5.4.4 Shape Determination in 3D

The sinusoid waves are generated in the head DNN and CPG that are passed through each segment with invariant frequency and phase lag. The muscles receive the outputs of DNN, and their lengths will be changed according to the DNN inputs. The changes of the lengths of muscles make the joint angles change accordingly, which yields the shape of *C. elegans* variable in 3D.

If the lengths of muscles, $l_{ru,i}(t)$, $l_{rd,i}(t)$, are known, we can calculate the $\theta_i(t)$ and $\theta_{v,i}(t)$ ($i=1, \dots, 11$) from Eqs. (5.21) and (5.23),

$$\theta_i(t) = (l_{ru,i}(t) + l_{rd,i}(t) - 2l_i)/(2d_i), \quad (5.54)$$

$$\theta_{v,i}(t) = (l_{ru,i}(t) - l_{rd,i}(t))/(2d_i). \quad (5.55)$$

Next, given the first link, $\phi_0(t) = A_0 \sin(\omega t + \phi_{start})$ and $\phi_{v,0}(t) = A_{v,0} \sin(2\omega t + 2\phi_{start})$, as shown in Fig. 5.7, ϕ_i and $\phi_{v,i}$ ($i=1, \dots, 11$) can be determined as

$$\phi_i(t) = \phi_{i-1}(t) - \theta_i(t), \quad (5.56)$$

$$\phi_{v,i}(t) = \phi_{v,(i-1)}(t) - \theta_{v,i}(t). \quad (5.57)$$

Once we know the location of first joint $(x_0(t), y_0(t), z_0(t))$, other joints ($i=1, \dots, 12$)

are determined:

$$x_i(t) = x_{i-1}(t) + l_i \cos(\phi_{i-1}(t)), \quad (5.58)$$

$$y_i(t) = y_{i-1}(t) + l_i \sin(\phi_{i-1}(t)), \quad (5.59)$$

$$z_i(t) = z_{i-1}(t) + l_i \sin(\phi_{v,(i-1)}(t)). \quad (5.60)$$

5.5 Optimization

For our model, the parameters of the head DNN and body DNN should be optimized to implement the undulatory locomotion behavior. In this section, the optimization procedures are discussed in detail.

5.5.1 Head DNN for Decision Making

The head DNN achieves the decision making function to decide whether to turn or go straightly during chemotaxis locomotion. Due to its learning ability, the head DNN can approximate any arbitrary nonlinear functions [101]. In this subsection we first construct some SLFs to approximate the chemotaxis behavior of *C. elegans*. Next, Differential Evolution (DE) specially designed for real value optimization is adopted to train the head DNN to approximate these SLFs.

Switching Logic Functions

In this work, we follow our preceding work [100] to construct the SLFs to denote the input-output mapping of the chemotaxis behavior. SLFs for food attraction and toxin avoidance are

$$D_{OUT}(t) = a_S \cdot \tanh(b_S \cdot \Delta C_{ft}(t) + c_S) + d_S, \quad (5.61)$$

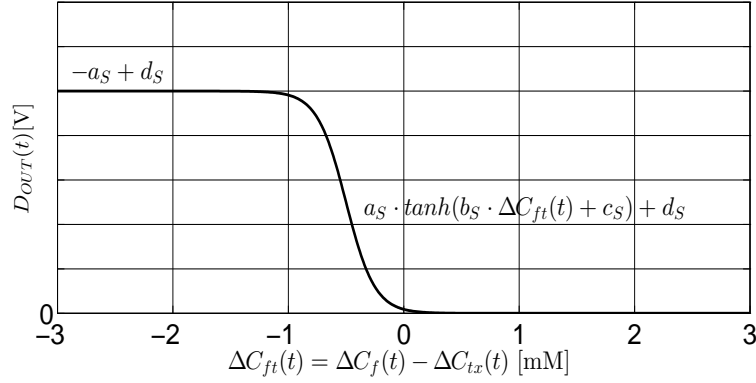


Figure 5.9: SLFs for food attraction and toxin avoidance. When $\Delta C_{ft}(t) \geq 0$, *C. elegans* goes towards the correct direction. $D_{OUT}(t) = 0$ means *C. elegans* does not need to turn its direction. When $\Delta C_{ft}(t) < 0$, *C. elegans* goes towards the wrong direction. In this case, $D_{OUT}(t)$ is greater than zero, which sends the turning signal to the body DNN.

where D_{OUT} is the desired output of V_{OUT} in the head DNN. a_S , b_S , c_S , and d_S are parameters should be determined.

$$\Delta C_{ft}(t) = \Delta C_f(t) - \Delta C_{tx}(t), \quad (5.62)$$

where $\Delta C_f(t) = C_f(t) - C_f(t-1)$ and $\Delta C_{tx}(t) = C_{tx}(t) - C_{tx}(t-1)$ are the changes of food concentration and toxin concentration at two time steps, respectively.

The shape of SLFs is shown in Fig. 5.9. When $\Delta C_{ft}(t) \geq 0$, the food concentration is higher than that at the previous time, or the toxin concentration is lower than that at the previous time. In this case, the direction is correct, and $D_{OUT}(t) = 0$ means that *C. elegans* does not need to turn. Otherwise, $\Delta C_{ft}(t) < 0$ indicates the food concentration is lower than that at the previous time, or the toxin concentration is higher than that at the previous time, which means *C. elegans* goes wrongly. In this case, $D_{OUT}(t)$ is greater than zero, which sends the turning signal to the body DNN.

Differential Evolution

There are several kinds of heuristic optimization algorithms that can be adopted to train the DNN, such as Particle Swarm Optimization (PSO), Genetic Algorithm (GA), and Differential Evolution (DE). Among them, DE is one of the powerful stochastic real-parameter optimization algorithms [107, 108]. DE operates through similar computational steps as employed by a standard evolutionary algorithm (EA). In the following, the details of five key components of DE, i.e., Chromosome with initialization, Fitness function, Mutation, Crossover, and Selection, are presented.

i) Chromosome with initialization: In the head DNN there are 86 parameters should be optimized: 6 for self-connections of neurons, 56 for the neuronal connections, 6 for τ , 6 for β , 6 for \overline{V} and 6 for b . Thus the parametric vector \mathbf{x} is encoded as a chromosome with 86 units, where each unit is called a gene. These genes are coded with real-valued $x_j (j = 1, \dots, 86)$. We define $x_{j,max}$ and $x_{j,min}$ ($j = 1, \dots, 86$) to be the upper bound and lower bound of the gene x_j . Thus at the generation $k = 0$, we initialize the j th gene of the i th chromosome as

$$x_{j,i,0} = x_{j,min} + rand_{i,j}[0, 1] \cdot (x_{j,max} - x_{j,min}), \quad (5.63)$$

where $i = 1, \dots, N$ (N is the number of chromosomes), and $rand_{i,j}[0, 1]$ is a uniformly distributed random number lying between 0 and 1.

ii) Fitness function: DE uses the fitness function to evaluate the quality of chromosome. To optimize the head DNN, in our work we construct N_t training data. The fitness function of the i th chromosome \mathbf{x}_i is

$$fit(\mathbf{x}_i) = \frac{1}{2} \sum_{k=1}^{N_t} [D_{OUT,i}(k) - V_{OUT,i}(k)]^2, \quad (5.64)$$

where $D_{OUT,i}(k)$ is calculated by Eq. (5.61), which is the desired output value of the head DNN with the k th training data as the input. $V_{OUT,i}(k)$ is the actual output of the head DNN with the k th training data as the input.

iii) Mutation: In DE, a parent chromosome from the current generation is called *target* vector, and a mutant vector obtained through the differential mutation operation is known as *donor* vector. The offspring, called *trial* vector, is formed by recombining the donor vector with the target vector. In one of the simplest forms of DE-mutation, to create the donor vector for each i th target vector from the current population, three other distinct parameter vectors, denoted as $\mathbf{x}_{r_1^i}$, $\mathbf{x}_{r_2^i}$, and $\mathbf{x}_{r_3^i}$ are sampled randomly from the current population. The indices r_1^i , r_2^i , and r_3^i , which are different from the base vector index i , are mutually exclusive integers randomly chosen from the range $[1, N]$. Now the difference of any two of the three vectors is scaled by a scalar F and the scaled difference is added to the third one. Hence we obtain the donor vector \mathbf{v}_i and the process can be expressed as for the k th generation

$$\mathbf{v}_{i,k} = \mathbf{x}_{r_1^i,k} + F \cdot (\mathbf{x}_{r_2^i,k} - \mathbf{x}_{r_3^i,k}). \quad (5.65)$$

iv) Crossover: For the crossover operation, the donor vector $\mathbf{v}_{i,k} = [v_{1,i,k}, \dots, v_{86,i,k}]$ exchanges its components with the target vector $\mathbf{x}_{i,k} = [x_{1,i,k}, \dots, x_{86,i,k}]$ to form the trail vector $\mathbf{u}_{i,k} = [u_{1,i,k}, \dots, u_{86,i,k}]$. In this work, *binomial mechanism* is adopted and the mechanism is outlined as

$$u_{j,i,k} = \begin{cases} v_{j,i,k}, & \text{if } (rand_{i,j}[0, 1] \leq C_r \text{ or } j = j_{rand}), \\ x_{j,i,k}, & \text{otherwise,} \end{cases} \quad (5.66)$$

where $j_{rand} \in [1, 86]$ is a randomly chosen index, which ensures that $\mathbf{u}_{i,k}$ gets at least one component from $\mathbf{v}_{i,k}$.

v) Selection: To determine whether the target or the trial vector survives to the next generation, selection procedure is performed.

$$\mathbf{x}_{i,k} = \begin{cases} \mathbf{u}_{i,k}, & \text{if } fit(\mathbf{u}_{i,k}) \leq fit(\mathbf{x}_{i,k}) \\ \mathbf{x}_{i,k}, & \text{otherwise.} \end{cases} \quad (5.67)$$

From Eq. (5.67), if the new trial vector yields an equal or lower fitness value, it replaces the corresponding target vector in the next generation; otherwise, the target vector is retained in the population.

With the above well defined DE components, the detailed procedure of DE is presented as follows.

Step 1): Set the control parameters of DE: scale factor $F = 0.5$, crossover rate $C_r = 0.5$, and the population size $N = 20$.

Step 2): Initialization. Set the generation number $k = 0$ and randomly initialize the 20 chromosomes with real-valued genes, by following Eq. (5.63).

Step 3): Evaluation. Each chromosome is assigned a fitness value according to Eq. (5.64). The lower the fitness value, the better the chromosome.

Step 4): Stop criteria. If the evolution generation index k reaches the maximum number 1000, or if there is no obvious decrease of the best fitness value after 50 consecutive generations, the DE stops; otherwise, go to Step 5).

Step 5): Do Mutation, Crossover, and Selection sequentially along with Eqs. (5.65) – (5.67).

Step 6): $k = k + 1$ and go to Step 3).

In our work, we use the DE toolbox for Matlab directly to optimize the head DNN.

5.5.2 Body DNN for Signal Transmission

The body DNN is responsible for the sinusoid wave transmission. After generated by CPG and the head DNN, the sinusoid wave is transmitted from the first segment to the last one for forward locomotion (from the last segment to the first one for backward locomotion). We incorporate the time delay $\Delta\tau$ to the sinusoid wave when it travels through each segment, which produces the phase lag. The body DNN in each segment owns the same structure, as shown in Fig. 5.6. There are 10 weights should be optimized in each segment.

For forward locomotion for the left side muscles, V_{VB} and V_{DB} are two sinusoid waves with opposite phases ($V_{VB} = -V_{DB}$), and it is in the same case for V_{VB} and V_{VD} [56]. Thus we let weight $w_{VD,DB} = 1$ for transmitting the signal from DB to VD . Since $V_{VB} = -V_{VD}$ and $w_{M,VB}$ is positive (excitatory synapse) and $w_{M,VD}$ is negative (inhibitory synapse), we can let $w_{M,VB} = -w_{M,VD}$ for simplification. In the same way, for the right side muscles, $w_{DD,VB} = 1$ and $w_{M,DB} = -w_{M,DD}$.

Thus for the inputs of the muscles, Eqs. (5.5) and (5.6) can be simplified as:

$$I_l(t) = 2w_{M,VB}V_{VB}(t), \quad (5.68)$$

$$I_r(t) = 2w_{M,DB}V_{DB}(t). \quad (5.69)$$

The values of $w_{M,VB}$ and $w_{M,DB}$ in our work are determined by trials, which are provided in Table 5.1. Other weights for backward locomotion are determined in the same way as for forward locomotion.

Table 5.1: Parameters settings

Parameter	Value	Description
τ_{VA}	0	Time constant in Eq. (5.3)
τ_{DA}	20	Time constant in Eq. (5.4)
w_{Mi,VB_i}	0.5	Weight from neuron VB_i to muscle M_i in Eq. (5.5)
w_{Mi,DB_i}	0.5	Weight from neuron DB_i to muscle M_i in Eq. (5.6)
w_{Mi,VA_i}	0.5	Weight from neuron VA_i to muscle M_i in Eq. (5.5)
w_{Mi,DA_i}	0.5	Weight from neuron DA_i to muscle M_i in Eq. (5.6)
w_{Mi,VD_i}	-0.5	Weight from neuron VD_i to muscle M_i in Eq. (5.5)
w_{Mi,DD_i}	-0.5	Weight from neuron DD_i to muscle M_i in Eq. (5.6)
A	0.6011	Magnitude of ϕ in Eq. (5.11)
ω	π rad/s	Speed of sinusoid wave in Eq. (5.11)
ϕ_{start}	$-\pi/8$ rad	Starting phase in Eq. (5.11)
ϕ_{Lag}	0.7854 rad	Phase lag in Eq. (5.11)
A_v	0.1777	Magnitude of ϕ_v in Eq. (5.13)
l	0.1 mm	Length of each link in Eqs. (5.21)–(5.24)
ϕ_0	$\pi/4$ rad	ϕ_0 at the beginning time in Eq. (5.56)
d	0.1 mm	Height of the muscle segment in Eqs. (5.21)–(5.24) and shown in Fig. 5.8
τ	2	Time constant of CPG in Eq. (5.2)
$A_{\theta,i}$	0.4601	Magnitude of θ in Eq. (5.26)
$A_{\theta_v,i}$	0.2513	Magnitude of θ_v in Eq. (5.27)
Δw_{MV_i}	1	Weight from $V_{VB,i}$ to the left side muscle in Eqs. (5.39) and (5.40)
Δw_{MD_i}	1	Weight from $V_{DB,i}$ to the right side muscle in Eqs. (5.41) and (5.42)
a_S	-0.285	Parameter of SLFs in Eq. (5.61)
b_S	20	Parameter of SLFs in Eq. (5.61)
c_S	3	Parameter of SLFs in Eq. (5.61)
d_S	0.285	Parameter of SLFs in Eq. (5.61)
$x_{j,max}$	20	Maximum value in Eq. (5.63)
$x_{j,min}$	-20	Minimum value in Eq. (5.63)
N	20	Population size for Eq. (5.63)
C_r	0.5	Crossover rate for Eq. (5.66)
V_{Max}	0.57	Largest value for V_{OUT} in Eq. (5.43)
N_t	200	Number of training data in Eq. (5.64)
$\Delta\tau$	0.25 s	Time delay for each segment
$w_{DD,VB}$	1	Fig. 5.6 weight from VB to DD
$w_{VD,DB}$	1	Fig. 5.6 weight from VD to DB
$w_{VD,DA}$	1	Fig. 5.6 weight from VD to DA
$w_{DD,VA}$	1	Fig. 5.6 weight from DD to VA

5.6 Testing Results

In this section, we test 1) the lengths of muscles in four quadrants, which vary periodically; 2) behaviors of forward and backward locomotions; 3) shape of *C. elegans* during locomotion in 3D; 4) finding food; 5) avoiding toxin; 6) finding food and avoiding toxin simultaneously. Parameter settings are listed in TABLE 5.1. All the tests are conducted in Matlab 2011(b) under the Windows 7 operating system.

5.6.1 Periodically Changing of Muscle Length

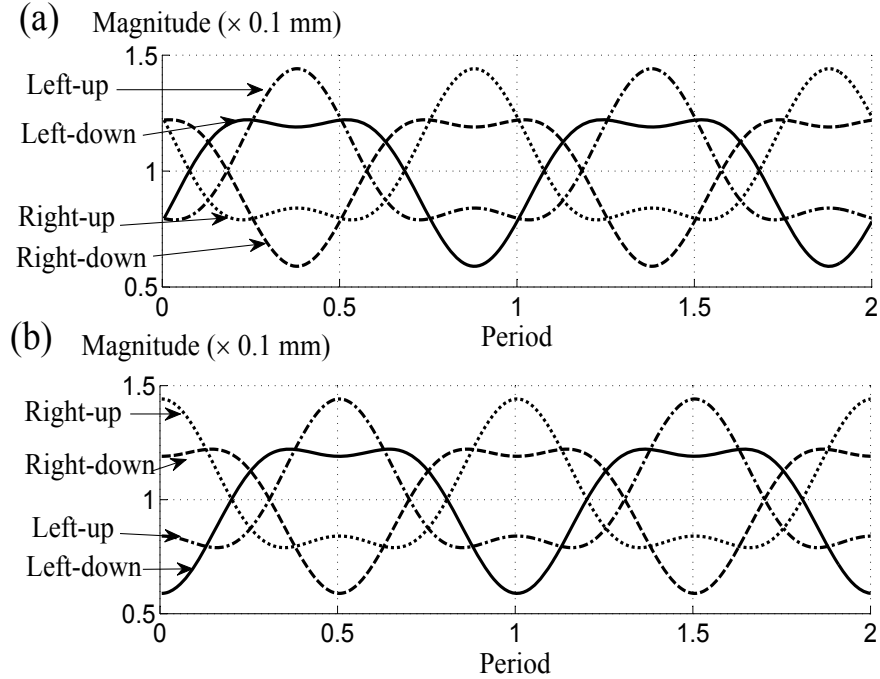


Figure 5.10: Periodically changing of the lengths of muscles. (a) The four muscles vary in the first muscle segment. (b) The four muscles vary in the second muscle segment.

The lengths of four quadrants muscles varying within 2 periods are show in Fig. 5.10. Fig. 5.10 (a) shows the changes of four muscles in the first muscle segment, which control the joint 1. Fig. 5.10 (b) shows the changes of four muscles in the second muscle segment, which control the joint 2. At $t = 0$, the configuration of *C. elegans* is shown in Fig. 5.7. For joint 1 at $t = 0$, the lengths of right-up and right-down muscles are identical, and

it is the same as the lengths of left-up and left-down muscles, as shown in Fig. 5.10 (a). At this time, the muscles on the right side are longer than the muscles on the left side. This makes the link 1 and link 2 have an angle $\theta_1 \neq 0$ on the x-y plane but $\theta_{v,1} = 0$ on the x-z plane. For the joint 2, which is bent heavily on the x-y plane at time $t = 0$, the right side muscles are longer than the left side muscles that produces the biggest angle of θ_2 on the x-y plane, as shown in Fig. 5.10 (b). On both left and right sides, the upper muscles are longer than the down muscles. Thus $\theta_{v,2} > 0$ on the x-z plane, and the joint 2 lifts up from the ground.

The muscles change periodically with the same period of CPG, and the phase lag between two consecutive links is one forth of a period. For instance, the changes of the lengths of muscles for segment 2 are one forth period delayed after segment 1, as shown in Figs. 5.10 (a) and (b).

5.6.2 Forward and Backward Locomotion

The 3D forward locomotion behavior of *C. elegans* is shown in Fig. 5.11. The period of one sinusoid wave is 2s. The speed is 0.4 mm/s and the start point is (-0.5, 0, 0.02). Figs. 5.11 (a), (b), and (c) show the appearances of *C. elegans* at time $t=0$ s, $t=1$ s, and $t=2$ s, respectively. These plots verify that our model can well perform the forward locomotion behaviors in 3D.

For the backward locomotion, the signal is transmitted from tail to head. We plot the outlines during backward locomotion at time $t=0$ s, $t=1$ s, and $t=2$ s, as shown in Figs. 5.12 (a), (b), and (c), respectively. From Fig. 5.12, we can observe that the proposed model also well performs the backward locomotion in 3D.

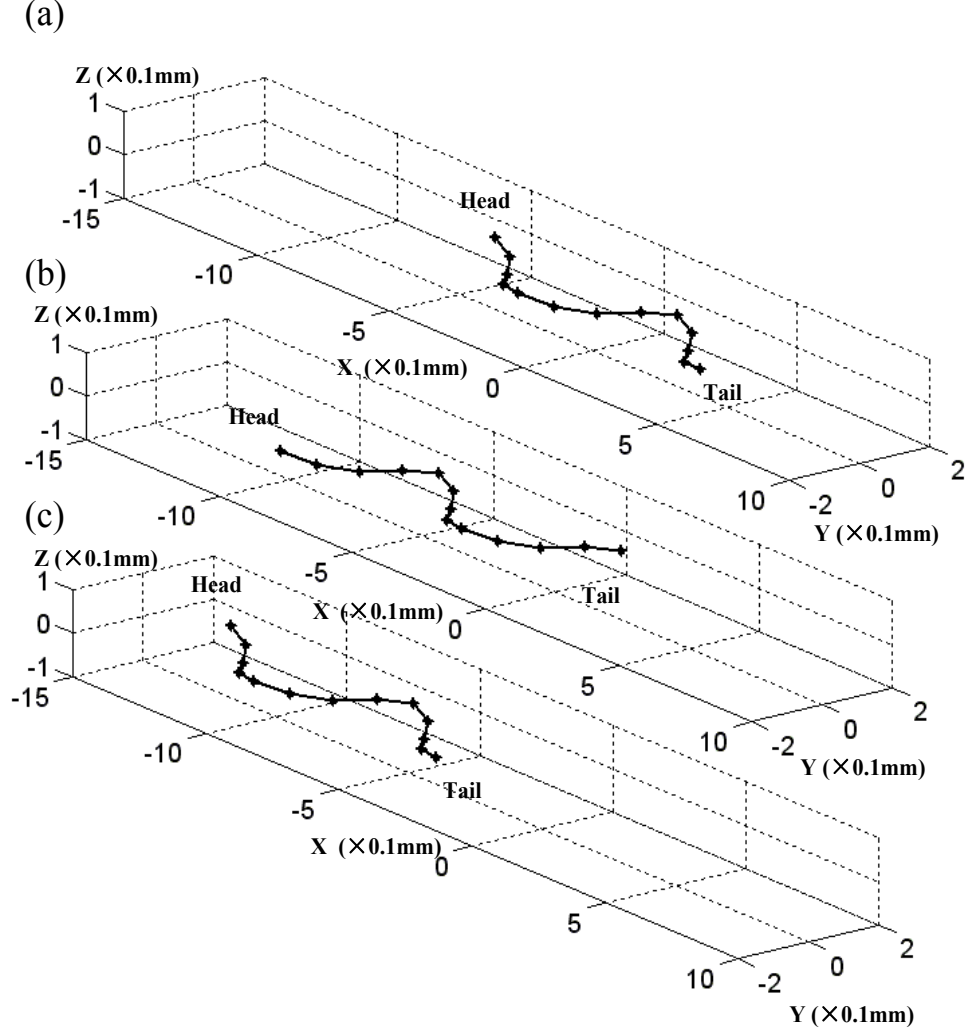


Figure 5.11: The 3D forward locomotion behavior of *C. elegans*. (a) The shape of *C. elegans* when it begins to move at the point $(-0.5, 0, 0.02)$ at $t = 0$ s. (b) The shape of *C. elegans* at $t = 1$ s. (c) The shape of *C. elegans* at $t = 2$ s. During one period (2 s), it is obviously that some body parts lift up during forward locomotion.

5.6.3 The Shape During Locomotion

We capture the images of *C. elegans* model during locomotion, as shown in Fig. 5.13. From Fig. 5.13 (a), we can observe that *C. elegans* lifts up parts of its body. Joints 2, 6, and 10 are most bent on the x-y plane and lift up highest on the x-z plane. Joints 0, 4, 8, and 12 touch the ground. Fig. 5.13 (b) is the projection of Fig. 5.13 (a) on the x-y plane. Here we can see that it shapes as a sinusoid wave on the x-y plane as the real

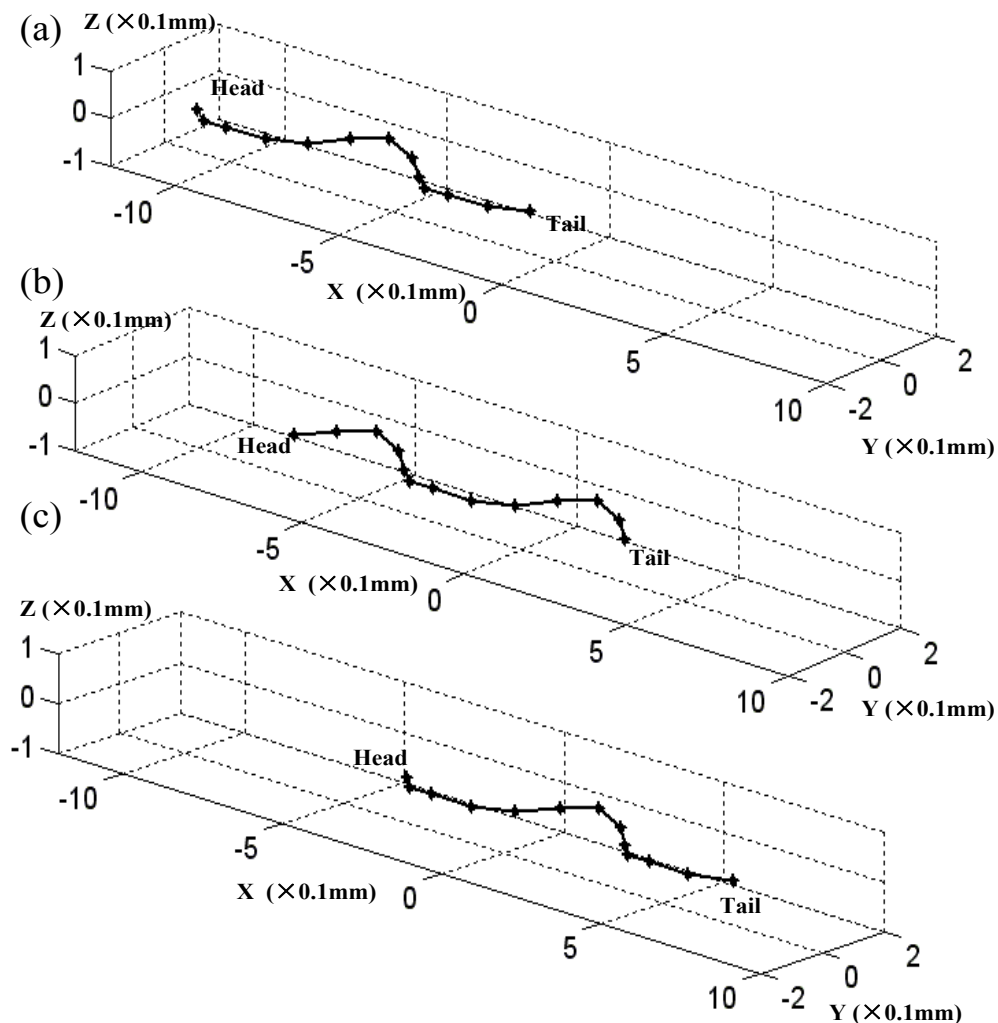


Figure 5.12: The 3D backward locomotion behavior of *C. elegans*. (a) The shape of *C.elegans* at the beginning time $t = 0$ s. (b) The shape of *C.elegans* at $t = 1$ s. (c) The shape of *C. elegans* at $t = 2$ s. From these figures, it is obviously that *C. elegans* lifts up parts of its body during backward locomotion.

worm does. Fig. 5.13 (c) is the projection of Fig. 5.13 (a) on to the x-z plane. Fig. 5.13 (c) verifies that the testing result of our model is in accordance with our theory that the bent parts on the x-y plane lift up on the x-z plane.

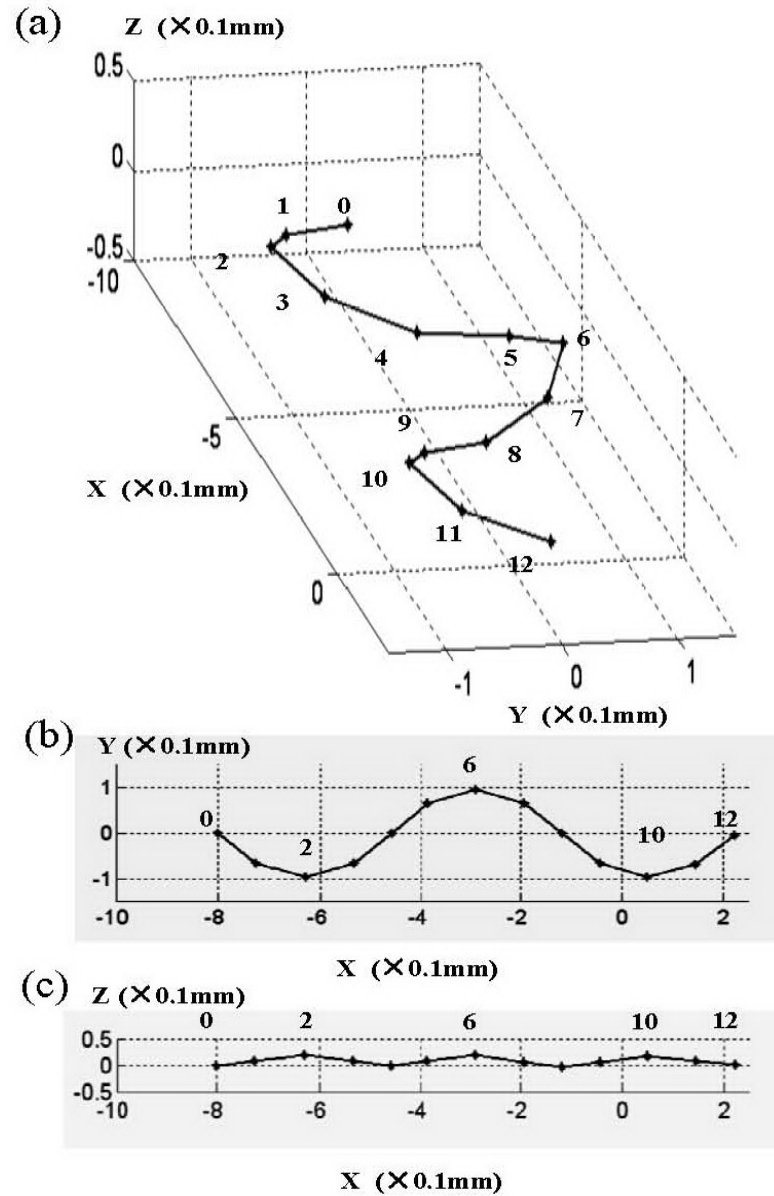


Figure 5.13: The shape of *C. elegans* during locomotion. (a) The outline of *C. elegans* at a random time. Joints 2, 6, and 10 are bent mostly and lifted up highest. Joints 0, 4, 8, and 12 touch the ground. (b) The projection of (a) on the $x-y$ plane. It appears as a formal sinusoid wave. (c) The projection of (a) on the $x-z$ plane. Some body parts of *C. elegans* lift up to the ground.

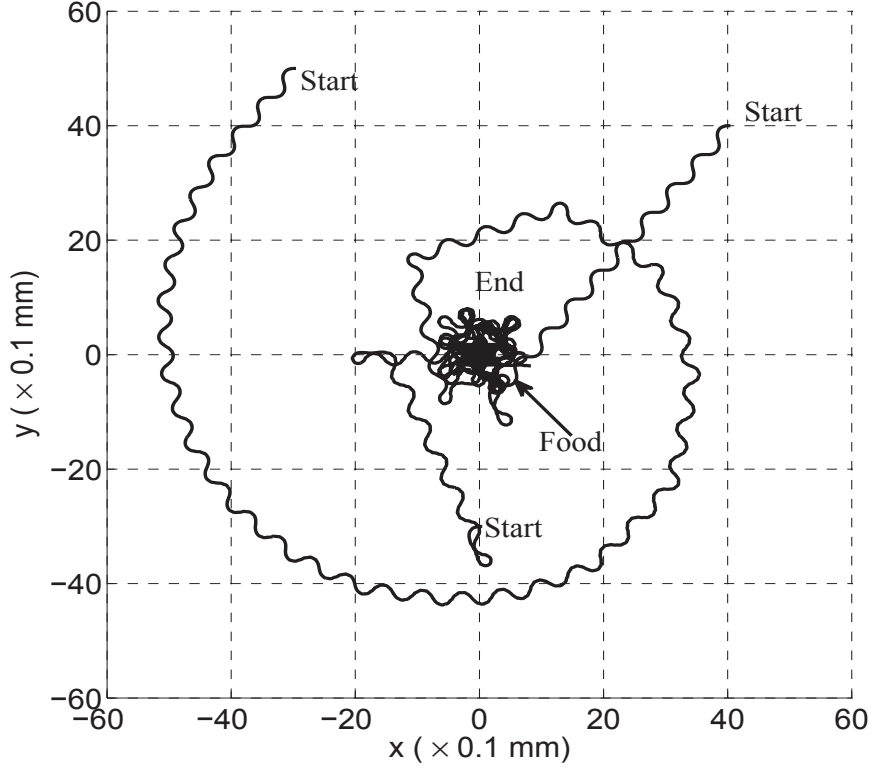


Figure 5.14: Testing results for food attraction. One food source is located at $(0, 0)$ with Gaussian distribution. *C. elegans* starts at three different locations $(-30, 30)$, $(0, -30)$, and $(40, 40)$, respectively. It moves towards the food source and finally moves around it.

5.6.4 Finding Food

In order to test whether our model can perform the task of finding food, we put the *C. elegans* into the scenario in which a food source is located at $(0, 0)$ with Gaussian distribution. By overlooking, the trajectories are shown in Fig. 5.14. *C. elegans* starts at three different locations $(-30, 30)$, $(0, -30)$, and $(40, 40)$, respectively. It moves towards the food source and finally moves around it. From the testing result, we can observe that *C. elegans* has successfully achieved the task of finding food. The movement similarity between our model and the experiment results is discussed in Section 5.7.

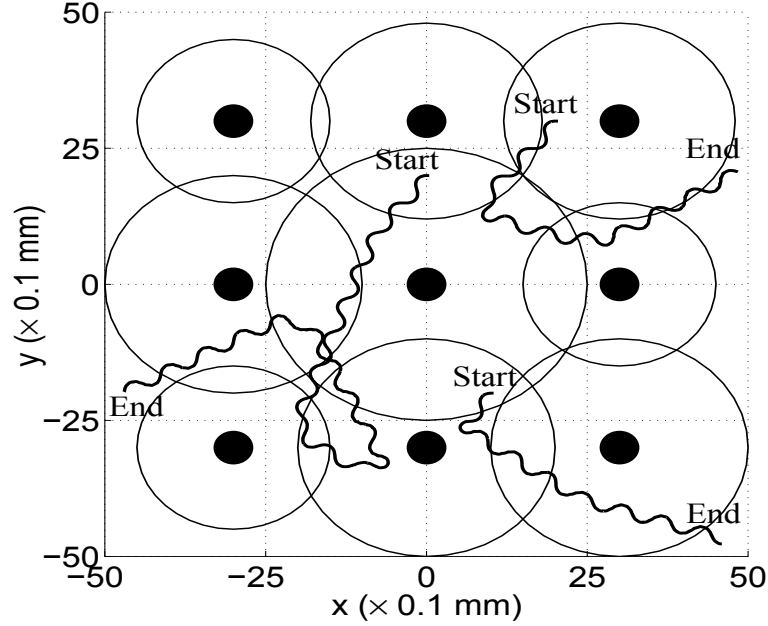


Figure 5.15: Testing results for toxin avoidance. Nine toxin resources are distributed nonuniformly as a 3×3 grid. The locomotion model starts at three different positions $(0, 20)$, $(20, 30)$, and $(10, -20)$, respectively. It successfully finds the zero toxin concentration places to settle down.

5.6.5 Avoiding Toxin

To test our model for toxin avoidance, nine toxin sources are distributed nonuniformly as a 3×3 grid, as shown in Fig. 5.15. In this figure, each dot indicates a toxin source and each circle line denotes the boundary of its corresponding toxin distribution. The locomotion model starts at three different positions $(0, 20)$, $(20, 30)$, and $(10, -20)$, respectively. It escapes the toxin sources successfully by a series of turns and arrives at the places without toxin concentration. From the trajectories in Fig. 5.15, it is obvious that the model can escape the toxin area where the toxin distributions are not uniform.

5.6.6 Finding Food and Avoiding Toxin Simultaneously

To test whether our model can perform the task of finding food and avoiding toxin simultaneously, we construct the scenario with nine sources distributed as a 3×3 grid. As shown in Fig. 5.16 (a), except the asterisk located at $(-30, 0)$ is the food source,

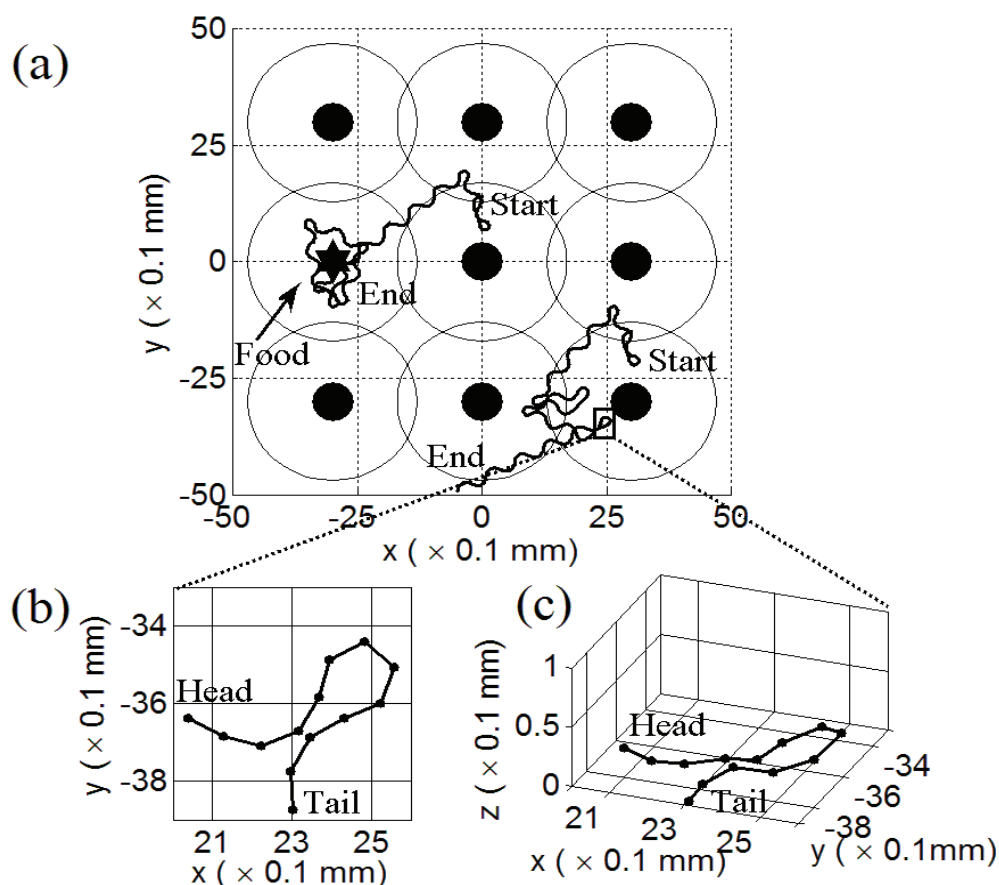


Figure 5.16: Testing results for finding food and avoiding toxin simultaneously. (a) Nine sources are distributed as a 3×3 grid. One food source (asterisk) is located at $(-30, 0)$ and other dots denote the toxin sources. *C. elegans* starts at two different locations $(0, 15)$ and $(30, -10)$, respectively. It successfully escapes from the toxin sources. Furthermore, once *C. elegans* smells the food concentration (starting from $(0, 15)$), it navigates itself towards the food source and finally moves around it. (b) The zoomed image of the rectangular area in (a). It shows the Ω turn in 2D. (c) The zoomed image of the rectangular area in (a). It shows the Ω turn in 3D. It can be observed that some parts of the body lift above the ground.

other eight dots denote the toxin sources. The circular lines are the boundaries of food and toxin concentrations. In our test, *C. elegans* starts at two different locations $(0, 15)$ and $(30, -10)$, respectively. From the trajectory starting from $(30, -10)$, it is obvious that *C. elegans* escapes from the toxin by passing the boundary areas where the toxin gradient and magnitude are relatively low. Finally *C. elegans* successfully escapes from the toxin and settles down at the places where no toxin concentration exists. When starting from $(0, 15)$, *C. elegans* escapes from the toxin sources first. Once it smells the food concentration, it moves towards the food source and finally surrounds it.

The zoomed image of the rectangular area in Fig. 5.16 (a) is shown as Fig. 5.16 (b) and Fig. 5.16 (c) in 2D and 3D, respectively. It is obviously that our model well mimics the Ω turn, as shown in Fig. 5.16 (b). Furthermore, the 3D body shape of omega turn is shown in Fig. 5.16 (c). From this figure we can observe that some parts of body lift above the ground, which is analogous to the real *C. elegans*, as shown in Fig. 5.1.

5.7 Comparative Analysis

5.7.1 Validation by Analyzing the Video of the Real Worm

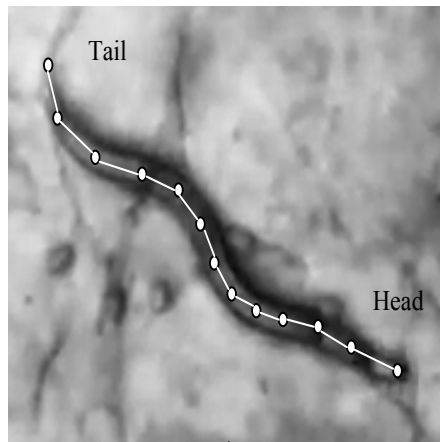


Figure 5.17: Image of actual *C. elegans* body are divided into 12 links in computer software to analyze.

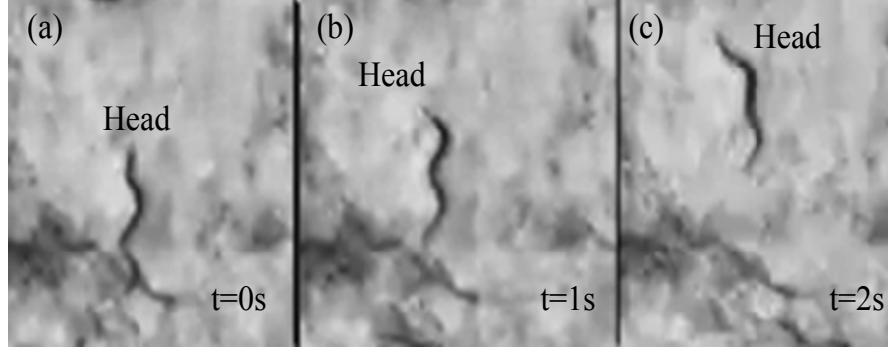


Figure 5.18: Images of *C. elegans* during fast forward locomotion at time $t=0, 1, 2$ s. The body shape is 1.5 periods of sinusoid wave length, and one periods time is 2 s

The video of actual *C. elegans* is provided by Yong Loo Lin School of Medicine, National University of Singapore, which can be accessed at website [109]. *C. elegans* is enlarged 50 times in the video. A software, Nandub, is used to transfer the video to image files in JPG format with 30 frames per second. These images are imported into the image processing software, Scion Image, for analyzing the velocity, joint angle, and body shape.

The velocity of the head is computed by using the Scion Image. The velocity depends on the worm size and the undulatory frequency. From our analysis, the velocity of actual worm is between 0.2 mm/s and 0.8 mm/s, which is close to [40]. For the joint angle variations, we divided the *C. elegans* into 12 segments, as shown in Fig. 5.17, and use the tool of the Scion Image to calculate the angles. The absolute value of angles varies from about 0 rad to 0.44 rad.

Finally, we select a *C. elegans* in high-speed forward locomotion, as shown in Fig. 5.18. From Figs. 5.18 (a), (b), and (c), we can observe that *C. elegans* shapes its body to be 1.5 periods of sinusoid wave length, and one period time is 2s. These biological results verify that the performance of the locomotion model does not lose the characters of real *C. elegans*, such as the body shape and the undulatory period.

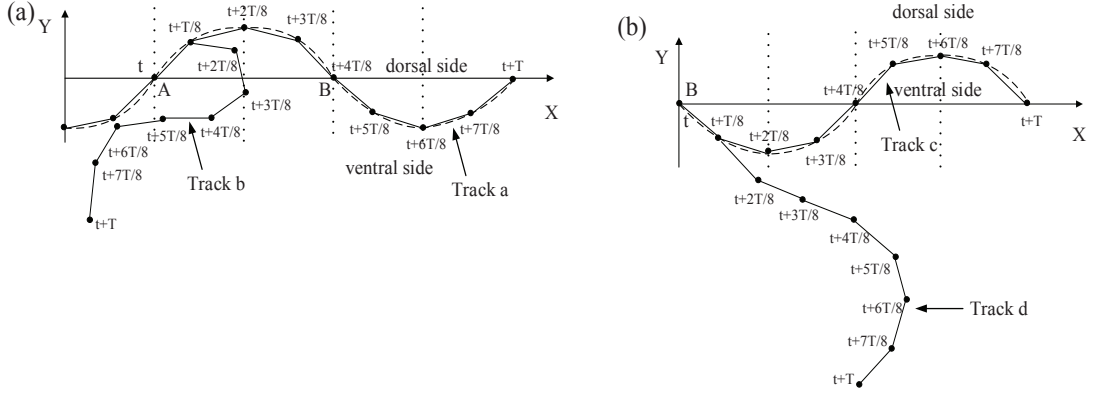


Figure 5.19: Analysis of the turning behaviors. (a) The decision making of the model happens at Point A and B. Track **a** is the trajectory of straightly forward locomotion. Track **b** is the trajectory of turning starting at Point A. The turning degree is decided by V_{OUT} . If V_{OUT} is large enough, Ω turn happens, otherwise the slightly turning happens. (b) Track **c** is the trajectory of straightly forward locomotion. Track **d** is the trajectory of turning starting at Point B. In this case, Ω turn cannot happen.

5.7.2 Turning Behaviors Analysis

From the trajectories in Fig. 5.14, Fig. 5.15, and Fig. 5.16 (a), there are two types of turning behaviors can be observed: the slight turn and the sharp turn. The turning behaviors are generated by the turning signal (V_{OUT}) of the head DNN. In this subsection, we analysis how V_{OUT} produces the turning behaviors.

For forward locomotion, the undulatory wave, which is the combination of the outputs of CPG and V_{OUT} , is transmitted from the head to tail. As shown in Fig. 5.19, tracks **a** and **c** show the trajectories of joint 1 during locomotion without turning. According to the turning mechanism, the locomotion model makes the turning decision when joint 1 at the points A and B. If it turns at point A, the turning trajectory is shown as track **b** in Fig. 5.19 (a). If it turns at point B, the turning trajectory is shown as track **d** in Fig. 5.19 (b).

If the model needs turning at point A, as shown in Fig. 5.19 (a), V_{OUT} is a constant from t to $t + T/2$. According to Eq. (5.50), $V_{OUT} \neq 0$ yields more turning towards the

ventral side. For example, in track **b** the model should turn more $\Delta\theta$ than its original direction at each time step $T/8$. Thus, from point A to point B, the model turns $4\Delta\theta$ more than its original direction. If it still needs turning at the point B, following the same way, within the next $T/2$, it also turns $4\Delta\theta$ more than its original direction. Above all, for a whole period T , the maximum direction change is $8\Delta\theta = 8A_\theta V_{OUT}$ according to Eq. (5.50). By substituting the values of A_θ and V_{OUT} in Table. 5.1, the maximum direction change of the model is 170° within one period T .

The shapes of the model are different when it turns at point A and point B. When turning at point A, the ventral side muscle will contract more severely than its original contraction since $V_{OUT} \neq 0$. If V_{OUT} is small, the turning angle is small, which yields the slight turn. If V_{OUT} is large, the great turning angle can yield the Ω turn, as shown in Fig. 5.19 (a). When turning at point B, the model cannot produce Ω turn. This is because when turning at time t and point B, as shown in Fig. 5.19 (b), the ventral side muscle should relax, and the dorsal side muscle should contract. The turning signal V_{OUT} can reduce the relaxing of the ventral side muscle, and decrease the contraction of the dorsal side muscle. Thus, the slight turn towards the ventral side happens. However, V_{OUT} is not large enough to make the contraction of the dorsal side muscle to be highly relaxed. Thus, Ω turn towards the ventral side could not happen in this case.

5.7.3 Trajectory Analysis

In this subsection, we analyze the trajectories of the locomotion model by following the method provided in [110]. As said in [110], all the undulatory locomotion trajectories

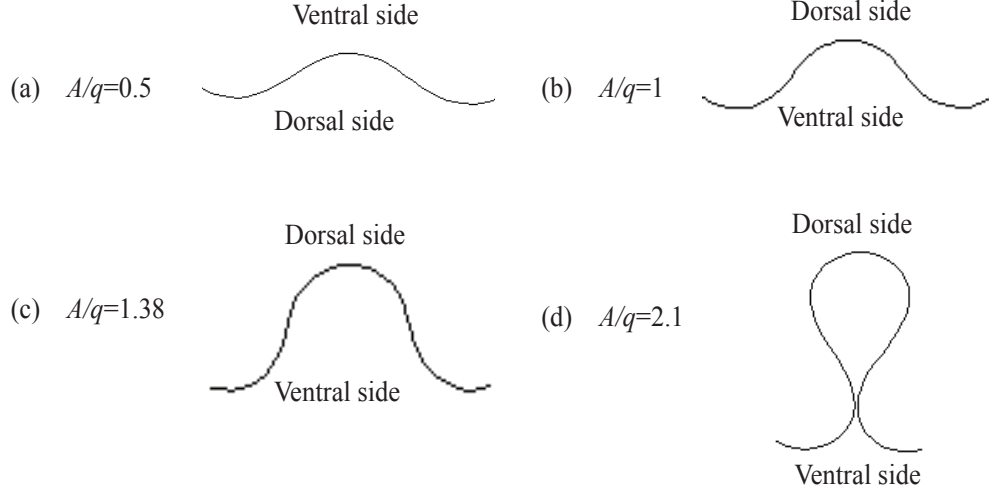


Figure 5.20: Trajectory analysis. (a) Trajectory of turning with small magnitude. (b) Trajectory of the straight forward locomotion. (c) Trajectory of the slight turn. (d) Trajectory of the Ω turn.

of *C. elegans* can be approximated by a set of coupled second-order differential equation,

$$\frac{d^2x}{ds^2} = -\kappa \frac{dy}{ds}, \quad (5.70)$$

$$\frac{d^2y}{ds^2} = \kappa \frac{dx}{ds}, \quad (5.71)$$

with the initial conditions

$$x(s=0) = x_0, \quad \left. \frac{dx(s)}{ds} \right|_{s=0} = t_{x_0}, \quad (5.72)$$

$$y(s=0) = y_0, \quad \left. \frac{dy(s)}{ds} \right|_{s=0} = t_{y_0}, \quad (5.73)$$

where (x_0, y_0) is the position of the worm tail at the beginning of the trajectory and the tangent unit vector, $\hat{t}_0 = (t_{x_0}, t_{y_0})$, describes the orientation of the trajectory at $t = 0$.

In Eqs. (5.70) and (5.71),

$$\kappa(s) = A_s \sin(q_s s + \phi_s), \quad (5.74)$$

where A_s is the magnitude, q_s is the wavevector, and ϕ_s is the phase of the wave.

The different values of A_s/q_s yield different shapes of trajectories. The range of A_s/q_s is between 0.6 and 3.0 for [110], and between 0.5 and 2.1 for our case. $A/q = 0.5$, as shown in Fig. 5.20 (a), indicates the trajectory of turning at Point B in Fig. 5.19 (b). In this case, V_{OUT} , which inhibits the contraction of dorsal side muscles, yields the small magnitude of curve towards the ventral side. $A/q = 1$, as shown in Fig. 5.20 (b), indicates the trajectory of the straight forward locomotion. Fig. 5.20 (c) with $A/q = 1.38$ and Fig. 5.20 (d) with $A/q = 2.1$ show the trajectories of the turning at Point A in Fig. 5.19 (a). In the two cases, V_{OUT} enlarges the contraction of ventral side muscles, which yields the large magnitude of curve towards the dorsal side. $A/q = 1.38$ indicates the slight turning, and $A/q = 2.1$ indicates the Ω turning.

From the analysis we can note that our results are in accord with the results in [110], which could verify the validity of the locomotion model in straight forward locomotion, slight turn, and Ω turn.

5.7.4 Head DNN Analysis

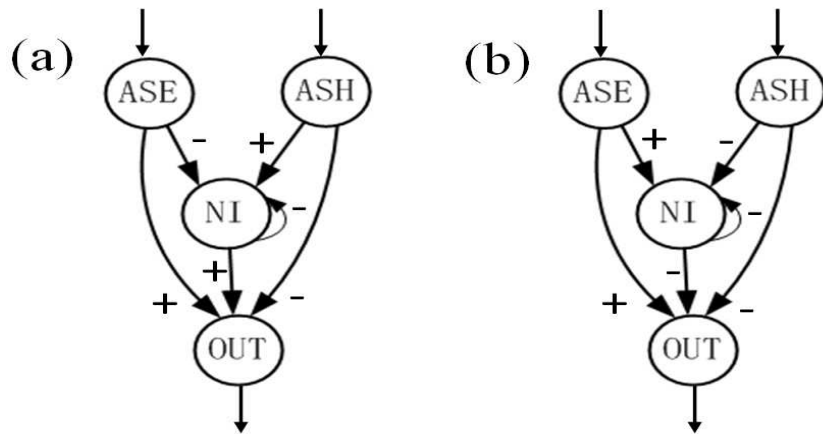


Figure 5.21: Two patterns in the optimized networks. For both patterns, direct connections from the input neurons to the output neuron exist, and the self-connection exists for the interneuron. The difference between them is the signs of the weights for interneuron.

In our work, we have optimized 30 head DNNs using DE. By following the method of

[25], we first find out the “all-off” neurons that are inactive and the “all-on” neurons that are saturated active. Next, we remove these “all-off” neurons from the networks and move these “all-on” neurons to their downstream neurons as bias. In this way, these networks are simplified to be structured as four neurons (two sensory neurons, one interneuron, and one output neuron). Two patterns are found among these resultant networks, as shown in Fig. 5.21 (a) and (b). The direct connections from the input neurons (ASE and ASH) to the output neuron (OUT) are preserved in both patterns, and the self-connection exists for the interneuron (NI). The difference between two patterns is the signs of the weights for the interneuron, which are opposite. Biologically, the positive and negative neuronal connections are existing in the brain of animals [111].

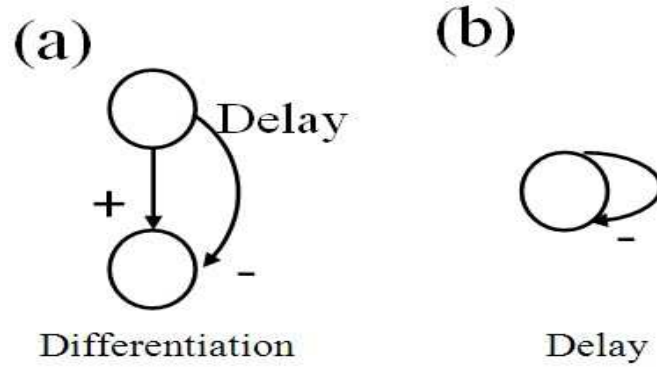


Figure 5.22: Two features are extracted among the simplified networks. The feature in (a) functions as a differentiator, and the feature in (b) functions as the time delay.

Furthermore, as shown in Figs. 5.22 (a) and (b), two features are extracted among the simplified networks, which are the same as the results of [47] and [25]. The feature in Fig. 5.22 (a) functions as a differentiator, and the self-feedback in Fig. 5.22 (b) functions as a time delay. For example, as shown in Fig. 5.21 (b), the signal coming from the sensory neuron ASE goes straightly to the output neuron where it is deducted by the delayed signal of ASE that passes through the interneuron NI. In this way, the differentiation information of $dC(t)/dt$ can be obtained.

5.8 Conclusion

In this chapter we investigate the undulatory locomotion of *C. elegans* and a 3D locomotion model is developed to perform the forward and backward locomotion, as well as the chemotaxis behavior of finding food and avoiding toxin. First, according to the biological muscle structure we use 12 multi-joint rigid links to represent the body. Each joint stands for the center of its corresponding muscle segment, and is controlled by four quadrants muscles. Second, the nervous system of *C. elegans* is depicted as a DNN, which is divided into three parts: the head DNN, CPG, and the body DNN. The head DNN produces the turning signal, and CPG generates the sinusoid wave. The function of body DNN is to transmit the sinusoid wave throughout the body as well as to muscles. Third, muscle models are constructed, in which the lengths of muscles vary according to the outputs of DNN. Fourth, the joint angles on the x-y plane and the x-z plane are controlled by the lengths of muscles, and the relation between them are determined. Furthermore, the relation between the lengths of muscles and outputs of DNN is known, so we can use DNN to control the joint angles. Fifth, the decision making of the chemotaxis behavior is approximated by SLFs, which are learned by the head DNN using DE. In the testing part, the proposed model performs well for both forward and backward movements in 3D. Furthermore, it successfully achieves the chemotaxis behaviors of finding food and avoiding toxin by performing a series of slight turns and Ω turns. At last, the quantitative analyses are provided to verify the effectiveness of our model by comparing with the experiment data of real *C. elegans*. In next chapter, the biological wire diagram of *C. elegans* will be investigated directly to perform these undulatory locomotion behaviors.

Chapter 6

Modeling the Undulatory Locomotion Behavior of *C. elegans* Based on the Biological Wire Diagram

In Chapter 5, we have investigated the 3D undulatory behavior of *C. elegans* based on the artificial DNN. In this chapter, instead of using the artificial DNN, we will explore the undulatory locomotion behavior directly based on the biological wire diagram. As an extended work of Chapter 5, our objective is to model the chemotaxis behavior based on the undulatory locomotion. There are two issues that are addressed in this chapter: (1) decision making for chemotaxis and (2) coordination of motor neurons and muscles for undulatory locomotion. Our model is tested in different simulated environments for the chemotaxis behavior. Furthermore, the quantitative analysis is conducted by comparing with the experimental result and other related work. At last, a worm-like robot has been constructed to perform the undulatory behavior based on the theoretical results.

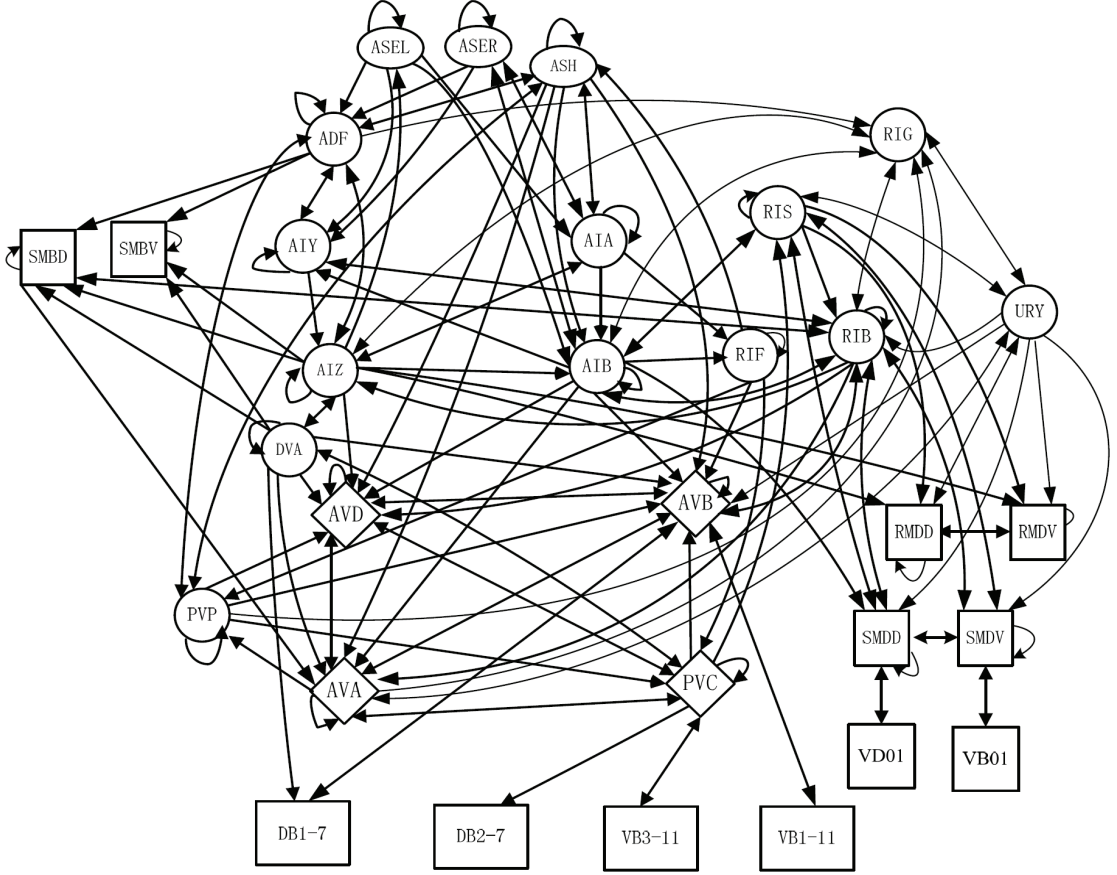


Figure 6.1: Head wire diagram. Three ellipses represent the sensory neurons. Circles represent the interneurons. Diamonds represent the command neurons. Rectangles represent the motor neurons.

6.1 Biological Model for Undulatory Locomotion

6.1.1 Head Wire Diagram

By following the same method in Section 3.1.1, we extract the neural wire diagram of *C. elegans* for undulatory locomotion, as shown in Fig. 6.1. Three sensory neurons (ellipses), ASEL, ASER, and ASH, function as input neurons. AVD, AVB, AVA, and PVC are four command neurons (diamonds). Twelve circles indicate the interneurons and the rectangles represent the motor neurons. The prominent difference between Fig. 6.1 and other biological wire diagrams in Chapter 3 and Chapter 4 involves two aspects. One aspect is that six motor neurons, RMD(D/V), SMB(D/V), and SMD(D/V), are involved

in Fig. 6.1. These neurons control the head and neck muscles and play the critical role in undulatory locomotion [18]. The second aspect is that two motor neurons DB and VB are expanded to be VB_i ($i = 1 \dots 11$) and DB_i ($i = 1 \dots 7$) in Fig. 6.1.

The function of the head wire diagram is to achieve the decision making function for chemotaxis. Furthermore, it also controls the oscillation of muscles in the head and neck. These contents will be discussed in Section 6.2.

6.1.2 Motor Neurons and Muscles

By using the data provided in [1, 83, 112], we extract the wire diagram of motor neurons and muscles for forward locomotion, as shown in Fig. 6.2. Command neuron AVB has the connections to VB_i ($i = 1 \dots 11$) and DB_i ($i = 1 \dots 7$), as well as PVC connects VB_i ($i = 3 \dots 11$) and DB_i ($i = 2 \dots 7$). Interneuron DVA has the connections to DB_i ($i = 1 \dots 7$) but does not have the connection to the ventral side motor neurons VB_i ($i = 1 \dots 11$). Six motor neurons, SMD(D/V), SMB(D/V) and SMD(D/V) that control the head and neck muscles do not connect the command neurons AVB and PVC, but they receive the synaptic inputs from head interneurons, as shown in Fig. 6.1. Each motor neuron (DB, DD, VB, VD) has the connection to muscles. VB and DB that are controlled by command neurons AVB and PVC activate the muscles, whereas VD and DD that only receive the signals from VB and DB inhibit the muscles. It is interesting that motor neurons in the same group are not fully connected. For instance, VB_7 and VB_8 are not connected between segments 8 and 9, where the vulva exists anatomically. This disconnection supports the hypothesis that the motor neurons alone are not the primary organs to propagate the undulatory wave along the body [14, 103]. The method to generate and propagate the undulatory wave by muscles and motor neurons will be discussed in Section 6.2.

6.2 Undulatory Locomotion Modeling

6.2.1 Sensory Neurons

The most recent research results in [54, 56, 57] indicate that there exists two types of sensory neurons for the chemotaxis: *on-cell* and *off-cell*. *On-cell* is the sensory neuron that only activates when outside stimulus increases, whereas *off-cell* only activates when outside stimulus decreases. It is well known that ASEL is the *on-cell* and ASER is the *off-cell* [54].

The mechanisms of “*on-cell*” and “*off-cell*” achieve the decision making function for chemotaxis. The simplest case is that the going or turning behaviors, in which the presence or absence of the behavior under investigation is dictated by the presence or absence of the stimulus and the internal state of the animal. In our work, we adopt the sensory neuron model from [56].

$$V_{\text{on}} = \sigma_s(D(t)), \quad (6.1)$$

$$V_{\text{off}} = \sigma_s(-D(t)), \quad (6.2)$$

where V_{on} is the voltage of *on-cell* and V_{off} is the voltage of the *off-cell*. $D(t) = C_N(t) - C_M(t)$, where $C_N(t)$ is the average concentration over the contiguous interval $[t - N, t]$, and $C_M(t)$ is the average concentration over the interval $[t - (N + M), t - N]$. N and M are the durations of the two intervals. $\sigma_s(\cdot)$ is the activation function

$$\sigma_s(x) = \frac{A}{1 + \exp(-k_s(x + x_0))}, \quad (6.3)$$

where A is the amplitude, and k_s controls the steepness, and the threshold x_0 is a constant. From Eqs. (6.1) and (6.2) we can observe that the logics of *on-cell* and *off-cell*

are opposite.

Except the sensory neurons ASEL and ASER that are responsible for the attractant (food), another sensory neuron ASH is responsible for the repellent source (toxin). Once *C. elegans* smells the repellent concentration, ASH will be activated to produce the turning behavior such as slight turn or Ω turn. The activation function for ASH is

$$V_{ASH} = \sigma_{ASH}(C_{tx}(t)), \quad (6.4)$$

where $C_{tx}(t)$ is the toxin concentration, and $\sigma_{ASH}(\cdot)$ is the activation function having the same form and parameter setting as Eq. (6.3).

6.2.2 CPG

The mechanism to generate the undulatory wave is another important aspect for the locomotion of *C. elegans*. The basic method to generate the undulatory locomotion pattern is to use a CPG. The research work [103] mentioned that there should be a pattern generator near the head to generate the rhythmic bending of the most anterior segment. Another research work in [61] found that there existed two potential CPGs in the head: AIZ-AIA-AWA-AIZ and RIB-RIG-URY-RIB. Biologically, AIZ, AIA, and AWA have the specific functions that are not suitable for the CPG [87, 113, 114, 115, 116]. Thus in our model we adopt the last choice by using neurons RIB, RIG, and URY to serve as the CPG.

Following Eq. (5.2), the CPG for the biological undulatory locomotion model is

$$\tau_b \dot{V}_b = A_b V_b, \quad (6.5)$$

where

$$\tau_b = \begin{bmatrix} \tau_{RIG} & 0 & 0 \\ 0 & \tau_{RIB} & 0 \\ 0 & 0 & \tau_{URY} \end{bmatrix}, \quad (6.6)$$

$$A_b = \begin{bmatrix} 0 & -2\pi & 0 \\ 2\pi & 0 & 0 \\ 1 & 0 & -1 \end{bmatrix}, \quad (6.7)$$

$$V_b = \begin{bmatrix} V_{RIG} \\ V_{RIB} \\ V_{URY} \end{bmatrix}. \quad (6.8)$$

By choosing the initial values $V_{RIG}(0) = 1$, $V_{RIB}(0) = 0$, and $\tau_{RIG} = \tau_{RIB}$, the inner periodic signal generators V_{RIG} and V_{RIB} can produce co-sinusoidal signals, $V_{RIG} = \cos(\omega t)$ and $V_{RIB} = \sin(\omega t)$, where $\omega = 2\pi/\tau_{RIG}$. V_{URY} can generate either $\cos(\omega t)$ or $\sin(\omega t)$ wave by adjusting τ_{URY} .

6.2.3 Motor Neuron

The connection of motor neurons is shown in Fig. 6.2. B-type neurons are activation neurons, whereas D-type neurons are inhibition neurons. According to [50], these motor neurons are not spiking neurons. Furthermore, they can receive the feedback of body shape to generate the undulatory wave and propel it forward or backward [14, 32, 103]. This feedback mechanism is called proprioception [103], and the proprioceptive coupling between neurons and muscles are transduced by B-type motor neurons. As suggested in [103], the bending of anterior segment directly determines the activity of posterior B-type motor neurons, and the potential of B-type neuron positively determines the activities of its connected muscles. Thus, it can be concluded that the bending of anterior body regions dictates the bending of posterior body regions during forward movement. B-type

neurons are modeled by following [32]

$$C_B \frac{dV_B}{dt} = -G_B(V_B - E_{rev}) - I_{shape} + I_{AVB}, \quad (6.9)$$

where C_B is the cell's membrane capacitance; E_{rev} is the cell's effective reversal potential; G_B is the total effective membrane conductance. For motor neuron i , $I_{shape,i} = \sum_{j=1}^n w_{ij}^{Pro} \sigma_j^{pro}(l_j)$ is the proprioceptive feedback from the shape of its connected muscles. w_{ij}^{Pro} is the proprioception weight from muscle j to motor neuron i . l_j is the length of muscle in segment j . $\sigma_j^{pro}(\cdot)$ is a sigmoid function

$$\sigma^{pro}(l) = \frac{A_p}{1 + \exp(-k_p(l - l_0))} + b_p, \quad (6.10)$$

where the steepness parameter k_p and the threshold l_0 are two constants. In Eq. (6.9), $I_{AVB} = G_{AVB}(V_{AVB} - V_B)$ is the command neuron input. AVB in our model functions as switching on or off the motor neurons for forward locomotion.

For D-type motor neurons, we use the model in [32] directly.

$$C_D \frac{dV_D}{dt} = -G_D(V_D - E_{rev}) - I_{syn}, \quad (6.11)$$

where $I_{syn} = \sigma_D(V_{pre})$ is the synaptic input from B-type neurons. V_{pre} is the summation of the presynaptic voltages and $\sigma_D(V_{pre})$ is the sigmoid function that has the same form and parameter setting as Eq. (6.10).

6.2.4 Muscle

Biological Function

The anatomical muscle structure of *C. elegans* has been discussed in Section 5.2.1 and shown in Fig. 5.2. It is well known that the periodical contraction and relaxation of

the muscles generate the undulatory wave, but how this wave being propagated is still an open issue.

In *Ascaris*, the body wall muscles are electrically coupled by gap junctions and appear to propagate the undulatory wave independently of the nervous system [117]. Similarly, it may not be surprised that *C. elegans* muscles have a similar pattern generating (or pattern modulation) role in locomotion. Thus, for a recent model in [61], the strong gap junction coupling is adopted to propagate the undulatory signal through the body. However, two latest experimental results indicate that the gap junctions between muscles are insufficient to propagate bending signal between neighboring body regions [95, 103]. Without using the muscles, another choice for the wave propagation is the motor neurons since they are connected by gap junctions. However, from the biological wire diagram, as shown in Fig. 6.2, these motor neurons are not fully connected, e.g. VB7 and VB8. So it is still a problem by using the motor neurons alone to propagate the undulatory wave.

Recently, a research work [103] has uncovered this issue. It claims that except a CPG near the head generates the undulatory wave of the most anterior segment, the proprioceptive coupling between muscles and motor neurons also can generate and propagate the undulatory wave. The bending of one body region requires the bending of its anterior neighbor and the muscle activity is positively correlated with the curvature of adjacent anterior neighbors. B-type motor neurons are directly responsible for this proprioceptive coupling. The phase lag of undulatory wave is produced by the neuromuscular delay, which is yielded by the synaptic transmission and/or the limiting speed of muscle contraction.

Muscle Modeling

Ventral (dorsal) muscle cells receive both excitatory and inhibitory inputs from VB (DB) and VD (DD) motor neurons, respectively. By following [95], the inputs to the ventral side and dorsal side muscles are

$$I_{V,i} = \sum_{j=1}^{11} w_{mVB,ij} V_{VB,j} + \sum_{j=1}^{13} w_{mVD,ij} V_{VD,j}, \quad (6.12)$$

$$I_{D,i} = \sum_{j=1}^6 w_{mDD,ij} V_{DD,j} + \sum_{j=1}^7 w_{mDB,ij} V_{DB,j}, \quad (6.13)$$

where $V_{VB,j}$, $V_{VD,j}$, $V_{DD,j}$ and $V_{DB,j}$ are the voltages of motor neurons VB_j , VD_j , DD_j and DB_j , respectively. $w_{mVB,ij}$, $w_{mVD,ij}$, $w_{mDD,ij}$ and $w_{mDB,ij}$ are the connection weights from neurons VB_j , VD_j , DD_j and DB_j to muscle cell i , respectively.

The activation states of muscles are represented by the variable $A_{M,i}^D$ and $A_{M,i}^V$ for the dorsal side and ventral side muscles in segment i , respectively [95],

$$\tau_M \frac{dA_{M,i}^{(D,V)}}{dt} = I_{(V,D),i} - A_{M,i}^{(D,V)}, \quad (6.14)$$

where τ_M is the time constant, and $I_{(V,D),i}$ comes from Eqs. (6.12) and (6.13). The muscle activation state decides the muscle length. We modify Eqs. (5.7)-(5.10) to represent the relation between the muscle activation state and the muscle length.

$$l_{D,i} = l_0 + \sigma_l(A_{M,i}^D), \quad (6.15)$$

$$l_{V,i} = l_0 + \sigma_l(A_{M,i}^V), \quad (6.16)$$

where $l_{D,i}$ and $l_{V,i}$ are the lengths of muscles in segment i on the dorsal side and ventral side, respectively. l_0 is the muscle length when relaxing.

The muscle activation function $\sigma_l(\cdot)$ is

$$\sigma_l(x) = \frac{A_l}{1 + \exp(-k_l(x - A_M^0))} + b_l, \quad (6.17)$$

where A_l , k_l , A_M^0 and b_l are constants should be determined and their values are provided in Section 6.3.

6.2.5 Body Segment

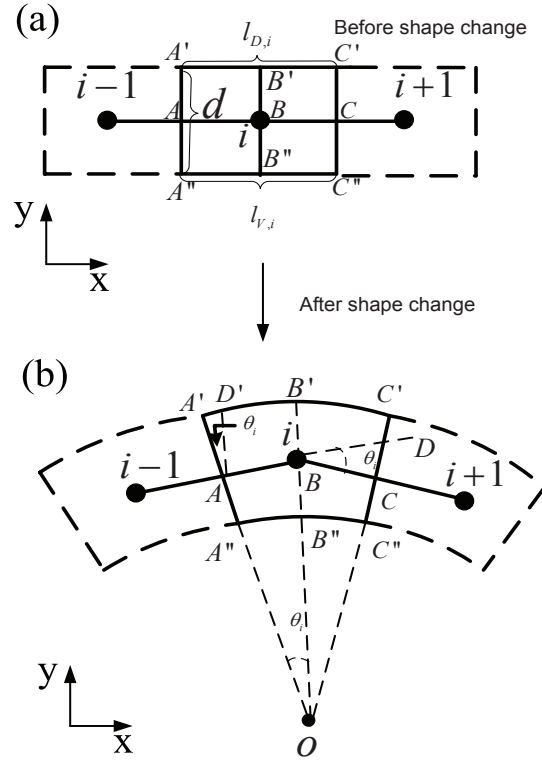


Figure 6.3: (a) One body segment without body changing. (b) One body segment with body changing.

In this chapter, the body of *C. elegans* is divided into 10 segments according to the muscle structure and represented as a multi-joint rigid link system with 12 joints and 11 links, as shown in Fig. 5.2. Each segment without shape changing is shown in Fig. 6.3(a). During locomotion, the muscle segment will change its shape, as shown in Fig. 6.3(b). Thus, we need to explore how the body shape changing influences the joint angle θ .

As shown in Fig. 6.3(a), for the segment i , the dorsal side muscle is $l_{D,i}$ in length and the ventral side muscle is $l_{V,i}$ in length, represented as $A'C'$ and $A''C''$, respectively. The original lengths of $l_{D,i}$ and $l_{V,i}$ are equal to l_0 . During locomotion, muscles change their lengths, so the shape of muscle as shown in Fig. 6.3(a) will change to the shape as shown in Fig. 6.3(b). Let the length of each link be l_0 , so in Fig. 6.3(b) $|AB| = \frac{l_0}{2}$ and $|A'A| = \frac{d}{2}$. It can be proved that $\angle DBC = \angle A'OB' = \theta_i$, and drawing $D'A//B'B$ yields $\angle A'AD' = \theta_i$ and $|AB| = |D'B'| = \frac{l_0}{2}$. Thus,

$$\begin{aligned}
 l_{D,i} &= |\widehat{A'C'}| = 2|\widehat{A'B'}| \\
 &= 2(|\widehat{A'D'}| + |\widehat{D'B'}|) \\
 &= 2\left(\frac{d}{2}\theta_i + \frac{l_0}{2}\right) \\
 &= l_0 + d\theta_i.
 \end{aligned} \tag{6.18}$$

Following the same way, the relation between $l_{V,i}$ and θ_i is:

$$l_{V,i} = l_0 - d\theta_i. \tag{6.19}$$

After resolving Eqs. (6.18) and (6.19), we obtain

$$\theta_i = \frac{l_{D,i} - l_{V,i}}{2d}. \tag{6.20}$$

From Eq. (6.20), we can observe that the joint angle θ_i is determined by the difference of muscle length between the dorsal and ventral muscles. Furthermore, $l_{D,i}$ and $l_{V,i}$ are determined by the outputs of motor neurons, referring Eqs. (6.12)-(6.16). Once the connection weights from motor neurons to muscles are determined, the muscles will change their lengths according to the outputs of the motor neurons.

6.3 Testing Results

In this section, we first provide the method to train our model and the parameter setting. Next, we test the chemotaxis behavior of our model for finding food and avoiding toxin in different scenarios. Third, the trajectories of our model are analyzed quantitatively by comparing with the experiment results. Last, the well trained wire diagrams are simplified, and two patterns are found.

6.3.1 Optimization and Parameter Setting

Body Optimization

Because of the very complicated neuronal and neuromuscular connections, as shown in Figs. 6.1 and 6.2, our first step for training is to simplify the wire diagram. From the neuromuscular structure, we assume that two ventral side (dorsal side) muscles are controlled by one motor neuron in the same muscle segment. In our model, the neuromuscular connections are listed in Table 6.1. As discussed in Section 6.2.5, we use 10 joint (refer to Fig. 5.2) to represent the 12 muscle segments. The last joint represents the last three muscle segments since only one B-type motor neuron (DB7) controls these dorsal side muscles, as shown in Fig. 6.2.

Table 6.1: Neuromuscular connection

Joint	Muscle segment	Ventral muscle	Dorsal muscle
1	1	RMDV	RMDD
2	2	SMBV	SMBD
3	3	SMDV	SMDD
4	4	VB1 VD1 VD2	DB1 DD1
5	5	VB2 VD3	DB2 DD2
6	6	VB3 VD4	DB3 DD3
7	7	VB4 VB5 VD5 VD6	DB4 DD4
8	8	VB6 VB7 VD7 VD8	DB5
9	9	VB8 VB9 VD9 VD10	DB6 DD5
10	10,11,12	VB10 VB11 VD11 VD12 VD13	DB7 DD6

To propagate the undulatory wave from head to tail, the motor neurons receive the curving status of their anterior muscles and active their connected muscles in current muscle segment. The curving status of muscles in the current segment can be sensed by the posterior motor neurons, which active the posterior muscles. In this way, the undulatory wave could be translated. For simplification, in our model each motor neuron for segment i only receives the curving status of muscles in segment $i - 1$.

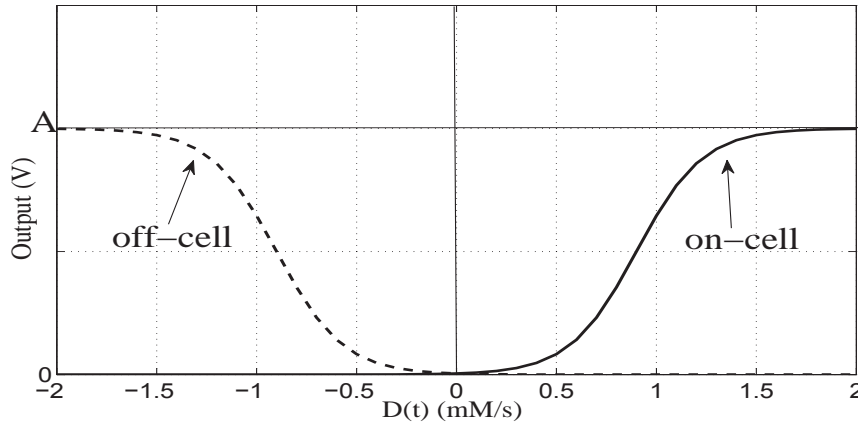


Figure 6.4: Activations of *on-cell* and *off-cell* according to temporal concentration difference.

Head Optimization

The head wire diagram in our model generates the undulatory wave and the turning signal that are transmitted to the motor neurons. Three sensory neurons (ASEL, ASER, ASH) as the input neurons receive the food (ASEL and ASER) and toxin (ASH) concentrations. ASEL and ASH are *on-cells*, whereas ASER is *off-cells*. According to Eqs. (6.1)-(6.3), these sensory neurons can compute the temporal concentration difference by themselves. The activations of *on-cell* and *off-cell* following the temporal concentration difference are shown in Fig. 6.4. The output of *on-cell* (solid line) is positive when $D(t)$ (temporal concentration difference) is greater than 0. Otherwise it maintains to be 0. *off-cell* (dashed line) has the opposite logic to *on-cell*.

The outputs of the three sensory neurons will be transmitted to their connected interneurons and finally to the motor neurons. In our model, the head wire diagram is a three-layer DNN. The input layer contains three sensory neurons and output layer contains two motor neurons (RMDV, RMDD). Except for three interneurons (RIG, URY, RIB) that function as CPG, others interneurons form the second layer. We use Eq. (5.1) to be the activation function of these interneurons.

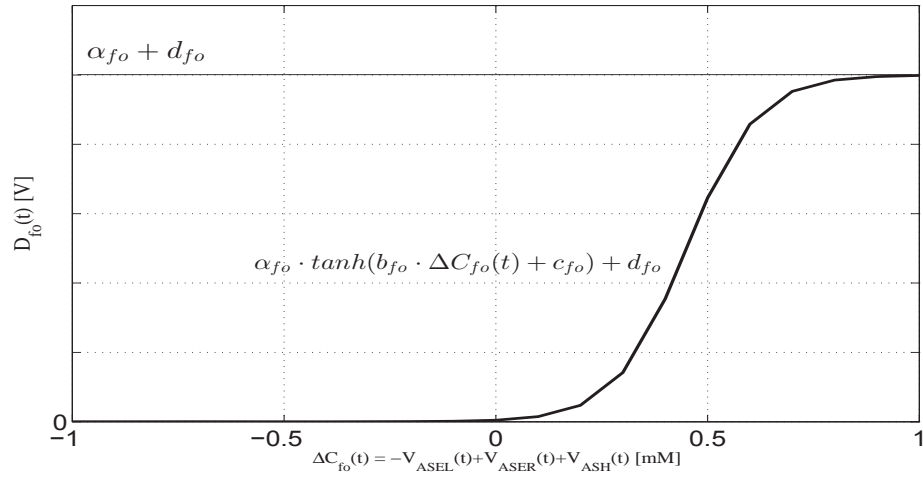


Figure 6.5: SLF for the chemotaxis behavior of *C. elegans*.

To achieve the decision making for chemotaxis, we construct the SLF to represent the chemotaxis behavior of *C. elegans*, as shown in Fig. 6.5. SLF for finding food and avoiding toxin is

$$D_{fo}(t) = \alpha_{fo} \cdot \tanh(b_{fo} \cdot \Delta C_{fo}(t) + c_{fo}) + d_{fo}, \quad (6.21)$$

where $D_{fo}(t)$ is the desired output of SLF. α_{fo} , b_{fo} , c_{fo} and d_{fo} are parameters to control the shape of SLF.

$$\Delta C_{fo}(t) = -V_{ASEL}(t) + V_{ASER}(t) + V_{ASH}(t), \quad (6.22)$$

where $V_{ASEL}(t)$, $V_{ASER}(t)$ and $V_{ASH}(t)$ are outputs of sensory neurons ASEL, ASER and ASH at time t , respectively. According to [54, 56, 57], ASEL and ASER cannot active at the same time. For food attraction, when *C. elegans* is towards the correct direction, *on-cell* ASEL will active to be a positive value $V_{ASEL}(t)$. $-V_{ASEL}(t)$ is a negative value that suppresses the output of $D_{fo}(t)$ to be zero, as shown in Fig. 6.5. Contrarily, when *C. elegans* is towards the wrong direction, *off-cell* ASER will be activated to a positive value, which generates a turning signal to the motor neurons. For avoiding toxin, once the temporal toxin concentration difference is greater than zero, $V_{ASH}(t)$ is a positive value, which generates the turning signal since $D_{fo}(t) > 0$.

To train the head wire diagram, we adopt the method in Chapter 4 to construct the training data. There are three inputs for the training data with the range $[-2, 2]$ and two outputs (target data) with the range $[0, 1]$. The head wire diagram is trained by Differential Evolution (DE). The details of DE have been discussed in Section 5.5.1.

Other Parameter Setting

Except for the parameters obtained by DE, other parameters are obtained by trial and error, which are listed in Table 6.2.

Table 6.2: Parameters setting

Parameter	Value	Description
M	1 s	Time duration in Eq.(6.1)
N	1 s	Time duration in Eq.(6.2)
A	1	Magnitude of activation function in Eq.(6.3)
k_s	6.5	Steepness of activation function in Eq.(6.3)
x_0	-1	Constant in activation function Eq.(6.3)
τ_{RIG}	2	Time constant for CPG in Eq.(6.6)
τ_{RIB}	2	Time constant for CPG in Eq.(6.6)
τ_{URY}	0	Time constant for CPG in Eq.(6.6)
C_B	0.01	Time constant for motor neuron in Eq.(6.9)
G_B	1	Membrane conductance in Eq.(6.9)
E_{rev}	0	Constant for cell's potential in Eq.(6.9)

A_p	43.5	Magnitude of activation function for proprioceptive feedback in Eq.(6.10)
k_p	0.2	Steepness of activation function for proprioceptive feedback in Eq.(6.10)
l_0	1 mm	Original muscle length in Eqs.(6.10), (6.15) and (6.16)
b_p	-21.75	Constant for proprioceptive feedback activation function in Eq.(6.10)
τ_M	0.01	Time constant for muscle activation function in Eq.(6.14)
A_l	9.23	Magnitude of muscle activation function in Eq.(6.17)
k_l	0.2	Steepness of muscle activation function in Eq.(6.17)
A_M^0	0	Constant for muscle activation function in Eq.(6.17)
b_l	-4.62	Constant for muscle activation function in Eq.(6.17)
α_{fo}	0.5	Parameters for the magnitude of SLF in Eq.(6.21)
b_{fo}	6	Parameters for the steepness of SLF in Eq.(6.21)
c_{fo}	2.7	Parameters for the location of SLF in Eq.(6.21)
d_{fo}	0.5	Parameters for the location of SLF in Eq.(6.21)

6.3.2 Chemotaxis Behavior

To test the chemotaxis behavior of our model, we put it into three different scenarios: (1) only one food source existed, and (2) both food and toxin existed with concentration slightly overlapped and (3) heavily overlapped.

One Food Source

As shown in Fig. 6.6, one food source is located at (0,0) with Gaussian distribution. *C. elegans* starts at four different locations, (20, 60), (57, 28), (-20, -40) and (-42, -14), respectively. It moves towards the food source and finally moves around it. From the resting result, we can observe that *C. elegans* has successfully achieved the task of finding food.

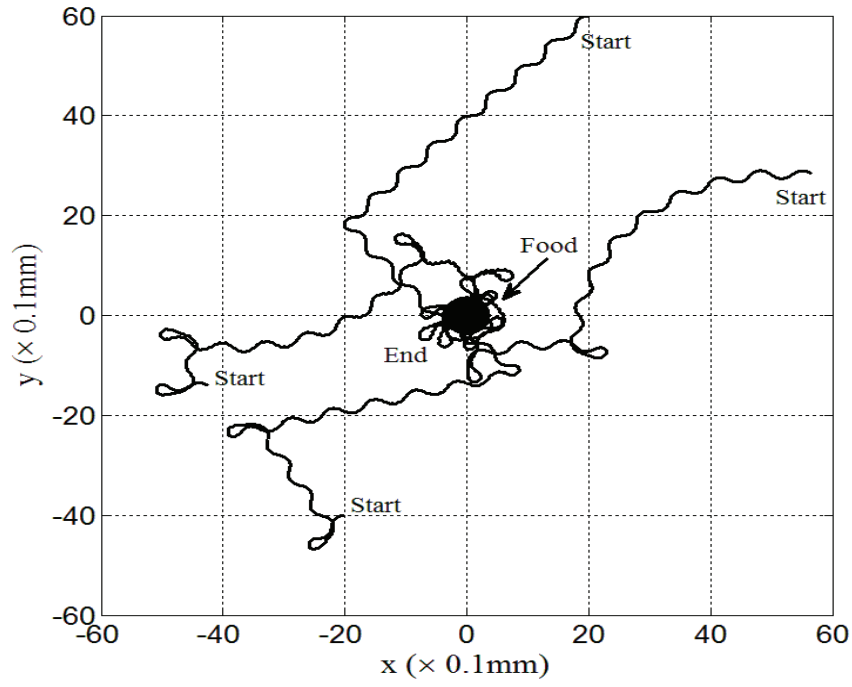


Figure 6.6: Testing result in the scenario that only one food is existed.

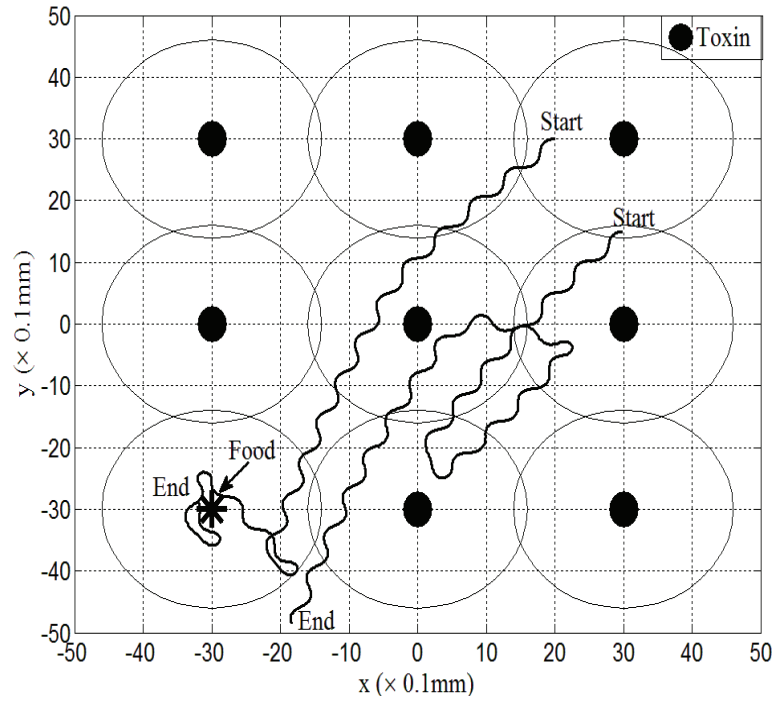


Figure 6.7: Testing result in the scenario that food and toxin concentrations are slightly overlapped.

Food and Toxin Concentrations Slightly Overlapped

To test whether our model can perform the task of finding food and avoiding toxin simultaneously, we construct the scenario with nine sources distributed as a 3×3 grid. As shown in Fig. 6.8, except for the asterisk located at $(-30, -30)$ denotes the food source, other eight dots denote the toxin sources. The circular lines are the boundaries of food and toxin concentrations. In the test, *C. elegans* starts at two different locations $(30, 15)$ and $(20, 30)$, respectively. From the trajectory starting from $(30, 15)$, it is obvious that *C. elegans* escapes from the toxin and finally settles down at the place where no toxin concentration exists. When starting from $(20, 30)$, *C. elegans* escapes from the toxin sources first. Once it smells the food concentration, it moves towards the food source and finally surrounds it.

Food and Toxin Concentrations Heavily Overlapped

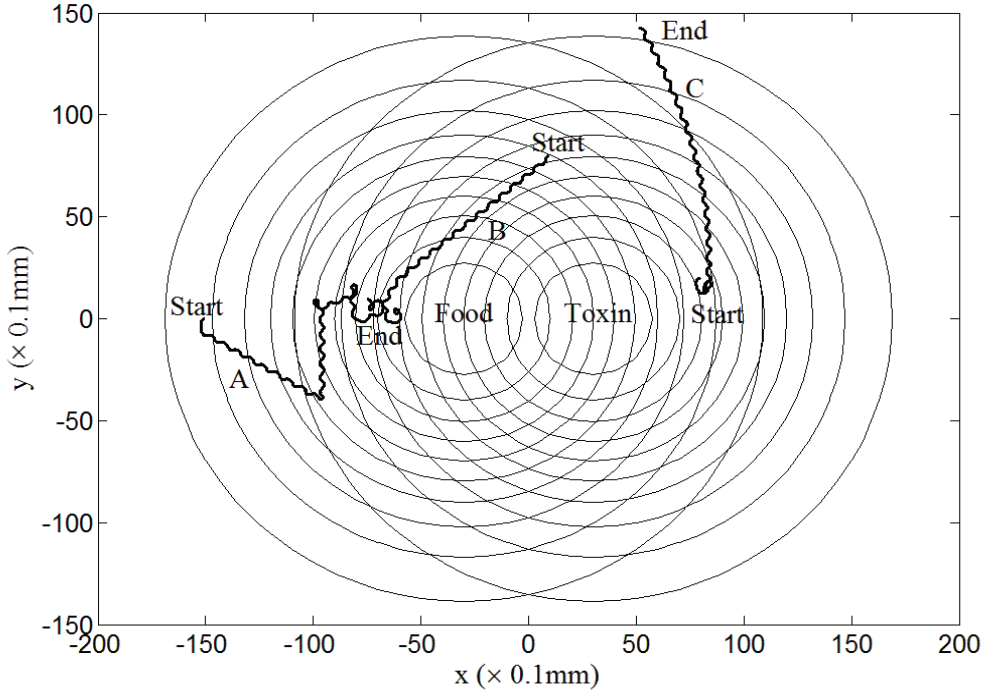


Figure 6.8: Testing result in the scenario that food and toxin concentrations are heavily overlapped.

In this test, we construct the scenario in which one food source and one toxin source are located at $(-30, 0)$ and $(30, 0)$, respectively, with concentrations largely overlapped, as shown in Fig. 6.8. The gradient distributions of the food and toxin concentrations can refer to Fig. 4.14(b). When the food and toxin concentrations overlap heavily, the best place for the worm is $(-65.72, 0)$, which has been discussed in Section 4.6.2. When starting from the point $(-150, 0)$, *C. elegans* moves towards the food and finally settles down around the target place at $(-65.72, 0)$ (track A). When *C. elegans* starts from $(10, 90)$, where both food and toxin concentrations exist, the worm avoids the toxin and approaches the food. Finally, it settles down at the target place $(-65.72, 0)$ (track B). When starting from the point $(60, 20)$, where both toxin and food concentrations exist, *C. elegans* avoids the toxin and navigates itself faraway from the toxin source. Finally, it settles down at the place without toxin concentration (track C).

6.3.3 Quantitative Analysis

To analyze the performance of our model, we provide the quantitative analysis of the trajectories by comparing with the results as shown in Fig. 5.20. Following the same method in Section 5.7.3, we investigate the relations between: (1) turning rate and concentration by following the method in [19]; (2) average curving rate and $dC(t)/dt$; and (3) probability of turning and $dC(t)/dt$ by following the method in [87]. The result is shown in Fig. 6.9.

In Fig. 6.9 (a) we can observe the turning rate weakly depends on the food concentration (solid line), and it is similar to the experiment result of [19] (dashed line). The relation between average curving rate and $dC(t)/dt$ is shown in Fig. 6.9 (b) (solid line). In this figure, the larger negative value of $dC(t)/dt$ yields the larger magnitude of curving rate. However, once $dC(t)/dt$ is positive, the curving rate reduces to zero. This result is

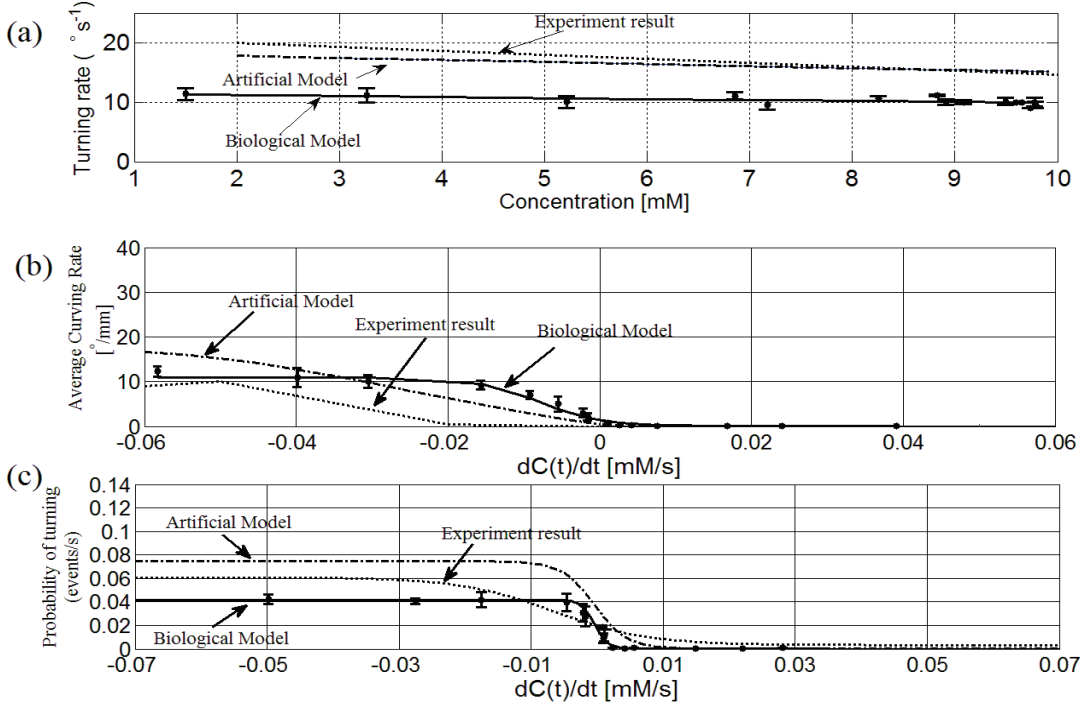


Figure 6.9: Quantitative analysis of the trajectories for food attraction. (a) The relation between turning rate and concentration. (b) The relation between average curving rate and $dC(t)/dt$. (c) The relation between probability of turning and $dC(t)/dt$.

similar to the experiment data of [87] (dotted line). The relation between probability of turning and $dC(t)/dt$ is shown in Fig. 6.9 (c). Following the method in [87], our result can be approximated by formula $y = 0.023/(a + e^{bx+d}) + c$, where y is the probability of turning, and x is the change of concentration $dC(t)/dt$, and a, b, c, d are constants. For our case, the values of these parameters are $a = 0.55, b = 1000, c = 0$, and $d = -0.2$, and the formula is plotted as the solid line. The experiment data of [87] is plotted as the dashed line and their parameters are $a = 0.40, b = 140, c = 0.0033$, and $d = 0$. From Fig. 6.9 (c), we can observe that our result is similar to the experiment result.

However, by comparing the solid lines and dash-dot lines in Fig. 6.9, we can observe that the results between our artificial model and biological model are different. By inspecting the trajectories in Fig. 6.6 and Fig. 5.14, the trajectories for the artificial model are smoother than those for the biological model, and more straight trajectories and sharp

turns appear for the biological model. These differences may account for the low turning rate, curving rate and turning probability for the biological model. Furthermore, deeper exploration is needed in the future work to uncover these differences.

6.3.4 Wire Diagram Patterns

We simplify the well trained head wire diagrams by following the method in [25] and find out two patterns, as shown in Figs. 6.10(a) and (b), respectively.

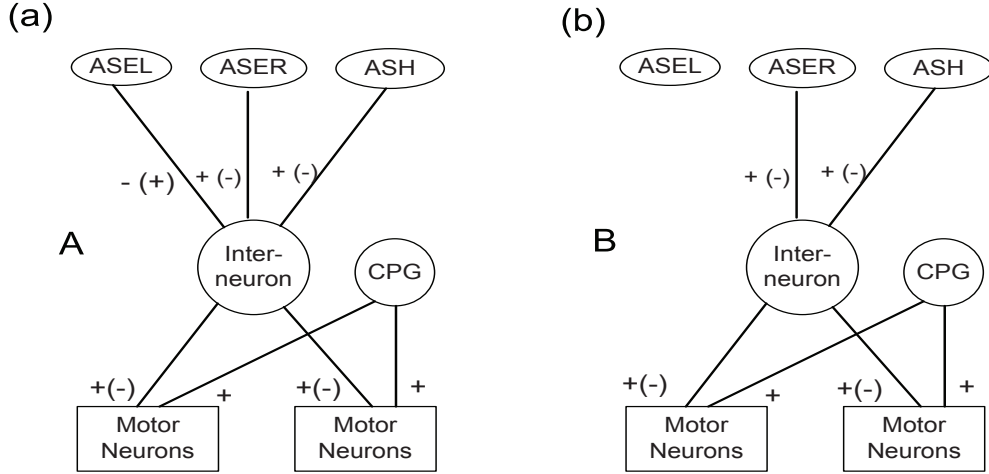


Figure 6.10: (a) The first pattern contains three sensory neurons. (b) The second pattern contains two sensory neurons.

The difference between two patterns is that in pattern A there exists the connection between ASEL and interneuron, whereas in pattern B, this connection is extremely weak and even eliminated. However, wire diagrams for both patterns can achieve the same task as finding food and avoiding toxin. Our result corresponds with the experimental result that the chemotaxis behavior of *C. elegans* is not impaired heavily after ASEL is ablated [118]. Furthermore, there exist two sub-patterns within either pattern A or B. The difference between two sub-patterns is the opposite signs of the weights from sensory neurons to motor neurons, as shown in Fig. 6.10.

6.4 Worm-like Robot

In this section, a worm-like robot has been constructed to perform the undulatory locomotion based on the theoretical results of this chapter. First, we describe the hardware components, which involve eight actuators, one micro-controller, two wireless modules, one distance sensor, one battery, and several connection equipments. Then, we illustrate the way to assemble these hardware components to be the worm-like robot. Last, we provide the experimental results for the forward and backward movements, as well as the turning behaviors.

6.4.1 Hardware Components

Actuators



Figure 6.11: Servomotor Dynamixel AX-12A

The actuator used in the robot is the AX-12 model under the Dynamixel series from ROBOTIS, as shown in Fig. 6.11. One of the key differences with the cheap and common servo motors is its ability to provide feedback information. It can provide feedback on angular position, angular velocity, load torque, motor temperature, etc. All these feedback information can be used in a closed loop system to implement highly complex algorithms. It should be noted that communication protocol for this kind of

actuator is based on half duplex serial (only 1 pin for receive and transmit), which is not supported by most micro-controller boards. Most of the micro-controllers these days provide support for only full duplex (separate pins for receive and transmit) serial communication and this limits the choices of micro-controllers that can be used for this robot.

Micro-controller

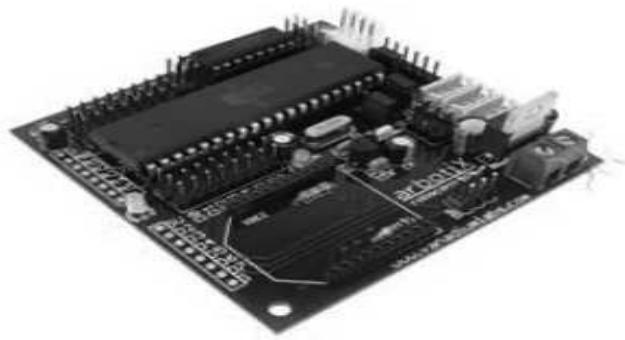


Figure 6.12: ArbotiX micro-controller

The micro-controller board used in this robot is the Arbotix RoboController from Vanadium Labs, as shown in Fig. 6.12. It provides the necessary half duplex serial communication support required by the chosen actuator AX-12. It also features an XBee wireless module which is based on the popular ZigBee protocol. It has complete compatibility with Arduino Integrated Development Environment (IDE) and provides support for most of the existing Arduino libraries.

XBee Wireless Module

The wireless module used for this project is the popular XBee module which follows the ZigBee wireless protocols, as shown in Fig. 6.13. The main reason behind choosing this wireless module is that the chosen micro-controller board has a built in socket for



Figure 6.13: XBee wireless module

this module. Also, it is highly compatible with Arduino based platforms, making wireless serial communication simple and convenient to perform.

Distance Sensor



Figure 6.14: Distance sensor

For the distance sensor, an ultrasonic range finder from Maxsonar is used, as shown in Fig. 6.14. It emits an ultrasonic beam and senses the echo reflected from any object in front. Depending on the time it takes for the echo to reflect back, it can determine the reflecting object's distance. It can theoretically detect objects from about 0 – 765 cm with very high resolution.

Battery

The AX-12 actuators require at least 7V for operation while the recommended range is around 11V. The Arbotix RoboController recommends a Lithium Polymer battery of 11.1V for reliable power supply to both the micro-controller as well as the actuators.



Figure 6.15: Battery

For this project, the Thunder Power RC 11.1V LiPo G6 Pro Lite battery is used. The battery is shown in Fig. 6.15.

6.4.2 Components Assembly

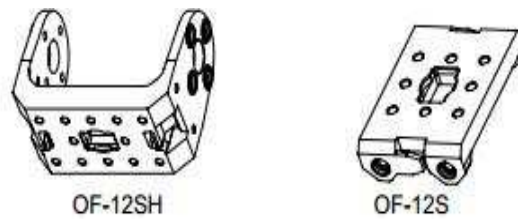


Figure 6.16: Frames

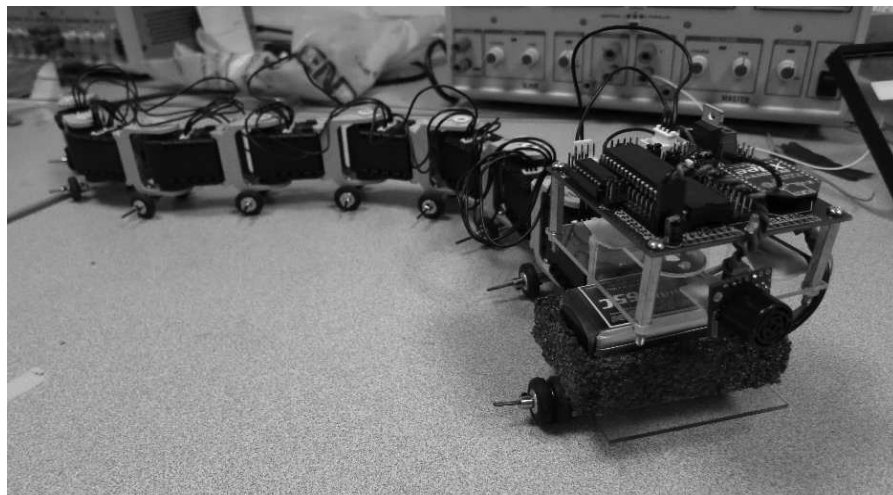


Figure 6.17: Worm-like robot

The body of the worm-like robot is formed by the actuators which are connected by

special frames. These frames are shown as Fig. 6.16. The frame named OF-12SH is the one that is connected to the moving part of the AX-12 actuator. The frame named OF-12S is just used to connect the rotating part of one actuator to the back side of the next actuator. Eight actuators are connected serially like a train to form the basic framework of the robot, as shown in Fig. 6.17. For attaching wheels underneath the body, 20 wheels with diameter 18 mm are used.

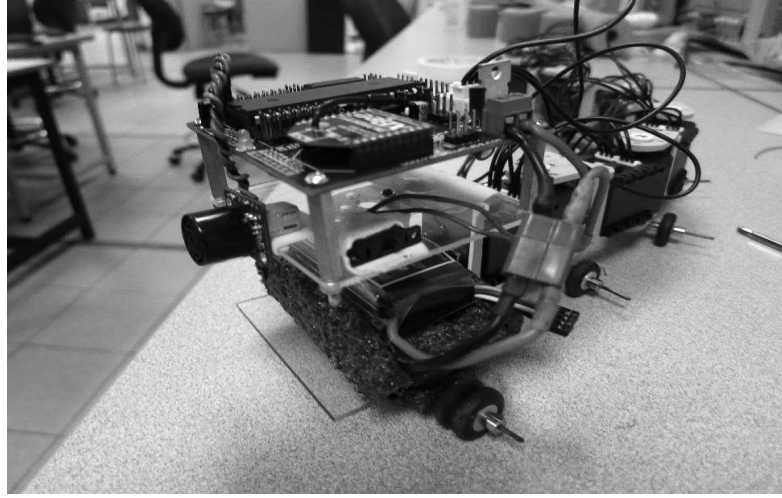


Figure 6.18: Head of the worm-like robot

The head of the robot, as shown in Fig. 6.18, is constructed to carry the micro-controller board, the distance sensor and the battery. There are two pieces of 2 mm transparent acrylic boards to compose the head frame. The top frame is assigned the task of holding the micro-controller board, and the bottom acrylic board is assigned the task of containing the battery. The distance sensor is fixed onto the top acrylic board.

6.4.3 Experimental Results

To control a particular actuator to turn a particular angular position, a value must be written to the memory location called “Goal Position”. Therefore, the serial data should include the actuator ID, the memory location address and the value to be written

in this location. The value of ID can range from 0 to 255, and 254 is the broadcast ID, meaning providing this value on the serial bus that will communicate with all the actuators in the network at once. AX-12 has a 10 bit resolution and an operating angle of 0 – 300 degrees. Thus, the whole operating range is divided into numbers represented within the range from 0 to 1023, with the resolution being $300/1023 = 0.294$ degrees. This means changing the value by 1 changes the angle by 0.294 degrees. As shown in

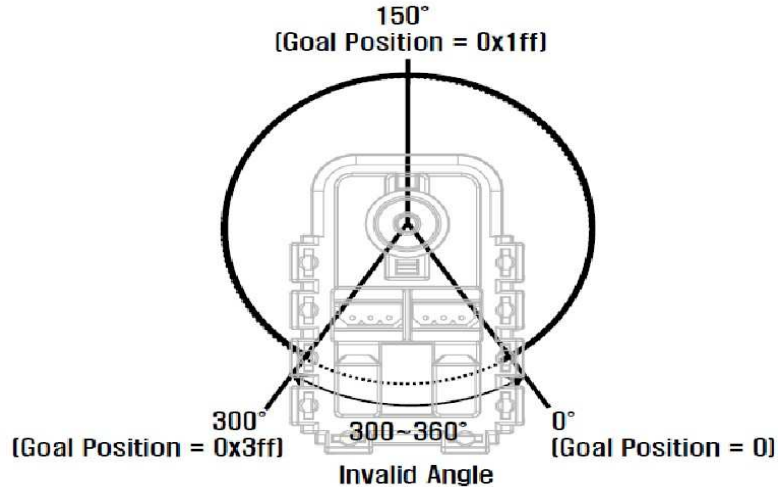


Figure 6.19: Ax-12 Goal Position

Fig. 6.19, the middle position is 150 degrees. To move the actuator to a certain angle x , for example, the value that must be written to the memory location “Goal Position” is

$$\text{ActuatorData} = (1023/300) * x = 3.41 * x \quad (6.23)$$

In order to write any serial value to the actuator control table, Arbotix RoboController board has a specialized built in library that can perform all the low level serial communication, making it highly convenient and easy to use. Using the functions of this library, values can be written to or read from any of the memory locations present inside the actuator control table.

Forward/Backward Locomotion

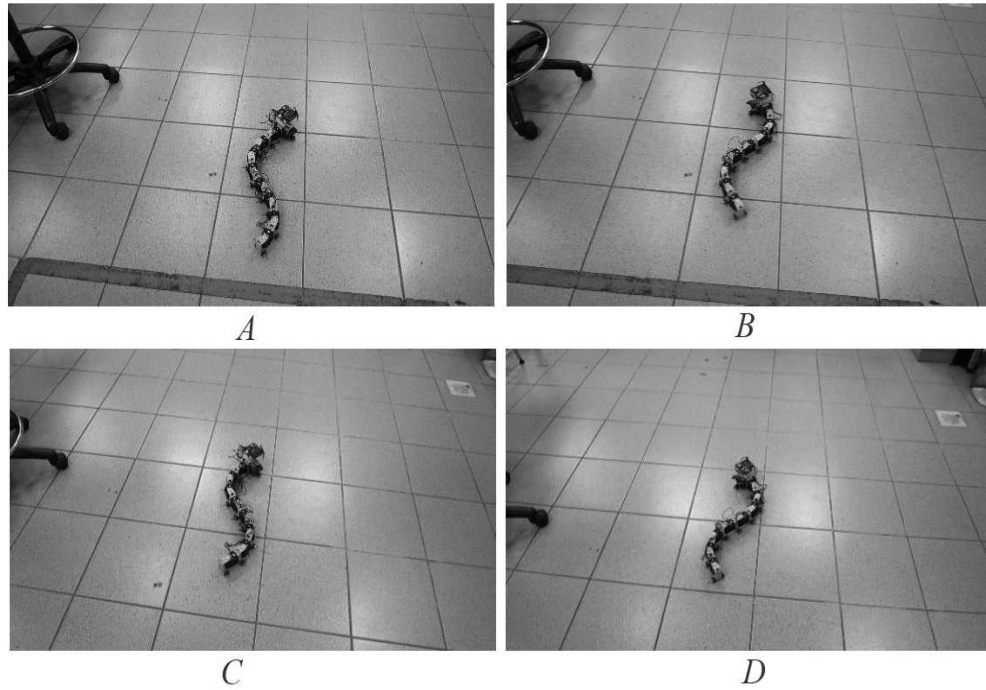


Figure 6.20: Forward locomotion

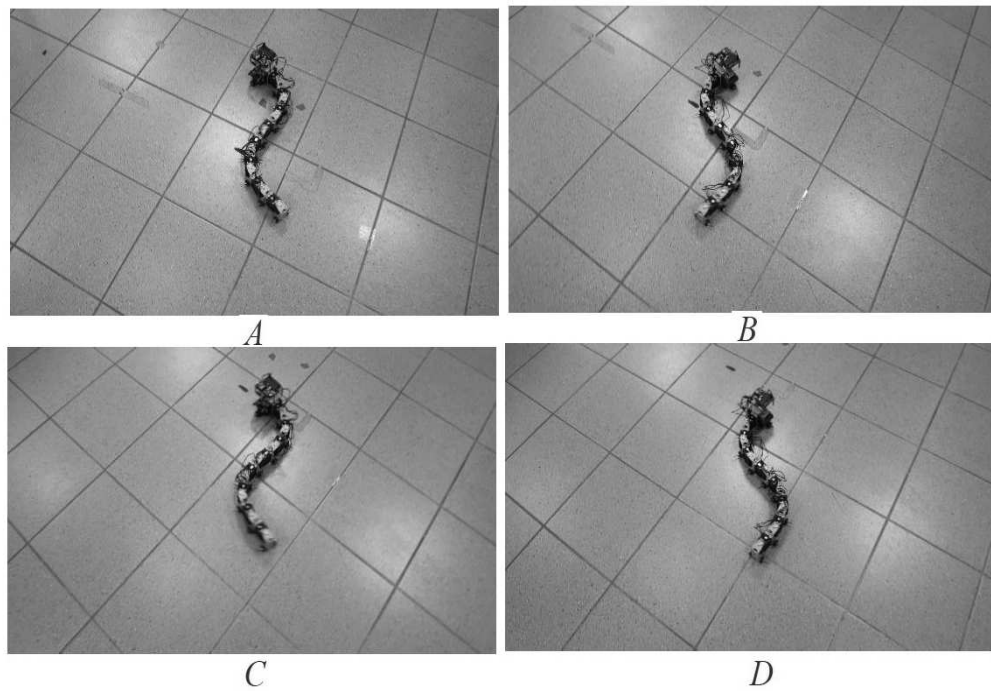


Figure 6.21: Backward locomotion

The forward locomotion of the robot is shown in Fig. 6.20. The wave travels along the robot's body as it performs lateral undulation to move forward. Figs. 6.20 A to D show the different positions of the robot as it creates the undulatory locomotion.

For backward locomotion, the wave is propagated in the opposite direction comparing with the wave for the forward locomotion. As shown in Fig. 6.21, two small patches can be seen in the plots. Judging from the change in position of these patches relative to the robot as we move from A to D, the robot is moving backward.

Turning Behaviors

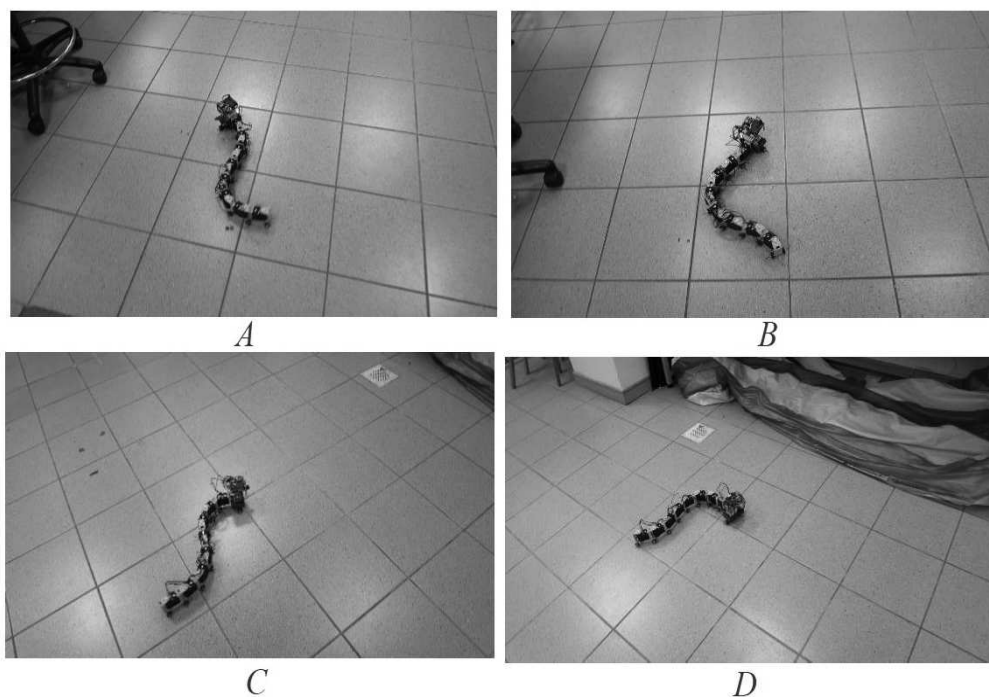


Figure 6.22: Right-side turning

With the same parameters for the forward locomotion, the right-side turning behavior is achieved by adding the deflection angle of 5 degrees or 0.0873 radians to the servomotors when they rotate towards the right side. The figures as shown in Fig. 6.22 demonstrate the right-side turning of the robot while moving forward.

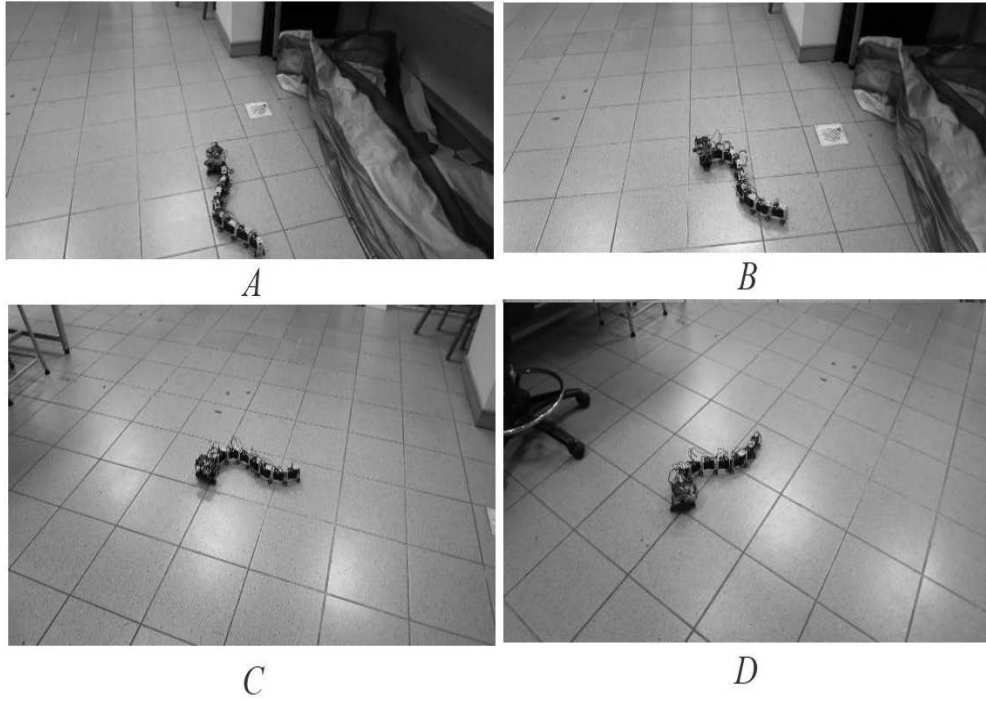


Figure 6.23: Left-side turning

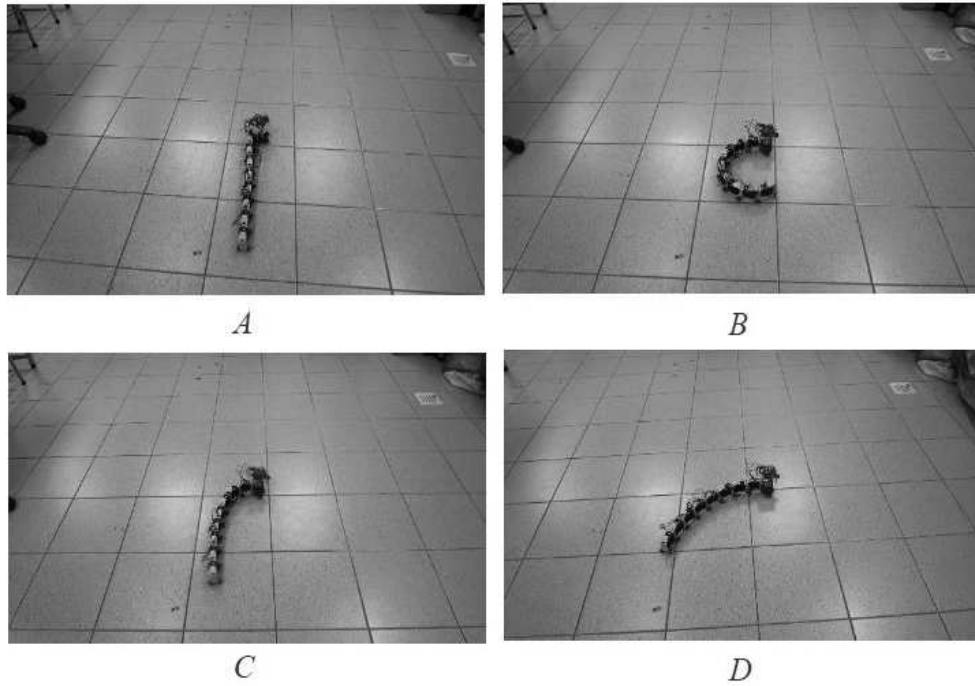


Figure 6.24: C-shape towards the right-side

Fig. 6.23 shows the left-side turning of the robot while moving forward. The left-side turning behavior is achieved by adding the deflection angle of 5 degrees or 0.0873 radians

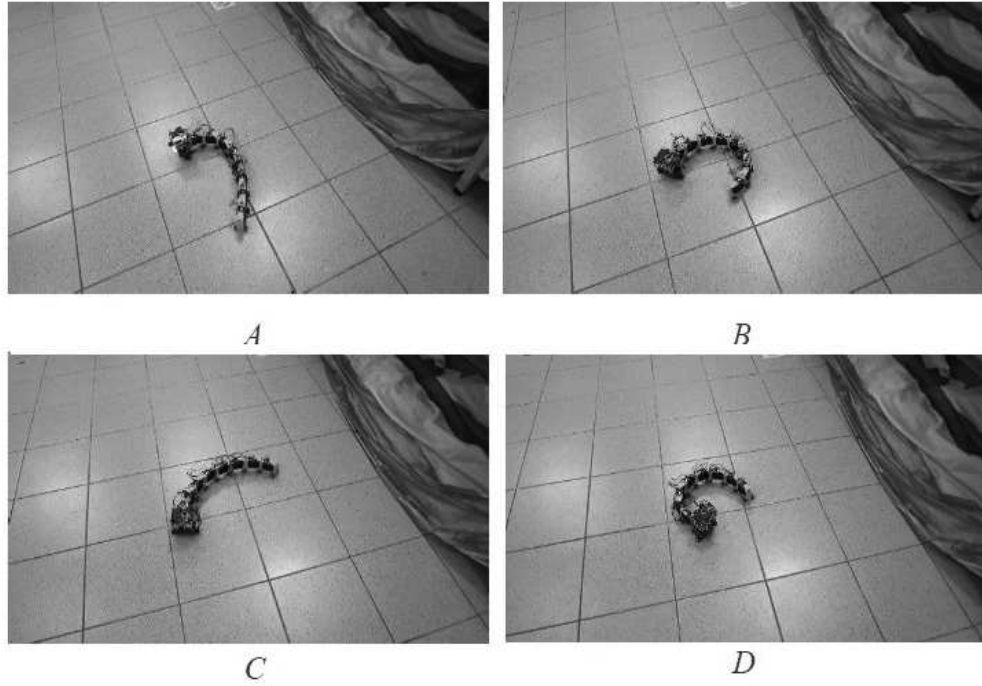


Figure 6.25: C-shape towards the left-side

to the servomotors when they rotate towards the left side.

C-shape Movement

In the experiment, we use the robot to the mimic the C-shape movement of *C. elegans*, which happens when it is in water. Fig. 6.24 shows the C-shape movement towards the right-side, and Fig. 6.25 shows the C-shape movement towards the left-side. As can be seen from these figures, the robot coils up into a C-shape and then returns to the zero position, which allows the robot to turn very sharply within a short distance.

6.5 Conclusion and Discussion

In this chapter, we investigate the undulatory locomotion of *C. elegans* based on the biological neural wire diagram and muscle structure. A locomotion model is developed to perform the chemotaxis behavior of finding food and avoiding toxin. First, the nervous

system is divided into two parts: the head DNN and the motor neurons of the body. The head DNN produces the turning signal and generates the sinusoid wave. The motor neurons control the activations of muscles. The proprioceptive mechanism is adopted, which makes the motor neurons have the ability to detect the curving grade of the anterior muscles. Incorporated with the proprioceptive mechanism, the undulatory wave can be propagated even the motor neurons are not fully connected biologically. Second, 11 multi-joint rigid links are adopted to represent the body. Each joint stands for the center of its corresponding muscle segment. Third, muscle models are constructed, in which the muscle lengths vary according to the outputs of DNN. Fourth, the joint angles are controlled by the muscle lengths, and the relation between the angles and muscle lengths are determined. Fifth, the latest biological results are adopted to model the sensory neurons, e.g. *on-cell* and *off-cell*. Sixth, in the testing part, the proposed model performs well for the chemotaxis behaviors of finding food and avoiding toxin. The quantitative analysis is also provided to verify the effectiveness of our model. At last, a worm-like robot has been constructed to perform the forward and backward movements, right-side and left-side turning, and C-shape movement.

The main differences between the models in Chapter 5 and Chapter 6 involve four aspects. First, the model in Chapter 5 is a bio-inspired model (artificial model), whose nervous system and muscular structure are not based on the anatomical structure of *C. elegans*. By contrast, the model in Chapter 6 is a biological model, whose nervous system and muscular structure are strictly based on the anatomical structure of *C. elegans*.

Second, the artificial model in Chapter 5 performs the snake-like locomotion in 3D, whereas the biological model in Chapter 6 performs the undulatory locomotion in 2D. The artificial model is based on the idea in [61]. However, the work of [61] does not provide

the kinematics model and its model cannot move, even for the chemotaxis behaviors. Thus, in Chapter 5 a 3D locomotion model inspired from *C. elegans* is constructed to perform the snake-like undulatory locomotion. The biological model can only perform the 2D undulatory locomotion because till now the mainstream viewpoint is that *C. elegans* restricts its performance in 2D. However, in future once the locomotion of *C. elegans* has been proved biologically in 3D, we can initiate the work to study how the biological model to perform the 3D undulatory locomotion.

Third, there is a head DNN in the artificial model that functions as the differentiator for the decision making of turning. Sensory neurons in the head DNN only function as the input neurons. However, in the biological model this differentiation function is achieved by the sensory neurons themselves. The sensory neurons are classified into *on-cell* and *off-cell*. Every *on-cell* and *off-cell* can produce the turning signal according to the gradient of input concentration.

Forth, the methods to propagate the undulatory waves are different. For the artificial model, the undulatory waves are transmitted by the motor neurons. However, for the biological model, the proprioceptive mechanism is adopted and the undulatory waves are transmitted by the cooperation of both muscles and motor neurons.

Furthermore, both artificial and biological models share two similarities. One is that there are a group of neurons serving as the pattern generator to produce the undulatory wave in the head. The other one is that the head DNNs in both models are trained to learn the SLFs for decision making and they can be optimized to smaller ones.

Chapter 7

Conclusions

7.1 Summary and Conclusion

This thesis investigates the chemotaxis behavior and undulatory locomotion of *C. elegans* by using both artificial and biological neural networks. The detailed modeling of chemotaxis behavior and undulatory locomotion of *C. elegans* has revealed the decision making mechanism of its nervous system, as well as the coordination mechanism of the nervous system and muscles.

In Chapter 2, the artificial models and in Chapter 3 the biological models are constructed to investigate the chemotaxis behavior of *C. elegans*. Two artificial and six biological behavioral models are constructed for food attraction, toxin avoidance, and integrated behaviors. The eight behavioral models are clustered into two groups, dual-sensory behavioral model and single-sensory behavioral model. The dual-sensory behavioral model uses the spatial concentration difference for navigation while the single-sensory behavioral model uses the temporal concentration difference for navigation. The wire diagram for each model is represented by a DNN, and each neuron is described as a nonlinear active function. We investigate the food attraction and toxin avoidance behaviors separately at the beginning, and then an integrated chemotaxis behavioral model

is exploited to perform the two behaviors simultaneously. In these models, the sensory neuron ASE receives the food concentration and ASH receives the toxin concentration. The neuron AIY serves as a memory neuron in the single-sensory behavioral model to record the concentration at the previous time for computing the temporal concentration gradient, which makes *C. elegans* have the ability to move towards the food or escape the toxin. To represent the chemotaxis behaviors, a set of nonlinear switching logic functions (SFLs) are introduced to map the relation between temporal gradient information of concentration (input) and motor neuron (output) that decides the navigation. SFLs in our work are inspired biologically and can mimic the logic of the brain cooperated with DNN. Once having learned SFLs, DNN can regenerate its corresponding chemotaxis behavioral motions.

In Chapters 2 and 3, we model the chemotaxis behavior of *C. elegans* base on the point of view that its speed is a constant. In Chapter 4, we have incorporated the speed regulation mechanism into these chemotaxis behavioral models so that the navigation is complete with the orientation control and speed control. By following the same method in Chapter 3, we explore the dual-sensory model, single-sensory model, and integrated behavioral model for finding food and avoiding toxin. The testing results show that *C. elegans* could not only approach the food source (avoid the toxin source), but also reduce its speed when getting close to the food source (far away from the toxin source) in different circumstances. We also quantitatively analyze the behaviors of our models by comparing with the experimental data, which verifies the effectiveness and authenticity of our models.

In Chapters 5, we extend our research to the undulatory locomotion behavior of *C. elegans*, and a 3D undulatory locomotion model is provided based on the artificial DNN.

According to the muscle structure, the whole body is represented as a multi-joint rigid link model. The 3D shape is determined by the joint angles projected onto the sagittal plane and the coronal plane. The relations between these joint angles and the lengths of four quadrant muscles are determined. Once the muscles receive the sinusoid waves from DNN, their lengths would change accordingly, which yield the variations of the joint angles. In the test part, the undulatory locomotion behavioral model is tested in different scenarios. In each scenario, *C. elegans* successfully performs the undulatory locomotion to approach the food source or escape the toxin source. We also have quantitatively analyzed our results and compared them with other work and found some similar results.

In Chapters 6, instead of the artificial DNN, we investigate the undulatory locomotion behavior of *C. elegans* directly on its biological neural wire diagram and muscle structure. The same as Chapters 5, the biological undulatory behavioral model can perform the undulatory locomotion to approach the food source or escape the toxin source. Furthermore, we also quantitatively analyze our results and compare them with other work. At last, a worm-like robot has been constructed to perform the undulatory behavior based on the theoretical results.

From the whole work, there are six points are concluded. First, the chemotaxis behaviors of *C. elegans* can be represented as a set of non-linear functions, which provide a new way to model the animal's behaviors. These nonlinear functions are constructed based on the logic of chemotaxis behaviors and the well trained models can be put into different environments to perform their desired tasks. The methods to design these nonlinear functions are not unique, and different forms of functions can be designed as long as the logic is correct.

Second, we verify the major chemotaxis strategy for *C. elegans*: biased turning. In

the thesis, all the locomotion models successfully achieve the chemotaxis behaviors even though they can only turn towards the ventral side. It proves that biologically the mechanism of biased turning is sufficient to accomplish the chemotaxis behaviors.

Third, there should be a group of neurons that function as the differentiator for the decision making of *C. elegans* during chemotaxis. From the analysis of the optimized wire diagrams, the inhibitory feedbacks are found for interneurons. The function of the inhibitory feedback is to regulate the response latency of the system's output relative to its input. Such regulation would be significant in the *C. elegans* nervous system to calculate the differentiation information $dC(t)/dt$.

Forth, the artificial undulatory model in Chapter 5 based on the anatomical structure of *C. elegans* can well perform the 3D snake-like undulatory locomotion. To implement the 3D movement, two undulatory waves should be transmitted through the body simultaneously: waves on the horizontal plane and on the vertical plane. The frequency of the wave on the vertical plane is doubled for that on the horizontal plane.

Fifth, biologically the motor neurons of *C. elegans* are not fully connected and the gap junctions between muscles are insufficient to propagate bending signal between neighboring body regions. It raises the problem that whether *C. elegans* uses the motor neurons or muscles alone to propagate the undulatory wave. The model in Chapter 6 by incorporating the proprioceptive mechanism well addresses the problem. A circuit near the head generates the undulatory wave for the most anterior segment, and the proprioceptive coupling between muscles and motor neurons is responsible for propagating the undulatory wave.

Sixth, the redundancy phenomenon of the sensory neuron is found in the locomotion model. In Chapter 6, we analyzed the well optimized models and found that the sensory

neuron ASEL can be eliminated for some models without affecting their chemotaxis behaviors. From the result we predicate that ASEL could serve as the redundant sensory neuron of ASEH, and this predication is supported by the experimental result that the chemotaxis behavior of *C. elegans* is not impaired after ASEL is ablated.

7.2 Suggestions for Future Work

While the results of this thesis have some contributions in the engineering field, we are still a long way from the ultimate goal of a complete understanding of the chemotaxis behaviors and undulatory locomotion of *C. elegans*. For the next step, we will investigate the 3D undulatory locomotion of *C. elegans* based on its biological structure. Furthermore, the 3D locomotion robot inspired by *C. elegans* will also be investigated. The structure of one segment of 3D robot is shown in Fig. 7.1, and the conceptual image of the 3D robot is shown in Fig. 7.2. Our final goal to construct the 3D robot is to benefit our life, e.g. for rescuing survivors, military use, and clinical use.

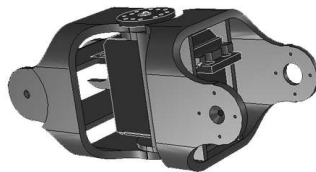


Figure 7.1: Structure of one segment of 3D robot



Figure 7.2: 3D worm-like robot

In the end, we should mention that the whole work in the thesis is based on the engineering point of view. However, the methods and results from biology are also very important to improve our efficiency and quality. In future work, we would better combine the experimental and modeling communities and this combined effort can yield results far beyond what could be achieved by either approach alone. Modelers cannot leave far away from the biological reality, and experimentalists should hold the principles of computational modeling and keep them in mind when designing experiments. Finally, we should learn to recognize the strengths of each other, as well as the weaknesses of ours.

Bibliography

- [1] Z. F. Altun and D. H. Hall. WormAtlas [Online]. Available: <http://www.wormatlas.org>.
- [2] T. M. Morse, T. C. Ferrée, and S. R. Lockery. Robust Spatial Navigation in a Robot Inspired by Chemotaxis in *Caenorhabditis elegans*. *Adaptive Behavior*, 6:391–408, 1998.
- [3] T. C. Ferrée, B. A. Marcotte, and S. R. Lockery. Neural Network Models of Chemotaxis in the Nematode *Caenorhabditis Elegans*. *Advances in Neural Information Processing Systems*, 9:55–61, 1996.
- [4] S. Brenner. Nature’s gift to science, 2002. [http://nobelprize.org/nobel prizes](http://nobelprize.org/nobel_prizes).
- [5] M. Chalfie. GFP: Lighting up life, 2008. [http://nobelprize.org/nobel prizes](http://nobelprize.org/nobel_prizes).
- [6] A. Z. Fire. Gene silencing by double stranded RNA, 2006. [http://nobelprize.org/nobel prizes](http://nobelprize.org/nobel_prizes).
- [7] H. R. Horvitz. Worms, life and death, 2002. [http://nobelprize.org/nobel prizes](http://nobelprize.org/nobel_prizes).
- [8] C. C. Mello. Return to the RNAi world: Rethinking gene expression and evolution, 2006. [http://nobelprize.org/nobel prizes](http://nobelprize.org/nobel_prizes).

- [9] O. Shimomura. Discovery of green fluorescent protein, GFP, 2008.
[http://nobelprize.org/nobel prizes](http://nobelprize.org/nobel_prizes).
- [10] J. E. Sulston. The cell lineage and beyond, 2002. [http://nobelprize.org/nobel prizes](http://nobelprize.org/nobel_prizes).
- [11] R. Y. Tsien. Constructing and exploiting the fluorescent protein paintbox, 2008.
[http://nobelprize.org/nobel prizes](http://nobelprize.org/nobel_prizes).
- [12] S. Brenner. The genetics of *C. elegans*. *Genetics*, 77:71–94, 1974.
- [13] E. Wolinsky and J. Way. The behavioral genetics of *C. elegans*. *Behavior Genetics*, 20:169–189, 1990.
- [14] J. G. White, E. Southgate, J. N. Thomson, and S. Brenner. The Structure of the Nervous System of the Nematode *Caenorhabditis elegans*. *Phil. Trans. R. Soc. Lond. B*, 314:1–340, 1986.
- [15] C. I. Bargmann and H. R. Horvitz. Chemosensory Neurons with Overlapping Functions Direct Chemotaxis To Multiple Chemicals in *C. elegans*. *Neuron*, 7(5):729–742, 1991.
- [16] D. B. Dusenbery. Analysis of chemotaxis in the nematode *C. elegans* by counter current separation. *Journal of Experimental Zoology*, 188:41–47, 1974.
- [17] S. Ward. Chemotaxis by the nematode *C. elegans*: identification of attractants and analysis of the response by use of mutants. *Proceedings of the National Academy of Sciences*, 70:817–821, 1973.

- [18] J. M. Gray, J. J. Hill, and C. I. Bargmann. A circuit for navigation in *Caenorhabditis elegans*. *Proceedings of the National Academy of Sciences of the United States of America*, 102(9):3184–3191, 2005.
- [19] J. T. Pierce-Shimomura, T. M. Morse, and S. R. Lockery. The fundamental role of pirouettes in *Caenorhabditis elegans* chemotaxis. *Journal of Neuroscience*, 19(21):9557–9569, 1999.
- [20] G. J. Stephens, B. Johnson-Kerner, W. Bialek, and W. S. Ryu. From Modes to Movement in the Behavior of *Caenorhabditis elegans*. *PLoS ONE*, 5(11):1–7, 2010.
- [21] S. R. Lockery. The computational worm: spatial orientation and its neuronal basis in *C. elegans*. *Current Opinion in Neurobiology*, 21(5):728–790, 2011.
- [22] T. Kawano, M. D. Po, S. Gao, G. Leung, W. S. Ryu, and M. Zhen. An Imbalancing Act: Gap Junctions Reduce the Backward Motor Circuit Activity to Bias *C. elegans* for Forward Locomotion. *Neuron*, 72(4):572–586, 2011.
- [23] B. J. Piggott, J. Liu, Z. Feng, S. A. Wescott, and X. Z. Shawn Xu. The Neural Circuits and Synaptic Mechanisms Underlying Motor Initiation in *C. elegans*. *Cell*, 147(4):922–933, 2011.
- [24] J. X. Xu and X. Deng. Biological modeling of complex chemotaxis behaviors for *C. elegans* under speed regulation: a dynamic neural networks approach. *Journal of Computational Neuroscience*, 35:19–37, 2013.
- [25] N. A. Dunn. *A Novel Neural Network Analysis Method Applied to Biological Neural Networks*. PhD thesis, University of Oregon, 2006.

- [26] R. E. Davis and A. O. Stretton. Passive membrane properties of motoneurons and their role in long-distance signaling in the nematode *Ascaris*. *Neuroscience*, 9:403–414, 1989.
- [27] T. H. Lindsay, T. R. Thiele, and S. R. Lockery. Optogenetic analysis of synaptic transmission in the central nervous system of the nematode *Caenorhabditis elegans*. *Nature Communications*, 2:306, 2011.
- [28] N. K. Sinha, M. M. Gupta, and D. H. Rao. Dynamic neural networks: an overview. In *Proceedings of IEEE International Conference on Industrial Technology*, pages 491–496, 2000.
- [29] E. Niebur and P. Erdős. *Computer simulation in brain science*, chapter Computer simulation of networks of electrotonic neurons, pages 148–163. Cambridge University Press, Cambridge, UK, 1988.
- [30] P. Erdős and E. Niebur. The neural basis of the locomotion of nematodes. *Lecture Notes in Physics*, 368:253–267, 1990.
- [31] E. Niebur and P. Erdős. Theory of the locomotion of nematodes: Dynamics of undulatory progression on a surface. *Biophysical Journal*, 60:1132–1146, 1991.
- [32] J. A. Bryden and N. Cohen. Neural control of *Caenorhabditis elegans* forward locomotion: the role of sensory feedback. *Biological Cybernetics*, 98:339–351, 2008.
- [33] J. H. Boyle, J. A. Bryden, and N. Cohen. An integrated neuro-mechanical model of *C. elegans* forward locomotion. *LNCS*, 4984:37–47, 2008.

- [34] S. Berri, J. H. Boyle, M. Tassieri, I. A. Hope, and N. Cohen. Forward locomotion of the nematode *C. elegans* is achieved through modulation of a single gait. *HFSP Journal*, 3:186–193, 2009.
- [35] N. Cohen and J. H. Boyle. Swimming at low Reynolds number: a beginner’s guide to undulatory locomotion. *Contemporary Physics*, 51:103–123, 2010.
- [36] J. H. Boyle, S. Berri, M. Tassieri, I. A. Hope, and N. Cohen. Gait modulation in *C. elegans*: It’s not a choice, it’s a reflex! *Frontiers in Behavioral Neuroscience*, 5(10):1–3, 2011.
- [37] J. H. Boyle, S. Berri, and N. Cohen. Gait Modulation in *C. elegans*: An Integrated Neuromechanical Model. *Front Comput. Neurosci.*, 6:1–15, 2012.
- [38] K. N. Bao, J. H. Boyle, A. A. Dehghani-Sani, and N. Cohen. A *C. elegans*-inspired micro-robot with polymeric actuators and online vision. In *IEEE International Conference on Robotics and Biomimetics (ROBIO)*, 2009.
- [39] J. H. Boyle, S. Johnson, and A. A. Dehghani-Sani. Adaptive Undulatory Locomotion of a *C. elegans* Inspired Robot. *IEEE/ASME Transactions on Mechatronics*, 18:1–10, 2013.
- [40] M. Suzuki, T. Goto, T. Tsuji, and H. Ohtake. A Motor Control Model of the Nematode *C. elegans*. In *Proc. of IEEE International Conference on Robotics and Biomimetics*, 2005.
- [41] M. Suzuki, T. Tsuji, and H. Ohtake. A model of motor control of the nematode *C. elegans* with neuronal circuits. *Artificial Intelligence in Medicine*, 35:75–86, 2005.

- [42] M. Suzuki, T. Tsuji, and H. Ohtake. A Neuromuscular Model of *C. elegans* with Directional Control. In *Proc. Of the First International Conference on Complex Medical Engineering*, pages 167–172, 2004.
- [43] M. Suzuki, T. Tsuji, and H. Ohtake. A dynamic body model of the nematode *C. elegans* with a touch-response circuit. In *Proc. of the IEEE International Conference on Robotics and Biomimetics (ROBIO)*, pages 538–543, 2005.
- [44] T. C. Ferrée and S. R. Lockery. Chemotaxis control by linear recurrent networks. In *Proc. of the sixth annual conference on Computational neuroscience: trends in research*, pages 373–377, 1998.
- [45] T. C. Ferrée and S. R. Lockery. Computational rules for chemotaxis in the nematode *C. elegans*. *Journal of Computational Neuroscience*, 6(3):263–277, 1999.
- [46] N. A. Dunn, J. S. Conery, and S. R. Lockery. Circuit Optimization Predicts Dynamic Networks for Chemosensory Orientation in the Nematode *Caenorhabditis elegans*. *Advances in Neural Information Processing Systems*, 16:1279–1286, 2004.
- [47] N. A. Dunn, S. R. Lockery, J. T. Pierce-Shimomura, and J. S. Conery. A neural network model of chemotaxis predicts functions of synaptic connections in the nematode *Caenorhabditis elegans*. *Journal of Computational Neuroscience*, 17(2):137–147, 2004.
- [48] N. A. Dunn, J. T. Pierce-Shimomura, J. S. Conery, and S. R. Lockery. Clustered Neural Dynamics Identify Motifs for Chemotaxis in *Caenorhabditis elegans*. In *Proc. of the International Joint Conference on Neural Networks (IJCNN’06)*, pages 547–554, 2006.

- [49] N. A. Dunn and S. R. Lockery. Circuit motifs for spatial orientation behaviors identified by neural network optimization. *Journal of Neurophysiology*, 98:888–897, 2007.
- [50] M. B. Goodman, D. H. Hall, L. Avery, and S. R. Lockery. Active Currents Regulate Sensitivity and Dynamic Range in *C. elegans* Neurons. *Neuron*, 20:763–772, 1998.
- [51] A. C. Miller, T. R. Thiele, S. Faumont, M. L. Moravec, and S. R. Lockery. Step-response analysis of chemotaxis in *Caenorhabditis elegans*. *Journal of Neuroscience*, 25:3369–3378, 2005.
- [52] J. T. Pierce-Shimomura, S. Faumont, M. R. Gaston, B. J. Pearson, and S. R. Lockery. The homeobox gene *lim-6* is required for distinct chemosensory representations in *C. elegans*. *Nature*, 410:694–698, 2001.
- [53] C. O. Ortiz, J. F. Etchberger, S. L. Posy, C. Frokjar-Jensen, S. Lockery, B. Honig, and O. Hobert. Searching for neuronal left/right asymmetry: Genome wide analysis of nematode receptor-type guanylyl cyclases. *Genetics*, 173:131–149, 2006.
- [54] T. R. Thiele, S. Faumont, and S. R. Lockery. The Neural Network for Chemotaxis to Tastants in *Caenorhabditis elegans* Is Specialized for Temporal Differentiation. *The Journal of Neuroscience*, 29(38):11904–11911, 2009.
- [55] J. T. Pierce-Shimomura, M. Does, and S. R. Lockery. Analysis of the effects of turning bias on chemotaxis in *C. elegans*. *Journal of Experimental Biology*, 24:4727–4733, 2005.

- [56] E. J. Izquierdo and S. R. Lockery. Evolution and analysis of minimal neural circuits for klinotaxis in *Caenorhabditis elegans*. *Journal of Neuroscience*, 30(39):12908–12917, 2010.
- [57] S. Faumont, T. H. Lindsay, and S. R. Lockery. Neuronal microcircuits for decision making in *C. elegans*. *Current Opinion in Neurobiology*, 22(4):580–591, 2012.
- [58] K. Sakata and R. Shingai. Neural network model to generate head swing in locomotion of *Caenorhabditis elegans*. *Network: Computation in Neural Systems*, 15(3):199–216, 2004.
- [59] S. Thill and C. P. Thill. Understanding complex behaviors by analyzing optimized models: *C. elegans* gradient navigation. *HFSP Journal*, 1(4):263–273, 2007.
- [60] M. Rönkkö and G. Wong. Modelling the *C. elegans* nematode and its environment using a particle system. *Journal of Theoretical Biology*, 253:316–322, 2008.
- [61] J. Karbowski, G. Schindelman, C. J. Cronin, A. Seah, and P. W. Sternberg. Systems level circuit model of *C. elegans* undulatory locomotion: mathematical modeling and molecular genetics. *Journal of Computational Neuroscience*, 24:253–276, 2008.
- [62] R. Mailler, J. Avery, J. Graves, and N. Willy. A Biologically Accurate 3D Model of the Locomotion of *Caenorhabditis Elegans*. In *Proc. of the International Conference on Biosciences*, pages 84–90, 2010.
- [63] H. Yuk, J. H. Shin, and S. Jo. Design and Control of Thermal SMA based small crawling robot mimicking *C. elegans*. In *Proceeding of the IEEE International Conference on Intelligent Robots and Systems*, pages 407–412, 2010.

- [64] H. Yuk, D. Kim, H. Lee, S. Jo, and J. H. Shin. Shape memory alloy-based small crawling robots inspired by *C. elegans*. *Bioinspiration & Biomimetics*, 6:046002, 2011.
- [65] L. F. Wang, K. C. Tan, and C. M. Chew. *Evolutionary Robotics: From Algorithms to Implementations*. World Scientific, 2006.
- [66] H. J. Tang, K. C. Tan, and Y. Zhang. *Neural Networks: Computational Models and Applications*. Springer-Verlag, 2007.
- [67] M. M. Gupta, L. Jin, and N. Homma. *Static and Dynamic Neural Networks*. John Wiley and Sons, 2003.
- [68] Y. Fang and T. G. Kincaid. Stability analysis of dynamical neural networks. *IEEE Transactions on Neural Networks*, 7(4):996–1006, 1996.
- [69] S. Hu and J. Wang. Global stability of a class of discrete-time recurrent neural networks. *Transactions on Circuits and Systems I*, 49(8):1104–1117, 2002.
- [70] Y. Zhang and K. K. Tan. *Convergence analysis of recurrent neural networks*. Kluwer Academic Publishers, Boston, Hardbound, 2004.
- [71] K. Patan. Stability analysis and the stabilization of a class of discrete-time dynamic neural networks. *IEEE Transactions on Neural Networks*, 18(3):660–673, 2007.
- [72] D.P. Mandic and J. Chambers. *Recurrent neural networks for prediction: Learning algorithms, architectures and stability*. John Wiley & Sons, Inc., 2001.
- [73] W. Maass. Networks of Spiking Neurons: The Third Generation of Neural Network Models. *NeuralNetworks*, 10(9):1659–1671, 1997.

- [74] P. J. Werbos. Generalization of backpropagation with application to a recurrent gas market model. *Neural Networks*, 1(4):339–356, 1988.
- [75] R. J. Williams and D. Zipser. A Learning Algorithm for Continually Running Fully Recurrent Neural Networks. *Neural Computation*, 1:270–280, 1989.
- [76] Y. Lee, S. H. Oh, and M. W. Kim. The effect of initial weights on premature saturation in back-propagation learning. In *Proc. of the International Joint Conference on Neural Networks*, pages 765–770, 1991.
- [77] M. Saseetharran. Experiments that reveal the limitations of the small initial weights and the importance of the modified neural model. In *Proc. of International Conference on Neural Networks*, pages 442–447, 1996.
- [78] Y. Wu and L. Zhang. The effect of initial weight, learning rate and regularization on generalization performance and efficiency. In *Proc. of International Conference on Signal Processing*, pages 1191–1194, 2002.
- [79] H. Lari-Najafi, M. Nasiruddin, and T. Samad. Effect of initial weights on back-propagation and its variations. In *IEEE International Conference on Systems, Man and Cybernetics*, pages 218–219, 1989.
- [80] L. Hamm, B. Wade Brorsen, and M. T. Hagan. Global optimization of neural network weights. In *Proc. of the International Joint Conference on Neural Networks (IJCNN 2002)*, pages 1228–1233, 2002.
- [81] H. Y. Ye and B. P. Ye. Molecular control of memory in nematode *Caenorhabditis elegans*. *Neuroscience Bulletin*, 24:49–55, 2008.

- [82] K. M. Huang, P. Cosman, and W. R. Schafer. Machine vision based detection of omega bends and reversals in *C. elegans*. *Journal of Neuroscience Methods*, 158(2):323–336, 2006.
- [83] B. L. Chen, D. H. Hall, and D. B. Chklovskii. Wiring optimization can relate neuronal structure and function. *Proceedings of the National Academy of Sciences of the United States of America*, 103(12):4723–4728, 2006.
- [84] N. Bhatla. WormWeb [Online]. Available: <http://www.wormweb.org>.
- [85] D. L. Riddle, T. Blumenthal, B. J. Meyer, and J. R. Preiss, editors. *C. elegans II*. Cold Spring Harbor Laboratory Press, NY, 1997.
- [86] M. C. K. Leung, P. L. Williams, A. Benedetto, C. Au, K. J. Helmcke, M. Aschner, and J. N. Meyer. *Caenorhabditis elegans*: An Emerging Model in Biomedical and Environmental Toxicology. *Toxicological Sciences*, 106(1):5–28, 2008.
- [87] Y. Iino and K. Yoshida. Parallel Use of Two Behavioral Mechanisms for Chemotaxis in *Caenorhabditis elegans*. *Journal of Neuroscience*, 29(17):5370–5380, 2009.
- [88] C. H. Rankin. Nematode Memory: Now, Where Was I? *Current Biology*, 15(10):374–375, 2005.
- [89] R. G. D. Steel and J. H. Torrie. *Principles and Procedures of Statistics*. New York: McGraw-Hill, 1960.
- [90] K. Jim, C. L. Giles, and B. G. Horne. An analysis of noise in recurrent neural networks: convergence and generalization. *IEEE Transactions on Neural Networks*, 7(6):1424–1438, 1996.

- [91] I. Erkmen, A. M. Erkmen, F. Matsuno, R. Chatterjee, and T. Kamegawa. Snake robots to the rescue! *Robotics & Automation Magazine*, 9:17–25, 2002.
- [92] R. J. Webster, J. M. Romano, and N. J. Cowan. Mechanics of Precurved-Tube Continuum Robots. *IEEE Transactions on Robotics*, 25(1):67–78, 2009.
- [93] J. Borenstein and A. Borrell. The omnitread ot-4 serpentine robot. In *Proceedings of IEEE International Conference on Robotics and Automation*, 2008.
- [94] A. Degani, H. Choset, A. Wolf, and M. A. Zenati. Highly articulated robotic probe for minimally invasive surgery. In *Proceedings of IEEE International Conference on Robotics and Automation*, 2006.
- [95] J. H. Boyle and N. Cohen. *Caenorhabditis elegans* body wall muscles are simple actuators. *Biosystems*, 94:170–181, 2008.
- [96] S. Hirose and H. Yamada. Snake-like robots [Tutorial]. *Robotics & Automation Magazine*, 16(1):88–98, 2009.
- [97] D. G. Ivashko, B. I. Prilutsky, S. N. Markin, J. K. Chapin, and I. A. Rybak. Modeling the spinal cord neural circuitry controlling cat hindlimb movement during locomotion. *Neurocomputing*, 52:621–629, 2003.
- [98] G. Bao and Z. Zeng. Analysis and design of associative memories based on recurrent neural network with discontinuous activation functions. *Neurocomputing*, 77(1):101–107, 2012.
- [99] J. G. Taylor. On artificial brains . *Neurocomputing*, 74:50–56, 2010.

- [100] J. X. Xu and X. Deng. Study on Chemotaxis Behaviors of *C. Elegans* Using Dynamic Neural Network Models: From Artificial To Biological Model. *Journal of Biological Systems*, 18:3–33, 2010.
- [101] L. Jin, P. N. Nikiforuk, and M. M. Gupta. Approximation of discrete-time state-space trajectories using dynamic recurrent neural networks. *Automatic Control*, 40(7):1266–1270, 1995.
- [102] N. Kwon, J. Pyo, S. Lee, and J. H. Je. 3-D Worm Tracker for Freely Moving *C. elegans*. *PLoS ONE*, 8(2):e57484, 2013.
- [103] Q. Wen, M. D. Po, E. Hulme, S. Chen, X. Liu, S. W. Kwok, M. Gershow, A. M. Leifer, V. Butler, C. Fang-Yen, T. Kawano, W. R. Schafer, G. Whitesides, M. W-yart, D. B. Chklovskii, M. Zhen, and A. D. T. Samuel. Proprioceptive Coupling within Motor Neurons Drives *C. elegans* Forward Locomotion. *Neuron*, 76:750–761, 2012.
- [104] J. X. Xu and W. Wang. A General Internal Model Approach for Motion Learning. *IEEE Transactions on Systems, Man, and Cybernetics, Part B: Cybernetics*, 38(2):477–487, 2008.
- [105] J. A. Bryden and N. Cohen. A simulation model of the locomotion controllers for the nematode *Caenorhabditis elegans*. In *Proceedings of the Eighth International Conference on the Simulation of Adaptive Behaviour*, pages 183–192, 2004.
- [106] S. Hirose. *Biologically Inspired Robots: Snake-Like Locomotors and Manipulators*. Oxford University Press, Oxford, 1993.

- [107] R. Storn and K. Price. Differential evolution - a simple and efficient heuristic for global optimization over continuous space. *Journal of Global Optimization*, 11:341–359, 1997.
- [108] S. Das and P. N. Suganthan. Differential evolution: A survey of the state-of-the-art. *IEEE Trans. on Evolutionary Computation*, 15(1):4–31, 2011.
- [109] L. Christie. *C. elegans* worms [Online]. Available: <http://www.youtube.com/user/longchristie/videos>.
- [110] V. Padmanabhan, Z. S. Khan, D. E. Solomon, A. Armstrong, K. P. Rumbaugh, and et al. Locomotion of *C. elegans*: A Piecewise-Harmonic Curvature Representation of Nematode Behavior . *PLoS ONE*, 7(7):e40121, 2012.
- [111] R. T. Gray and P. A. Robinson. Stability of random brain networks with excitatory and inhibitory connections. *Neurocomputing*, 72:1849–1858, 2009.
- [112] L. R. Varshney, X. B. L. Chen, X. E. Paniagua, and X. D. H. Hall. Structural Properties of the *Caenorhabditis elegans* Neuronal Network. *PLOS Computational Biology*, 7(2):e1001066, 2011.
- [113] H. Sasakura and I. Mori. Behavioral plasticity, learning, and memory in *C. elegans*. *Current Opinion in Neurobiology*, 23(1):92–99, 2013.
- [114] E. L. Ardiel and C. H. Rankin. Some like it hot: decoding neurotransmission in the worm’s thermotaxis circuit. *The EMBO Journal*, 30:1192–1194, 2011.
- [115] S. H. Chalasani, S. Kato, D. R. Albrecht, T. Nakagawa, L. F. Abbott, and Co. I. Bargmann. Neuropeptide feedback modifies odor-evoked dynamics in *Caenorhabditis elegans* olfactory neurons. *Nature Neuroscience*, 13:615–621, 2010.

- [116] J. Q. White and E. M. Jorgensen. Sensation in a single neuron pair represses male behavior in hermaphrodites. *Neuron*, 75(4):593–600, 2012.
- [117] D. A. Weisblat and R. L. Russell. Propagation of electrical activity in the nerve cord and muscle syncytium of the nematode *Ascaris lumbricoides*. *Journal of Comparative Physiology*, 107:293–307, 1976.
- [118] H. Suzuki, T. R. Thiele, S. Faumont, M. Ezcurra, S. R. Lockery, and W. R. Schafer. Functional asymmetry in *Caenorhabditis elegans* taste neurons and its computational role in chemotaxis. *Nature*, 454:114–117, 2008.

Appendix: Published/Submitted Papers

Journal Paper

- [1] Xin Deng, Jian-Xin Xu. An Undulatory Locomotion Robot Inspired by Nematode *C. elegans*. Preparing. (Chapters based on this work: Chapter 7)

- [2] Xin Deng, Jian-Xin Xu. Modeling the chemotaxis behaviors of *C. elegans* by exploring its undulatory locomotion based on its biological structure. *Journal of Bioinformatics and Computational Biology*. Under review. (Chapters based on this work: Chapter 6)

- [3] Xin Deng, Jian-Xin Xu. Modeling the chemotaxis behaviors of *C. elegans* by exploring its 3D undulatory movement using Neural Networks approach. *Neurocomputing*. Under review after minor revision. (Chapters based on this work: Chapter 5)

- [4] Deqing Huang, Jian-Xin Xu, Xin Deng, and etc. Hybrid Evolutionary Computing Method Based High-Order Peak Filter Design and Application to Compensation of Contact-Induced Vibration in HDD Servo Systems. *Simulation Modeling Practice and Theory*. Under review.

- [5] Xin Deng, Jian-Xin Xu, A 3D Undulatory Locomotion System Inspired by Nematode *C. elegans*, *Bio-Medical Materials and Engineering*. Accepted, 2013. (Chapters based

on this work: Chapter 5)

[6] Jian-Xin Xu, Xin Deng, Biological modeling of complex chemotaxis behaviors for *C. elegans* under speed regulation—A Dynamic Neural Networks approach. *Journal of Computational Neuroscience*, 35, 19–37, 2013. (Chapters based on this work: Chapter 4)

[7] Jian-Xin Xu, Xin Deng. Study on Chemotaxis Behaviors of *C. elegans* Using Dynamic Neural Network Models: From Artificial to Biological Models. *Journal of Biological Systems*, 18, 3–33, 2010. (Chapters based on this work: Chapters 2 and 3)

Conference Paper

[1] Deqing Huang, Jian-Xin Xu, Xin Deng, and etc. GA Based High-Order Peak Filter Design With Application to Compensation of Contact-Induced Vibration in HDD Servo Systems. In *Proceeding of IEEE Congress on Evolutionary Computation (CEC)*, 3380–3387, 2012.

[2] Jian-Xin Xu and Xin Deng, Complex Chemotaxis Behaviors of *C. elegans* with Speed Regulation Achieved by Dynamic Neural Networks, In *Proceeding of IEEE International Joint Conference on Neural Networks (IJCNN)*, 2128–2135, 2012. (Chapters based on this work: Chapter 4)

[3] Jian-Xin Xu, Xin Deng. Biological neural network based chemotaxis behaviors modeling of *C. elegans*. In *Proceeding of IEEE International Joint Conference on Neural Networks (IJCNN)*, 2010. (Chapters based on this work: Chapter 3)

[4] Jian-Xin Xu, Xin Deng, Dongxu Ji. Study on *C. elegans* behaviors using recurrent neural network model. In *Proceeding of IEEE Conference on Cybernetics and Intelligent Systems (CIS)*, 2010. (Chapters based on this work: Chapter 2)